

# System Identification and Calibration Techniques for Force Measurement in Active Magnetic Bearings

Robert Jack Prins

Dissertation submitted to the faculty of the Virginia Polytechnic Institute and State  
University in partial fulfillment of the requirements for the degree of

Doctor of Philosophy  
In  
Mechanical Engineering

Mary Kasarda  
Christopher D. Hall  
Daniel J. Inman  
R. Gordon Kirk  
Donald Leo

December 8, 2005  
Blacksburg, Virginia

**Keywords:** Magnetic bearing, force measurement, Eddy current

Copyright 2005, Robert J. Prins

# System Identification and Calibration Techniques for Force Measurement in Active Magnetic Bearings

Robert Jack Prins

## ABSTRACT

Many processes involving rotating machinery could benefit from the continuous feedback of force applied to the bearings that support the machinery. Such a system could be used to provide diagnostics for process monitoring in a manufacturing application or to provide information for machine health monitoring. Active Magnetic Bearings (AMBs) have the capability to act concurrently as a shaft force sensor and support bearing. This capability stems from the AMB's control system, which is designed to maintain a specific rotor position, regardless of forces acting on the rotor. Researchers have demonstrated the force sensing ability of AMBs; current state of the art methods typically rely on a direct measurement of magnetic flux density as provided by a Hall probe inserted in the magnetic field. In this work, a system identification approach to force measurement is proposed; the proposed approach is applicable to all active magnetic bearings and does not require Hall probes.

Recent developments in system identification of bearing forces (Kasarda et al., 2000) indicate that a different approach is feasible. In the work of Marshall (Marshall et al., 2001), a variety of perturbations are applied to an AMB while the AMB controller signals are interrogated, no outside instrumentation such as force transducers or Hall probes are required. The work of Kasarda and Marshall is the starting point for the work presented here.

The initial work was expanded to include a general characterization of air gap for any rotor position. Although this characterization relies on static testing to identify system parameters, the identified parameters can then be used in the measurement of dynamic forces. The identification procedure provides a measurement of effective air gap length. Effective gap length is used to infer the effective position of the rotor with respect to the stator. This measurement is made for several specific rotor locations. The relationship between the effective rotor positions provided by the identification and the rotor positions reported by the AMB system sensors establishes a coordinate transformation. The procedure is also applied at different shaft rotation angles. In this way, runout can be identified.

## Dedication

First of all I thank Dr Mary Kasarda, my advisor and friend, for the opportunity to pursue this degree. I also wish to thank those that I shared the laboratory space with over my time here; Travis Bash, Eric Stasiunas, and Eric Blumber, for the camaraderie.

My parents, Ray and Gert Prins, have always been supportive of me regardless of endeavor. I am happy to have the opportunity to thank them in person as well as here in writing.

Finally, I thank my wife Sam for her love and support during this effort. It's done now!

# Acknowledgements

The author would like to acknowledge the National Science Foundation for supporting the work presented in this dissertation under Grant Number DMI9733124.

I wish to acknowledge my committee members for their efforts and their time, specifically Dr Gordon Kirk, Dr Dan Inman, Dr Chris Hall, and Dr Don Leo. I also wish to acknowledge Dr Mike Seigler for serving as a proxy member.

Dr Mary Kasarda was my advisor and committee chair, I acknowledge her support, her efforts, and her input in this research.

I also acknowledge the input and collaboration of Drs Joe Imlach of Innovative Concepts in Engineering and Christian Ehmann of Darmstadt University.

My wife, Dr Samantha Prins, deserves credit for her efforts both as a sounding board for ideas and for editing and formatting this document.

# Table of Contents

<b>Chapter 1 Introduction.....</b>	<b>1</b>
1.1 introduction.....	1
1.1.1 <i>Contributions</i> .....	3
1.2 Force Generated by Electromagnets .....	5
1.3 Active Magnetic Bearing (AMB) Background .....	6
1.4 AMB Force Measurement Background .....	9
1.5 Development of a Lumped GAP Model.....	11
1.6 Issues Related to Application of Current-Based Force Measurement to rotating systems.....	12
1.6.1 <i>Mechanisms that Effect Force Measurement in Rotating Systems</i> .....	13
1.7 Review of Relevant Literature .....	14
1.7.1 <i>Multi-Point Method (MPM)</i> .....	14
1.7.2 <i>Conventional Current-Based Techniques</i> .....	15
1.7.3 <i>Conventional Flux Based Techniques</i> .....	16
1.7.4 <i>Novel Techniques</i> .....	17
1.7.5 <i>Other Relevant Topics</i> .....	17
1.7.6 <i>Conclusion</i> .....	19
1.8 Overview of Document.....	20
<b>Chapter 2 Experimental Procedure .....</b>	<b>22</b>
2.1 Static Experiments .....	23
2.1.1 <i>Current Perturbation – The Multi-Point Method</i> .....	23
2.1.2 <i>Coordinate Transformation Overview</i> .....	30
2.1.3 <i>Procedure to Determine Effective Rotor Origin (Transform Offset)</i> .....	33
2.1.4 <i>Procedure to Determine Transform Scale and Rotation</i> .....	35
2.1.5 <i>Summary of Static Experiments</i> .....	38
2.2 Dynamic Experiments .....	38
2.2.1 <i>Decimation</i> .....	40
2.2.2 <i>Magnetic Circuit Model</i> .....	40
2.2.3 <i>Curve Fit</i> .....	41
2.2.4 <i>Calculation of Vertical Force</i> .....	41
2.2.5 <i>Reduction and Analysis of Transducer Data</i> .....	41
<b>Chapter 3 Experimental Setup .....</b>	<b>43</b>
3.1 Introduction .....	43
3.1.1 <i>Overview of Experimental Systems</i> .....	43
3.1.2 <i>Overview of Data Acquisition</i> .....	45
3.2 AMB Rotor System Hardware .....	45
3.2.1 <i>Platform 1</i> .....	46
3.2.2 <i>Platform 2</i> .....	50
3.3 Instrumentation Hardware.....	55
3.3.1 <i>AMB System Signals and Calibration</i> .....	55
3.3.2 <i>Force Transducers and Signal Conditioners</i> .....	56
3.4 Data Acquisition .....	56
3.4.1 <i>Data Acquisition Hardware</i> .....	57

3.4.2 Data Acquisition Software .....	57
3.5 Dynamic Effects of Test Platforms .....	57
3.5.1 Base Dynamics - Platform 2 .....	58
<b>Chapter 4 Effective Origin .....</b>	<b>59</b>
4.1 Abstract .....	59
4.2 Introduction .....	59
4.2.1 Applications .....	60
4.2.2 Technique .....	62
4.3 Approach .....	62
4.3.1 AMB Force Measurement Background .....	62
4.3.2 Bias Current Perturbation (Multi-Point Method) .....	64
4.3.3 Determination of the Effective Origin .....	65
4.4 Description of Test Platforms .....	66
4.4.1 Platform 1 .....	66
4.4.2 Platform 2 .....	67
4.5 Experiment .....	67
4.5.1 Experimental Procedure – Platform 1 .....	68
4.5.2 Experimental Results – Platform 1 .....	68
4.5.3 Experimental Procedure – Platform 2 .....	72
4.5.4 Experimental Results – Platform 2 .....	72
4.6 Conclusion .....	74
<b>Chapter 5 Coordinate Transformation .....</b>	<b>75</b>
5.1 Introduction .....	75
5.1.1 AMB Force Measurement Background .....	76
5.1.2 Foundation of Multi-Point Method (MPM) .....	78
5.1.3 Coordinate Transformation Overview .....	78
5.2 Description of Test Platforms .....	80
5.2.1 Platform 1 .....	80
5.2.2 Platform 2 .....	80
5.3 Procedure .....	81
5.3.1 Translation (Effective origin) .....	82
5.3.2 Scale .....	82
5.3.3 Rotation .....	85
5.3.4 Confirmation via Known Applied Load .....	85
5.4 Results .....	86
5.4.1 Transformation Components .....	86
5.4.2 Comparison of Model Output to Known Applied Load .....	86
5.5 Conclusions .....	87
<b>Chapter 6 AMB Based Dynamic Force Measurement – Pilot Study .....</b>	<b>89</b>
6.1 Introduction .....	89
6.2 Force Model Modification .....	90
6.3 Experimental Setup .....	91
6.4 Parameter Estimation .....	92
6.5 Experimental Results .....	93
6.6 Key Conclusions From Pilot Study .....	97
<b>Chapter 7 Force Measurement Applied to a Rotating System .....</b>	<b>98</b>
7.1 Introduction .....	98
7.1.1 Force Models .....	99
7.2 Test Setup .....	102

7.2.1 Test Systems.....	102
7.2.2 Dynamic effects of Test Systems .....	102
7.3 Test Data.....	103
7.3.1 Platform 1 .....	103
7.3.2 Platform 2 .....	107
7.4 Data Collection.....	120
7.5 Data Reduction and Analysis .....	120
7.5.1 Decimation .....	121
7.5.2 Magnetic Circuit Model.....	123
7.5.3 Curve Fit.....	127
7.5.4 Calculation of Vertical Force .....	128
7.5.5 Reduction and Analysis of Transducer Data .....	128
7.6 Results of Force Comparison.....	129
7.6.1 Platform 1 Results .....	130
7.6.2 Platform 2 Results .....	137
7.6.3 Summary of Results .....	153
7.7 Effect of Characterization on Model Results .....	154
7.7.1 Significance of Runout Correction .....	154
7.8 Conclusion .....	158
<b>Chapter 8 Conclusions and Recommendations .....</b>	<b>160</b>
8.1 Test Systems .....	161
8.2 Static Characterization .....	161
8.2.1 Effective origin.....	161
8.2.2 Runout Identification.....	161
8.2.3 Coordinate Transform .....	162
8.3 Force Measurement in Rotating Systems .....	162
8.4 Future Work and Recommendations .....	163
8.4.1 Recommendations for Static Testing .....	163
8.4.2 Recommendations for Dynamic Testing .....	163
8.4.3 Global Recommendations .....	163
<b>References.....</b>	<b>165</b>
<b>Appendix A Mechanisms that Affect Force Measurement in Rotating Systems ..</b>	<b>168</b>
A.1 Hysteresis.....	169
A.2 Eddy Current.....	170
A.3 Skin Effect.....	172
<b>Appendix B Uncertainty Analysis.....</b>	<b>173</b>
B.1 Uncertainty in Brief .....	173
B.2 Overview of Calculations Required for Force Measurement .....	174
B.2.1 Identification of Rotor Position .....	175
B.2.2 Development of Characterization of Rotor Position Identification.....	175
B.2.3 Force Calculated from Characterized Model .....	175
B.2.4 Test Setups.....	175
B.3 Uncertainty in Identification of Rotor Position .....	176
B.3.1 Uncertainty in Constituent Terms in MPM Calculation.....	176
B.3.2 Uncertainty of Position Determined by MPM - Results .....	177
B.4 Uncertainty in Characterization of Rotor Position Identification.....	179
B.4.1 Uncertainty of "Origin Offset" Portion of Coordinate Transformation .....	179
B.4.2 Uncertainty of Axes Rotation Portion of Coordinate Transformation .....	179
B.4.3 Uncertainty of Axes Scale Portion of Coordinate Transformation.....	180

<i>B.4.4 Aggregate Uncertainty of Entire Transformation</i> .....	181
B.5 Uncertainty of Force Measurement .....	182
<i>B.5.1 Uncertainty of Force Equation Constituents</i> .....	182
<i>B.5.2 Sampling Effects on Force Measurement</i> .....	184
<i>B.5.3 Force Measurement Uncertainty Associated with the MPM</i> .....	185
<i>B.5.4 Force Measurement Uncertainty Associated with the Characterized Model         (Static)</i> .....	186
<i>B.5.5 Force Measurement Uncertainty Associated with the Characterized Model         (Dynamic)</i> .....	190
B.6 Transducer Uncertainty .....	191
B.7 Comment on Curve Fit Uncertainty .....	192
<b>Appendix C Dynamic Force Measurement Results: Raw Data</b> .....	<b>203</b>

# List of Figures

Figure 1.1: Electromagnet circuit .....	5
Figure 1.2: Flux path in AMB.....	7
Figure 1.3: Components of a simple Active Magnetic Bearing .....	7
Figure 1.4: An example of an AMB control axis .....	8
Figure 1.5: 8 pole radial magnetic bearing.....	9
Figure 1.6: Assumed flux paths associated with lumped models.....	10
Figure 1.7: AMB reluctance network.....	10
Figure 2.1: AMB stator geometry and monitored signals.....	24
Figure 2.2: Loci of solutions to Equation 1.13 based on two sets of coil current: $(i_{upper,1}, i_{lower,1})$ and $(i_{upper,2}, i_{lower,2})$ .....	27
Figure 2.3: Example of an axes offset transformation.....	31
Figure 2.4: Relationship between system coordinates $(v_s, w_s)$ and effective coordinates $(v_e, w_e)$ .....	32
Figure 2.5: Simplified example of finding the effective origin .....	35
Figure 2.6: Rotor set-points for system identification of axes scale (Platform 1) .....	36
Figure 2.7: Example of scaling between system coordinates and effective coordinates.....	37
Figure 2.8: Example of rotation between system coordinates and effective coordinates.....	38
Figure 3.1: Photograph of Platform 1 with scale included to show approximate sizes ...	44
Figure 3.2: Photograph of Platform 2 with scale included to show approximate sizes ...	45
Figure 3.3: Typical stator geometry and stator pole polarity .....	46
Figure 3.4: Stator of Platform 1 .....	47
Figure 3.5: Typical rotor for Platform 1.....	47
Figure 3.6: Platform 1 balance disk.....	48
Figure 3.7: Inboard bearing housing and spacer block.....	49
Figure 3.8: Close-up photograph of force transducers and sandwich plates .....	49
Figure 3.9: Stator of Platform 2 .....	50
Figure 3.10: Typical rotor for Platform 2.....	51
Figure 3.11: Platform 2 balance disk.....	52
Figure 3.12: Detail photograph of slots in base plate.....	52
Figure 3.13: Inboard bearing housing and spacer block.....	53
Figure 3.14: Outboard bearing housing and transducer mounting system .....	53
Figure 3.15: Close-up photograph of force transducers and sandwich plates .....	54
Figure 3.16: Motor mount and spacer block.....	54
Figure 3.17: Transfer function between modal hammer and force transducers.....	58
Figure 4.1: Platform 1 laboratory rotor with outboard AMB mounted on force transducers .....	66
Figure 4.2: Platform 2 laboratory rotor with outboard AMB mounted on force transducers .....	67
Figure 4.3: Position set-points and associated error predictions for successive iterations (first experiment, repetition 1; V axis results).....	70
Figure 4.4: Position set-points and associated error predictions for successive iterations (second experiment; V axis results).....	71
Figure 4.5: Effective origin location predictions from Case I and Case II.....	72

Figure 4.6: Phase relationship of effective position; numbers on graph are phase angles associated with the $V$ and $W$ axis offsets .....	73
Figure 5.1: Platform 2 laboratory rotor with outboard AMB mounted on force transducers .....	81
Figure 5.2: Relationship between intermediate coordinates ( $v_{Trans}, w_{Trans}$ ), system coordinates ( $v_s, w_s$ ), and effective coordinates ( $v_e, w_e$ ) .....	83
Figure 5.3: Rotor set-points in intermediate coordinates ( $v_{Trans}, w_{Trans}$ ) for system identification of axes scale (Platform 1).....	83
Figure 5.4: Effective rotor positions calculated by MPM for the rotor set-points of Figure 5.3 .....	84
Figure 5.5: Linear fit of effective rotor offset determined by MPM to the rotor offset in system coordinates for the $V$ axis (Platform 1).....	85
Figure 6.1: Transducer force and AMB force (from an unmodified model; based on total $i_m$ ) for the 0g added unbalance data set .....	94
Figure 6.2: Comparison of transducer data and model data (based on $i_e$ ) for all Bias settings of load Case 3 (0.6g added unbalance).....	94
Figure 6.3: Model error for bias Case 1 (1.3 Amps).....	95
Figure 6.4: Model error for bias Case 2 (1.5 Amps).....	96
Figure 6.5: Model error for bias Case 3 (1.7 Amps).....	96
Figure 7.1: Typical AMB system mounted to test platform.....	98
Figure 7.2: Dynamic load amplitude versus rotor speed. Platform 1, System 1. 0 mg added unbalance. 1.3, 1.5, and 1.7 Amp bias currents.....	104
Figure 7.3: Dynamic load amplitude versus rotor speed. Platform 1, System 1. 400 mg (0.48 gm-in) added unbalance. 1.3, 1.5, and 1.7 Amp bias currents ..	105
Figure 7.4: Dynamic load amplitude versus rotor speed. Platform 1, System 1. 600 mg (0.72 gm-in) added unbalance . 1.3, 1.5, and 1.7 Amp bias currents .	105
Figure 7.5: Dynamic load amplitude versus rotor speed. Platform 1, System 1. 800 mg (0.96 gm-in) added unbalance. 1.3, 1.5, and 1.7 Amp bias currents ..	106
Figure 7.6: Dynamic load amplitude versus rotor speed. Platform 1, System 1. 1000 mg (1.2 gm-in) added unbalance. 1.3, 1.5, and 1.7 Amp bias currents ....	106
Figure 7.7: Dynamic load amplitude versus rotor speed. Platform 2, System 1. 0 mg added unbalance. 0.5, 0.6, and 0.7 Amp bias currents.....	108
Figure 7.8: Dynamic load amplitude versus rotor speed. Platform 2, Setup 1. 100 mg (0.23 gm-in) added unbalance. 0.5, 0.6, and 0.7 Amp bias currents .....	108
Figure 7.9: Dynamic load amplitude versus rotor speed. Platform 2, Setup 1. 200 mg (0.45 gm-in) added unbalance. 0.5, 0.6, and 0.7 Amp bias currents .....	109
Figure 7.10: Dynamic load amplitude versus rotor speed. Platform 2, Setup 1. 300 mg (0.68 gm-in) added unbalance. 0.5, 0.6, and 0.7 Amp bias currents ...	109
Figure 7.11: Dynamic load amplitude versus rotor speed. Platform 2, Setup 2. 0 mg added unbalance. 1.2, 1.6, and 2.0 Amp bias currents.....	110
Figure 7.12: Dynamic load amplitude versus rotor speed. Platform 2, Setup 2. 200 mg (0.45 gm-in) added unbalance. 1.2, 1.6, and 2.0 Amp bias currents ..	111
Figure 7.13: Dynamic load amplitude versus rotor speed. Platform 2, Setup 2. 400 mg (0.9 gm-in) added unbalance. 1.2, 1.6, and 2.0 Amp bias currents ....	111
Figure 7.14: Dynamic load amplitude versus rotor speed. Platform 2, Setup 2.....	112
Figure 7.15: Dynamic load amplitude versus rotor speed. Platform 2, Setup 2. 800 mg (1.8 gm-in) added unbalance. 1.2, 1.6, and 2.0 Amp bias currents .....	112
Figure 7.16: Dynamic load amplitude versus rotor speed. Platform 2, Setup 2.....	113

Figure 7.17: Dynamic load amplitude versus rotor speed. Platform 2, Setup 3. 0 mg added unbalance. 0.5, 0.65, and 0.8 Amp bias currents.....	114
Figure 7.18: Dynamic Load amplitude versus rotor speed. Platform 2, Setup 3. 100 mg (0.23 gm-in) added unbalance. 0.5, 0.65, and 0.8 Amp bias currents ..	114
Figure 7.19: Dynamic load amplitude versus rotor speed. Platform 2, Setup 3. 200 mg (0.45 gm-in) added unbalance. 0.5, 0.65, and 0.8 Amp bias currents ..	115
Figure 7.20: Dynamic load amplitude versus rotor speed. Platform 2, Setup 4. 0 mg added unbalance. 1.4, 1.7, and 2.0 Amp bias currents.....	116
Figure 7.21: Dynamic load amplitude versus rotor speed. Platform 2, Setup 4. 200 mg (0.45 gm-in) added unbalance. 1.4, 1.7, and 2.0 Amp bias currents ..	116
Figure 7.22: Dynamic load amplitude versus rotor speed. Platform 2, Setup 4. 300 mg (0.68 gm-in) added unbalance. 1.4, 1.7, and 2.0 Amp bias currents ..	117
Figure 7.23: Dynamic load amplitude versus rotor speed. Platform 2, Setup 4. 400 mg (0.9 gm-in) added unbalance. 1.4, 1.7, and 2.0 Amp bias currents ....	117
Figure 7.24: Dynamic load amplitude versus rotor speed. Platform 2, Setup 4. 500 mg (1.13 gm-in) added unbalance. 1.4, 1.7, and 2.0 Amp bias currents ..	118
Figure 7.25: Dynamic load amplitude versus rotor speed. Platform 2, Setup 4. 600 mg (1.35 gm-in) added unbalance. 1.4, 1.7, and 2.0 Amp bias currents ..	118
Figure 7.26: Dynamic load amplitude versus rotor speed. Platform 2, Setup 4. 700 mg (1.58 gm-in) added unbalance. 1.4, 1.7, and 2.0 Amp bias currents ..	119
Figure 7.27: Dynamic load amplitude versus rotor speed. Platform 2, Setup 4. 800 mg (1.8 gm-in) added unbalance. 1.5, 1.6, and 1.7 Amp bias currents .....	119
Figure 7.28: Raw and decimated current data.....	122
Figure 7.29: Raw and decimated position data.....	122
Figure 7.30: Calculated Flux Density Based on Decimated Current and Position Values in Conjunction With Equation 7.1 .....	124
Figure 7.31: calculated upper actuator force in V-axis based on decimated flux density.....	126
Figure 7.32: V-axis force calculated from Equation 1.13 (upper actuator force – lower actuator force) and decimated data.....	127
Figure 7.33: Decimated data from force transducers and resulting curve fit.....	129
Figure 7.34: Comparison of measured and calculated forces versus rotor speed. Platform 1 System 1. Added Unbalance: 0 mg .....	132
Figure 7.35: Comparison of measured and calculated forces versus rotor speed. Platform 1 System 1. Added Unbalance: 0 mg .....	133
Figure 7.36: Comparison of measured and calculated forces versus rotor speed. Platform 1 System 1. Added Unbalance Sections (left to right) 0, 400, 600, 800, and 1000 mg (0, 0.48, 0.72, 0.96, and 1.2 gm-in).....	135
Figure 7.37: Comparison of errors in calculated force versus rotor speed. Platform 1 System 1. Added Unbalance Sections (left to right) 0, 400, 600, 800, and 1000 mg (0, 0.48, 0.72, 0.96, and 1.2 gm-in).....	136
Figure 7.38: Comparison of measured and calculated forces versus rotor speed. Platform 2 System 1. Added Unbalance (left to right) 0, 100, 200 and 300mg (0, 0.23, 0.45, 0.68 gm-in).....	139
Figure 7.39: Comparison of errors in calculated force versus rotor speed. Platform 2 System 1. Added Unbalance (left to right) 0, 100, 200 and 300mg (0, 0.23, 0.45, 0.68 gm-in) .....	140

Figure 7.40: Comparison of Measured and Calculated Forces versus Rotor Speed. Platform 2 System 2. Added Unbalance (left to right) 0, 200, 400, 600, 800, and 1000mg (0, 0.45, 0.9, 1.35, 1.8, and 2.25 gm-in) .....	143
Figure 7.41: Comparison of Errors in Calculated Force versus Rotor Speed. Platform 2 System 2. Added Unbalance (left to right) 0, 200, 400, 600, 800, and 1000mg (0, 0.45, 0.9, 1.35, 1.8, and 2.25 gm-in) .....	144
Figure 7.42: Comparison of measured and calculated forces vs rotor speed. Platform 2 System 3. Added Unbalance (left to right) 0, 100, and 200mg (0, 0.23, 0.45 gm-in) .....	147
Figure 7.43: Comparison of errors in calculated force versus rotor speed. Platform 2 System 3. Added Unbalance (left to right) 0, 100, and 200mg (0, 0.23, 0.45 gm-in) .....	148
Figure 7.44: Comparison of measured and calculated forces vs rotor speed. Platform 2 System 4. Added Unbalance (left to right) 0, 200, 300, 400, 500, 600, 700, and 800mg (0, 0.45, 0.68, 0.9, 1.13, 1.35, 1.58, 1.8 gm-in) .....	151
Figure 7.45: Comparison of errors in calculated force versus rotor speed. Platform 2 System 4. Added Unbalance (left to right) 0, 200, 300, 400, 500, 600, 700, and 800mg (0, 0.45, 0.68, 0.9, 1.13, 1.35, 1.58, 1.8 gm-in) .....	152
Figure 7.46: Comparison of Measured and Calculated Forces vs Rotor Speed; (perturbed model). Platform 2 System 3. Added Unbalance (left to right) 0, 100, and 200mg (0, 0.23, 0.45 gm-in) .....	156
Figure 7.47: Comparison of Errors in Calculated Force versus Rotor Speed; (perturbed model). Platform 2 System 3. Added Unbalance (left to right) 0, 100, and 200mg (0, 0.23, 0.45 gm-in) .....	157
Figure A.1: Hysteresis due to cyclic coil current .....	169
Figure A.2: Model of eddy current path .....	171
Figure A.3: Direction of flux generated by eddy current $i_e$ (Lenz's Law) .....	171
Figure B.1: Comparison of curve fit uncertainty versus Rotor Speed. Platform 1 System 1. Added Unbalance Sections (left to right) 0, 400, 600, 800, and 1000 mg (0, 0.48, 0.72, 0.96, and 1.2 gm-in) .....	193
Figure B.2: Comparison of curve fit uncertainty versus Rotor Speed as a percent of measured load. Platform 1 System 1. Added Unbalance Sections (left to right) 0, 400, 600, 800, and 1000 mg (0, 0.48, 0.72, 0.96, and 1.2 gm-in) ..	194
Figure B.3: Comparison of curve fit uncertainty versus Rotor Speed. Platform 2 System 1. Added Unbalance (left to right) 0, 100, 200 and 300mg (0, 0.23, 0.45, 0.68 gm-in) .....	195
Figure B.4: Comparison of curve fit uncertainty versus Rotor Speed as a percent of measured load. Platform 2 System 1. Added Unbalance (left to right) 0, 100, 200 and 300mg (0, 0.23, 0.45, 0.68 gm-in) .....	196
Figure B.5: Comparison of curve fit uncertainty versus Rotor Speed. Platform 2 System 2. Added Unbalance (left to right) 0, 200, 400, 600, 800, and 1000mg (0, 0.45, 0.9, 1.35, 1.8, and 2.25 gm-in) .....	197
Figure B.6: Comparison of curve fit uncertainty versus Rotor Speed as a percent of measured load. Platform 2 System 2. Added Unbalance (left to right) 0, 200, 400, 600, 800, and 1000mg (0, 0.45, 0.9, 1.35, 1.8, and 2.25 gm-in) .....	198

Figure B.7: Comparison of curve fit uncertainty versus Rotor Speed. Platform 2 System 3. Added Unbalance (left to right) 0, 100, and 200mg (0, 0.23, 0.45 gm-in) .....	199
Figure B.8: Comparison of curve fit uncertainty versus Rotor Speed as a percent of measured load. Platform 2 System 3. Added Unbalance (left to right) 0, 100, and 200mg (0, 0.23, 0.45 gm-in) .....	200
Figure B.9: Comparison of curve fit uncertainty versus Rotor Speed. Platform 2 System 4. Added Unbalance (left to right) 0, 200, 300, 400, 500, 600, 700, and 800mg (0, 0.45, 0.68, 0.9, 1.13, 1.35, 1.58, 1.8 gm-in) .....	201
Figure B.10: Comparison of curve fit uncertainty versus Rotor Speed as a percent of measured load. Platform 2 System 4. Added Unbalance (left to right) 0, 200, 300, 400, 500, 600, 700, and 800mg (0, 0.45, 0.68, 0.9, 1.13, 1.35, 1.58, 1.8 gm-in) .....	202

## List of Tables

Table 2.1: Summary of coil current data collected for MPM .....	29
Table 4.1: AMB specifications for Platform 1 .....	66
Table 4.2: AMB specifications for Platform 2 .....	67
Table 4.3: Position set-points and associated position errors ( $\mu\text{m}$ ) .....	69
Table 4.4: Final effective origin predictions for five cases.....	70
Table 4.5: Effective origin locations determined for four systems on Platform 2 .....	74
Table 5.1: AMB Specifications for Platform 1.....	80
Table 5.2: AMB specifications for Platform 2 .....	81
Table 5.3: Identified transformation components for five AMB systems .....	86
Table 5.4: Calculated loads based on a simple model with and without a coordinate transformation applied.....	87
Table 5.5: Standard deviations of calculated loads based on a simple model with and without a coordinate transformation applied.....	87
Table 6.1: Summary of rotor test conditions and resulting dynamic load ( <i>lb</i> ) .....	92
Table 7.1: Characteristics of the setup associated with Platform 1.....	104
Table 7.2: Characteristics of the four systems associated with Platform 2 .....	107
Table 7.3: Summary of force model errors associated with Figure 7.36 and Figure 7.37 .....	137
Table 7.4: Summary of force model errors associated with Platform 2, Setup 1 as shown in Figure 7.38 and Figure 7.39.....	141
Table 7.5: Summary of force model errors associated with Platform 2, Setup 2 as shown in Figure 7.40 and Figure 7.41.....	145
Table 7.6: Summary of force model errors associated with Figure 7.42 and Figure 7.43. ....	149
Table 7.7: Summary of force model errors associated with Figure 7.44 and Figure 7.45. ....	153
Table 7.8: Mean errors associated with characterized model and simple model for each test along with mean error in terms of max load.....	154
Table 7.9: Summary of basic, characterized, and perturbed force model errors associated with Figure 7.42, Figure 7.43, Figure 7.46 and Figure 7.47. ....	158
Table B.1: Uncertainty in Equation 2.6 and its Effect on Identified Rotor Location (Platform 1).....	178
Table B.2: Uncertainty in Equation 4 and its Effect on Identified Rotor Location (Platform 2, 0.010" Nominal Gap).....	178
Table B.3: Uncertainty in Equation 4 and its Effect on Identified Rotor Location (Platform 2, 0.030" Nominal Gap).....	179
Table B.4: Angular Uncertainty of Axes Rotation Angle due to Position Uncertainty....	180
Table B.5: Uncertainty of Scale Factor due to Position Uncertainty .....	181
Table B.6: Sampling associated with different force measurement methods .....	184
Table B.7: Uncertainty in Equation 1.13 and its Effect on Calculated Force (Platform 1) .....	185
Table B.8: Uncertainty in Equation 1.13 and its Effect on Calculated Force (Platform 2, 0.010" Nominal Gap).....	186

Table B.9: Uncertainty in Equation 1.13 and its Effect on Calculated Force (Platform 2, 0.030" Nominal Gap) .....	186
Table B.10: Uncertainty in Equation 1.13 and its Effect on Calculated Force (Platform 1) .....	187
Table B.11: Uncertainty in Equation 1.13 and its Effect on Calculated Force (Platform 2, 0.010" Nominal Gap) .....	188
Table B.12: Uncertainty in Equation 1.13 and its Effect on Calculated Force (Platform 2, 0.030" Nominal Gap) .....	188
Table B.13: Uncertainty in Equation 1.13 and its Effect on Calculated Force (25 $\mu$ m Offset) (Platform 1) .....	189
Table B.14: Uncertainty in Equation 1.13 and its Effect on Calculated Force (25 $\mu$ m Offset) (Platform 2, 0.010" Nominal Gap) .....	189
Table B.15: Uncertainty in Equation 1.13 and its Effect on Calculated Force (25 $\mu$ m Offset) (Platform 2, 0.030" Nominal Gap) .....	190
Table B.16: Uncertainty in Equation 1.13 and its Effect on Calculated Force (50 $\mu$ m Offset) (Platform 1) .....	190
Table B.17: Uncertainty in Equation 1.13 and its Effect on Calculated Force .....	191
Table B.18: Uncertainty in Equation 1.13 and its Effect on Calculated Force .....	192
Table C.1: Platform 1 SetUp 1 .....	203
Table C.2: Platform 2 SetUp 1 .....	207
Table C.3: Platform 2 SetUp 2 .....	210
Table C.4: Platform 2 SetUp 3 .....	214
Table C.5: Platform 2 SetUp 4 .....	216
Table C.6: Platform 2 SetUp 3 (perturbed model) .....	221

# Chapter 1 Introduction

## **1.1 INTRODUCTION**

The ability of a magnetic bearing to concurrently support and monitor a load facilitates significant improvements for machine condition and performance monitoring as well as information for process control in manufacturing applications. Several researchers have demonstrated this force measurement capability; the current state of the art relies on additional hardware in the form of Hall probes to gauge the magnetic flux present in the air gap. Although use of Hall probes often leads to reliable force data, the use of Hall probes is not necessarily appropriate for all applications. For example, physically harsh environments may pose problems for such techniques due the delicate nature of Hall probes. The research presented here is part of an effort to provide dynamic force data by analyzing information that is inherent to a typical magnetic bearing system: coil current and rotor displacement. In this manner, a strong foundation has been laid to develop a force measurement technique applicable to the general classification of active magnetic bearings (AMBs). Furthermore, the research has led to advances in AMB system characterization to aid field tuning of AMB systems.

AMBs are based on electromagnets. Electromagnets provide the lift force required to support a shaft by generating magnetic flux. The magnetic flux follows a circuit that includes the core of the electromagnet coil of the AMB (stator), a specialized hub made of soft iron (rotor) that is mounted to the shaft, and the air gap between the rotor and stator. The amount of magnetic flux in the air gap determines the attractive force between the rotor and stator. In an AMB, the amount of magnetic flux is changed by varying the amount of current applied to the electromagnet coil. Control of current in the electromagnet coil allows a means to regulate the attractive force between the rotor and stator.

AMB force models that are based on magnetic circuit theory can be used to predict the amount of attractive force between the rotor and stator based on the amount of coil current applied to the stator and the length of the air gap between the rotor and stator. Such models have been used to provide accurate measurement of static forces (Fittro et al., 1997). The accuracy of this type of model is reduced if it is applied to a rotating load.

This accuracy reduction was generally considered to be due to unmodeled dynamic effects such as hysteresis and eddy currents. This research has shown that AMB force models that rely on coil current and rotor position measurements must also account for position runout of the rotor position sensors.

Current state-of-the-art AMB techniques for force measurement rely on Hall probes because they are capable of direct flux measurements and as such are not affected by dynamic effects such as hysteresis and eddy currents. Immunity to dynamic effects is particularly important when measuring rapidly changing loads, such as those observed in a rotating system, where significant portions of the measured control current will be required to overcome these magnetic losses. Aenis and Nordmann (2000), for example, chose to use Hall probes over a current and displacement-based model when developing frequency response functions related to the operation of a centrifugal pump. In a similar study concerning measurement of journal bearing forces, Knopf and Nordmann (1998) also showed that Hall probes were the better choice for force measurements on a dynamic system. In general, research regarding AMB-based force measurement has concentrated on the development of force measurement capability for laboratory applications. The controlled nature of the intended environment for AMB-based force measurement systems has encouraged the implementation of instrumentation and system identification techniques that are not appropriate for field application. Specifically, their reliance on Hall probes could lead to difficulties in some cases. Furthermore, such systems typically require application of several known loads for calibration; application of several known loads may not be practical for a field environment.

The potential difficulties with Hall probes stem from the expense and complexity they add to a system. Additionally, Hall probes are delicate; if they fail they are difficult to replace due to their location in the air gap. These issues with Hall probes, combined with the readily available nature of coil current and rotor displacement data, serves as a motivation to develop dynamic force measurement using only magnetic bearing system data. Such a system could be applied to any AMB system thus making force measurement available to a broad cross section of the rotating machinery community. Traditional difficulties with such an approach have been related to correctly determining the relationship between measured values of coil current and the amount of magnetic flux in the air gap when dynamic effects are present. Additional difficulties are associated with accurately determining air gaps. Air gaps are typically inferred from knowledge of a nominal air gap in conjunction with rotor offset data supplied by rotor position sensors. Inference of air gaps from nominal air gap and rotor offset relies on the assumption that the rotor is initially centered in the stator, and that no sensor/stator collocation errors exist.

In this work the foundation has been developed for the measurement of dynamic AMB forces using only coil current and rotor displacement data. Air gaps are inferred through system identification, and as such do not rely solely on data supplied by rotor position sensors. The system identification of air gap is used in conjunction with a magnetic circuit model of bearing force to accurately predict bearing loads. The effect of rotor runout on the force measurement is accounted for so that the force measurement technique can be applied to a rotating system. The proposed system identification relies on perturbations of AMB coil currents and subsequent interrogation of the AMB system

response, all of which can be achieved via the AMB controller. In situ system calibration is facilitated since application of known loads is not required.

### **1.1.1 Contributions**

The work described in this dissertation is part of an ongoing effort to develop a current-based force measurement technique that can be broadly applied to AMBs. Because contributions from multiple researchers were necessary in order to achieve the current state of the technique, it is appropriate to point out the contributions that can be directly attributed to this doctoral research.

#### **DIRECT SOLUTION METHOD OF MULTI-POINT METHOD**

The Multi-Point Method (MPM) is a system identification technique that relies on perturbations of AMB bias currents and subsequent observation of the AMB controller to monitor system response. The responses to multiple perturbations are analyzed in conjunction with a magnetic circuit model of the AMB system to infer values of variables within the model. The initial form of the Multi-Point Method, as described by Kasarda et al. (2000) and implemented by Marshall et al. (2001), requires simulation of many rotor positions (5000) for each bias current case. This form was computationally intensive and required a computer code to reach a result. The research we performed led to a closed form solution of the MPM, referred to here as the direct solution method. The direct solution simplifies the MPM analysis to the point that a result could be determined by a hand calculation.

#### **ORIGIN OF EFFECTIVE COORDINATES**

The output of the MPM includes a position value as well as a force measurement. The position value output is taken to be the effective value of rotor position. We developed an iterative method to locate the effective origin based on the MPM output of effective rotor position. The effective origin is the position at which the MPM force model behaves as though the rotor is at position (0,0). In general the effective origin does not coincide with the rotor location that the system sensors report as (0,0). Knowledge of the location of the effective origin is useful for multiple reasons.

Most AMB control systems are based on a model of the non-linear AMB system that has been linearized about a certain theoretical rotor location, typically (0,0). Such a model most accurately represents the real system when it is applied near the location that the model was linearized about. In operation, the control model will assume the coordinates reported by the system sensors. In general, the origin of the system coordinates will not coincide with the origin of the effective coordinates. Model behavior could be improved if the position sensor bias were adjusted so that the origin of the system axes coincided with the location where the rotor behaves as though it is at position (0,0). This is the effective origin.

Our primary interest in locating the effective origin is related to characterization of an AMB force model. The effective origin is the position at which the MPM force model behaves as though the rotor is at position (0,0). The effective origin provides the starting point for a broader characterization, described below.

## **RUNOUT**

Further experimentation revealed that the rotor location corresponding to the effective origin was a function of rotation angle. We recognized this as runout that could be due to sensor effects or non-collocation effects and were able to account the runout. Sensor runout refers to changes in position probe signals that are not related to real changes in the position of the rotor relative to the stator. Non-collocation refers to the difference in the axial locations of the stator and the rotor position sensors. Air gap measured at the axial location of the position sensors may not be the same as the “true” air gap at the stator. A bowed shaft will cause a change in the runout with shaft rotation. The AMB controller reacts to runout as it would react to a real change in rotor position; control currents are applied as necessary to move the rotor to the location for which the position probe signals indicate zero offset. Such action by the controller has the undesirable effect of creating a rotor orbit as the controller continuously reacts to “phantom” rotor motion.

## **COORDINATE TRANSFORMATION**

The output of the MPM includes a position value as well as a force measurement. The position value output is taken to be the effective value of rotor position. Our contribution in this area was to generalize the relationship between effective rotor position determined through perturbation and the rotor position reported by the controller. This was done by applying the MPM at several well-chosen rotor positions and comparing the effective position to the reported position at each location. A coordinate transformation between effective rotor position and the rotor position reported by the controller can be determined from these comparisons. Since perturbations are not required after the relationship has been characterized, the coordinate transformation provides a way to estimate the effective rotor position based on instantaneous system measurements. In this way force measurements with roughly the same accuracy as MPM based force measurements can be made “on the fly” since the MPM force value can be directly calculated given an estimated effective rotor location. Generalization of the MPM results is a key step to application of an MPM-based force measurement technique to the measurement of dynamic forces.

## **LIBRARY OF DYNAMIC FORCE MEASUREMENT DATA**

Five different AMBs were operated in order to test AMB-based force measurement techniques. Operation of each AMB included a variety of unbalance loads, bias currents, and rotational speeds. The entire library consists of over 500 dynamic test conditions.

Force transducers were mounted underneath the AMB to provide a measurement of bearing reaction force. Data pertaining to the bearing system was acquired during AMB operation. This data consists of coil current amperages in the upper and lower coils of each axis. Force transducer data was also acquired to allow a comparison and evaluation of calculated values of force based on different models. The data was acquired at a high rate (20000 samples/channel/second) and was acquired synchronously. The entire library covers over 500 dynamic test conditions. For each test condition 20000 samples of system data and force transducer data were acquired over a period of 1 second.

This data represents a range of speed, unbalance, and bias current conditions. The library of real data gives the AMB community a resource for testing proposed models of dynamic force. The accompanying force transducer data allows an immediate comparison of proposed models.

## 1.2 FORCE GENERATED BY ELECTROMAGNETS

The following description of force generated by electromagnets is provided as background. Additional information regarding electromagnetics can be found in Plonus (1978), or Hammond (1978).

AMBs are based on electromagnets. Electromagnets provide lift force by generating magnetic flux. The magnetic flux follows a circuit that includes the electromagnet coil, the “target” to which force is applied, and the air gap between the two. Figure 1.1 shows a simple electromagnetic circuit. The direction of the flux field,  $\phi$ , depends on the direction of the coil current,  $I$ , in accordance with the right hand rule. Magnetic flux in the air gap is a source of attractive force between the electromagnet coil and the “target”, regardless of flux direction.

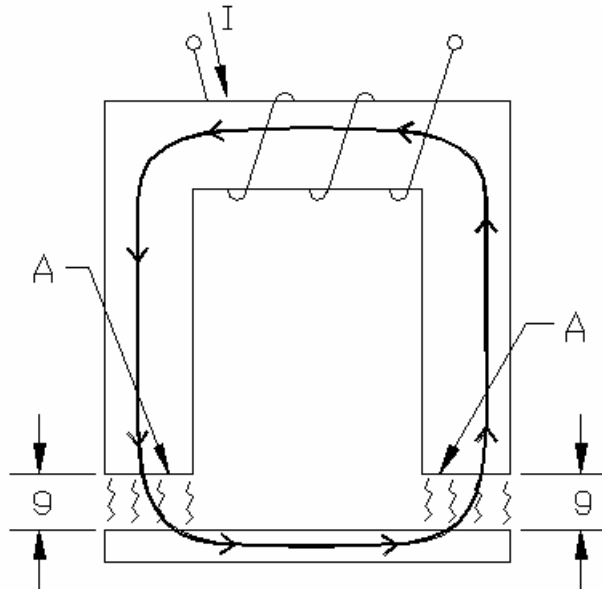


Figure 1.1: Electromagnet circuit

The force applied by an electromagnet is :

$$F = \frac{\phi^2}{\mu_0 A} \quad (1.1)$$

where  $F$  is magnetic force,  $\phi$  is magnetic flux,  $A$  is the pole face area of both poles, and  $\mu_0$  is the magnetic permeability of air. Alternatively, the lift force can be described as a function of the flux density in the air gap and the area of the electromagnet pole faces:

$$F = \frac{B^2 A}{\mu_o} \quad (1.2)$$

where  $F$  is magnetic force,  $B$  is magnetic flux density,  $A$  is the pole face area of both poles, and  $\mu_o$  is the magnetic permeability of air.

Equation 1.2 can be written in terms of coil currents and air gaps based on the following relationship between flux density, coil current, coil wire turns, and air gap length:

$$B = \frac{\mu_o N I}{2g} \quad (1.3)$$

where  $B$  is magnetic flux density,  $\mu_o$  is the magnetic permeability of air,  $N$  is the number of wire turns in a coil,  $I$  is the coil current, and  $g$  is the length of each air gap. Equation 1.3 shows that flux density is a function of current in the electromagnet coil, and air gap. Flux density increases with increased coil current and decreases with increased air gap length.

The force exerted by an electromagnet can be determined directly from Equation 1.2 if flux density is known. A direct measurement of flux density can be made by a Hall probe placed in the air gap. Alternatively, if coil current and air gap are known, magnetic flux density can be calculated from Equation 1.3 first, and the calculated flux density value can be used in Equation 1.2. Combination of Equations 1.2 and 1.3 leads to:

$$F = \frac{\mu_o^2 N^2 I^2 A}{\mu_o (2g)^2} = \frac{\mu_o N^2 I^2 A}{(2g)^2} \quad (1.4)$$

where

$F$  = mechanical force developed by electromagnet

$\mu_o$  = magnetic permeability of air

$N$  = number of wire turns on actuator coil

$I$  = actuator coil current

$A$  = area of pole face

$g$  = air gap between actuator pole and rotor.

### **1.3 ACTIVE MAGNETIC BEARING (AMB) BACKGROUND**

The following description of basic radial AMB operation is provided as a background to the proposed research. Additional information regarding AMB operation can be found in the work of Allaire et al. (1993) and Schweitzer et al. (1993).

AMBs are based on electromagnets. Electromagnets provide the lift force required to support a shaft by generating magnetic flux. The magnetic flux follows a circuit that includes the electromagnet coil of the AMB (stator), a specialized hub made of soft iron (rotor) that is mounted to the shaft, and the air gap between the rotor and stator. Such a circuit is shown in Figure 1.2. Magnetic flux in the air gap is the source of an attractive force between the stator and rotor.

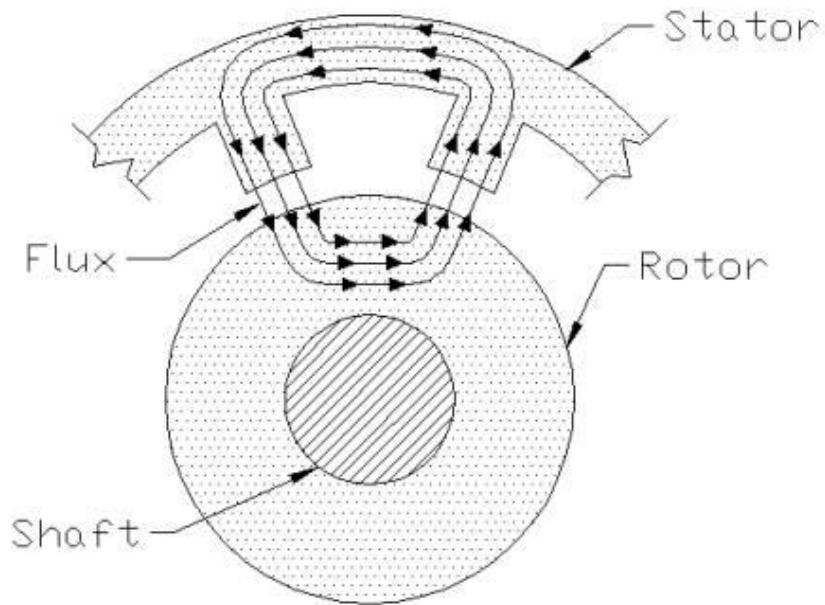


**Figure 1.2: Flux path in AMB**

Active magnetic bearings require several hardware components for operation as shown schematically in Figure 1.3. AMBs are closed-loop controlled; the input to the AMB system controller is provided by a rotor position sensor (proximity probe) that monitors deviation in rotor location. Should the rotor deviate from its prescribed location, changes in the actuator coil current, and thus applied magnetic force, are issued by the controller through a power amplifier to remedy the anomaly.

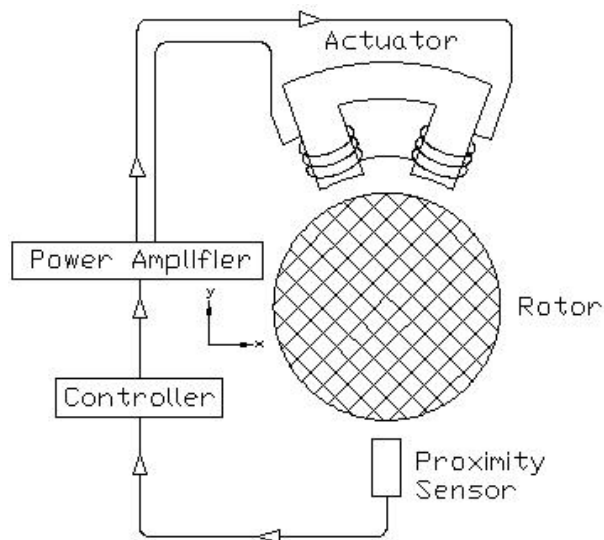


**Figure 1.3: Components of a simple Active Magnetic Bearing**

In typical operation, two actuators are paired such that their applied forces are in direct opposition to each other. Paired actuators form a control axis. An example of such an axis is shown in Figure 1.4. In the figure and in the systems used in this research, each actuator has two poles.

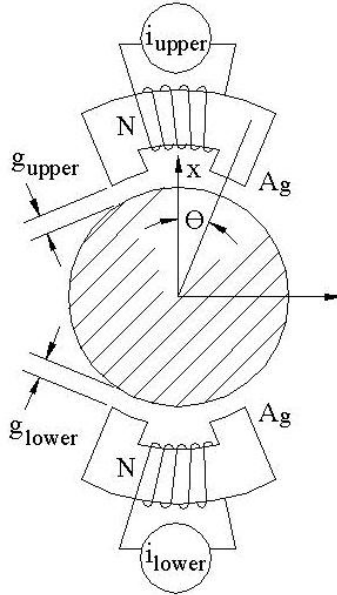


**Figure 1.4: An example of an AMB control axis**

In operation, the controller supplies current to each actuator in the amount required to keep the rotor at a prescribed rotor position. The amount of current supplied by the controller is the sum of two components, a bias current  $i_b$  and a control current  $i_c$ . The control current is distributed differentially, meaning that the control current for opposing actuators is opposite in sign as shown:

$$i_{upper} = i_b + i_c \quad (1.5)$$

$$i_{lower} = i_b - i_c \quad (1.6)$$

For a given load, rotor position, and bias current setting, the resulting actuator coil currents,  $(i_{upper}, i_{lower})$ , are referred to as a current pair. If the bias  $i_b$  is changed, the controller determines the appropriate level of control current  $i_c$  to apply in order to maintain equilibrium resulting in a new current pair. The system identification procedures used in this research leverage this feature of the controller to generate multiple sets of currents,  $(i_{upper}, i_{lower})$ , that are associated with the same rotor offset and same load. Perturbation of the controller bias current,  $i_b$ , by the user is employed to force the controller to respond with multiple sets of unique actuator coil currents. Hence the general name for the technique is “current perturbation”.

The 8-pole radial AMBs used for the research described in this document incorporate two axes similar to the axis shown in Figure 1.5. Figure 1.5 shows that the bearing has two axes of control,  $V$  and  $W$ . Control forces are applied along the control axes. The bearing axes are designed perpendicular to each other, and  $45^\circ$  to vertical as shown in Figure 1.5.

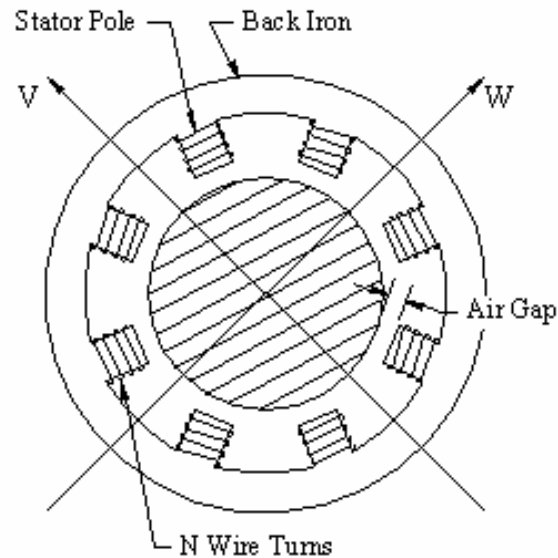
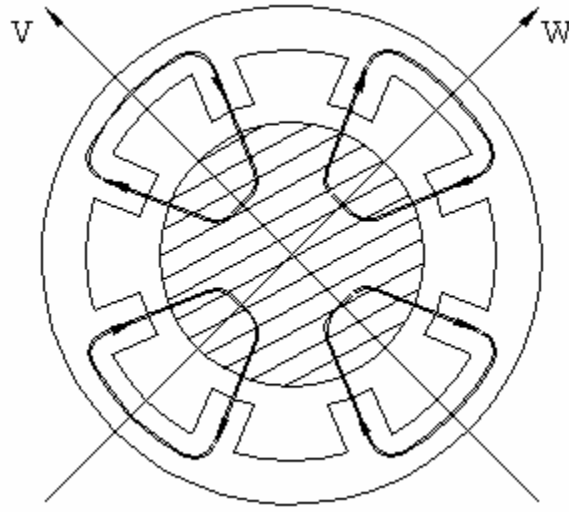


Figure 1.5: 8 pole radial magnetic bearing

## **1.4 AMB FORCE MEASUREMENT BACKGROUND**

The basic equations used to describe the force generated by an electromagnet discussed in Section 1.2 can be applied to AMBs. A variety of methods of varying complexity have been applied to modeling magnetic bearing force as a function of coil current and rotor position. These methods can be generally categorized as “lumped gap” and “reluctance network”. The work presented here is primarily based on a lumped gap model.

Lumped gap methods treat each axis independently. For example, air gap calculations for poles associated with the  $V$ -axis do not account for  $W$ -axis position; both poles of a given actuator are assigned the same value of air gap. Furthermore, the flux path for a given actuator is assumed to travel through a specific actuator only; no flux coupling between axes is accounted for. Flux loops related to a closed form equation are shown in Figure 1.6.



**Figure 1.6: Assumed flux paths associated with lumped models**

Alternatively, the entire AMB can be considered simultaneously as a reluctance network by modeling it as a system of magnetic circuit equations. Such an approach relies on the electrical circuit analog to magnetic circuits. An analogy to Ohm's law is written as:

$$NI = \phi R \quad (1.7)$$

where  $NI$ , the magnetomotive force, represents the number of Amp-turns associated with a pole,  $\phi$  is magnetic flux, and  $R$  is magnetic reluctance.  $NI$ ,  $\phi$ , and  $R$  are the magnetic circuit analogues of voltage, current and resistance in an equivalent electrical circuit. A reluctance network of an 8-pole radial bearing is shown in Figure 1.7.

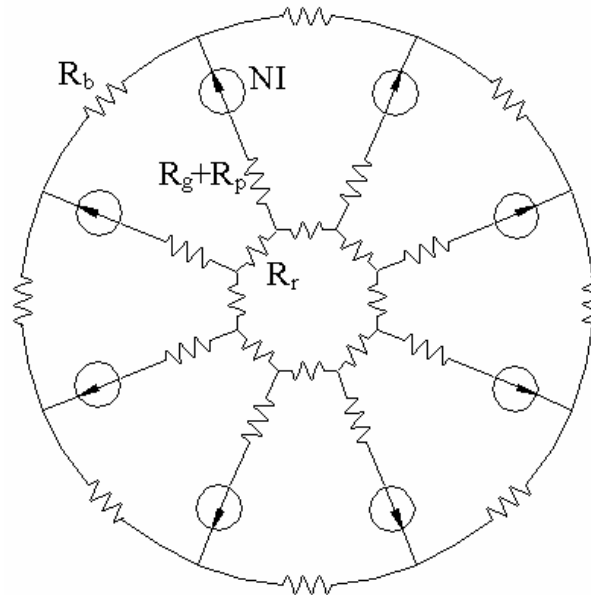


**Figure 1.7: AMB reluctance network**

Each AMB element (poles, back iron, air gaps, rotor) has an equivalent magnetic reluctance,  $R$ , associated with it. These reluctances are shown in Figure 1.7 as  $R_p$ ,  $R_b$ ,  $R_g$ , and  $R_r$ . The actuator coils (which are supplied current by the AMB controller) generate a magnetomotive force  $NI$ . The amount of flux in any part of the circuit can be calculated using Equation 1.7 in conjunction with the magnetic equivalent of Kirchoff's laws.

## **1.5 DEVELOPMENT OF A LUMPED GAP MODEL**

The model used in the research presented here is a lumped gap model. In a lumped gap model the forces due to each pole of an actuator are resolved into a single force acting along the actuator center line. Use of a lumped gap model allows for closed-form calculation of system identification parameters (which will be discussed later). However, the system identification methods used in this research could also be applied to reluctance network models. This section provides additional familiarity with the lumped gap model.

As discussed in Section 1.2, Equations 1.2 and 1.3 can be combined to provide an equation for magnetic force as a function of coil current and air gap as given by Equation 1.4. Equation 1.4 describes the force in a single actuator. In order to determine the net force applied to the rotor for an opposed pair of actuators, such as those depicted in Figure 1.4, the difference in the actuator forces must be calculated as shown in the following equation:

$$F = \frac{\mu_o N^2 i_{upper}^2 A}{g_{upper}^2} - \frac{\mu_o N^2 i_{lower}^2 A}{g_{lower}^2} \quad (1.8)$$

Equation 1.8 is the general form of a lumped gap model. Equation 1.8 can be used to calculate the force along one axis. Bearing geometry related to the angle of the stator poles to the force axis and the magnetic reluctance of the rotor and stator, which are not considered in Equation 1.8., can also be accounted for. Consider Figure 1.4, position sensors provide feedback regarding the offset of the rotor along the vertical axis ( $x$ ) however, the air gaps  $g_{upper}$  and  $g_{lower}$  are dependent on pole angle ( $\theta$ ) as well. The relationship between position offset as reported by the controller and bearing gap is summarized as (Allaire et al., 1993):

$$g_{upper} = g_o - x \cos \theta \quad (1.9)$$

$$g_{lower} = g_o + x \cos \theta \quad (1.10)$$

where  $g_o$  is the nominal bearing clearance,  $x$  is the distance traveled along the bearing axis, and  $\theta$  is the angle between the bearing axis and the axis of an individual magnetic pole.

Another significant geometry consideration is that the magnetic force developed by an individual pole will occur along the axis of that pole. Consider the upper actuator: from Figure 1.4 it can be seen that resolution of the force associated with each pole into horizontal and vertical components will result in some cancellation of force. The net force developed by the upper actuator in this situation is  $F \cos \theta$ , where  $F$  is the magnetic force calculated by Equation 1.8 and  $\theta$  is the angle between the bearing axis and the axis of an individual magnetic pole. Such a model is detailed by Gahler and Forch

(1994). A version of the Gahler model that applies to the laboratory rig used in the research presented here is as shown:

$$F = \mu_o AN^2 \cos \theta \left[ \frac{i_{upper}^2}{(2(g_o - x \cos \theta))^2} - \frac{i_{lower}^2}{(2(g_o + x \cos \theta))^2} \right] \quad (1.11)$$

When considering the magnetic reluctance along any of the flux paths in Figure 1.4, the most significant reluctance is in the air gaps. In general, reasonable force approximations can be obtained with Equation 1.11 in which only the reluctance of the air gaps  $g_{upper}$  and  $g_{lower}$  are considered, while rotor and stator reluctance are neglected. However, in order to improve model accuracy, the rotor and stator reluctances are both accounted for. The equivalent iron path length is represented as (Baun et al., 1996):

$$b = \frac{L_i}{\mu_r} \quad (1.12)$$

where

$b$  = equivalent air gap due to the flux path through the rotor and stator

$L_i$  = approximation of flux path through rotor and stator

$\mu_r$  = the relative permeability of the rotor and stator material (relative to  $\mu_o$ )

Taking the above geometric and material considerations into account leads to the final lumped gap formulation of the magnetic force generated by an AMB axis:

$$F = k \cos \theta \left[ \frac{i_{upper}^2}{(2(g_o - x \cos \theta) + b)^2} - \frac{i_{lower}^2}{(2(g_o + x \cos \theta) + b)^2} \right] \quad (1.13)$$

where:

$k = \mu_o AN^2 \cos \theta$

$\mu_o$  = magnetic permeability of air

$A$  = area of pole face

$N$  = number of wire turns on actuator coil

$\theta$  = angle between bearing axis and axis of an individual magnetic pole.

$i_{upper}$  = coil current in upper actuator

$i_{lower}$  = coil current lower actuator

$g_o$  = nominal air gap

$x$  = rotor displacement along bearing axis

$b = L_i / \mu_r$  = equivalent air gap due to the flux path through the rotor and stator

$L_i$  = approximation of flux path through rotor and stator

$\mu_r$  = the relative permeability of the rotor and stator material (relative to  $\mu_o$ )

## **1.6 ISSUES RELATED TO APPLICATION OF CURRENT-BASED FORCE MEASUREMENT TO ROTATING SYSTEMS**

The models of AMB force that rely on measurements of coil current and air gap discussed in Sections 1.4 and 1.5 are applicable to static loading. In a typical case involving rotating machinery, dynamic forces will act on the bearings. Direct application of such models to measurement of force in rotating systems can lead to large errors. Traditional difficulties with such an approach have been related to properly accounting for dynamic mechanisms such as hysteresis and other flux generating effects such as eddy currents. It will be shown that runout can also be a significant source of error.

Such difficulties have led researchers to make direct flux density measurements with Hall probes, thereby eliminating the need to account for dynamic effects. As mentioned earlier, the potential difficulties with Hall probes stem from the expense and complexity they add to a system. Furthermore, they are delicate; if they fail they are difficult to replace due to their location in the air gap. These issues with Hall probes, combined with the readily available nature of coil current and rotor displacement data, serves as a motivation to develop dynamic force measurement using only the magnetic bearing system data that is readily available on a typical AMB system. Such a technique could be applied to the general classification of AMBs, thus making force measurement available to a broad cross section of the rotating machinery community.

### **1.6.1 Mechanisms that Effect Force Measurement in Rotating Systems**

The general case of bearing loads in rotating machinery includes dynamic forces. Dynamic forces due to rotating unbalance cause the rotor to move in an orbit that is synchronous with the speed of rotation. Consider a single axis of an AMB (Figure 1.4) for the case of a cyclic orbit. Shaft orbit implies that the air gaps of  $g_{upper}$  and  $g_{lower}$  will vary with time. The controller will respond to the position perturbation resulting in time varying coil current values  $i_{upper}$  and  $i_{lower}$ . Variation of coil currents leads to hysteresis, eddy current, and skin effect. Each of these effects will affect the magnetic force generated by an AMB; Appendix A addresses these effects in greater detail.

Initially, the aim of this work was to develop modifications to an existing AMB force model to account for dynamic effects associated with eddy currents and hysteresis in magnetic bearings. Tests were run and as expected, errors existed between measured and calculated forces. However, the trends did not indicate that the errors were necessarily due to effects associated with eddy currents and hysteresis. Further analysis led us to the development of techniques to characterize rotor position runout. It will be shown that runout has significant effect on the modeling of forces in a rotating system. Without first characterizing the effect of runout on force measurement, appropriate correction factors for eddy current and hysteresis effects cannot be developed.

Sensor runout refers to changes in position probe signals that are not related to real changes in the position of the rotor relative to the stator. Changes in the position sensor signal may be due to mechanical runout of the sensor target surface, or electrical runout caused by sub-surface material irregularities in the sensor target. Sensor runout is typically a function of rotation angle and is noticeable at both low (quasi-static) and high rotational speeds. The AMB controller reacts to sensor runout by applying control currents as necessary to move the rotor to the location for which the position probe signals indicate zero offset. The controller's response has the undesirable effect of creating a rotor orbit as the controller continuously reacts to "phantom" rotor motion. Force models that rely on the AMB controller to provide coil current and rotor position information will naturally experience a degradation in accuracy if the information from the controller is contains error due to sensor runout.

Another form of runout results from non-collocation between the rotor position sensors and the stator. Typically, the rotor position sensors are axially offset from the stator. In the case of a bowed rotating shaft, if the rotor position stays constant at the location of the position sensors, non-collocation will lead to runout of the portion of the rotor that is aligned with the stator.

## **1.7 REVIEW OF RELEVANT LITERATURE**

References to force measurement with AMBs extend back roughly twenty years. With few exceptions, the motivation has been to provide a laboratory tool to facilitate the study of forces associated with rotating machinery elements such as journal bearings and seals. Due to the controlled laboratory environment in which such AMB systems are employed, the calibration and instrumentation requirements that have evolved in the quest for improved accuracy are not appropriate for general field application. Specifically, current state of the art AMB force measurement systems employ Hall probes to provide a direct measurement of magnetic flux and require force transducer feedback during calibration. Recent developments in system identification of bearing forces indicate that a different approach is feasible. The system identification technique relies on measured coil current and rotor offset data that can be provided by interrogation of the system controller. The coil current and rotor offset data provided by the interrogation is used in conjunction with a standard model of AMB force to provide identification of unknown parameters in the model; this technique is known as the Multi-Point Method.

### ***1.7.1 Multi-Point Method (MPM)***

The static characterizations discussed in this document rely on a streamlined version of a system identification technique that was developed to identify static AMB forces. This technique was introduced by Kasarda et al. (2000). Marshall et al. (2001) later applied this technique, the Multi-Point Method (MPM), for the identification of static forces using an AMB.

As described by Marshall, the MPM relies on the response of the AMB controller to perturbations that are input by the user. In an AMB axis, the upper and lower coil current magnitudes required to support a given load are not unique, there are an infinite number of current pairs  $i_{upper}$  and  $i_{lower}$  that are solutions (Section 1.3). The controller is forced to solve for a new current pair if the user perturbs the bias current. In typical MPM practice, three sets of bias currents are applied in conjunction with a given load. The resulting coil currents are sampled for each bias current scenario and used as input to the MPM calculation.

The MPM calculation used by Marshall is similar in form to the lumped gap model developed in Section 1.4.

$$F = \epsilon K_{th} \left( \frac{i_1^2}{(2(g_o - x) + b_{th})^2} - \frac{i_2^2}{(2(g_o + x) + b_{th})^2} \right) \quad (1.14)$$

where

$i_1$  = coil current in upper actuator  
 $i_2$  = coil current in lower actuator  
 $g_o$  = nominal air gap  
 $x$  = rotor offset  
 $b_{th}$  = equivalent iron flux path length  
 $k_{th}$  = system constants  
 $\varepsilon$  = correction factor

The correction factor,  $\varepsilon$ , was determined based on an initial subset of results to be 0.88. Upon application of the correction factor, a broader range of loads was measured with rotor offsets of 127 $\mu\text{m}$ , 64 $\mu\text{m}$ , and 0 $\mu\text{m}$  along both directions of the vertical axis. Marshall's results show a mean error of 3%.

The technique behind the MPM is also of interest. The MPM relies on a computer program to calculate potential force values ( $F$  in Equation 1.14) for a given current pair. A force value can be calculated for any rotor position offset value by applying Equation 1.14. Application of the MPM requires stepping through the range of all "possible" rotor position offset values ( $x$  in Equation 1.14) in small increments and calculating the force value associated with each rotor position. The range of  $x$  is determined by the nominal gap so that  $x$  assumes values varying from  $-g_o$  to  $g_o$ , which correspond to the maximum physical range of the rotor within the stator. In a typical MPM application the range of possible rotor positions is broken into 5000 steps.

The computer program generates calculated force value,  $F$ , that corresponds to each possible rotor position offset,  $x$ . Such a list is generated for each set of current pairs. As shown in Equation 1.14, a matrix is generated with this data where each row represents the force calculated by assuming a different rotor position,  $x$ , and each column of the resulting calculated forces represents a different current pair.

$$F_{x,i_1,i_2} = \begin{bmatrix} F(-g_o, i_{10}, i_{20}) & F(-g_o, i_{11}, i_{21}) & \dots & F(-g_o, i_{1m}, i_{2m}) \\ F(-g_o + x, i_{10}, i_{20}) & F(-g_o + x, i_{11}, i_{21}) & \dots & F(-g_o + x, i_{1m}, i_{2m}) \\ \dots & \dots & \dots & \dots \\ F(-g_o + nx, i_{10}, i_{20}) & F(-g_o + nx, i_{11}, i_{21}) & \dots & F(-g_o + nx, i_{1m}, i_{2m}) \end{bmatrix} \quad (1.15)$$

In this matrix,  $m$  indicates the total number of current pairs and  $n$  is the spatial increment of  $x$ . Since the same values of  $x$  are used in the generation of each list, each row of the matrix corresponds to a specific rotor offset. Given that the net force required to levitate the rotor must be constant for all coil current conditions, and that the feedback loop forces the rotor to be in a specific location regardless of required current, the only case that is physically possible is the row of the matrix where the calculated forces  $F$  are equal. In this way the identified value of AMB force,  $F$ , and the corresponding effective offset,  $x$ , are determined. The offset  $x$  refers to the position that must be assumed for the rotor in order to make Equation 1.14 valid. Therefore the offset  $x$  represents the effective air gap between the rotor and stator.

## 1.7.2 Conventional Current-Based Techniques

Conventional current-based techniques rely on a model to establish a theoretical relationship between known quantities that are constant or measurable, and force. The

model, developed from electromagnetic theory and described by Equation 1.4, was discussed in Section 1.2. Equation 1.4 is a model of the force applied by a single electromagnet. Allaire applied such an equation to a model of AMB force in 1993 (Allaire et al., 1993).

Gahler and Forch (1994) applied electromagnetic theory to the explicit model of an 8-pole magnetic bearing. The work published by Gahler includes the derivation of multiple approaches including a flux-based approach and a reluctance network approach. Also discussed in Section 0 and described by Equation 1.11 is a simpler lumped gap model that accounts for bearing geometry as it applies to both the applied force and the rotor motion. Gahler's work is of special interest because the bearing equations derived are directly applicable to the AMB systems used in our research.

Fittro et al. (1997) applied a current-based approach to AMB based force measurement. In this research, a radial AMB was calibrated for use as a force measurement tool. Three force models were employed, a lumped gap model and two variations of a reluctance network model as discussed in Section 1.4 and depicted in Figure 1.7. The first variation of the reluctance network model was that detailed by Meeker et al. (1996), the second was a simplified version of the Meeker model.

Calibration of Fittro's system was achieved by applying a variety of coil currents at a variety of rotor locations while monitoring the resulting magnetic force via force transducers. The calibration was extensive; 5675 combinations of rotor position and applied current were observed. The force transducer data was taken as true force and was used to determine fit parameters within the models. Final results showed that calibrated reluctance network models were capable of static force measurements with ~1% mean error and ~3.5% standard deviation. During calibration the researchers concluded that the lumped gap model was inferior to the reluctance network models so that further testing was not performed with the lumped gap model. The techniques discussed in this paper were later applied to the measurement of radial forces in a plexiglas research pump (Baun and Flack, 1999).

Of particular relevance to the research discussed and proposed in this document is that their technique requires knowledge of actual forces via force transducers as part of the calibration. It will be shown that reliance on force transducers is not required if a system identification based on current perturbations is applied.

### ***1.7.3 Conventional Flux Based Techniques***

As discussed in Section 1.6, current-based techniques must account for system dynamics. Flux-based techniques avoid such issues by making a direct measurement of the flux density in an air gap. In the 1994 work of Gahler a flux based technique was proposed in which Hall probes would be mounted to the faces of the North poles of the stator. Gahler discusses the advantages and disadvantages to a flux based approach. On the positive side, dynamic effects and magnetic saturation are taken into account. The chief disadvantage given is the requirement for additional air gap to accommodate the Hall probes.

Research performed by Knopf and Nordmann (1998) is concerned with the development of a force measurement rig to allow exploration of the dynamic characteristics of turbomachinery components in a laboratory. Their system is based on an 8-pole radial AMB that is fitted with a Hall probe on each pole. A static calibration is described in which the rotor is moved through a large portion of the available volume (75% of backup bearing space), with a variety of loads applied at each location via a load cell.

The results of the static calibration show a maximum static force error of less than 1% of maximum load for the case of zero rotor offset. At eccentric positions they observe average errors of 2.1% for a 25% (0.1mm) rotor offset, and 5% for a 75% (0.3mm) rotor offset.

A series of dynamic tests are performed in which the AMB is used to excite the system at known frequencies from 20 – 120 Hz. The excitement frequencies are independent of rotational speed, two rotational speeds are examined, static and 5000 RPM. FRF methods are used to determine the rotor mass, this determined value is compared to the known mass of the rotor. In the worst case, the quoted error was 4%, this was for a 0.01 amplitude displacement at 5000 RPM with a center offset of 0.1mm.

The rig discussed in this paper was designed to explore the dynamic forces associated with turbomachinery. To date it has been used for research related to fluid bearings (Knopf and Nordmann, 1998), a single stage centrifugal pump (Aenis and Nordmann, 2000), and turbulent journal bearings (Knopf and Nordmann, 2001).

### ***1.7.4 Novel Techniques***

Recently, other researchers have used fiber-optic strain gauges embedded in AMBs to obtain AMB forces (Zutavern et al., 2004). Although such a system has been shown to exhibit significantly reduced uncertainty (0.25% of bearing load capacity, static), the additional instrumentation required makes the technique unattractive for field applications.

### ***1.7.5 Other Relevant Topics***

#### **SENSOR RUNOUT**

Sensor runout refers to changes in position probe signals that are not related to real changes in the position of the rotor relative to the stator. Two general approaches have been applied to the issue of runout in AMBs; reduction of the runout signal and controller compensation of the runout signal.

The first approach, which calls for the reduction of signal runout, requires some combination of improved sensors and sensor targets. Improvement is generally achieved upgrading the sensor technology or applying special manufacturing techniques. The first approach is the approach used by Jansen et al. (2002) in the redesign of an AMB suspended flywheel. Jansen cites two rounds of sensor upgrades: first the original optical position sensors were replaced with eddy current position sensors; and second, the eddy current position sensors were scheduled to be replaced

with an improved eddy current position sensor at the time of the publication. Jansen also indicates that tight control of sensor target surface finish was required.

The controller compensation approach is less invasive. Rather than eliminate the runout signal, the runout signal is identified so that it can be compensated. Kim and Lee (1997) discuss the application of an *in-situ* identification based on extended influence coefficients. In this method, an additional position disturbance signal is injected to the system via the AMB controller. The system's response to the additional disturbance is used along with the systems response to the runout disturbance alone to identify the required compensation. This method is valid for the operating speed at which it is applied and is reported to be sensitive to speed change. In order to achieve compensation over a range of speeds, the method must be applied at several speeds within the range. The method requires a host PC in addition to the system controller in order to run the compensation algorithm.

Wu (2001) discusses potential stability issues associated with applying gain scheduled  $H_{\infty}$  controllers to runout compensation due to the requirement of slow varying parameters. Also discussed is the application of a  $\mu$ -synthesis approach which offers improved stability, but is sensitive to rotor speed. Wu proposes an LPV approach in which multiple LPV controllers, each tuned for a specific speed, may be strung together.

Setiawan et al. (2001) proposes an adaptive compensation algorithm in which rotor stability is achieved through estimation and feedforward cancellation of sensor runout. This method was tested in simulation and on a well-balanced rotor at 1200 RPM.

In general, approaches that have been applied to runout rely on significant system changes. Reduction of runout signal requires that changes be made to the rotor position sensors and/or the sensor target. Controller based approaches require additional computing power to run control algorithms not typically associated with an AMB.

In contrast, application of the MPM only requires access to control signals that are inherent to an AMB; specifically, coil current and rotor position. The MPM uses system data in conjunction with a simple model of the AMB to infer the air gap distance between the rotor and stator. Air gap distance can be used to estimate actual rotor runout (as opposed to sensor runout). The rotor runout determined in this way can be compared to the sensor runout as reported by the rotor position sensors to arrive at a compensation.

## **SYSTEM IDENTIFICATION**

Numerous references on system identification are available, including Goodwin and Payne (1977), and Hsia (1977). In a system identification problem, inputs and outputs of the system to be identified are monitored. If practical the inputs may be perturbed in order to realize input/output relationships in a controlled manner. The object of system identification is to provide a model in which the outputs can be estimated based on the inputs. According to Hsia, models generally fall into one of three different categories;

- White box: a model derived entirely from physical first principles; no identification is required
- Black box: an entirely empirical model is developed based solely on observed system input/output relations

- Gray box: Certain aspects of the model are known such as applicable physical laws.

Although system identification in a classic sense provides a black box model, in practice gray box models are the norm. In the case of a gray box model, a model (or perhaps several models) of the system is proposed, and the problem is reduced to parameter identification. Other ways in which system identification techniques are categorized include parameter estimation method, parameter error criterion, and the operating mode in which the parameter estimation is carried out.

The system identification applied here relies on a proposed “gray box” model for which certain parameters must be estimated. The parameters are estimated such that the “output error”, or deviation of model output from system output is minimized. The parameter estimation occurs in an off-line mode; all observations are made prior to parameter estimation.

System identification as applied to this discussion of AMB based force measurement relies on a formulation of a magnetic force model as shown in Equation 1.13. The inputs to the model include universal physical constants and physical dimensions that are constant for a specific magnetic bearing as well as observed currents. The identification technique, outlined in Section 1.3, relies on multiple current perturbations. Each current perturbation results in a unique set of observed currents such that multiple instances of Equation 1.2 can be written. The true applied force and rotor offset are unknown but constant regardless of current perturbation. The output of the model is the value of rotor offset  $x$  that, when used in Equation 1.13 along with the different sets of observed currents, causes the least variation between the calculated values of applied force  $F$ .

Although the ability to monitor bearing force is built into the system via force transducers, it is there as an audit feature only, and not as a means to supply system output data. Rather, in a departure from traditional system identification, the output of the system is assumed to be *unknown but constant* over a variety of perturbations to system input.

### **1.7.6 Conclusion**

Several examples of the use of AMBs to provide dynamic force measurement are discussed in the literature. In general, the research to date has focused on providing a laboratory tool to enhance the study of dynamic force effects related to elements of turbomachinery such as bearings, seals, and pumps. The controlled nature of the intended environment of the AMB force measurement systems has encouraged the implementation of instrumentation and system identification techniques that are not appropriate for field application. The exception is the development of a system identification technique (MPM) to allow identification of AMB loads. The method is unique in that no external instrumentation is required, instead, perturbations of coil current are applied via the system controller and the response of the system is observed. The research discussed in this dissertation is focused on further development of system identification techniques that leverage the instrumentation and control system inherent to an AMB system. Such techniques could be readily applied to any AMB system for force measurement or runout compensation.

## **1.8 OVERVIEW OF DOCUMENT**

The presentation of this research begins with a description of the experimental setup and procedures. Next are separate discussions of a static characterization of a force model, and the application of such a model to measurement of force in a rotating system.

The work falls into two categories: characterization of a force model using Multi-Point Method (MPM), and application of the characterized model to the measurement of dynamic forces. The MPM, discussed in Section 1.7.1, was developed by Kasarda et al. (2000) and Marshall et al. (2001) for system identification of AMB forces. The method does not require instrumentation in addition to that inherent to an AMB system, and does not require application of a known force. As such it is appropriate for field application.

The MPM employs a force model that is based on values of coil current as reported by the system controller. The method relies on current perturbations applied to the system by the user and subsequent interrogation of coil current to gauge the system response. The method was tested experimentally by Marshall and shown to provide measurement of static AMB force with an accuracy of ~3% of applied load. The techniques behind the MPM were explored and leveraged to generate a more efficient technique. The new technique relies on the same system perturbations as the MPM coupled with a direct solution method.

Although current perturbation techniques are capable of acceptable accuracy, they require that applied force be kept constant (non-rotating, static load) while the user applies a variety of system perturbations. As such they are not appropriate for measurement of forces typically found in a rotating system. However, they can be used to generate a system identification of the relationship between the rotor offset as reported by the system controller and effective air gap. This identification is expressed as a coordinate transformation that contains an offset term that varies with rotor angle to account for runout. The coordinate transformation is applied in conjunction with a force model that is based on values of coil currents and rotor position offset as reported by the system controller. In this way, once the transform is established, AMB force measurements are made without system perturbation. As such the technique is appropriate for application to force measurement in a rotating system. The technique has been tested experimentally on non-rotating static loads with an accuracy of ~2% - 6% of applied load.

The characterized force model was also applied to the measurement of bearing forces in rotating systems. Five such AMB systems were operated under a variety of unbalance, rotational speed, and bias current conditions. Force transducers were mounted beneath the AMBs to provide a direct measurement of dynamic force. The results of the characterized model were compared to the force transducer data as well as to the results from a basic (uncharacterized) force model. The results of the tests shows that the characterized model provides force measurements that are more accurate than the force measurements provided by the basic model. In terms of estimated force values, errors associated with the characterized model are typically 2.5N compared to a 3.6N error associated with the basic model. This represents a 30% improvement over the

basic model. From a percent of measured load standpoint, errors associated with the characterized model are typically ~16% compared to ~40% associated with the basic model. This represents a 60% improvement over the basic model.

We believe that the runout aspect of the characterization plays a large role in the accuracy improvement. In order to bound the significance that angular errors introduced during runout characterization may have on the results of the characterized model, a simulated perturbation was applied to the runout correction table corresponding to one of the test rotors. The errors associated with the perturbed model are shown to be ~60% - 70% of the errors associated with the unperturbed, characterized model. This demonstrates a strong correlation between static runout characterization and force model accuracy. Furthermore, it underscores the requirement that a comprehensive static calibration must be applied prior to attempting a dynamic force measurement. The effects of dynamic phenomena such as eddy current and hysteresis cannot be determined until static effects such as runout are first compensated.

Descriptions of the experimental procedures are given in Chapter 2 followed by description of the experimental setup in Chapter 3. In later chapters the procedures will be discussed in greater detail along with their associated results. Chapter 4 and Chapter 5 address the details of the static model characterization; specifically, location of the effective origin and runout compensation is discussed in Chapter 4, and a transformation to effective coordinates discussed in Chapter 5. Chapter 6 describes a dynamic force measurement “pilot study” that occurred prior to the static characterization work. A force model that has been characterized by the methods described by Chapter 4 and Chapter 5 is applied to rotating systems in Chapter 7. Chapter 7 presents the results of the data collection and shows dynamic force estimates from both characterized and uncharacterized models along with a direct measurement of bearing force from force transducers. Finally, Chapter 8 presents the conclusions of the research along with recommendations for future work.

## Chapter 2 Experimental Procedure

In broad terms, the experiments that were performed as part of this research can be put into one of two classifications: static or dynamic. Static experiments were performed on the AMB experimental systems without shaft rotation and with the motor uncoupled from the shaft. The motivation behind the static experiments was to identify system parameters that can be applied in conjunction with a simple AMB force model to improve force measurement accuracy. Dynamic experiments were performed with the added element of a shaft rotation. The motivation behind the dynamic experiments was to observe how the accuracy of the force measurement varied as other system parameters such as rotational speed, bias current, and unbalance load were varied. The dynamic measurements were further motivated as a platform to test dynamic AMB force models.

### TEST SYSTEMS

The experiments described here were carried out on 5 separate AMB systems that were based on two platforms. The first platform (Platform 1) is a typical high-speed laboratory rotor kit from Revolve Magnetic Bearings and has a 0.015in. radial gap and 0.014in. rotor laminations. One system was tested on this platform. The second platform (Platform 2) is a custom built magnetic bearing test bed, also built by Revolve Magnetic Bearings. This platform was designed with a common stator and four interchangeable rotors. Each rotor has a unique combination of nominal air gap and lamination thickness. In this way, Platform 2 can be configured as 4 unique systems.

1. 0.010in. radial gap, 0.005in. lamination (Arnon 5)
2. 0.030in. radial gap, 0.005in. lamination (Arnon 5)
3. 0.010in. radial gap, 0.014in. lamination (M19)
4. 0.030in. radial gap, 0.014in. lamination (M19)

Additional specifications for each test system are found in Chapter 3.

## **2.1 STATIC EXPERIMENTS**

Static experiments were performed on the AMB rigs without shaft rotation. The motivation behind the static experiments was to identify system parameters that can be applied in conjunction with a simple AMB force model to improve force measurement accuracy. The Multi-Point Method (MPM) described in detail below was used extensively during the system identification procedure. The rotor position offset provided by the MPM is considered to be an “effective” offset. This value, when compared to the rotor position offset reported by the system controller, provides information relating the rotor position system coordinates to an “effective” coordinate system. The goal of the system identification procedure is to determine a mapping between system coordinates and effective coordinates. The effective coordinates are determined by observation of the AMB’s actual behavior; as such they account for unmodeled effects.

System coordinates are based on the rotor position reported by the system controller. The origin of the system coordinates is typically based on the center of the associated retainer bearing. AMBs employ a conventional bearing, referred to as a retainer bearing, to support the shaft when the bearing is not operational. Retainer bearings are designed with a nominal clearance to the shaft so that they do not contact the shaft during normal operation. In general, the retainer bearing will not be concentric with the stator; this is one contributor to the difference between the system coordinate origin and the effective coordinate origin. Other contributions include variations between the bearing model and the actual bearing. For instance, bearing pole parameters such as pole face area and number of wire turns per pole are generally modeled to be constant for all poles of a bearing stator. Variation of these parameters due to manufacturing or damage will cause unmodeled variation in the bearings behavior. Such behavior may be accounted for by identification of an effective coordinate system that is based on the observed behavior of the bearing.

### ***2.1.1 Current Perturbation – The Multi-Point Method***

The system identification techniques that are the focus of this part of the research rely on a current perturbation technique known as the Multi-Point Method (Kasarda et al., 2000; Marshall et al., 2001). It is based on the idea that a system can be perturbed with multiple currents (“multi-points”) and information about the system can be inferred from its response to the perturbations.

## **SYSTEM REQUIREMENTS**

The MPM requires a basic geometric model of the AMB system including the number and arrangement of the stator poles and position sensors. In our case, all systems consisted of 8-pole heteropolar bearings. The bearing poles were 22.5° offset from the force axes  $V$  and  $W$ . The sensor axes lay along their respective force axes. The force axes are positioned 90° from each other, and 45° from vertical. This configuration is shown in Figure 2.1.

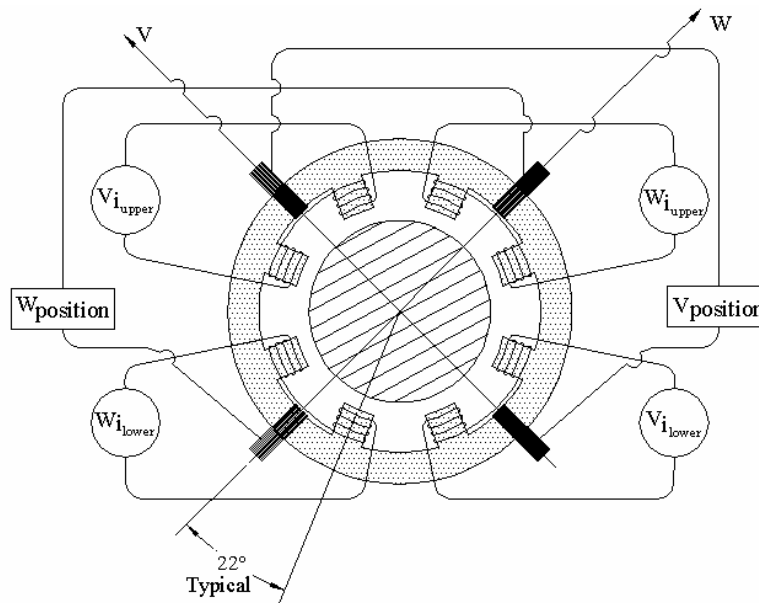


**Figure 2.1: AMB stator geometry and monitored signals**

The MPM requires that the following system specifications be known:

- Area of a single stator pole face:  $A_g$
- Number of wire turns per pole:  $N$
- Nominal air gap:  $g_o$
- Estimate of flux path length through iron core:  $L_i$
- Estimate of magnetic permeability of iron core:  $\mu_r$

The above information is generally available from the bearing manufacturer. The MPM also requires that certain control signals can be monitored, specifically:

- Position sensor output:  $x$  for a given axis
- Coil currents:  $i_{upper}$  and  $i_{lower}$  for a given axis

The ability to specify one of the following system parameters is required in order to use the MPM

- Coil current bias
- Control current injection

Additionally, the ability to specify the following system parameters is required in order to use the MPM to find the effective origin of the rotor.

- Rotor position set-point

Although it is taken for granted that the above requirements can be met in the general case, it is also understood that such access may be within the purview of the manufacturer or manufacturer's representative. The systems studied under this research were specifically built as research systems so that access to the required signals was straightforward.

## SYSTEM MODEL

A mathematical model of the bearing force is required as well, modeling of bearing force is discussed in Section 1.5. The general model for a typical force axis of the bearings

used in this research, as developed in Equation 1.13, is repeated here. Figure 1.4, repeated below, contains the corresponding schematic of a typical force axis.

$$F = k \cos \theta \left[ \frac{i_{upper}^2}{(2(g_o - x \cos \theta) + b)^2} - \frac{i_{lower}^2}{(2(g_o + x \cos \theta) + b)^2} \right] \quad (1.13)$$

where:

$$k = \mu_o AN^2 \cos \theta$$

$\mu_o$  = magnetic permeability of air

$A$  = area of pole face

$N$  = number of wire turns on actuator coil

$\theta$  = angle between bearing axis and axis of an individual magnetic pole.

$i_{upper}$  = coil current in upper actuator

$i_{lower}$  = coil current lower actuator

$g_o$  = nominal air gap

$x$  = rotor displacement along bearing axis

$b = L_i / \mu_r$  = equivalent air gap due to the flux path through the rotor and stator

$L_i$  = approximation of flux path through rotor and stator

$\mu_r$  = the relative permeability of the rotor and stator material (relative to  $\mu_o$ )

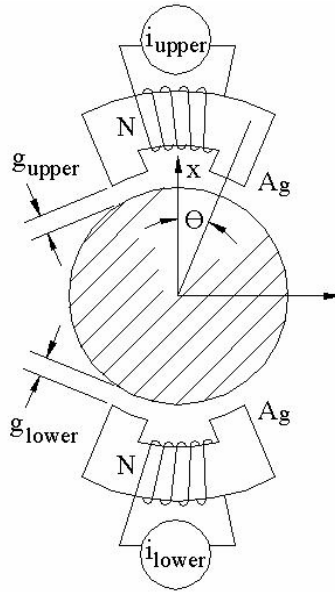


**Figure 1.4: Typical force axis (V or W)**

With the above listed bearing specifications and signals, the MPM can be implemented.

## FOUNDATION OF MPM

Current perturbation techniques make use of the controller's ability to support a certain load at a specific location for any bias current setting within the operating envelope of the system. For a given load and position scenario, a change in bias current will result in a change in the controller current pair  $i_{upper}$  and  $i_{lower}$ . Bias current perturbation is used in our test set-up to generate multiple pairs of controller currents. Alternatively, injected

current signals could be used to perturb the system. Each controller current pair is then substituted into separate expressions of a simple AMB force equation (Equation 1.13). Since neither the load nor the rotor position is varied between these expressions, they can be considered simultaneous equations. These equations can be solved either directly or through simulation to provide values of load ( $F$ ) and effective rotor position offset ( $x$ ). This technique is known as the Multi-Point Method or MPM. A simulation technique and a direct solution are discussed in the following sections.

### **Origin of Multi-Point Method (MPM)**

The Multi-Point Method was developed by Kasarda et al. (2000), and Marshall et al. (2001). The key advantage of the MPM is that it allows system identification of an AMB using only the AMB system itself; no additional hardware or physical access is required. Perturbations to coil currents are applied by the user, and the system response to the perturbations is monitored. In practice, coil current perturbation is realized by changing the bias current setting in the system controller. MPM measurements require multiple system perturbations; the response of the system is gauged by monitoring corresponding coil currents. The MPM is based on a lumped gap model. The equation describing the model as it pertains to the laboratory rig is given by Equation 1.13.

To measure a given force, the MPM requires multiple sets of measured currents ( $i_{upper}$ ,  $i_{lower}$ ). Such currents are obtained by perturbing the AMB system and monitoring its response. Typical operation requires three such sets of current pairs. The solution technique developed by Kasarda (2000) and Marshall (2001) requires several thousand simulations based on Equation 1.13. This process generates a locus of possible solutions for each bias current set-point. Figure 2.2 shows an example of two such loci. Each locus was generated by solving Equation 1.13 for a given current pair ( $i_{upper}$ ,  $i_{lower}$ ), and  $h$  simulated rotor offsets  $x(h)$ . The maximum and minimum values of  $x$  used in the simulation were determined by the likely maximum position offset of the rotor: in this case 0.010in. or  $\sim 250\mu\text{m}$ . Each simulated value of  $x(h)$  applied to Equation 1.13 results in a simulated value of force  $F(h)$ . The loci in the figure were generated from two sets of current pairs: ( $i_{upper,1}$ ,  $i_{lower,1}$ ), and ( $i_{upper,2}$ ,  $i_{lower,2}$ ). For these cases, Equation 1.13 becomes:

$$F_1(h) = k \cos \theta \left[ \frac{i_{upper,1}^2}{(2(g_o - x(h) \cos \theta) + b)^2} - \frac{i_{lower,1}^2}{(2(g_o + x(h) \cos \theta) + b)^2} \right] \quad (2.1)$$

and

$$F_2(h) = k \cos \theta \left[ \frac{i_{upper,2}^2}{(2(g_o - x(h) \cos \theta) + b)^2} - \frac{i_{lower,2}^2}{(2(g_o + x(h) \cos \theta) + b)^2} \right] \quad (2.2)$$

where  $-250\mu\text{m} \leq x(h) \leq 250\mu\text{m}$ .

Since the bearing load is not changed from Equation 2.1 to Equation 2.2, the intersection of the equations represents the identified value of force  $F$  ( $F = F_1 = F_2$ ) that is valid for the model represented by Equation 1.13. The corresponding position value  $x$  represents the effective rotor position.

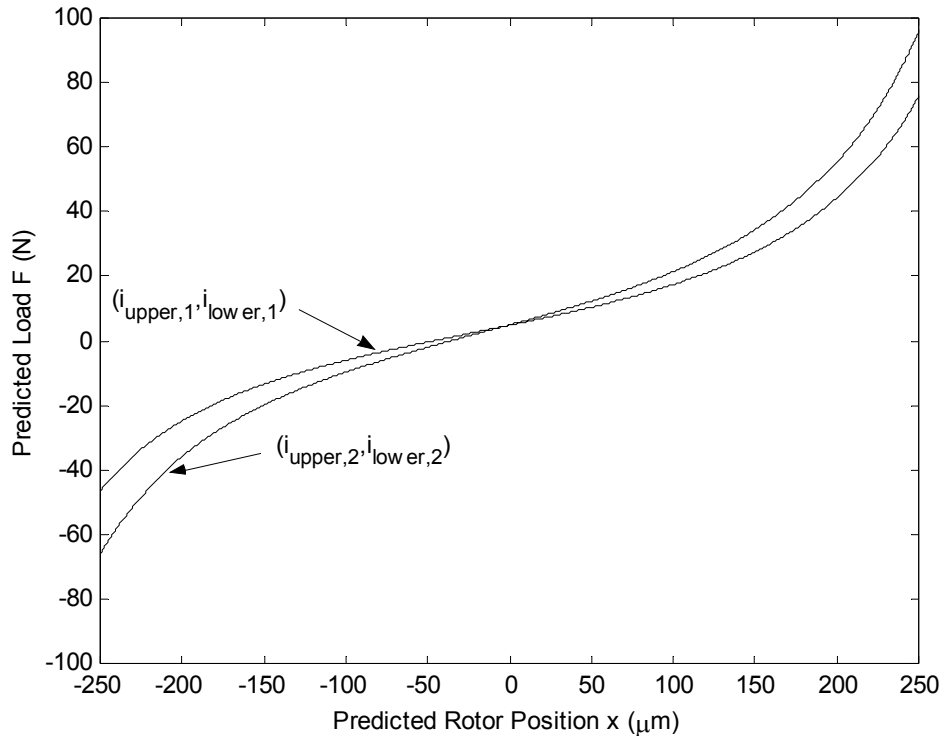


**Figure 2.2: Loci of solutions to Equation 1.13 based on two sets of coil current:  $(i_{upper,1}, i_{lower,1})$  and  $(i_{upper,2}, i_{lower,2})$**

As mentioned, in practice a minimum of three current pairs (and therefore three loci) are used to identify the AMB force. Three current pairs are used to reduce the sensitivity of the system identification to errors in input current values.

Marshall employed the above technique in conjunction with a linear correction to measure AMB forces throughout the bearing volume with an accuracy of  $\sim 3\%$ . Although the linear correction was determined from knowledge of the actual load, Marshall's experiments demonstrate the repeatability of the method.

Although this MPM solution technique is effective, it is not closed form; the computer program must perform many calculations ( $\sim 20000$ ) to reach a solution.

### ***Direct Solution of Multi-Point Method***

A direct solution to the MPM, as applied by Prins et al. (2005), is both faster computationally and more elegant. Similar to the MPM solution described in the previous section, the direct solution also requires multiple sets of measured currents,  $(i_{upper}, i_{lower})$ , that correspond to the same applied force. These currents are obtained by perturbing the AMB system and monitoring its response. System perturbation is achieved by changing the bias current setting of the system controller. Resulting sets of coil currents  $(i_{upper}, i_{lower})$  are used to populate Equation 1.13. Two such equations, corresponding to two sets of measured current pairs,  $(i_{upper,1}, i_{lower,1})$ , and  $(i_{upper,2}, i_{lower,2})$  are shown below.

$$F_1 = k \cos \theta \left[ \frac{i_{upper,1}^2}{(2(g_o - x \cos \theta) + b)^2} - \frac{i_{lower,1}^2}{(2(g_o + x \cos \theta) + b)^2} \right] \quad (2.3)$$

and

$$F_2 = k \cos \theta \left[ \frac{i_{upper,2}^2}{(2(g_o - x \cos \theta) + b)^2} - \frac{i_{lower,2}^2}{(2(g_o + x \cos \theta) + b)^2} \right] \quad (2.4)$$

Direct results can be obtained by setting the right hand sides of Equations 2.3 and 2.4 equal to each other. Equating Equations 2.3 and 2.4 results in Equation 2.5, all of the variables in equation 2.5 are known except for the effective rotor offset,  $x$ .

$$\frac{i_{upper,1}^2}{(2(g_o - x \cos \theta) + b_{th})^2} - \frac{i_{lower,1}^2}{(2(g_o + x \cos \theta) + b_{th})^2} = \frac{i_{upper,2}^2}{(2(g_o - x \cos \theta) + b_{th})^2} - \frac{i_{lower,2}^2}{(2(g_o + x \cos \theta) + b_{th})^2} \quad (2.5)$$

Equation 2.5 can be manipulated to solve for the effective rotor offset  $x$  as seen in Equation 2.6.

$$x = \frac{1}{\cos \theta} \left[ \frac{2g_o + b_{th}}{i_{lower,1}^2 - i_{lower,2}^2 - i_{upper,1}^2 + i_{upper,2}^2} \right] \left[ \frac{i_{lower,1}^2 - i_{lower,2}^2 + i_{upper,1}^2 - i_{upper,2}^2}{2} \pm \sqrt{(i_{lower,1}^2 - i_{lower,2}^2)(i_{upper,1}^2 - i_{upper,2}^2)} \right] \quad (2.6)$$

Although Equation 2.6 is quadratic the correct root is easily determined since it is the only value of  $x$  that exists within the physical confines of the stator. The effective rotor offset  $x$  identified in this manner can then be used in Equation 1.13 to solve for force if desired.

### **Importance of MPM Results**

Since Equation 1.13 describes the force in one axis, the result of Equation 2.6 is the effective rotor offset for that axis. The MPM is applied to both axes so that an effective rotor position offset ( $v_e, w_e$ ) can be determined. The effective rotor position is the rotor position value that, when used in conjunction with the AMB force model in Equation 1.13, causes the force model to behave like the real system.

The controller also reports a value of rotor position. The rotor position reported by the controller is the offset of the rotor from a nominal location as measured by the position sensors that are part of the AMB feedback system. Since the measured rotor position is the position used in the system control loop, it is referred to as ( $v_s, w_s$ ). In general, the rotor offset reported by the position sensors ( $v_s, w_s$ ) will differ from the effective offset ( $v_e, w_e$ ) determined via the MPM. The difference is due to the choice of origin location for the ( $v_s, w_s$ ) coordinates and unmodeled behavior of the real system.

Rotor positions ( $v_s, w_s$ ) are readily available from the system controller. However, if the system reported values of rotor position ( $v_s, w_s$ ) are used in the force model described by Equation 1.13, large errors may result. Effective position values ( $v_e, w_e$ ) are based on the behavior of the real system. If they are used in the force model described by

Equation 1.13, reasonable accuracy is achieved. If the MPM is applied at several rotor locations, a systematic rule (coordinate transformation) can be determined to relate the measured rotor offset ( $v_s, w_s$ ) to the effective rotor offset ( $v_e, w_e$ ). Knowledge of this relationship gives us the ability to calculate an effective rotor offset directly from a reported rotor offset without the need to perturb the system. Since effective offsets can be used to calculate forces, this also gives us the ability to make force measurements with approximately the same accuracy as the MPM based force technique (~3%) without the need to perturb the system.

### **Collection of MPM Data – Procedure**

A typical data set collected for the MPM is based on a single rotor set-point and three bias current settings. For each bias current setting the system was levitated and allowed 10 seconds to stabilize to eliminate transients. The data acquisition program ran for 1 second at a sample frequency rate of 20 kHz/channel. The average upper and lower coil current values, ( $i_{upper}, i_{lower}$ ), associated with both axes, ( $V$  and  $W$ ), are recorded. The coil current collection procedure is repeated for each bias current setting so that three sets of four coil current values were collected. This data is described in Table 2.1.

**Table 2.1: Summary of coil current data collected for MPM**

<b>Bias Current Setting</b>	<b>V axis</b>	<b>W axis</b>
<b>1</b>	( $i_{upper,1}, i_{lower,1}$ )	( $i_{upper,1}, i_{lower,1}$ )
<b>2</b>	( $i_{upper,2}, i_{lower,2}$ )	( $i_{upper,2}, i_{lower,2}$ )
<b>3</b>	( $i_{upper,3}, i_{lower,3}$ )	( $i_{upper,3}, i_{lower,3}$ )

### **Interpretation of MPM data – Process**

As described in the previous section, coil current data associated with the upper and lower coils of both axes were collected for three bias current settings. The coil current data was entered into a Matlab code that contained a model of effective bearing position  $x$  based on Equation 2.6. The Matlab code treats each axis independently. Equation 2.6 requires two sets of coil current data corresponding to a constant force; the data collection described above provides three such sets of coil currents. The third data set is used as a safeguard against having a bad coil current data point significantly skewing the resulting effective rotor offset value  $x$ . Three combinations of coil currents ( $i_{upper}, i_{lower}$ ) can be made from the data shown in Table 2.1, the possible combinations for a given axis are;

1. [( $i_{upper,1}, i_{lower,1}$ ), ( $i_{upper,2}, i_{lower,2}$ )]
2. [( $i_{upper,1}, i_{lower,1}$ ), ( $i_{upper,3}, i_{lower,3}$ )]
3. [( $i_{upper,2}, i_{lower,2}$ ), ( $i_{upper,3}, i_{lower,3}$ )]

Equation 2.6 is solved for each of the three combinations shown above resulting in three corresponding effective rotor position values. The median of the three calculated values is taken as the effective position value of record for that axis.

### **Static Force Measurement**

Effective rotor position is used in Equation 1.13 to provide a force measurement. Since a minimum of two bias current settings corresponding to an identical load are required to generate the data to populate Equation 2.6, this method is not applicable for dynamic

force measurement in which the load fluctuates. However, it can be used to establish a static load value.

The systems tested as part of this research were equipped with force transducers to record the reaction forces of the bearings. The force transducers used are of a design that is primarily for the measurement of dynamic force. If a static load is applied to such a transducer, the transducer signal will leak down to zero exponentially over time, with significant leakage (~15%) over the first 5 seconds. As a “work around”, static loading of a bearing was measured by first applying the load for several minutes to allow the transducer reading to return to zero, then removing the load rapidly (<0.1 seconds transition). Transducer data was acquired over the time of the unloading so that the resulting load change could be determined. Transducer data was acquired to verify the calculated force values. The results, discussed in chapter 6, show that the accuracy of calculated force values is in the range of 2% - 6%, depending on test platform.

### 2.1.2 Coordinate Transformation Overview

A transformation that accounts for variations in origin location (offset), axes rotation, and axes scale between system coordinates and effective coordinates is desired. Such a transformation will allow for accurate force measurement without the requirement of perturbations.

#### REVIEW OF COORDINATE TRANSFORMATIONS

A coordinate transformation is a mathematical tool that is used to describe one coordinate system in terms of a different coordinate system. Coordinate transformations can be used to describe a location that is known in one coordinate system in terms of a second coordinate system. For example, consider the coordinate systems in Figure 2.3. Coordinate system “A” consists of two axes,  $X_A$  and  $Y_A$ . Any point in system A can be described in terms of its distance from the origin along the  $X_A$  and  $Y_A$  axes respectively,  $(x_A, y_A)_A$ . Coordinate system “B” is similar to A, but has its origin at a different location. Any position  $(x_A, y_A)_A$  can also be described by its corresponding position in the B coordinate system  $(x_B, y_B)_B$ . For instance, it can be seen that point  $(7, 4)_A$  corresponds to point  $(4, 2)_B$ , and that point  $(5, 5)_A$  corresponds to point  $(2, 3)_B$ . The relationship between the points in A and the points in B can be generalized by a coordinate transformation

from A to B. The transform can be thought of as an operator  $T^{A \rightarrow B}$  such that  $T^{A \rightarrow B} [(x_A, y_A)] = (x_B, y_B)$ . For the example shown in Figure 2.3,  $T^{A \rightarrow B} = [(x_A - 3, y_A - 2)]$ .

$T^{A \rightarrow B}$  can be used to map any position that is expressed in terms of  $(x_A, y_A)_A$  into its equivalent position  $(x_B, y_B)_B$ . In a more general case, a transformation can be used to describe not only the relative offset, but also the relative rotation and scale between two coordinate systems.

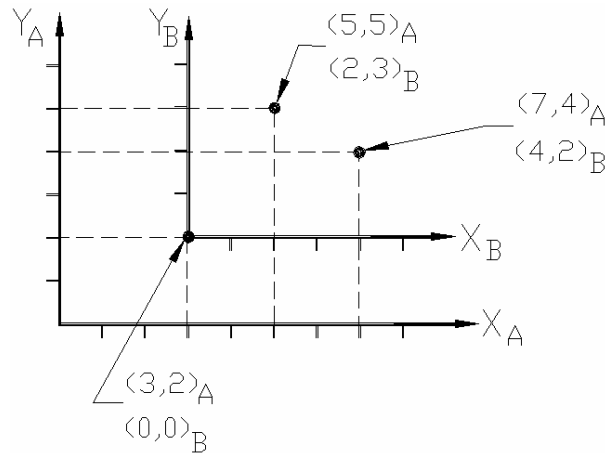
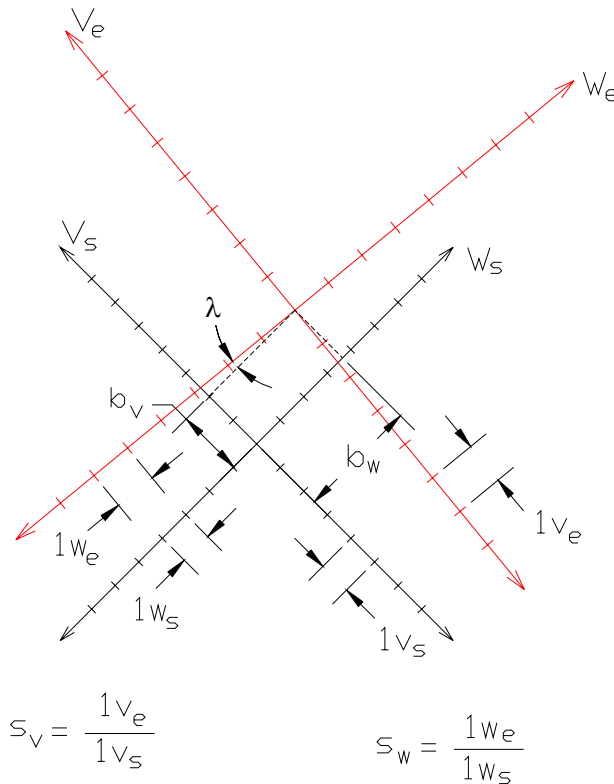


Figure 2.3: Example of an axes offset transformation

### TRANSFORMATION OF POSITION DATA FROM $(V_s, W_s)$ TO $(V_e, W_e)$

As part of our research, a coordinate transformation was developed in order to map a rotor position that is expressed in terms of its system coordinates  $(v_s, w_s)$  into its corresponding effective coordinates  $(v_e, w_e)$ . The controller reports a rotor's position in system coordinates; this information is readily available. In the previous section a procedure known as the Multi-Point Method (MPM) was used to determine an effective rotor offset  $(v_e, w_e)$  that corresponds to a specific system offset  $(v_s, w_s)$ . If this process is repeated at several specific locations along the system coordinate axes so that several sets of effective offset values that correspond to known system offset values are collected, a coordinate transformation between the system axes and the effective axes can be calculated. Since effective offsets can be used to calculate forces, knowledge of effective offset gives us the ability to make force measurements with approximately the same accuracy as the MPM based force technique ( $\sim 3\%$ ) without the need to perturb the system.

Figure 2.1 shows the schematic of an 8-pole radial AMB that is representative of the bearings used in our research. The schematic shows the force axes,  $V$  and  $W$ , of the bearing as well as the position sensors. The position sensors are used to measure the rotor's offset from a nominal origin, the position sensor data is available via the controller and is reported in system coordinates;  $(v_s, w_s)$ . Figure 2.4 shows the relationship between the system coordinates and the effective coordinates for arbitrary values of offset, rotation, and scale. In the figure the system coordinates are represented by black axes and subscripted with an  $s$ . The effective coordinates are represented by red axes and subscripted with an  $e$ .



**Figure 2.4: Relationship between system coordinates ( $v_s, w_s$ ) and effective coordinates ( $v_e, w_e$ )**

The required transformation consists of an axes offset, rotation, and scale to allow position data to be mapped from system coordinates to effective coordinates. Each transformation is considered separately below and is applied serially to the system coordinate data ( $v_s, w_s$ ).

- **Offset:** The offset transformation,  $T_{OFFSET} = [(v_s - b_v, w_s - b_w)]$ , is applied first and is similar to the offset transform applied in the earlier example. In the transformation the values of  $b_v$  and  $b_w$  represent the distance (expressed in system coordinates) from the system coordinate origin to the effective coordinate origin along the  $V_s$  and  $W_s$  axes respectively. This transform, when applied to data that is expressed in terms of system coordinates, results in an expression of the rotor position in an intermediate coordinate system, ( $v_{OFFSET}, w_{OFFSET}$ ):

$$T_{OFFSET}(v_s, w_s) = (v_{OFFSET}, w_{OFFSET}) \quad (2.7)$$

- **Rotation:**  $T_{ROTATION} = [v_{OFFSET} \cos \lambda - w_{OFFSET} \sin \lambda, v_{OFFSET} \sin \lambda + w_{OFFSET} \cos \lambda]$ , where  $\lambda$  is the angular offset between the system coordinate axes and the effective axes. This transform, when applied to data that is expressed in terms of the first intermediate coordinate system, ( $v_{OFFSET}, w_{OFFSET}$ ), results in an expression of the rotor position in a second intermediate coordinate system, ( $v_{ROTATED}, w_{ROTATED}$ ).

$$T_{ROTATION}(v_{OFFSET}, w_{OFFSET}) = (v_{ROTATED}, w_{ROTATED}) \quad (2.8)$$

- **Scale:**  $T_{SCALE} = [s_v \cdot v_{ROTATED}, s_w \cdot w_{ROTATED}]$ , where  $s_v$  and  $s_w$  are the scaling factors between the system coordinates and effective coordinates along the V and W axes respectively. This transform, when applied to data that is expressed in terms of the second intermediate coordinate system,  $(v_{ROTATED}, w_{ROTATED})$ , results in an expression of the rotor position in the effective coordinate system,  $(v_e, w_e)$ , and is the final result.

$$T_{SCALE}(v_{ROTATED}, w_{ROTATED}) = (v_e, w_e) \quad (2.9)$$

### 2.1.3 Procedure to Determine Effective Rotor Origin (Transform Offset)

The effective origin is the location for which the MPM returns effective offset values of zero for each axis:  $(v_e, w_e) = (0,0)$ . In general this will not coincide with the origin in system coordinates:  $(v_s, w_s) = (0,0)$ . In Figure 2.4 and the accompanying text of Section 2.1.2 the offset of the origin of the effective coordinates was described in terms of system coordinates as  $(b_v, b_w)$ . Initial research regarding the transformation from system coordinates to effective coordinates focused on this element of the transform.

#### PROCEDURE TO DETERMINE TRANSFORM OFFSET

Since the goal at this stage was to determine the origin of the effective coordinate system, the rotor location that corresponded to an effective rotor offset of  $(0,0)$  was required. Recall that the origin of the effective coordinate system occurs at the rotor location for which the MPM returns effective rotor offsets ( $x$ ) of zero for both axes. The location of the effective origin is found by manually changing the rotor offset setting of the system controller so that the effective rotor position as calculated by the MPM is  $(0,0)$ .

The initial rotor position of the bearings tested coincided with the center of the retainer bearing which generally coincides with the system coordinate origin:  $(v_s, w_s) = (0,0)$ . The MPM was applied at this location to determine the corresponding position in effective coordinates  $(v_e, w_e)$ . For the initial position it is expected that the effective rotor offset will be non-zero. The effective offset determined by the MPM is used as an error signal in order to estimate a more appropriate rotor position. The rotor position set-point is adjusted according to the error estimate. Since the relative scale between the system coordinates and the effective coordinates is initially unknown, multiple iterations of rotor position adjustment are required to find the effective origin.

#### PROCEDURE TO DETERMINE TRANSFORM OFFSET - EXAMPLE

Consider the example in which the initial rotor location is at the origin of the system coordinates  $(v_{s,0}, w_{s,0}) = (0,0)$ . The MPM applied at this location determines that the corresponding position in effective coordinates is  $(v_{e,0}, w_{e,0}) = (10,5)$ . To simplify the example, only the V axis component is considered. The goal is to find the rotor offset set-point that corresponds to an effective offset of  $v_e = 0$ . The previous section instructs

that the effective offset should be used as an error signal. The rotor set-point is adjusted based on the initial set-point of  $v_{s,0} = 0$  and the  $v_{e,0} = +10\mu\text{m}$  error determined by the MPM as shown:

$$v_{s,1} = v_{s,0} - v_{e,0} = 0 - 10 = -10 \quad (2.10)$$

where:

$v_{s,0}$  = the initial rotor offset set-point (in system coordinates)

$v_{e,0}$  = the initial effective rotor offset

$v_{s,1}$  = the second iteration rotor offset set-point (in system coordinates)

The rotor set-point is changed from  $v_{s,0} = 0$  to  $v_{s,1} = -10$  per Equation 2.10, and the MPM is re-applied at the new rotor location. If the scaling between the system axes and the effective axes were identical, it would be expected that the effective rotor position would now be  $v_{e,1} = 0$ . In general this is not the case. In this example the effective location is calculated  $v_{e,1} = -4$ . An updated version of Equation 2.10 can be applied as shown:

$$v_{s,2} = v_{s,1} - v_{e,1} = -10 - (-4) = -6 \quad (2.11)$$

where:

$v_{s,1}$  = the second iteration rotor offset set-point (in system coordinates)

$v_{e,1}$  = the second iteration effective rotor offset

$v_{s,2}$  = the third iteration rotor offset set-point (in system coordinates)

The rotor set-point is now changed from  $v_{s,1} = -10$  to  $v_{s,2} = -6$  per Equation 2.11, and the MPM is re-applied at the new rotor location. The next effective location is calculated by the MPM to be  $v_{e,2} = 1.6$ . Another updated version of Equation 2.10 can be applied as shown:

$$v_{s,3} = v_{s,2} - v_{e,2} = -6 - 1.6 = -7.6 \quad (2.12)$$

where:

$v_{s,2}$  = the third iteration rotor offset set-point (in system coordinates)

$v_{e,2}$  = the third iteration effective rotor offset

$v_{s,3}$  = the fourth iteration rotor offset set-point (in system coordinates)

The rotor set-point is changed from  $v_{s,2} = -6$  to  $v_{s,3} = -7.6$  per Equation 2.12, and the MPM is again re-applied at the new rotor location. The corresponding effective location is now calculated  $v_{e,3} = -0.64$ . The final updated version of Equation 2.10 can be applied as shown:

$$v_{s,4} = v_{s,3} - v_{e,3} = -7.6 - (-0.64) = -6.96 \quad (2.13)$$

Since this represents less than  $1\mu\text{m}$  of error, the iteration sequence is stopped and the effective origin for the V axis is said to occur at  $v_s = -6.96$ . These steps are also shown in Figure 2.2 on two different number lines, one corresponding to the system coordinates and the other corresponding to the effective coordinates. In the figure the upper number line, labeled  $V_e$ , corresponds to the effective coordinates, and the lower number line, labeled  $V_s$ , corresponds to the system coordinates. Iteration numbers are shown in the circles.

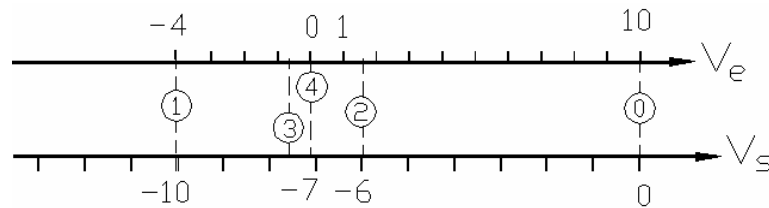


**Figure 2.5: Simplified example of finding the effective origin**

A more intelligent approach is possible if relative scaling between the system and effective coordinates is assumed up front. From the first iteration it can be seen that a  $10\mu\text{m}$  change in system position resulted in a  $14\mu\text{m}$  change in effective position. The difference in the position change as measured in system coordinates versus the position change as measured by the effective coordinates implies a relative scale of

$s_v = \frac{v_e}{v_s} = \frac{14}{10} = 1.4$ . If this scale factor is applied to Equation 2.12 as shown below, the

result is approximately equal to  $v_{s,4}$ , the iterated result.

$$v_{s,2} = v_{s,1} - v_{e,1} = -10 - \left( -4 \frac{1}{1.4} \right) = -7.14 \approx v_{s,4} = -6.96$$

### 2.1.4 Procedure to Determine Transform Scale and Rotation

During the work related to identification of the effective origin (Section 2.1.3), it was noted that a set-point change in rotor offset as reported by the system ( $v_s, w_s$ ) did not result in the same change in effective rotor offset ( $v_e, w_e$ ) as reported by the MPM. For instance, a  $10\mu\text{m}$  change to the rotor set-point would result in  $\sim 14\mu\text{m}$  change as measured by the MPM. Hence, multiple iterations were required to find the effective origin. The ratio of controller set-point change to MPM calculated change was consistent for a given test system. As such, it acts as a scale factor between the system coordinates and the effective coordinates.

While determining the scale factor between the systems, a small relative rotation was also noted. Although the rotation was typically small ( $\sim 2^\circ$  maximum) it is included in the transformation discussion for completeness.

#### RELATIVE AXIS SCALE FACTOR

In order to better define the relative scale between the coordinate systems, the rotor was positioned at a number of specific locations along each axis (in system coordinates). The rotor position was changed by varying the rotor position set-point on the controller. The MPM provided an effective rotor offset value corresponding to each known rotor location. Comparison of the known rotor offsets to the MPM calculated offsets was used to determine the relative scale between the two coordinate systems.

Figure 2.6 shows a schematic of the rotor position set-point locations along each axis that were used to determine the scale of the first test system (Platform 1). For the case of Platform 1, eight rotor position set-points were considered per axis. These set-points

were located along the  $V$  and  $W$  axes at  $\pm 25\mu\text{m}$ ,  $\pm 50\mu\text{m}$ ,  $\pm 75\mu\text{m}$ , and  $\pm 100\mu\text{m}$  relative to the effective origin. For the remaining systems, (Platform 2; Systems 1-4), the points considered were  $\pm 25\mu\text{m}$  and  $\pm 50\mu\text{m}$  relative to the effective origin.

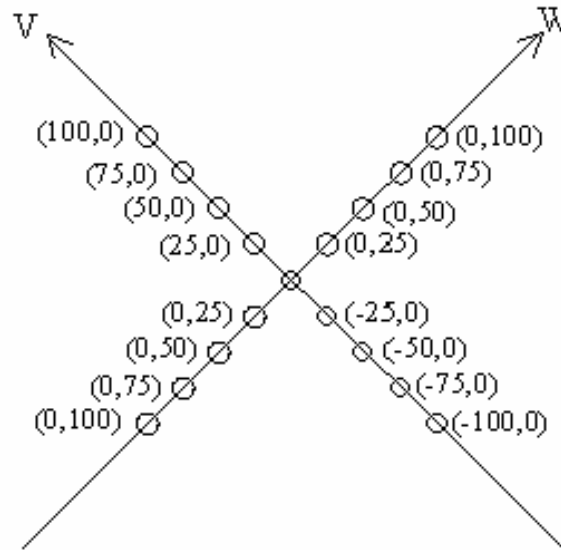


**Figure 2.6: Rotor set-points for system identification of axes scale (Platform 1)**

A comparison of the rotor set-points to their corresponding effective offsets as determined by the MPM revealed a linear relationship between the two coordinate systems. Each axis ( $V$  and  $W$ ) was treated independently so that it is possible to have a  $V$  axis scale that differs from the  $W$  axis scale for the same system. A best fit line with intercept forced to zero was used to approximate the relationship between the effective offsets and the rotor set-points, the slope of the line represents the system identification of the scale factor and is represented by  $s_v$  and  $s_w$  in the transform.

### RELATIVE AXIS SCALE FACTOR - EXAMPLE

Figure 2.7 shows an example of how the scale factor was determined for a particular axis. The rotor set-point was manually adjusted so that the rotor was located at the effective origin;  $(v_e, w_e) = (0,0)$ . Additional changes to the rotor set-point of  $\pm 25\mu\text{m}$ ,  $\pm 50\mu\text{m}$ ,  $\pm 75\mu\text{m}$ , and  $\pm 100\mu\text{m}$  were made relative to the effective origin. At each location the MPM was applied so that a corresponding effective rotor offset was found for each offset of the rotor in system coordinates. The rotor offset distances manually entered into the controller are plotted on the  $x$  axis. The corresponding offsets as determined by the MPM are plotted on the  $y$  axis. It can be seen that the resulting group of points can be described by a linear fit that passes through the origin. The slope of the fit line is the scale factor between rotor offset as measured by the system and rotor offset as calculated by the MPM.

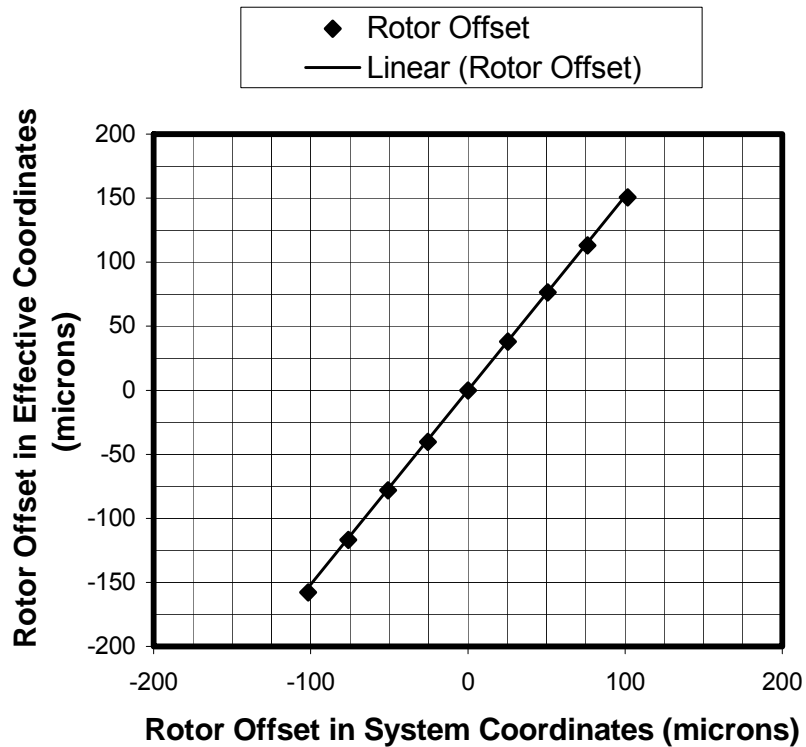


**Figure 2.7: Example of scaling between system coordinates and effective coordinates**

## RELATIVE AXIS ROTATION

During the scaling procedure a relative rotation between the system axes and the effective axes was noted. The MPM was applied to each axis during the scaling procedure, although the rotor set-point was changed along only one axis at a time. Small effective offsets were noted in the unchanged axis. It was further noted that the effective offsets in the unchanged axis tended to increase as larger changes were made to the rotor offset in the other axis. An average angle, based on the ratio of the effective offsets for the unchanged and changed axes, was determined for each system. This angle is represented by  $\lambda$  in the transform.

## RELATIVE AXIS ROTATION – EXAMPLE

In the previous example involving relative scale, a plot is made of the effective rotor offset along the  $V$  axis calculated by the MPM versus the corresponding rotor offset applied by the system along the  $V$  axis. When determining scale, rotor offsets are applied to only one axis at a time; for the plot in Figure 2.7 the corresponding  $W$  axis offset applied to the system is always zero. However, the MPM did report small changes in the effective rotor offset in the  $W$  axis corresponding to zero change in the  $W$  axis system set-point. Figure 2.8 shows an example of  $W$  axis offset calculated by the MPM versus applied rotor offset changes in the  $V$  axis.

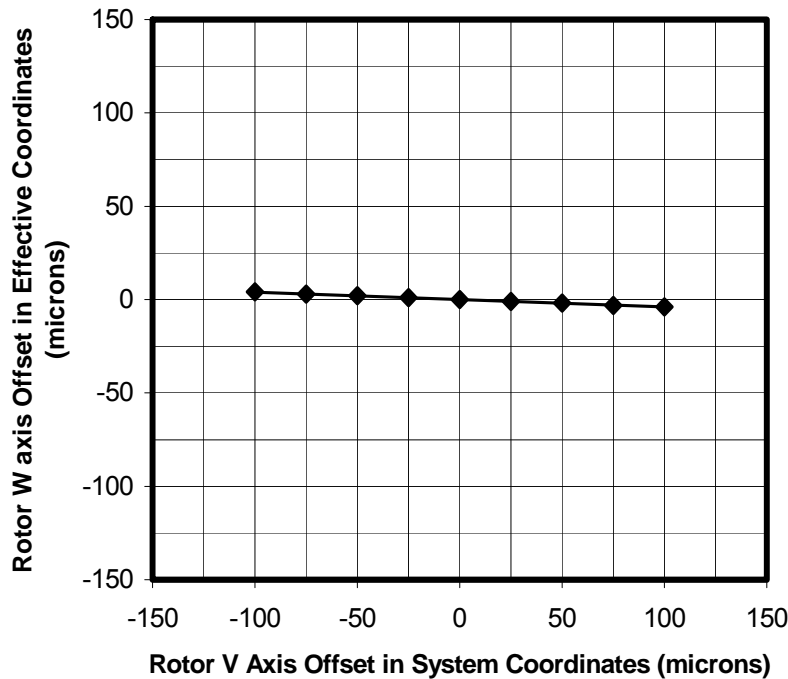


**Figure 2.8: Example of rotation between system coordinates and effective coordinates**

The figure shows the existence of small  $W$  axis effective offsets that correspond to system offsets purely in the  $V$  axis. In the tests these offsets were small and corresponded to maximum relative rotations of  $\sim 2^\circ$ .

### **2.1.5 Summary of Static Experiments**

The experiments performed on static systems led to a generally applicable characterization of an AMB force model. Characterization of the force model is based on the Multi-Point Method (MPM), and therefore requires system perturbation. However, once the model has been characterized, force measurements can be made without further perturbations. The characterized model allows force measurements to be made that have approximately the same accuracy as the MPM based force measurement ( $\sim 3\%$ ).

## **2.2 DYNAMIC EXPERIMENTS**

Dynamic experiments were performed on all 5 AMB systems with the added element of a shaft rotation. The 5 AMB systems include a variety of nominal air gap and lamination thickness combinations that are expected to impact parasitic power loss. Shaft rotational speeds were kept constant for any particular test, but a variety of rotational speeds were applied. The motivation behind the dynamic experiments was to observe how accuracy of the model-based force measurement varied as the applied system parameters such as rotational speed, bias current, and unbalance load were varied. Furthermore, the differences between the 5 systems were also expected to impact

model accuracy. Potential correlation between model accuracy and parasitic power loss mechanisms such as eddy current was of particular interest. The dynamic measurements were also motivated as a platform to develop and test AMB force models that account for such mechanisms.

## **INITIAL PREPARATION**

The test setup for each of the 5 AMB systems was similar. A balance disk was positioned on the rotor shaft between the support bearings; varying amounts of unbalance load was applied by adding small masses to the disk. The unbalance disks are pre-drilled and tapped along their perimeter to accept set screws, set screws of a variety of lengths and materials were inserted into the tapped holes as a means to add mass to the disk at specific angular locations.

Each system was run up to 10000 RPM prior to collection of AMB data. During such a run up, a Bentley Nevada ADRE system was used to monitor the phase and magnitude of the rotor orbit. This data was used to apply mass to the balance disk in an attempt to balance the system. The goal was to collect data from a system that was initially balanced and to add increasing amounts of unbalance.

## **TEST DATA**

A typical test of a system called for AMB data (coil current and rotor position) and force transducer data to be collected for specific settings of rotor speed, bias current, and rotor unbalance. Rotor speed and unbalance were varied in order to affect the dynamic load of the system, bias current was varied in order to observe its effect. Typically, rotor speeds ranged from 4000 RPM to 10000 RPM, and added unbalance ranged from 0 to 2.25 gram-inches. Bias currents were varied as much as possible while maintaining control of the system over the speed and unbalance ranges. In one extreme case this led to a bias current range of only 0.5 – 0.7 Amps, in another extreme case bias currents ranged from 1.2 – 2.0 Amps. In general, less data was collected for the systems with small nominal air gaps because these systems were more difficult to control over a wide range of the parameters.

## **DATA COLLECTION**

System data was observed for each set of operating parameters. The observed data consisted of a keyphase signal, coil current and rotor position signals as reported by the AMB system controller, and force transducer signals. Data was collected for one second at a sample rate of 20000Hz/channel. Care was taken to allow the system to achieve a steady state for the given operating parameters prior to data acquisition. Two processes were performed on the incoming data streams prior to writing them to a file. A low-pass filter was applied to the incoming signals, then conversion factors were applied to the incoming voltage signals. The conversion factors served to convert the voltage signals to their associated physical units.

## **REDUCTION, AND ANALYSIS**

After data collection, the files containing AMB system data as well as force transducer data were analyzed. Each file consists of 20000 samples of each of the variables that correspond to a single test. In order to apply a variety of models to the data with some

agility, the data needed to be reduced as described below. The collected data was reduced in two ways;

- decimation to a lower frequency
- curve fit to a sine function

The decimation process was applied to raw coil current, rotor position, and transducer signals. The decimated coil current for a given actuator along with the decimated rotor position data for the corresponding axis were then applied to a magnetic circuit model to determine the magnetic flux density associated with the actuator. A flux density calculation was performed for each of the decimated data points. Knowledge of the flux density in an actuator allowed an actuator force to be calculated. A force calculation was performed for each of the decimated flux density points for a given actuator. Upper and lower actuator forces calculated in this way were summed to arrive at a axis force value. At this point the second data reduction was applied; decimated force data was curve fit to a sine function. The curve fit allowed for many cycles of data to be described by three parameters; a DC offset, an amplitude, and a phase. The data was reduced in order to accommodate the analysis of large amounts of data in an efficient manner. Following the curve fit process a vertical force value was determined by summing the force amplitudes associated with both axes and multiplying by the cosine of  $45^\circ$ , the angle between each axis and the vertical direction.

### ***2.2.1 Decimation***

The first reduction step was to decimate the 20000 Hz data to a lower frequency. The frequency of the decimated data was determined as a function of rotor speed. The decimation frequency was set such that at least 30 points were in each cycle of a given decimated data.

### ***2.2.2 Magnetic Circuit Model***

The decimated current and position data was used in conjunction with Equation 1.3 to calculate a flux density at each of the points in the decimated data set. In Section 1.2 Equation 1.3 is written generically; a version that is specific to our system is developed in Chapter 6. Application of a specific version of Equation 3 resulted in a flux density  $B$  that corresponds to each of the decimated values. The flux density values can be converted to a magnetic force by taking the pole face area into account as shown in Equation 1.4. In order to allow Equation 1.4 to be directly applied to an AMB actuator that is typical of a test bearing configuration, a version that is specific to our AMB configurations was developed as discussed in Chapter 7. In this way, the attractive force developed by the upper and lower actuators of a typical force axis was determined.

The force developed by a force axis must take both the upper and lower actuator forces into account. The upper and lower actuator forces are accounted for by taking the vector sum of the forces of the upper and lower actuators. Since the forces in the upper and lower actuators have opposite sense, the vector summation can be accomplished by subtracting the force of the lower actuator from the force of the upper actuator. The result is the basic magnetic circuit model discussed in Chapter 1 and described by Equation 1.13. The force given by Equation 1.13 is an axis force. Such a force is

calculated for both the  $V$ -axis and  $W$ -axis corresponding to each of the decimated data points.

### 2.2.3 Curve Fit

The coil current, rotor position, and force transducer data that was collected for a given test is expected to be periodic since it was collected at a continuous rotor speed. Since the system is harmonically driven due to the synchronous unbalance, the coil current, rotor position, and force transducer data can be well approximated with a trigonometric function. The second reduction step was to fit a representative sample of nineteen cycles to a sine function. The curve fit allowed the nineteen cycles of data to be described by three parameters; a DC offset, an amplitude, and a phase. The curve fit minimizes residual error in a least-squares sense (de Callafon et al., 1996). Forcing the data to fit a specific function results in uncertainty because the collected data does not fit the function perfectly. The uncertainty is further discussed in Appendix B. The data reduction was applied in order to efficiently analyze a large amount of data in a reasonable amount of time.

### 2.2.4 Calculation of Vertical Force

The  $V$ -axis and  $W$ -axis are configured at  $90^\circ$  to each other and  $45^\circ$  from the vertical direction as discussed earlier and is shown in Figure 2.1. The figure shows two force axes, the  $V$ -axis and the  $W$ -axis. The force amplitudes for each axis were determined by first calculating a force for every decimated data point using Equation 1.13, and then applying a curve fit as discussed in Section 2.2.3. Application of curve fit results in a  $V$ -axis force amplitude,  $F_V$ , and a  $W$ -axis force amplitude,  $F_W$ . A value of vertical force was then calculated as shown:

$$F_{Model} = (F_V + F_W) \cos \theta \quad (2.14)$$

where:

$F_{model}$  = the vertical force determined by the model

$F_V$  = the amplitude parameter of the  $V$  force

$F_W$  = the amplitude parameter of the  $W$  force

$\theta = 45^\circ$ : the angle between each force axis and the vertical direction

Equation 2.14 provides a single value of calculated force that can be compared to the maximum force amplitude measured by the force transducers.

### 2.2.5 Reduction and Analysis of Transducer Data

Sections 2.2.1 and 2.2.3 discuss a data decimation and curve fit process respectively. The same processes were applied to the force transducer data. Forcing the data to fit a specific function results in added uncertainty because the collected data does not fit the function perfectly. The uncertainty is further discussed in Appendix B. The data reduction was applied in order to efficiently analyze a large amount of data in a reasonable amount of time. The curve fit process allowed the transducer force from a

given test to be described by a DC offset, an amplitude, and a phase. The resulting transducer force amplitude was compared to the calculated vertical force from Equation 2.14.

### **COMPARISON OF MEASURED AND CALCULATED FORCES**

AMB system data corresponding to a variety of dynamic loading scenarios was used to calculate force using two different models. The results of each model were then compared to the measured force provided by the force transducers.

# Chapter 3 Experimental Setup

## 3.1 INTRODUCTION

This chapter provides details on the AMB systems that were tested. Details related to additional components involved in the testing such as force transducers and data acquisition hardware are included as well. A discussion of the tests themselves is found in Chapter 2.

The research performed as part of this dissertation included a significant experimental component. In broad terms, the experiments that were performed as part of this research can be put into one of two classifications: static or dynamic. Static experiments were performed on the AMB experimental systems without shaft rotation and with the motor uncoupled from the shaft. The motivation behind the static experiments was to identify system parameters that can be applied in conjunction with a simple AMB force model to improve force measurement accuracy. Dynamic experiments were performed with the added element of a shaft rotation. Force transducers were mounted underneath the AMB housings to provide a direct measurement of dynamic bearing load.

The motivation behind the dynamic experiments was to observe how the accuracy of force models varies as other system parameters such as rotational speed, bias current, and unbalance load are varied.

### ***3.1.1 Overview of Experimental Systems***

The experiments were carried out on five separate setups based on two platforms. Each platform included a motor, rotor shaft, two AMBs, and a balance disk placed between the AMBs. The inboard bearing (closest to the motor) provided support for the rotor, but was not monitored. The sensor signals and control signals associated with the outboard bearing were monitored and acquired for later analysis. In order to audit the analysis, the outboard bearing was mounted onto force transducers. The inboard bearing and motor were likewise mounted on blocks to maintain alignment.

### PLATFORM 1

The first platform is a typical high-speed laboratory rotor kit from Revolve Magnetic Bearings, one setup was tested on Platform 1. Figure 3.1 shows a photograph of Platform 1. Many of the components that make up the test setup are visible in the figure including the motor, rotor shaft, two AMBs, a balance disk placed between the AMBs, force transducers and mounting blocks. Additional photographs highlighting the details of the test setup are included in subsequent sections of this chapter.

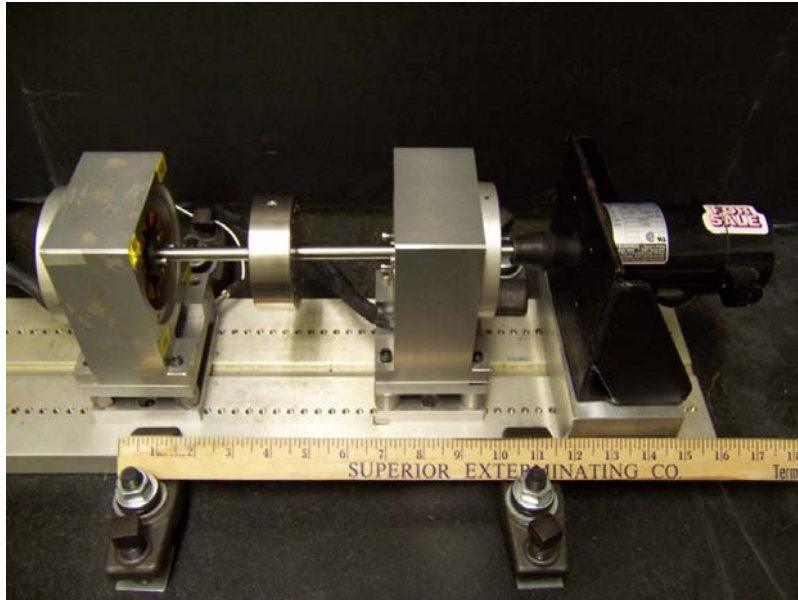


**Figure 3.1: Photograph of Platform 1 with scale included to show approximate sizes**

### PLATFORM 2

The second platform consists of a custom magnetic bearing test system, also built by Revolve Magnetic Bearings. Platform 2 was designed to accommodate four interchangeable rotors, each with a unique combination of nominal air gap and lamination thickness. Figure 3.2 is a photograph of a typical experimental setup on Platform 2 including motor, coupling, rotor shaft, balance disk, and two AMBs. Also visible are the force transducers and mounting blocks. Additional photographs highlighting these details are included in subsequent sections of this chapter.

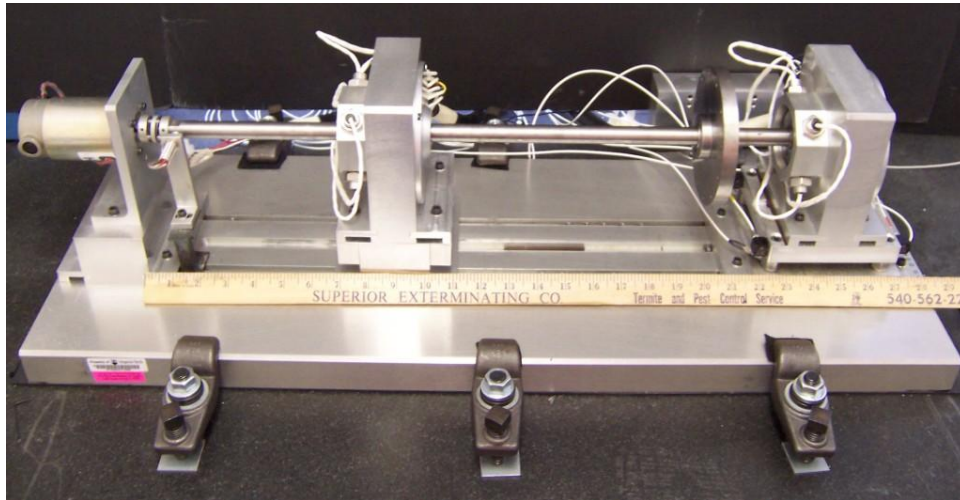


**Figure 3.2: Photograph of Platform 2 with scale included to show approximate sizes**

### ***3.1.2 Overview of Data Acquisition***

Data acquisition was performed using two boards from National Instruments. A Labview “virtual instrument” (VI) program was written to filter the data, apply calibrations, and store the data. A data set corresponding to a specific test scenario was collected over one second at a rate of 20 kHz. For each test scenario AMB system data consisting of a keyphase signal, applied coil currents, and rotor positions was acquired. Also acquired were force transducer signals.

## **3.2 AMB ROTOR SYSTEM HARDWARE**

The experiments were carried out on five separate setups based on two platforms. Each platform included a motor, rotor shaft, two AMBs, and a balance disk placed between the AMBs. The inboard bearing (closest to the motor) provided support for the rotor, but was not monitored. In order to audit the analysis, the outboard bearing was mounted onto force transducers. The inboard bearing and motor were likewise mounted on blocks to maintain alignment.

### **MATERIALS**

The materials used in the stator and rotor are laminated from either Arnon 5 or M19. Both materials are low resistivity silicon steels in common use for soft magnetic applications. The bulk resistivity of Arnon 5 is given by Revolve Magnetic Bearings as  $40\mu\Omega\cdot\text{cm}$ . The bulk resistivity of M19 is given by Revolve Magnetic Bearings as  $54\mu\Omega\cdot\text{cm}$ .

### 3.2.1 Platform 1

The first platform (Platform 1) is a typical high-speed laboratory rotor kit from Revolve Magnetic Bearings and has a 0.015in. radial gap and 0.014in. rotor laminations. One setup was tested on Platform 1. The static load capacity of the bearing is 12lb<sub>f</sub>.

#### BEARING DETAILS (STATOR, ROTORS)

The stator is an 8 pole heteropolar stator. The polarity of the stator poles is N-N-S-S-N-N-S-S, they are arranged such that adjacent poles at quadrant boundaries have the same polarity. A schematic of the stator, showing the polarity of each pole in red, is shown in Figure 3.3.

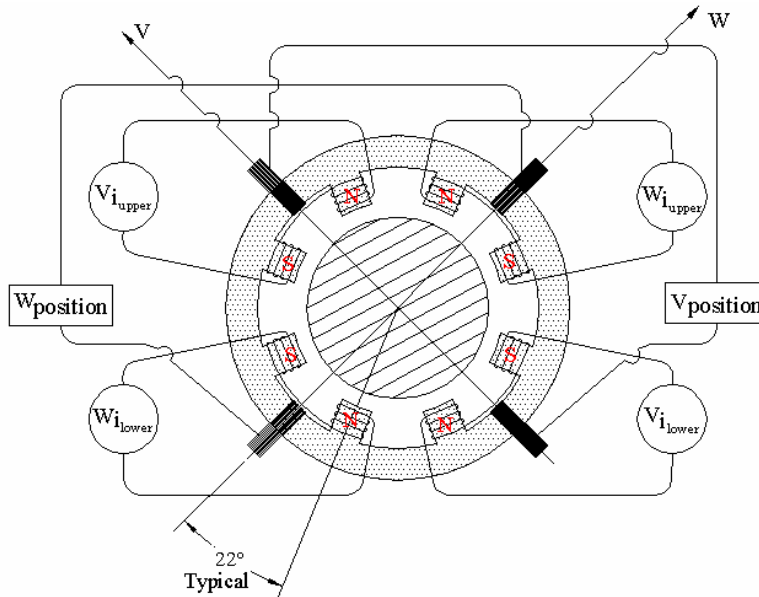


**Figure 3.3: Typical stator geometry and stator pole polarity**

The stator is 0.50in. thick and is constructed of 0.014in. thick laminations of M19. Other stator dimensions are as follows: stator OD: 2.788in., stator ID: 1.380in., pole width: 0.207in., pole gap: 0.331in., wire turns: 114 turns per pole. Figure 3.4 contains a close-up photograph of the stator.

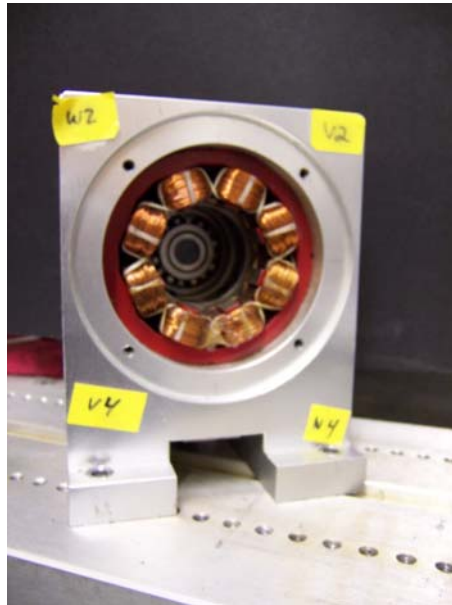


**Figure 3.4: Stator of Platform 1**

Each stator is mounted in an aluminum bearing housing, also visible in the figure. A retainer bearing, a rolling element bearing visible in Figure 3.4, is mounted to the stator housing. The purpose of the retainer bearing is to support the shaft when the AMB system is not operational. It also serves to keep the rotor and stator from contacting each other in the event that AMB control is lost during bearing operation. Retainer bearings are generally designed with enough clearance to allow movement of the rotor within the stator cavity, but not so much movement that the rotor can touch the stator. The retainer bearing associated with Platform 1 allows 0.005in. radial movement.

The rotor OD is 1.350in. leading to a nominal gap of 0.015in.. The rotor is constructed of 0.005in. thick laminations of Arnon 5. The rotor is attached to the rotor shaft via a taper fit hub. Figure 3.5 contains a picture of a typical rotor. The screws seen in the picture are used to engage and disengage the tapered hub.



**Figure 3.5: Typical rotor for Platform 1**

### **MECHANICAL DETAILS (SHAFT, COUPLING, MOTOR, BALANCE DISK)**

The rotors were each mounted to a steel shaft, the nominal shaft diameter is 0.375in., the total shaft length is 12in.. A flat area was machined on the shaft, outboard of the outboard bearing to act as a keyphasor pickup.

A flexible rubber coupling was used to connect the shaft to a high-speed electric motor capable of turning the system at 10000 RPM. Motor speed was controlled by an external control unit.

A balance disk was positioned mid-span between the bearing housings. The balance disk has an OD of 3in. and is 1in. thick; Figure 3.6 contains a picture of the balance disk. It is attached to the shaft with a pair of opposing set screws. The balance disk has tapped holes 1.2in. from its center; the holes are evenly spaced in 22.5° intervals. Additional mass can be attached to the disk at specific phase locations by inserting set screws into the tapped holes to allow for dynamic balancing of the system. In our case, the holes were also used to apply additional unbalance loads.

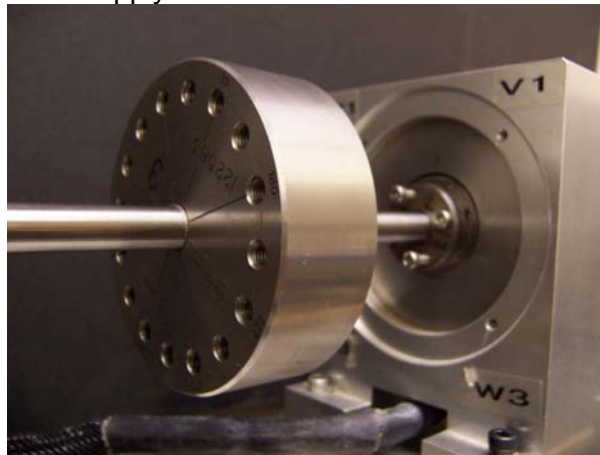
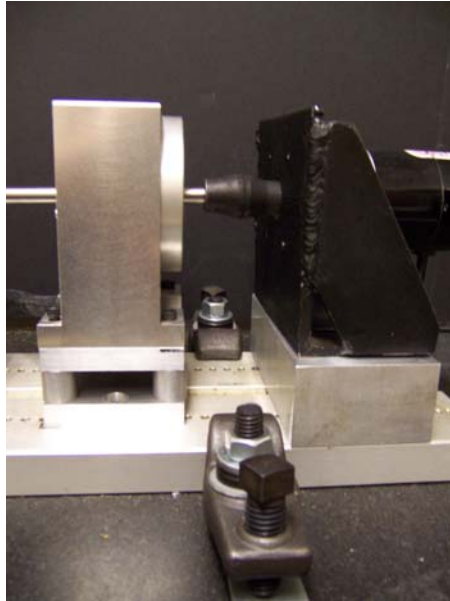


**Figure 3.6: Platform 1 balance disk**

### **BASE PLATE AND MOUNTING**

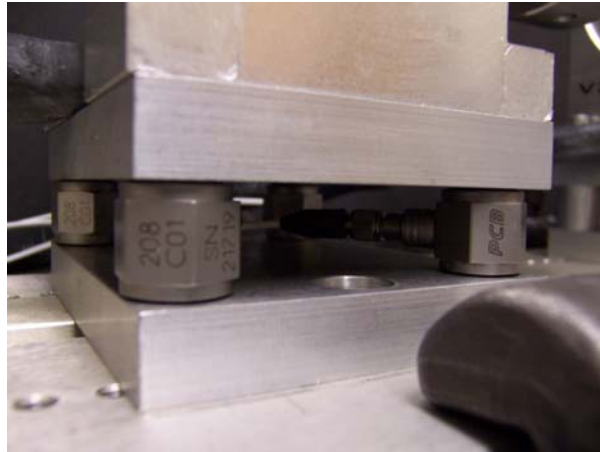
The bearing housings and motor were mounted to an aluminum plate. The aluminum plate is 31in. long, 6in. wide, and 1in. thick. The plate surface has a series of tapped holes to allow for the bearing housings to be repositioned axially along the plate.

Figure 3.7 shows the mounting of the inboard bearing housing and motor. The bearing housing is supported by spacers to account for the height of the force transducers mounted beneath the outboard bearing. Similarly, the motor was mounted to a spacer plate that is bolted to the base plate. Also visible in Figure 3.7 is the flexible rubber coupling.



**Figure 3.7: Inboard bearing housing and spacer block**

The transducer mounting system associated with the outboard bearing is shown in Figure 3.8. The transducer mounting system consists of two 0.50in. thick plates that sandwich the force transducers. The lower plate is attached to the base plate with two bolts, placed between the transducers. Bolts run through ears in the housing, then through a mounting plate and into the force transducers.



**Figure 3.8: Close-up photograph of force transducers and sandwich plates**

The aluminum base plate was mounted to an inertial base. The inertial base is a 1500lb<sub>f</sub> slab of granite that has been fitted with anchor nuts. A thin layer of rubber was placed between the test platform and the granite base to assure broad contact between them. Six clamps placed along the edges of the platform were used to secure the platform to the granite block. The clamps and granite base are visible in Figure 3.1, located near the beginning of this chapter.

### 3.2.2 Platform 2

Platform 2 is a custom magnetic bearing test bed, built by Revolve Magnetic Bearings. Platform 2 was designed with a common stator and four interchangeable rotors. Each rotor has a unique combination of nominal air gap and lamination thickness so that Platform 2 can be configured as 4 unique setups.

1. 0.010in. radial gap, 0.005in. lamination (Arnon 5)
2. 0.030in. radial gap, 0.005in. lamination (Arnon 5)
3. 0.010in. radial gap, 0.014in. lamination (M19)
4. 0.030in. radial gap, 0.014in. lamination (M19)

Each setup is expected to have different dynamic behavior. For instance, eddy current magnitude is directly related to path resistance, a function of lamination thickness. The static load capacity of the setup is a function of nominal gap, for the 0.030in. gap cases the load capacity is 24lb<sub>f</sub>, for the 0.010in. gap case the load capacity is 60lb<sub>f</sub>.

#### BEARING DETAILS (STATOR, ROTORS)

The stator is an 8 pole heteropolar stator. The polarity of the stator poles is N-N-S-S-N-N-S-S, they are arranged such that adjacent poles at quadrant boundaries have the same polarity. A schematic of the stator, showing the polarity of each pole in red, is shown in Figure 3.3.

The stator is 0.875in. thick and is constructed of laminations of Arnon 5. Other stator dimensions are as follows: stator OD: 4.528in., stator ID: 1.920in., pole width: 0.53in., pole gap: 0.23in., wire turns: 124 turns per pole. Figure 3.9 contains a close-up photograph of the stator.

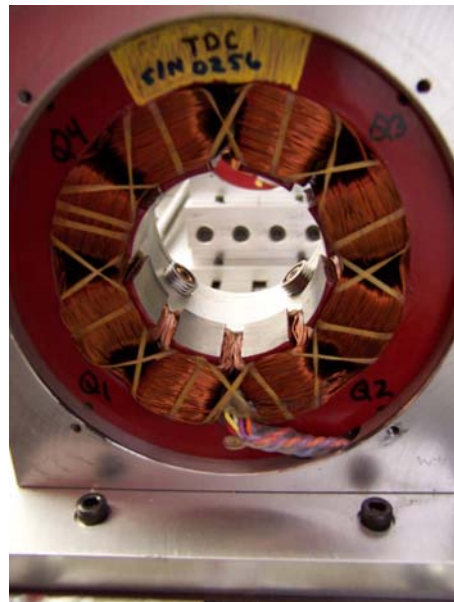


Figure 3.9: Stator of Platform 2

Each stator is mounted in an aluminum bearing housing, also visible in the figure. Not shown is the retainer bearing, a rolling element bearing that gets mounted to the stator

housing. The purpose of the retainer bearing is to support the shaft when the AMB system is not operational. It also serves to keep the rotor and stator from contacting each other in the event that AMB control is lost during bearing operation. Retainer bearings are generally designed with enough clearance to allow movement of the rotor within the stator cavity, but not so much movement that the rotor can touch the stator. The retainer bearing associated with Platform 2 allows 0.005in. radial movement.

Four rotor designs were used in conjunction with the second platform. Each rotor has two laminate sections, one is aligned with the sensors and one is aligned with the stator. The rotors were attached to the rotor shaft via a pressure fit; the pressure fit was achieved by turning a jack screw against a volume of grease within internal passages of the rotor. Figure 3.10 contains a picture of a typical rotor. The holes in the face of the rotor are part of the pressure fit system.



**Figure 3.10: Typical rotor for Platform 2**

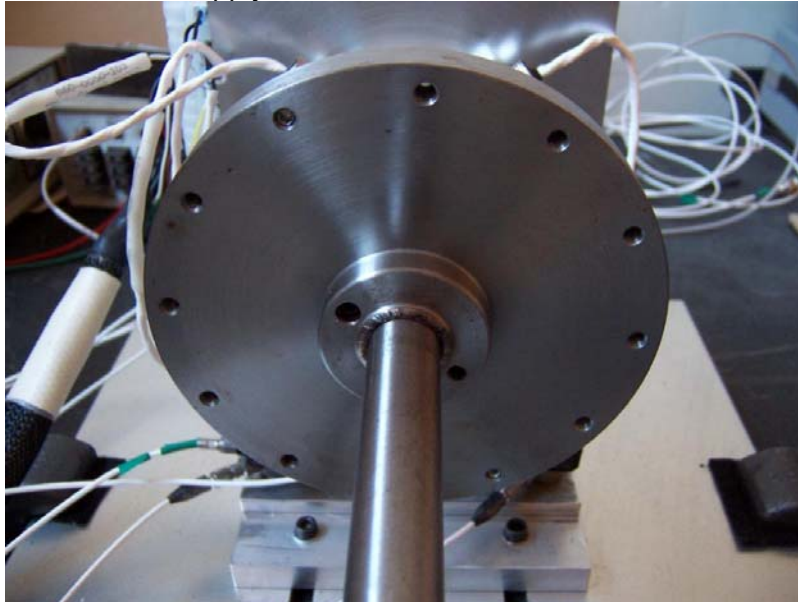
The rotors are 2.4in. long, a 0.63in. nominal diameter hole runs lengthwise through the rotor to accommodate the shaft. The rotor OD varies with AMB setup (to generate the different air gaps) but is roughly 1.9in..

### **MECHANICAL DETAILS (SHAFT, COUPLING, MOTOR, BALANCE DISK)**

The rotors were each mounted to a steel shaft, the nominal shaft diameter is 0.65in., the total shaft length is 25in.. The drive end of the shaft was turned down to 0.38in. to accommodate a flexible disk coupling. A flat area was machined on the shaft near the coupling to act as a keyphase pickup.

The coupling was used to connect the shaft to a high speed electric motor capable of turning the system at 10000 RPM. The motor speed was controlled via the system controller.

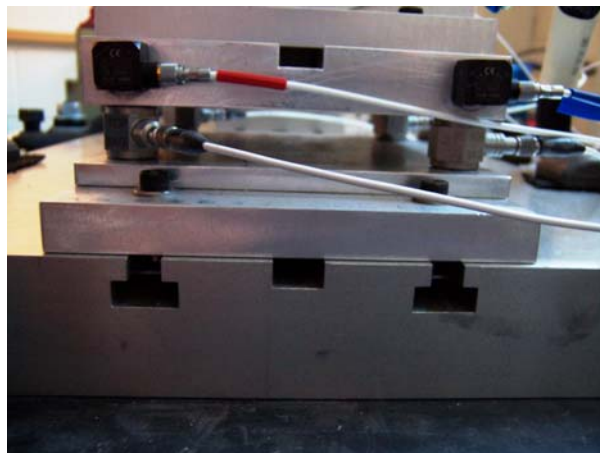
A balance disk was positioned between the bearing housings, closer to the outboard bearing so that the instrumented bearing would bear most of the load. The balance disk has an OD of 5in. and is 0.5in. thick; Figure 3.11 contains a picture of the balance disk. It is attached to the shaft with the same style pressure fit as the rotors. The balance disk has tapped holes 2.25in. from its center; the holes are evenly spaced in 30° intervals. Additional mass can be attached to the disk at specific phase locations by inserting set screws into the tapped holes to allow for dynamic balancing of the system. In our case, the holes were also used to apply additional unbalance loads.



**Figure 3.11: Platform 2 balance disk**

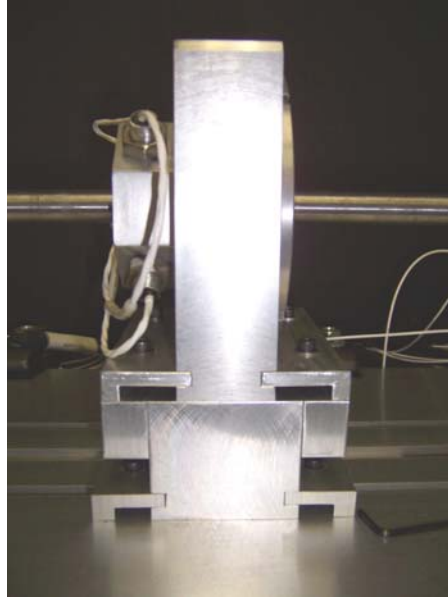
### **BASE PLATE AND MOUNTING**

The bearing housings and motor were mounted to an aluminum plate. The aluminum plate is 32in. long, 12in. wide, and 1.5in. thick. The plate surface was slotted as shown in Figure 3.12 to accommodate “T-nuts” that could be positioned along the slots. The slots allow for the bearing housings to be repositioned axially along the plate.



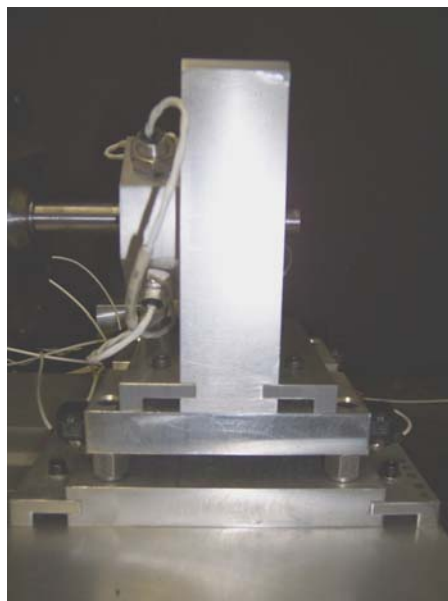
**Figure 3.12: Detail photograph of slots in base plate**

Figure 3.13 shows the mounting of the inboard bearing housing in detail. The bearing housing is mounted to a thick spacer block with pinch mounts. The spacer block is likewise attached to the base plate.



**Figure 3.13: Inboard bearing housing and spacer block**

A similar view of the outboard bearing housing is shown in Figure 3.14. The figure shows the bearing housing as well as the transducer mounting system associated with the outboard bearing. The transducer mounting system consists of two 0.75in. thick plates that sandwich the force transducers. The lower plate is attached to the base plate with pinch mounts, the bearing housing is attached to the top plate in the same manner. Both of the transducer mounting plates are drilled and countersunk to accommodate the force transducer mounting screws.



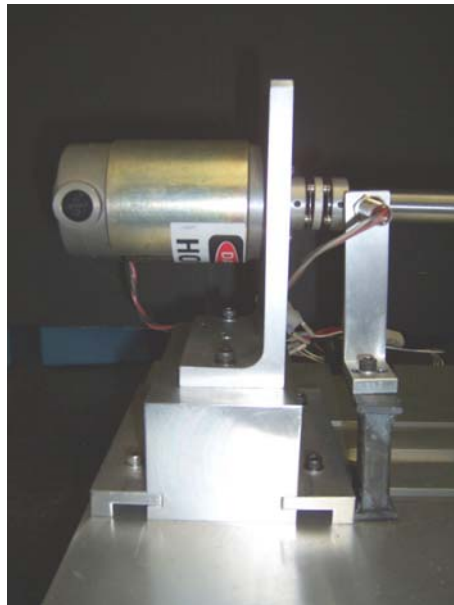
**Figure 3.14: Outboard bearing housing and transducer mounting system**

Figure 3.15 shows a close up photograph of the transducer location between the sandwich plates.



**Figure 3.15: Close-up photograph of force transducers and sandwich plates**

The motor was mounted to the base plate in a similar manner as the bearing housings. Figure 3.16 shows a side view photograph of the motor. As with the inboard bearing housing, the motor was mounted on a spacer block in order maintain alignment to the outboard bearing.



**Figure 3.16: Motor mount and spacer block**

Also visible in Figure 3.16 is the disk coupling and the mounting for the keyphase sensor.

The aluminum base plate was mounted to an inertial base. The inertial base is a 1500lb<sub>r</sub> slab of granite that has been fitted with anchor nuts. A thin layer of rubber was placed

between the test platform and the granite base to assure broad contact between them. Six clamps placed along the edges of the platform were used to secure the platform to the granite block. The clamps and granite base are visible in Figure 3.2, located near the beginning of this chapter.

## **CONTROLLER**

The AMB was controlled using a PID based controller, also provided by the bearing manufacturer, Revolve Magnetic Bearings. The controller allows the user to tune the PID characteristics in order to allow stable operation. The controller also allows the user to apply high pass, notch, and lead-lag filters for tuning purposes. In addition to control parameter adjustment, the controller also allows the user to adjust the bearing bias current and the rotor offset from center.

## **3.3 INSTRUMENTATION HARDWARE**

The sensor signals that were acquired in the data acquisition process can be separated into two groups; those that are part of the AMB system and those that are not. The AMB system signals (keyphase, coil current, and rotor position) could be monitored via a signal “breakout” box provided by Revolve (MBResearch). The force transducer signals were monitored through their signal conditioning units.

### ***3.3.1 AMB System Signals and Calibration***

Software is available from the bearing manufacturer that allows the user to view bearing sensor and control signals in real time, however the real time signal monitoring software does not support data acquisition. To allow for the acquisition of bearing sensor and control data, the manufacturer (Revolve Magnetic Bearings) provides a signal breakout box called MBResearch. The breakout box is connected to the controller and provides access to a variety of system signals including position sensor output, coil currents, and keyphase. The signals that we monitored via the MBResearch box were:

- Keyphase
- V Axis Top Current
- W Axis Top Current
- V Axis Bottom Current
- W Axis Bottom Current
- V Axis Rotor Position
- W Axis Rotor Position

The current and position signals consist of a voltage signal that is proportional to the monitored value of current or rotor position. Both of these signals required calibration.

## **CURRENT SIGNAL CALIBRATION**

A calibration was required to convert the voltage output of the MBResearch unit to the value of current associated with a given quadrant. The current supplied by the controller is sent to the bearings on top of a 20kHz carrier signal, therefore current magnitudes cannot be measured directly using simple means. Instead, current values as reported

by the real time signal monitor provided by Revolve were relied on. The values reported by Revolve have two decimal places; to achieve greater precision the rotor position was varied in small increments (sub micron) until the current value was seen to change. The threshold at which the current value changed from a lower value to a higher value was taken to be the instant at which the third decimal was zero. The corresponding voltage provided by the MBResearch unit was noted as well. A linear calibration between voltage and current was determined from several such measurements.

### **POSITION SIGNAL CALIBRATION**

The position offset calibration was more straightforward since position offset could be audited by an external gauge. For calibration the rotor position was varied via the controller interface, and its offset from nominal center was monitored using a precision dial indicator. The dial indicator is a Starrett “Bestest” mechanical gauge with a full scale of 0.008in. and a precision of 0.0001in. At each position, the gauge reading and the voltage provided by the MBResearch unit were noted. After several positions were traversed over a range of  $\pm 0.004$ in., a linear calibration between actual position-offset and reported voltage was determined.

### ***3.3.2 Force Transducers and Signal Conditioners***

The outboard bearing was mounted to four force transducers. The transducers are PCB Piezotronics model 208C01 and each has a  $10\text{lb}_f$  capacity. Their sensitivity is nominally  $500\text{ mV/lb}_f$ , they have an uncertainty of  $\pm 1\%$  at a 95% confidence level. The transducers have a structural stiffness of  $6\text{lb}/\mu\text{in}$ . The transducers are PCB Piezotronics ICP type, which are charge mode sensors. Each has an on-board amplifier that converts the high impedance charge generated by the stressed quartz crystals into a low impedance voltage signal for recording. A significant feature of ICP type of transducers is that a constant electrostatic charge, such as that associated with a static load, will leak away so that after a certain amount of time the transducer output will be zero regardless of static load magnitude. In our system, the amount of time required for 1% of the electrostatic charge to leak away is  $\sim 0.05$  seconds. Since the lowest speed at which dynamic load measurement was performed was 4000 RPM (67 Hz), charge leakage is considered negligible.

Each force transducer has its own signal conditioner/power supply, also manufactured by PCB Piezotronics. The model number of the signal conditioners is 480C02; they are battery-powered units.

## **3.4 DATA ACQUISITION**

Data acquisition was handled with hardware and software from National Instruments. The sensor signals, provided either by the MBResearch unit or directly from transducer signal conditioners, were sent to a data acquisition board. A data acquisition program was written to sample and filter the data. Each data channel was also converted from a voltage signal to its corresponding value in physical units before storage in a file.

### **3.4.1 Data Acquisition Hardware**

Data acquisition was performed using two PCI DAQ boards from National Instruments. The model of the boards is PCI-MIO-16E. To accommodate synchronous data acquisition, the boards are connected with a ribbon cable (RTSI). Eleven channels of data were collected, they correspond to the following signals:

- Keyphase
- Current (Top Quadrant V24)
- Current (Top Quadrant W24)
- Current (Bottom Quadrant V24)
- Current (Bottom Quadrant W24)
- Position Offset (V24 Axis)
- Position Offset (W24 Axis)
- Force (Force Transducer 1)
- Force (Force Transducer 2)
- Force (Force Transducer 3)
- Force (Force Transducer 4)

Of these channels, the first seven were monitored through the MBResearch unit; the remaining signals were provided directly by the transducers.

### **3.4.2 Data Acquisition Software**

National Instruments Labview software was used to write a “virtual instrument” (VI) program to automate data collection. The Labview code synchronizes the clocks on the data acquisition boards prior to collecting data to ensure synchronous data collection. The data sampling rate and the number of samples to collect is also set within the Labview code, in this research each channel was sampled for one second at a rate of 20 kHz.

Each channel was filtered using a low pass filter. The characteristics of the filter were varied according to rotational speed such that the first order signal amplitude was affected by less than 1% over the frequency range of interest. After filtering, a calibration was applied to the data prior to storage so that the units of stored data values were the proper engineering units associated with each data channel. For instance, the voltage signal generated by a force transducer would be multiplied by the  $\text{lb}_f/\text{V}$  calibration factor specified for that transducer. The calibration factors for the force transducers were provided by their manufacturers. The calibration factors for the currents and positions needed to be determined experimentally as described in Section 3.3.1.

## **3.5 DYNAMIC EFFECTS OF TEST PLATFORMS**

Care was taken to minimize the effect of the test setup structure on the force measurements. As discussed, the AMB platforms were mounted to a massive (1500lb<sub>f</sub>) granite base; a thin layer of rubber was placed between the test platform and the granite base to assure broad contact between them. Six clamps placed along the edges of the

platform were used to secure the platform to the granite block. The clamps and the base can be seen in Figure 3.2. The mounting method provided the platform with a solid foundation, however, there was some concern regarding the bearing housing mounting.

### 3.5.1 Base Dynamics - Platform 2

The bearing housings were mounted on force transducers so that dynamic loads could be directly measured. Figure 3.8 shows the configuration. It would be preferable to mount the bearing housings directly to a large mass, such as the granite block that is underneath the base of the AMB platform. Introduction of additional structure between the platform base and the bearing housings, such as that required to accommodate the force transducers, can lead to additional system dynamics.

#### FREQUENCY ANALYSIS

A test of the bearing housing's dynamic response was performed in order to observe its dynamic response. The test consisted of determining the transfer function between a vertical input force (provided by a modal hammer), to the forces measured by the force transducers. Figure 3.17 shows the magnitude and phase plots of the transfer function. It can be seen that the transducer response is quasi-static in the range of ~20 to ~200 Hz. The spikes that are visible at 60 Hz and 180 Hz are assumed to be due to noise in the AC power source.

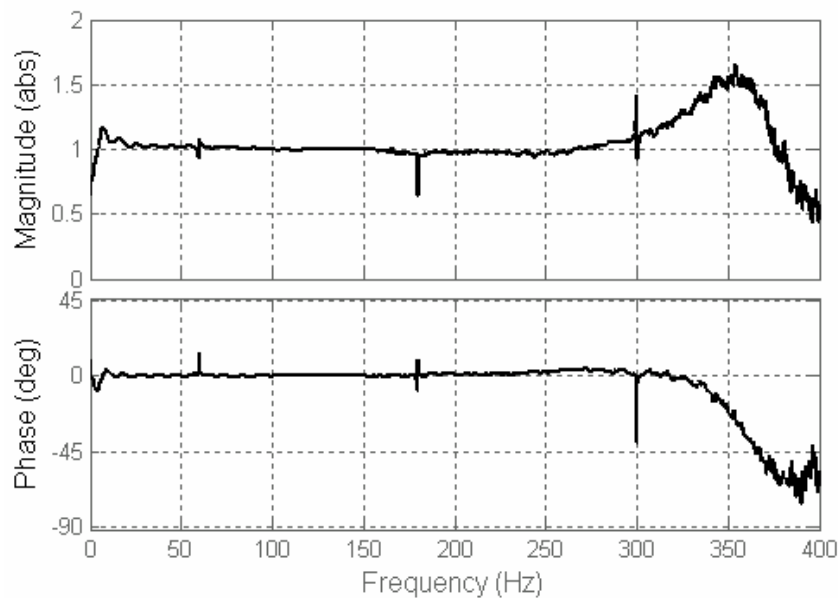


Figure 3.17: Transfer function between modal hammer and force transducers.

## Chapter 4 Effective Origin

### 4.1 ABSTRACT

Locating the effective origin of a radial Active Magnetic Bearing (AMB) is an important step towards accurate characterization of the bearing air gaps for field tuning, performance analyses, and some shaft force measurement techniques. Specifically, application of current-based force measurement techniques to AMBs requires accurate modeling of air gaps in order to predict dynamic forces with accuracy. This paper discusses the application of a system identification technique that employs perturbation of the bias current and allows the user to establish the location of the effective origin, an important step in characterizing the actual bearing gap. The technique analyzes the AMB system's response to the perturbation of bias currents in conjunction with a magnetic circuit model to infer the center position. The effective origin identification technique developed here does not require additional hardware and is suitable for the general class of AMBs in field applications.

For our purposes, the effective origin of an electromagnet biased magnetic bearing is defined as the unique rotor location for which a magnetic circuit based force model of the bearing is satisfied for zero position offset of the rotor along each control axis.

### 4.2 INTRODUCTION

The control of radial Active Magnetic Bearings (AMBs) typically involves an operational set-point for the rotor. A controller then acts to maintain the rotor at the operational point. The operational point may be based on the position of the associated mechanical back-up bearing or possibly other system components such as seals. Although the operational point may be the preferred location for rotational center from a system standpoint, it may not be the effective origin of the bearing. For this paper, the effective origin of an electromagnet biased magnetic bearing is defined as the location for which a force model of the bearing is satisfied for zero position offset of the rotor along each control axis.

Tuning of AMB controllers in the field can present challenges as experienced by Schroder et al. (2001), knowledge of the location of the effective origin of an AMB is useful as a diagnostic aid during field tuning as well as in the case of trouble-shooting an under-performing bearing. In addition, operation near the effective origin will best approximate linear behavior of the bearing and provide better performance characteristics in general. Furthermore, the effective origin locating technique can be applied at several rotor angles in order to quantify rotor position runout. The authors' particular interest is the usefulness of the effective origin locating technique for improving current-based force measurement.

### **4.2.1 Applications**

An important attribute of magnetic bearings is that they can be used to measure the load that they support. One way to assess the load is through the use of a magnetic circuit model with accurate knowledge of air gaps and the distribution of current to the electromagnets that make up the bearing. This chapter discusses the application of a system identification technique that employs perturbation of the bias current and allows the user to establish the location of the effective origin, an important step in characterizing the actual bearing gap.

The authors are primarily interested in determining the effective origin for the purposes of characterizing air gap in a magnetic bearing for accurate current-based force measurement. A system identification approach is employed so that air gap characterization can be performed in the field using bias current perturbation techniques such as those used in the Multi-Point Method (MPM) by Kasarda et al. (2000) and Marshall et al. (2001). The system identification approach could also be applied to establish fringing factors for use in a flux-based force measurement method such as that proposed by Imlach et al. (2000).

Although the authors' primary interest in determining the effective origin is for the purposes of accurately mapping a magnetic bearing to improve force measurement, it is noted that there are other applications for the technique. For instance, finding the location of the effective origin and its relationship to the rotor center set-point may be of interest when troubleshooting an under-performing magnetic bearing. The effective origin locating technique can also be applied to determining rotor runout.

### **RUNOUT**

Sensor runout refers to changes in position probe signals that are not related to real changes in the position of the rotor relative to the stator. Such changes are due to non-uniformities in the circumference of the sensor target. The non-uniform phenomena may be mechanical, as in the case of a non-concentric rotor and stator or anomalies in the contour of the sensor surface. The non-uniformity may also be electrical, as in the case of variations in the material properties in the sensor target region. Sensor runout is a function of rotation angle and is noticeable at low, even quasi-static, rotational speeds (Setiawan et al., 2001).

The AMB controller reacts to sensor runout as it would react to a real change in rotor position; control currents are applied as necessary to move the rotor to the location for which the position probe signals indicate zero offset. The controller's reaction has the undesirable effect of creating a rotor orbit as the controller continuously reacts to "phantom" rotor motion. Two general approaches have been applied to the issue of runout in AMBs; reduction of the runout signal and controller compensation of the runout signal.

The first approach, which calls for the reduction of signal runout, requires some combination of improved sensors and sensor targets. Such improvement is generally achieved by upgrading the sensor technology or applying special manufacturing techniques such as in the approach used by Jansen et al. (2002) in the redesign of an AMB suspended flywheel. Jansen cites two rounds of sensor upgrades; first the original optical position sensors were replaced with eddy current position sensors, second, the eddy current position sensors were scheduled to be replaced with an improved eddy current position sensor at the time of the publication. Jansen also indicates that tight control of sensor target surface finish was required.

The controller compensation approach is less invasive. Rather than eliminate the runout signal, the runout signal is identified so that it can be compensated. Kim and Lee (1997) discuss the application of an *in-situ* identification based on extended influence coefficients. In the method of Kim and Lee, an additional position disturbance signal is injected to the system via the AMB controller. The system's response to the additional disturbance is used along with the systems response to the runout disturbance alone to identify the required compensation. The method of Kim and Lee is valid for the operating speed at which it is applied and is reported to be sensitive to speed change. In order to achieve compensation over a range of speeds, the method must be applied at several speeds within the range. The method requires a host PC in addition to the system controller in order to run the compensation algorithm.

Wu (2001) discusses potential stability issues associated with applying gain scheduled  $H_{\infty}$  controllers to runout compensation due to the requirement of slow varying parameters. Also discussed is the application of a  $\mu$ -synthesis approach which offers improved stability, but is sensitive to rotor speed. Wu proposes an LPV approach in which multiple LPV controllers, each tuned for a specific speed, may be strung together.

Setiawan et al. (2001) proposes an adaptive compensation algorithm in which rotor stability is achieved through estimation and feedforward cancellation of sensor runout, the method was tested in simulation and on a well-balanced rotor at 1200 RPM.

Another form of runout results from non-collocation between the rotor position sensors and the stator. Typically, the rotor position sensors are axially offset from the stator. In the case of a bowed rotating shaft, if the rotor position stays constant at the location of the position sensors, non-collocation will lead to runout of the portion of the rotor that is aligned with the stator.

In general, approaches that have been applied to runout rely on significant system changes. Reduction of runout signal requires that changes be made to the rotor position

sensors and/or the sensor target. Controller based approaches require additional computing power to run control algorithms not typically associated with an AMB.

In contrast, application of the MPM only requires access to control signals that are inherent to an AMB; specifically, coil current and rotor position. The MPM uses system data in conjunction with a simple model of the AMB to infer the air gap distance between the rotor and stator. Air gap distance can be used to estimate actual rotor runout (as opposed to sensor runout). The rotor runout determined by the MPM can be compared to the runout reported by the rotor position sensors to arrive at a compensation.

## **EQUILIBRIUM POINT OF LINEARIZED SYSTEM**

The location of the effective origin relative to the rotor set-point also has implications for the system controller. Various control schemes have been applied to AMBs, a number of which are outlined in a special issue on AMB control by various authors (IEEE, 1996). It can be seen that the control laws are typically based on a version of the governing force equation of the AMB system (shown in Equation 1.13). In general the system is assumed to be at equilibrium ( $x = 0$ ) to simplify construction of the control law. It is common to linearize the force equation about  $x = 0$ , or use the position of  $x = 0$  when calculating parametric coefficients. Even in the case that position disturbance, or known initial offset from equilibrium, is incorporated into a control scheme such as that proposed by Namerikawa et al. (2004), the amount of position offset is based on an assumption of an equilibrium location. By definition, true equilibrium occurs at the effective origin since the effective origin is the point at which the force equation is satisfied for  $x = 0$  for any set of control currents. The real system will best match the chosen controller when the origin of the system position coordinates coincides with the effective origin.

### **4.2.2 Technique**

The Multi-Point Method (MPM) as described by Kasarda (2000) and Marshall (2001) leverages the AMB controllers' response to user applied bias current perturbations in conjunction with a system model. The system model is based on magnetic circuit theory and is used to predict bearing load and position. In general, when the rotor position sensors report a position offset of zero, the effective position offset calculated by the MPM will be non-zero. Manual adjustments to the rotor position set-point can be made that will result in an effective rotor position of zero, as calculated by the MPM. The rotor location for which MPM methods predict zero rotor position offset along each control axis is the effective origin.

## **4.3 APPROACH**

### **4.3.1 AMB Force Measurement Background**

Models for the force developed by an AMB have been in use by a number of researchers and are discussed in Sections 1.2 - 1.5. In particular, Gahler and Forch (1994) developed magnetic force models that are directly applicable to an 8 pole AMB with two axes of control, such as the one used in this research. The simplest form of the

model assumes that the AMB axes are completely independent of each other; for such a case the force in either axis can be written as the difference between the forces produced by the upper and lower magnets of that axis. A mathematical model of the bearing force is required as well; modeling of bearing force is discussed in Section 1.5. An equation describing the general model for a typical force axis of the bearings used in this research, as developed in Section 1.5, is repeated here along with a schematic of a single force axis.

$$F = k \cos \theta \left[ \frac{i_{upper}^2}{(2(g_o - x \cos \theta) + b)^2} - \frac{i_{lower}^2}{(2(g_o + x \cos \theta) + b)^2} \right] \quad (1.13)$$

where:

$$k = \mu_o AN^2 \cos \theta$$

$\mu_o$  = magnetic permeability of air

$A$  = area of pole face

$N$  = number of wire turns on actuator coil

$\theta$  = angle between bearing axis and axis of an individual magnetic pole.

$i_{upper}$  = coil current in upper actuator

$i_{lower}$  = coil current lower actuator

$g_o$  = nominal air gap

$x$  = rotor displacement along bearing axis

$b = L_i / \mu_r$  = equivalent air gap due to the flux path through the rotor and stator

$L_i$  = approximation of flux path through rotor and stator

$\mu_r$  = the relative permeability of the rotor and stator material (relative to  $\mu_o$ )

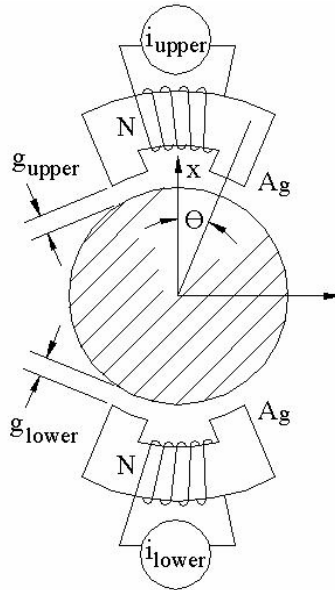


**Figure 1.4: Typical force axis (V or W)**

Figure 2.1 shows the bearings' two axes of control;  $V$  and  $W$ . Equation 1.13 is applied to each axis independently so that the force associated with each axis is calculated.



load and position scenario, a change in the bias current associated with a given axis  $V$  or  $W$  will result in a change in the controller current pair  $i_{upper}$  and  $i_{lower}$  (Figure 1.4) in order to maintain the rotor at the operational set-point. The bias current perturbation method generates multiple pairs of controller currents ( $i_{upper}, i_{lower}$ ) in order to infer system information from their relative relationships to the calculated force. Specifically, each controller current pair is substituted into separate expressions of Equation 1.13. Since neither the load nor the rotor position is varied between these expressions, they can be considered simultaneous equations. These equations can then be solved to provide values of load ( $F$ ) and rotor position ( $x$ ).

For example, consider the case of two bias current points resulting in two distinct current pairs; ( $i_{upper,1}, i_{lower,1}$ ) and ( $i_{upper,2}, i_{lower,2}$ ) to demonstrate the technique. These current pairs are used in two separate expressions of Equation 1.13 and values for  $x$  are obtained by setting both expressions equal to each other as follows:

$$\frac{i_{upper,1}^2}{(2(g_o - x \cos \theta) + b)^2} - \frac{i_{lower,1}^2}{(2(g_o + x \cos \theta) + b)^2} = \frac{i_{upper,2}^2}{(2(g_o - x \cos \theta) + b)^2} - \frac{i_{lower,2}^2}{(2(g_o + x \cos \theta) + b)^2} \quad (2.5)$$

Since all parameters are known except  $x$ , Equation 2.5 can be manipulated to solve for the position  $x$  as follows:

$$x = \frac{1}{\cos \theta} \left[ \frac{2g_o + b}{i_{lower,1}^2 - i_{lower,2}^2 - i_{upper,1}^2 + i_{upper,2}^2} \right] * \left[ \frac{i_{lower,1}^2 - i_{lower,2}^2 + i_{upper,1}^2 - i_{upper,2}^2}{2} \pm \sqrt{(i_{lower,1}^2 - i_{lower,2}^2)(i_{upper,1}^2 - i_{upper,2}^2)} \right] \quad (2.6)$$

Equation 2.6 is quadratic so that the solution for  $x$  has two roots. The correct root is easily identified since it is the only value of  $x$  that exists within the physical confines of the stator. The position  $x$  determined by Equation 2.6 can then be used in Equation 1.13 along with the associated measured currents to solve for load ( $F$ ) if so desired. Although only two bias current pairs are required to establish a value of  $x$ , in practice more than two bias current perturbations are performed in order to minimize the effect of a possible outlier current measurement on the position result. To accommodate the surplus of data resulting from more than two bias current perturbations, Equation 2.6 is solved for multiple combinations of current pairs of  $i_{upper}$  and  $i_{lower}$  resulting in multiple values of  $x$ , their resulting median value is taken as the final result.

The MPM is applied to each axis ( $V$  and  $W$ ) independently. The controller set-point is modified based on the value of  $x$  calculated in the above manner to move the bearing to the effective origin as described below.

### 4.3.3 Determination of the Effective Origin

Bias current perturbation as described above in conjunction with Equation 2.6 is applied to each axis ( $V$  and  $W$ ) independently. That is, the controller set-point is modified based on the value of  $x$  calculated in Equation 2.6 to move the bearing to the effective origin of the AMB. In determining the location of the effective origin the calculated position  $x$  is

treated as an error signal and is used to guide the rotor toward the center of the AMB axes. The effective origin can be defined for a control axis ( $V$  or  $W$ ) as the rotor location for which Equation 2.6 produces a position offset  $x$  of zero. Typically, several iterations of the approach are necessary as demonstrated in the experimental results shown below. In part due to use of a simplified force model (Equation 1.13).

## 4.4 DESCRIPTION OF TEST PLATFORMS

The method to determine the effective origin described above was used to determine the effective origin for five radial AMB systems. The five systems are associated with two test platforms; one system on Platform 1 and four systems on Platform 2. The five systems are briefly described below, further details related to the specifications of the AMB systems can be found in Chapter 3.

### 4.4.1 Platform 1

The AMB system associated with Platform 1 is part of a laboratory test rotor setup as shown in Figure 4.1. The test rotor system consists of two eight-pole heteropolar AMBs with a 35mm (1.38in.) stator inner diameter, 37mm (1.46in.) in axial length, driven by a digital PID controller manufactured by Revolve Magnetic Bearings, Inc. The tests to demonstrate the method to determine the effective origin concentrated on the outboard bearing, with the other used only for support. Additional specifications of the AMB are shown in Table 4.1.

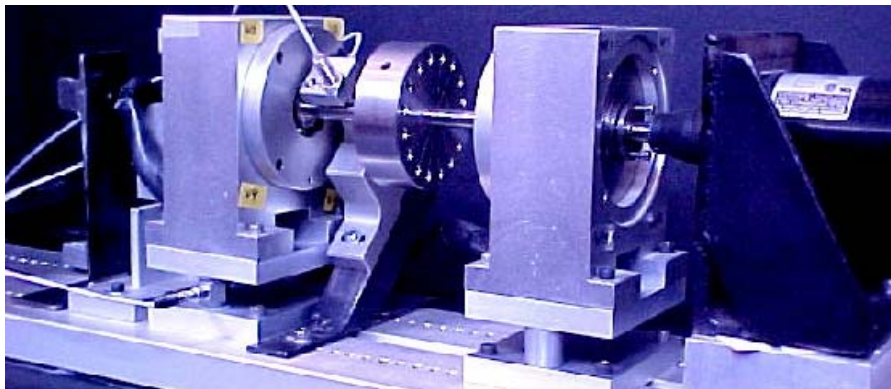


**Figure 4.1: Platform 1 laboratory rotor with outboard AMB mounted on force transducers**

**Table 4.1: AMB specifications for Platform 1**

Feature	SI	English
<b>Nominal Air Gap</b>	0.381mm	0.015in.
<b>Shaft Diameter</b>	9.5mm	0.37in.
<b>Bearing Span</b>	200mm	7.87in.
<b>Rated Bearing Capacity</b>	53N	12lb <sub>f</sub>

### 4.4.2 Platform 2

The four AMB systems associated with Platform 2 are part of a laboratory test rotor setup as shown in Figure 4.2. The test rotor system consists of two eight-pole heteropolar AMBs with a 115mm (4.53in.) stator inner diameter, 22mm (0.875in.) stator axial length, driven by a digital PID controller manufactured by Revolve Magnetic Bearings, Inc. The tests to demonstrate the method to determine the effective origin concentrated on the outboard bearing, with the other used only for support.

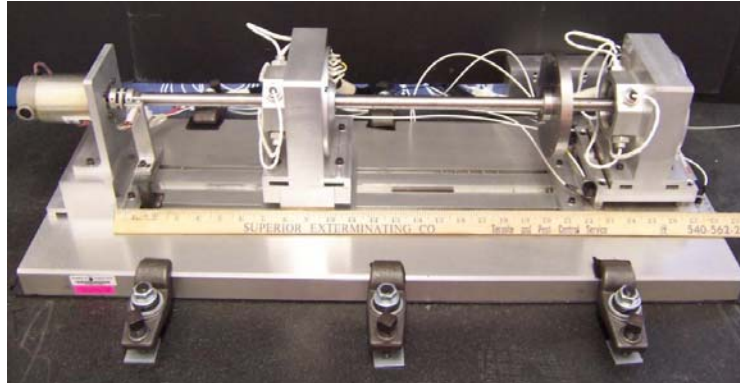


**Figure 4.2: Platform 2 laboratory rotor with outboard AMB mounted on force transducers**

Platform 2 is capable of being configured as four different systems. The different system configurations are achieved by using rotors that have a variety of diameter and lamination thickness characteristics. The rotors had the following variations in characteristics:

1. 0.010in. nominal gap, 0.005in. lamination (Arnon 5)
2. 0.030in. nominal gap, 0.005in. lamination (Arnon 5)
3. 0.010in. nominal gap, 0.014in. lamination (M19)
4. 0.030in. nominal gap, 0.014in. lamination (M19)

Additional specifications of the AMB are shown in Table 4.2.

**Table 4.2: AMB specifications for Platform 2**

Feature	System	SI	English
<b>Shaft Diameter</b>	all	16.5mm	0.65in.
<b>Bearing Span</b>	all	406mm	16in.
<b>Rated Bearing Capacity</b>	0.030in. nominal gap	107N	24lb <sub>f</sub>
	0.010in. nominal gap	267N	60lb <sub>f</sub>

## 4.5 EXPERIMENT

The AMB controller includes a utility program for centering the rotor within the mechanical back-up bearing. In the utility program the rotor is “walked” along an axis until it contacts the mechanical back-up bearing, the maximum position in both directions

is noted, the midpoint between the extremes is then set by the controller as the zero offset location for that axis. The rotor is walked along each axis so that the mechanical back-up bearing center position is considered to be at (0,0) in AMB system coordinates. Different desired rotor offsets can be manually input to the controller.

Two test cases were examined, in the first test case the rotor was moved from the mechanical back-up bearing center, referred to as (0,0) in AMB system coordinates, to the effective origin of the bearing, a net move of about  $30\mu\text{m}$  (0.0012in.). The first test case was repeated five times to examine repeatability. A second test case required the rotor to move about  $100\mu\text{m}$  (0.0039in.) to reach the effective origin. The procedure was performed once for the second test case. The procedure predicted the same rotor location within  $\pm 1\mu\text{m}$  (0.000039in.) in both test cases.

### **4.5.1 Experimental Procedure – Platform 1**

For each test case, with the rotor levitated at (0,0) in AMB system coordinates, controller current data (pairs of  $i_{upper}$  and  $i_{lower}$ ) was collected for five bias current settings. Since the maximum sustained current output for the controller is 3.0 Amps, a typical operational bias current setting would be 1.5 Amps. For the tests discussed here, the bias current settings used were 0.7, 0.9, 1.1, 1.3, and 1.5 Amps, respectively. For each of the five bias current settings the controller currents for each electromagnet of the bearing were recorded ( $i_{upper}$  and  $i_{lower}$  for both  $V$  and  $W$  axes). These values of current were used in Equation 2.6 to calculate an associated value of rotor position  $x$  in each axis as described in detail in Section 4.3.2.

For a given axis, the calculated rotor position  $x$  represents a prediction of the existing location offset of the effective origin relative to the operational rotor set-point. After a location offset was calculated, the operational rotor set-point on the controller was manually changed to coincide with the predicted the effective origin location. For verification, the bias current perturbation method was repeated at the new location. In practice, several iterations (usually around ten) of set-point modification were required before further iterations predicted minimal offset (less than  $1\mu\text{m}$  distance) from the effective origin.

### **4.5.2 Experimental Results – Platform 1**

#### **CASE I: ROTOR START POSITION AT BACK-UP BEARING MECHANICAL SET-POINT**

As discussed in the previous section, the effective origin is found by calculating a predicted offset from the effective origin in each control axis based on the rotors' initial position. The rotor set-point is then changed to account for the predicted offset. Due to an over-prediction of the offset between the rotor position and the effective origin (due to use of a simplified model) the method requires multiple iterations.

Table 4.3 tabulates the rotor set-points and associated offset predictions for the first of the five tests associated with locating the effective origin when the rotor is mechanically

centered in the back-up bearing. Recall that the initial set-point of the rotor is at (0,0) in AMB system coordinates.

**Table 4.3: Position set-points and associated position errors ( $\mu\text{m}$ )**

Iteration	V axis		W axis	
	System Position Set-point	Predicted Offset	System Position Set-point	Predicted Offset
1	0.00	-35.12	0.00	11.78
2	35.12	21.33	-11.78	-2.52
3	13.79	-11.64	-9.26	-1.65
4	25.43	5.87	-7.61	2.03
5	19.95	-2.85	-9.90	-1.39
6	22.80	1.92	-11.29	-2.56
7	20.88	-1.79	-8.73	0.46
8	22.67	0.82	-9.19	0.05
9	21.85	0.05	-9.24	-0.04
10	21.80	-0.19	-9.20	-0.04

Each row in Table 4.3 contains the iteration number, system position set-points, and predicted offsets from the effective origin for each iteration. The position set-points are the values entered into the controller as the rotor position to be maintained by the control system. The predicted offset values are the predicted positions  $x$  as determined by the Bias Current Perturbation Technique. The predicted offsets are used to update the position set-points for the next iteration as shown in the table.

Consider iteration 1 in Table 4.3 which shows a system position set-point of (0,0). A system position of (0,0) is the center of the mechanical back-up bearing and acts as a first prediction of the effective origin. The table shows that the bias current perturbation technique predicts that the rotor is offset from the effective origin by  $-35.12\mu\text{m}$  in  $V$  and by  $11.78\mu\text{m}$  in  $W$ . These offsets are used to determine the required change to operational rotor set-point. An apparent over-prediction of about 40% is inherent to the method due to use of a simplified model. The overprediction required the process to be repeated nine times before further iterations yielded minimal ( $< 1\mu\text{m}$ ) predicted offsets in both axes. Specifically, it can be seen (iteration 9) that a rotor position set-point of (21.85, -9.24) is predicted to be offset from the effective origin by less than  $1\mu\text{m}$  ( $3.937\text{e-}5\text{in.}$ ). The tenth iteration was performed to show that the method is stable and does not predict significant offset when the effective origin is achieved within reasonable error bounds ( $< 1\mu\text{m}$ ).

The over-prediction of the effective origin position offset is more easily seen if a portion of the above data is presented in graphical form. Figure 4.3 shows the progression of the  $V$  axis position set-point (column 2 of Table 4.3) to its' final value as the error (column 3 of Table 4.3) tends to zero.

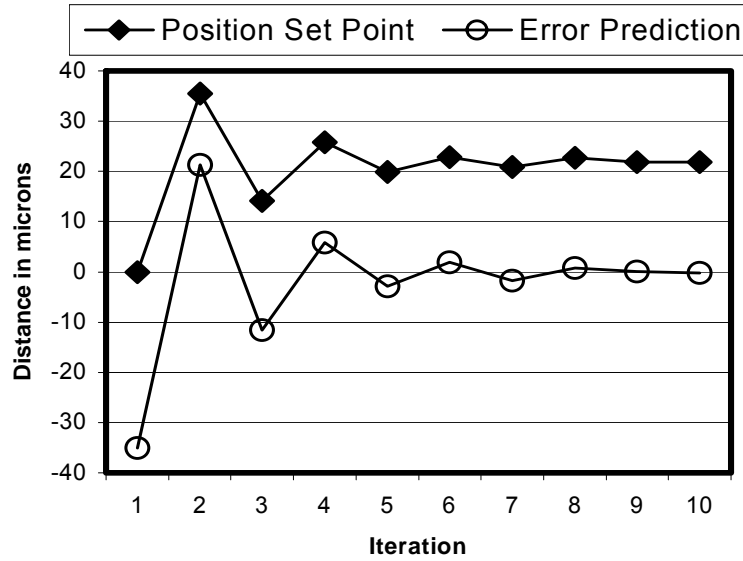


**Figure 4.3: Position set-points and associated error predictions for successive iterations (first experiment, repetition 1; V axis results)**

Figure 4.3 demonstrates the approximately 40% over-prediction in predicted position associated with each iteration. Sources of the over-prediction error are linked to the simplified magnetic force model (Equation 1.13). For instance, Gahler and Forch (1994) predicts a variation between the results stemming from a simple model such as was used here and the more comprehensive reluctance model. Furthermore, Equation 1.13 does not attempt to account for flux fringing as discussed by Imlach et al. (2000) or other non-ideal phenomena that may affect the predicted offset values. Although choosing a more complex force model may minimize the amount of iterations required, the end result is that each method predicts the same final location of the effective origin.

The first test (initial rotor set-point located at the center of the mechanical backup bearing) was performed five times to demonstrate the repeatability of the method. The first repetition of the test has been detailed in Table 4.3 and Figure 4.3, the resulting final location of the effective origin for all five repetitions are shown in Table 4.4 below.

**Table 4.4: Final effective origin predictions for five cases**

Repetition	Predicted Effective origin	
	V axis	W axis
1	21.85	-9.24
2	22.40	-7.90
3	22.30	-8.80
4	22.40	-7.60
5	22.10	-8.80

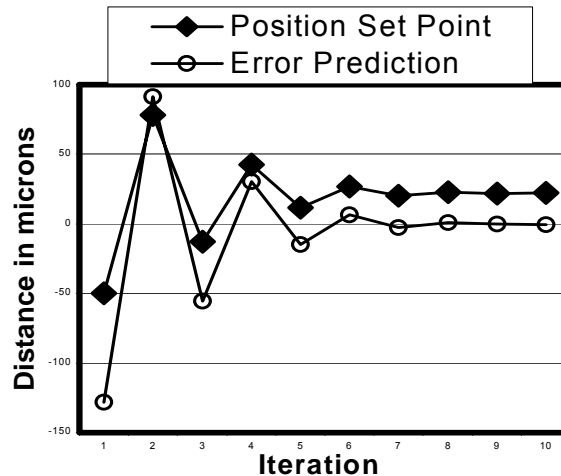
The average location of the effective origin based on the 5 repetitions is (22.21, 8.47). The greatest variation from the average effective origin location to a predicted effective origin location is 0.85 $\mu$ m (3.35e-5in.) and occurs in repetition 1. In terms of the nominal

air gap (0.381mm) shown in Table 4.1, the greatest variation ( $0.85\mu\text{m}$ ) is  $\sim 0.2\%$  of the nominal air gap.

### CASE II: ROTOR START POSITION AT (-50,60)

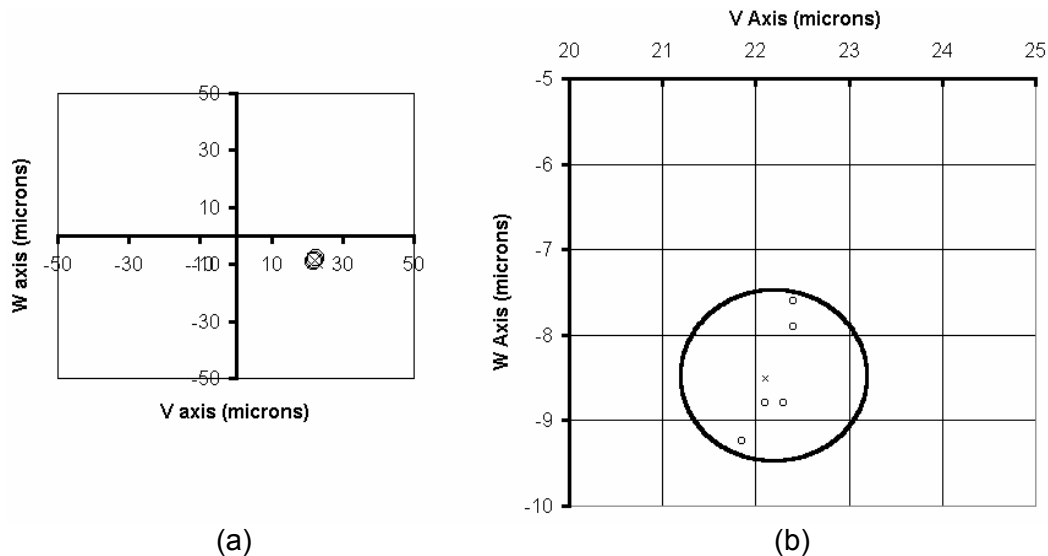
To show that the method will also work for larger initial offsets, a second experiment was performed in which the initial rotor position set-point was arbitrarily changed from (0,0) to (-50,60).

Figure 4.4 shows the iterative progression of the rotor toward the effective origin in the  $V$  axis as well as the error associated with each iteration. The technique predicts the effective origin at position (22.1, -8.5), about a 100 micron net move from the initial rotor position of (-50,60). Comparison of the predicted effective origin location of the second experiment to the average effective origin location predicted in the first experiment shows that the predictions are in agreement to  $0.11\mu\text{m}$  ( $4.33\text{e-}6\text{in.}$ ) or  $\sim 0.03\%$  of nominal air gap.



**Figure 4.4: Position set-points and associated error predictions for successive iterations (second experiment;  $V$  axis results)**

To summarize the results for the location of the effective origin for both experiments, the resulting effective origin predictions all of the test cases are plotted in Figure 4.5. In the figure the  $V$  and  $W$  axes of the magnetic bearing are shown on the  $x$  and  $y$  axes respectively. The origin of each plot is the origin of the AMB system coordinates, which is located at the center of the mechanical back-up bearing.



**Figure 4.5: Effective origin location predictions from Case I and Case II**

Figure 4.5(a) is a larger scale overview of the V and W axes showing the approximate location of the effective origin. Figure 4.5(b) shows a zoomed in view of the same data; the small circles represent the effective origin prediction from Case I (as tabulated in Table 4.4), the 'x' represents the effective origin prediction of Case II. Also shown in Figure 4.5(b) is a larger circle, the circle has a  $1\mu\text{m}$  radius and is plotted to demonstrate that all of the predicted effective origin locations fall within a  $1\mu\text{m}$  ( $3.937\text{e-}5\text{in.}$ ) radius circle. Uncertainty associated with the effective origin locations is discussed in Appendix B.

### 4.5.3 Experimental Procedure – Platform 2

The tests of the systems on Platform 2 were performed similar to the Case 1 test on Platform 1 described above. The work performed on Platform 1 instilled confidence in the procedure so that the effective origin locating process was streamlined. Three bias current settings were used in the Multi-Point Method for determining the effective origin of the systems associated with Platform 2 in contrast to five bias current settings as used for the system on Platform 1. Furthermore, the effective origin location was determined only one time for each of the systems on Platform 2 since repeatability of the method was demonstrated on system 1.

### 4.5.4 Experimental Results – Platform 2

While performing the effective origin procedure on the systems associated with Platform 2, the need for an additional correction was discovered. It was noticed that the rotor position value ( $x$ ) returned by Equation 2.6 changed if the rotation angle of the rotor changed. There proved to be a consistent relationship between rotor rotation angle and the rotor position value determined by Equation 2.6. The relationship was accounted for by noting the rotation angle of the rotor associated with calculated rotor positions for twelve rotational positions of the shaft. An example of the relationship between rotation

angle and effective offset is shown in Figure 4.6, associated with Platform 2; System 3. The  $x$  and  $y$  axes of the graph are the effective  $V$  and  $W$  axes. The numbers inside the graph are the rotor rotation angles. The process started at a rotation angle of  $210^\circ$ , seen at the top center of Figure 4.5 and proceeded to each of the remaining eleven rotational positions. After the MPM was applied to each of the twelve rotational positions, it was applied again at the original rotational position of  $210^\circ$ . The position corresponding to the second application of the MPM is marked as 210-b. Comparison of the two locations shows that the method was repeatable to  $\sim 2\mu\text{m}$ .

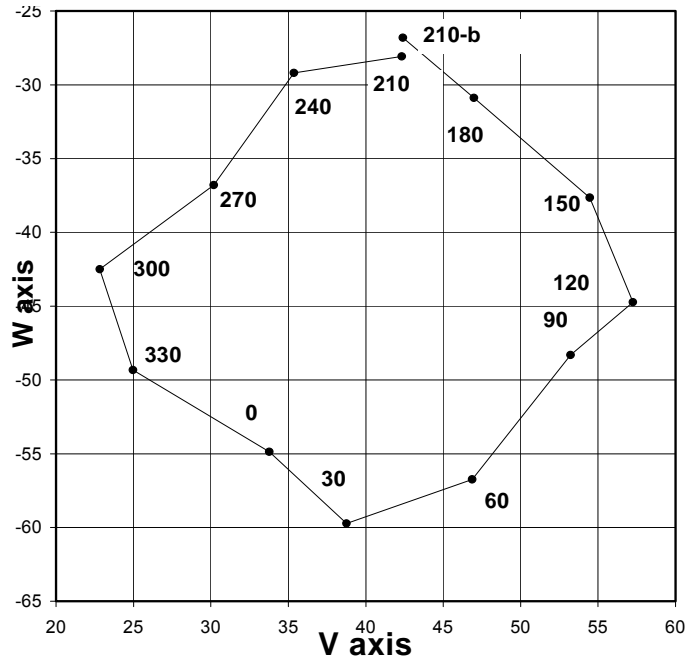


**Figure 4.6: Phase relationship of effective position; numbers on graph are phase angles associated with the  $V$  and  $W$  axis offsets**

The figure shows a total runout of  $\sim 25\mu\text{m}$  or  $0.001\text{in.}$ , the existence of runout was confirmed with a mechanical gauge. The runout is likely due to non-uniformity in the portion of the rotor that is aligned with the position sensors. The AMB controller reacts to runout as it would react to a real change in rotor position; control currents are applied as necessary to move the rotor to the location for which the position probe signals indicate zero offset.

In order to determine the effective origin in these cases (Platform 2), the centroid of the measured points was taken as the effective origin position and additional offset was added as a function of rotor angle. The effective offsets were assembled with their associated phase angles into a lookup table. The additional rotor angle based translation is accounted for when determining the effective origin for the systems associated with Platform 2.

The resulting locations of the effective origin for the four systems associated with Platform 2 are tabulated below in Table 4.5. Uncertainty associated with the effective origin locations is discussed in Appendix B.

**Table 4.5: Effective origin locations determined for four systems on Platform 2**

<b>System</b>	<b>System Specifications</b>	<b>Effective origin</b>
<b>1</b>	0.010in. gap; 0.005in. laminations	(7.6,7.3)
<b>2</b>	0.030in. gap; 0.005in. laminations	(-14.5,44)
<b>3</b>	0.030in. gap; 0.014in. laminations	(5.6,40.9)
<b>4</b>	0.010in. gap; 0.014in. laminations	(-26.7, 31)

## **4.6 CONCLUSION**

This chapter discusses a field applicable system identification using a bias current perturbation technique (the Multi-Point Method) for determining the effective origin in a radial magnetic bearing. Steps required to determine the effective origin are outlined. The Multi-Point Method used to predict the offset of the rotor from the effective origin is described. An experiment is detailed in which the method is applied to a laboratory AMB system. The method is shown to be repeatable within  $1\mu\text{m}$  ( $3.94\text{E-}5\text{in.}$ ) or within 0.26% of nominal radial gap for Platform 1.

The Multi-Point Method was then applied to four additional AMB systems. During testing a relationship between the location of the effective origin and the phase of the rotor was recognized and accounted for.

Knowledge of a rotors' set-point relative to the effective origin is beneficial. It can aid the diagnosis of an under-performing bearing and the bearing will best match its' controller when operating about the effective origin. Of greater importance to the authors, however, is the capability to characterize air gaps. Current-based load measurement techniques benefit from accurate knowledge of rotor position within the stator. The ability to determine the effective origin of a bearing is an important step toward providing a current-based model that can be used to accurately predict shaft forces without the use of additional hardware such as Hall-effect probes.

# Chapter 5 Coordinate Transformation

## 5.1 INTRODUCTION

Locating the radial effective origin of an Active Magnetic Bearing (AMB), as discussed in the previous chapter, is an important step towards accurate characterization of bearing air gaps for field tuning, performance analyses, and some shaft force measurement techniques. Specifically, application of current-based force measurement techniques to AMBs requires accurate modeling of air gaps in order to predict dynamic forces with accuracy. This chapter extends the methods used to determine the effective origin to include a coordinate transformation. The coordinate transformation further enhances AMB based force measurement accuracy by accounting for otherwise unmodeled effects that occur at eccentric rotor locations. A system identification technique that analyzes the AMB system's response to the perturbation of bias currents in conjunction with a magnetic circuit model is used to infer rotor positions. Comparison of an inferred rotor position to the rotor position reported by the system forms the basis of the coordinate transformation. The system identification technique discussed here does not require additional hardware and is suitable for use in the general class of AMBs in field applications.

Our goal is to provide an AMB based force measurement technique that can be applied in the field without extensive calibration, without application of known loads, and without the use of Hall probes. Instead, the technique relies on a system identification method in which the AMB system is perturbed and interrogated. The systems' response to the perturbations is then used in conjunction with an AMB force model of the system to provide identification. The identification technique, known as the Multi-Point Method (MPM) provides identified values of bearing force and rotor offset.

The MPM was introduced to identify an effective value of rotor offset to be used in the force model such that the force model produced accurate force measurement results. In Chapter 4, the MPM was applied to AMBs in order to establish the relationship between the rotor position origin as measured by the system and the rotor position origin inferred by the system model. In this chapter, the idea of an effective origin that differs from the system origin is expanded to consider an effective coordinate system that differs from

the system coordinates. System coordinates are based on the rotor position reported by the system controller. The geometric center of the backup bearing and the axes of the position feedback sensors inherent to an AMB define the system coordinates. Effective coordinates are based on the observed behavior of the system and a simple force model of the AMB.

This chapter discusses the process used to determine a transformation between system coordinates and effective coordinates. The process was applied to five different magnetic bearing systems so that a unique transformation was determined for each system. After the transformation from system coordinates to effective coordinates was determined, the transformed values of rotor position were used in an AMB force model to calculate the applied load. Force transducers mounted beneath the bearing provided a direct measurement of applied load. Calculated load values were compared to the measured load values as a way to validate the coordinate transformation.

The results show that the technique produced static force measurements with ~4% mean error, and an associated standard deviation of ~4%. If the coordinate transformation was not applied, the model produced static force measurements with ~15% mean error, and an associated standard deviation of ~22%.

### 5.1.1 AMB Force Measurement Background

Models for the force developed by an AMB have been in use by a number of researchers and are discussed in Sections 1.2 - 1.5. In particular, Gahler and Forch (1994) developed magnetic force models that are directly applicable to an 8 pole AMB with two axes of control, such as the one used in this research. The simplest form of the model assumes that the AMB axes are completely independent of each other; for such a case the force in either axis can be written as the difference between the forces produced by the upper and lower magnets of that axis. A mathematical model of the bearing force is required as well; modeling of bearing force is discussed in Section 1.5. An equation describing the general model for a typical force axis of the bearings used in this research, as developed in Section 1.5, is repeated here along with a schematic of a single force axis.

$$F = k \cos \theta \left[ \frac{i_{upper}^2}{(2(g_o - x \cos \theta) + b)^2} - \frac{i_{lower}^2}{(2(g_o + x \cos \theta) + b)^2} \right] \quad (1.13)$$

where:

$$k = \mu_o AN^2 \cos \theta$$

$\mu_o$  = magnetic permeability of air

$A$  = area of pole face

$N$  = number of wire turns on actuator coil

$\theta$  = angle between bearing axis and axis of an individual magnetic pole.

$i_{upper}$  = coil current in upper actuator

$i_{lower}$  = coil current lower actuator

$g_o$  = nominal air gap

$x$  = rotor displacement along bearing axis

$b = L_i / \mu_r$  = equivalent air gap due to the flux path through the rotor and stator

$L_i$  = approximation of flux path through rotor and stator



### 5.1.2 Foundation of Multi-Point Method (MPM)

The Multi-Point Method (MPM) is discussed in Chapter 2. Current perturbation techniques such as the MPM make use of the controller's ability to support a certain load at a specific location for any bias current setting within the operating envelope of the system. For a given load and position scenario, a change in bias current will result in a change in the controller current pair  $i_{upper}$  and  $i_{lower}$ . Bias current perturbation is used to generate multiple pairs of controller currents. Each controller current pair is then substituted into separate expressions of a simple AMB force equation (Equation 1.13). Since neither the load nor the rotor position is varied between these expressions, they can be considered simultaneous equations. As discussed previously, equating two such instances of Equation 1.13 results in Equation 2.5, all of the variables in Equation 2.5 are known except for the effective rotor offset,  $x$ .

$$\frac{i_{upper,1}^2}{(2(g_o - x \cos \theta) + b_{th})^2} - \frac{i_{lower,1}^2}{(2(g_o + x \cos \theta) + b_{th})^2} = \frac{i_{upper,2}^2}{(2(g_o - x \cos \theta) + b_{th})^2} - \frac{i_{lower,2}^2}{(2(g_o + x \cos \theta) + b_{th})^2} \quad (2.5)$$

Equation 2.5 can be manipulated to solve for the effective rotor offset  $x$  as seen in Equation 2.6.

$$x = \frac{1}{\cos \theta} \left[ \frac{2g_o + b_{th}}{i_{lower,1}^2 - i_{lower,2}^2 - i_{upper,1}^2 + i_{upper,2}^2} \right] \left[ \frac{i_{lower,1}^2 - i_{lower,2}^2 + i_{upper,1}^2 - i_{upper,2}^2}{2} \pm \sqrt{(i_{lower,1}^2 - i_{lower,2}^2)(i_{upper,1}^2 - i_{upper,2}^2)} \right] \quad (2.6)$$

Although Equation 2.6 is quadratic the correct root is easily determined since it is the only value of  $x$  that exists within the physical confines of the stator. In practice a minimum of three current pairs are used. The effective rotor offset  $x$  determined by the MPM can then be used in Equation 5.6 to solve for force if desired.

### 5.1.3 Coordinate Transformation Overview

The result of Equation 2.6 is the effective rotor offset in one axis. The procedure is applied to both axes so that an effective rotor position offset  $(v_e, w_e)$  that corresponds to a specific offset in system coordinates  $(v_s, w_s)$  is determined. The procedure is repeated at several specific locations along the system coordinate axes so that a coordinate transformation between the system axes and the effective axes can be calculated. The transformation acts as a mapping between the system coordinates and the effective coordinates.

Figure 2.4 (repeated below) shows the relationship between the system coordinates and the effective coordinates for arbitrary values of offset, rotation, and scale. The system coordinates, shown in black with axes labels of  $(V_s, W_s)$ , correspond to the rotor position reported by the system controller. The origin of the system coordinates is generally located at the geometric center of the backup bearing, and the axes of system coordinates are defined by the position feedback sensors inherent to an AMB. The effective coordinates, shown in red with axes labels of  $(V_e, W_e)$ , correspond to the

observed behavior of the system as interpreted by MPM. As seen in the figure, the system and effective coordinates have different origins, different axes angles, and differences in unit length. It is desired to identify a transformation that accounts for the differences between the system coordinates and the effective coordinates. Specifically, the transformation must account for variation in origin location (offset), axes angles (rotation), and axes unit lengths (scale) between the two coordinate systems.

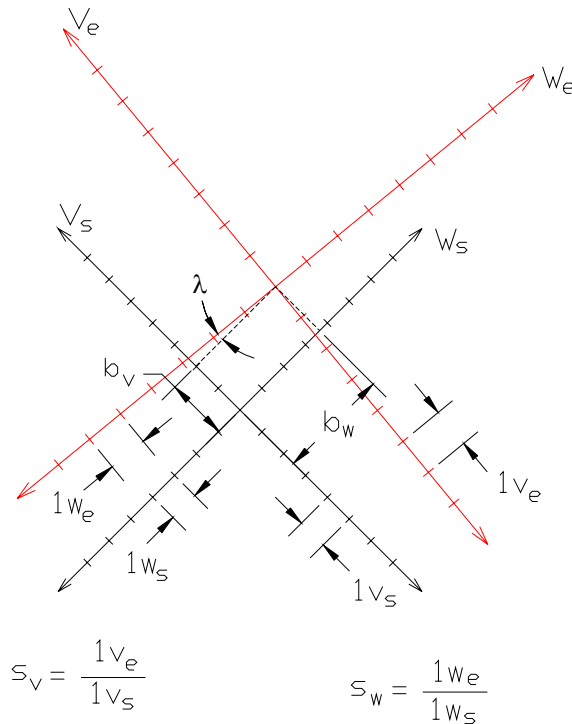


**Figure 2.4: Relationship between system coordinates ( $v_s, w_s$ ) and effective coordinates ( $v_e, w_e$ )**

As stated, the required transformation consists of an offset, axes rotation, and scale to allow position data to be mapped from system coordinates to effective coordinates. Each component of the transformation is considered individually below.

- Translation:  $v_{Trans} = v_s + b_v$ ,  $w_{Trans} = w_s + b_w$ ; where  $(b_v, b_w)$  is the offset between the system coordinate origin and the effective coordinate origin
- Rotation:  $v_{Rot} = v_{Trans} \cos \lambda - w_{Trans} \sin \lambda$ ,  $w_{Rot} = v_{Trans} \sin \lambda + w_{Trans} \cos \lambda$ ; where  $\lambda$  is the angular offset between the system coordinate axes and the effective axes
- Scale:  $v_e = v_{Rot} * s_v$ ,  $w_e = w_{Rot} * s_w$ ; where  $s_v$  and  $s_w$  are the scaling factors between the system coordinates and effective coordinates along the V and W axes respectively

The effective rotor offsets can be used in Equation 1.13 to calculate applied load. If the applied load is known, it can be compared to the calculated value of the load to validate the transformation.

## 5.2 DESCRIPTION OF TEST PLATFORMS

The above method was used to determine coordinate transformation for actual radial AMBs. The method was applied to five AMB systems on two platforms; one system on Platform 1 and four systems on Platform 2. The five systems are briefly described below, further details related to the specifications of the AMB systems can be found in Chapter 3.

### 5.2.1 Platform 1

The AMB system associated with Platform 1 is part of a laboratory test rotor setup as shown in Figure 4.3. The test rotor system consists of two eight-pole heteropolar AMBs with a 35mm (1.38in.) stator inner diameter, 37mm (1.46in.) in axial length, driven by a digital PID controller manufactured by Revolve Magnetic Bearings, Inc. The tests to demonstrate the coordinate transformation method concentrated on the outboard bearing, with the other used only for support. Force transducers mounted beneath the outboard bearing housing to provide an audit of AMB force measurement are also visible in the figure. The force transducers are PCB Piezotronics model 208C01 and each has a 10lb<sub>f</sub> capacity. Additional specifications of the AMB are shown in Table 5.1.

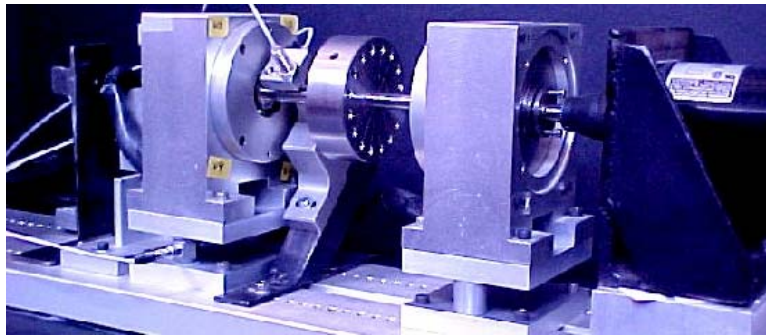


Figure 4.3: Platform 1 laboratory rotor with outboard AMB mounted on force transducers

Table 5.1: AMB Specifications for Platform 1

Feature	SI	English
Nominal Air Gap	0.381mm	0.015in.
Shaft Diameter	9.5mm	0.37in.
Bearing Span	200mm	7.87in.
Rated Bearing Capacity	53N	12lb <sub>f</sub>

### 5.2.2 Platform 2

The four AMB systems associated with Platform 2 are part of a laboratory test rotor setup as shown in Figure 5.1. The test rotor system consists of two eight-pole heteropolar AMBs with a 115mm (4.53in.) stator inner diameter, 22mm (0.875in.) stator

axial length, driven by a digital PID controller manufactured by Revolve Magnetic Bearings, Inc. The tests to demonstrate the coordinate transformation method concentrated on the outboard bearing, with the other used only for support. Force transducers mounted beneath the outboard bearing housing to provide an audit of AMB force measurement are also visible in the figure. The force transducers are PCB Piezotronics model 208C01 and each has a  $10\text{lb}_f$  capacity.

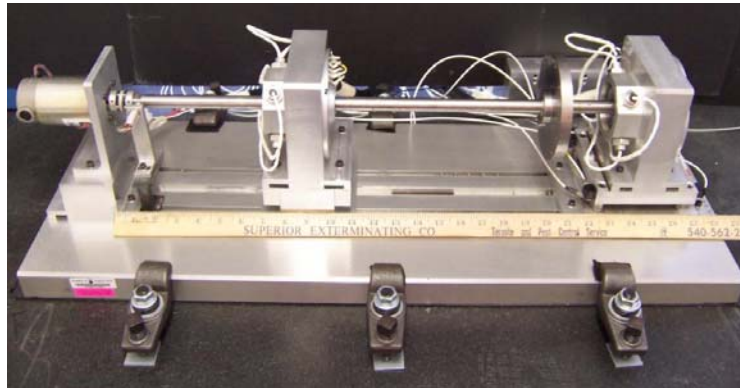


**Figure 5.1: Platform 2 laboratory rotor with outboard AMB mounted on force transducers**

Platform 2 is capable of being configured as four different systems. The different system configurations are achieved by using rotors that have a variety of diameter and lamination thickness characteristics. The rotors had the following variations in characteristics:

1. 0.010in. nominal gap, 0.005in. lamination (Arnon 5)
2. 0.030in. nominal gap, 0.005in. lamination (Arnon 5)
3. 0.010in. nominal gap, 0.014in. lamination (M19)
4. 0.030in. nominal gap, 0.014in. lamination (M19)

Additional specifications of the AMB are shown in Table 5.2.

**Table 5.2: AMB specifications for Platform 2**

Feature	System	SI	English
Shaft Diameter	all	16.5mm	0.65in.
Bearing Span	all	406mm	16in.
Rated Bearing Capacity	0.030in. nominal gap	107N	24lb <sub>f</sub>
	0.010in. nominal gap	267N	60lb <sub>f</sub>

### **5.3 PROCEDURE**

It has been shown that variation exists between the origin of an AMBs system coordinates and its effective coordinates. Chapter 4 details a procedure to locate the origin of the effective coordinate system using a mathematical model of the AMB in question and a bias current perturbation technique known as the Multi-Point Method (MPM). The Multi-Point Method is used to determine an effective rotor offset ( $v_e, w_e$ ) that corresponds to a specific offset ( $v_s, w_s$ ) in system coordinates. The procedure has

been extended to a more comprehensive transformation between the system coordinates and the effective coordinates that accounts for relative offset, rotation and scale. The procedure is applied to a static (non-rotating) rotor.

### 5.3.1 Translation (Effective origin)

The effective origin is the location for which the MPM returns effective offset values of zero for each axis:  $(v_e, w_e) = (0, 0)$ . In general the effective origin will not coincide with the origin in system coordinates:  $(v_s, w_s) = (0, 0)$ . The rotor offset measured by the system coordinates that corresponds to an effective offset of  $(v_e, w_e) = (0, 0)$  defines the required translation  $(b_v, b_w)$ .

The initial rotor position of the bearings tested coincided with the center of the backup bearing and with the origin in system coordinates:  $(v_s, w_s) = (0, 0)$ . The MPM was applied at  $(v_s, w_s) = (0, 0)$  to determine the corresponding position in effective coordinates  $(v_e, w_e)$ . For the initial position it is expected that the effective rotor offset will be non-zero. The effective offset  $(v_e, w_e)$  determined by the MPM is used as an error signal in order to estimate a more appropriate rotor position. The rotor position set-point is adjusted according to the error estimate. Since the relative scale between the system coordinates and the effective coordinates is initially unknown, multiple iterations of rotor position adjustment are required to find the effective origin. The method is further discussed in Chapter 4.

### 5.3.2 Scale

The results of the translation procedure described above were used to position the rotor at the effective origin. An intermediate coordinate system, referred to as  $(v_{trans}, w_{trans})$ , has its origin at the effective origin,  $(b_v, b_w)$  in system coordinates. The intermediate coordinate system was used to identify the rotation and scale of the effective coordinates. The intermediate coordinate system is shown in relation to the system coordinates and effective coordinates in Figure 5.2. The figure shows that the intermediate coordinate system has the same axes angles and scale as the system coordinates, but has been translated so that its origin coincides with the origin of the effective coordinates.

In order to define the relative scale between the coordinate systems, the rotor was positioned at a number of specific locations along each axis  $(v_{Trans}, w_{Trans})$  by varying the rotor position set-point on the controller. The MPM provided an effective rotor offset value corresponding to each rotor location. Figure 5.3 shows a schematic of the rotor position set-point locations along each axis in intermediate coordinates  $(v_{Trans}, w_{Trans})$  for the case of Platform 1. For the case of Platform 1, eight rotor position set-points were considered per axis;  $\pm 25\mu\text{m}$ ,  $\pm 50\mu\text{m}$ ,  $\pm 75\mu\text{m}$ , and  $\pm 100\mu\text{m}$  relative to the effective origin. In the case of Platform 2 the points considered were  $\pm 25\mu\text{m}$  and  $\pm 50\mu\text{m}$  relative to the effective origin.

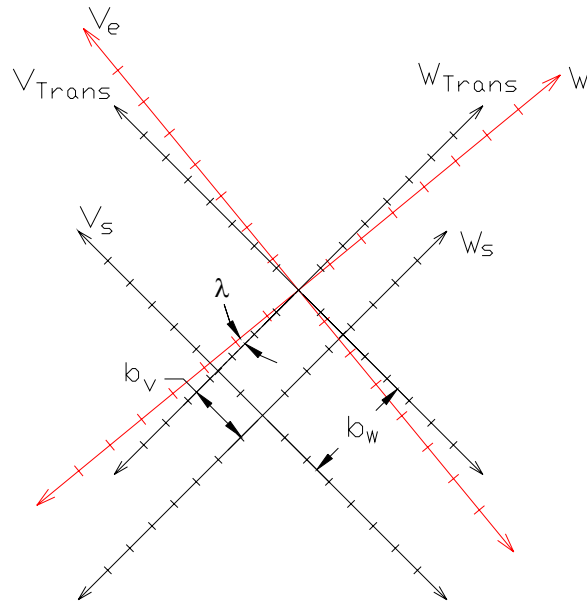


**Figure 5.2: Relationship between intermediate coordinates ( $v_{Trans}, w_{Trans}$ ), system coordinates ( $v_s, w_s$ ), and effective coordinates ( $v_e, w_e$ )**

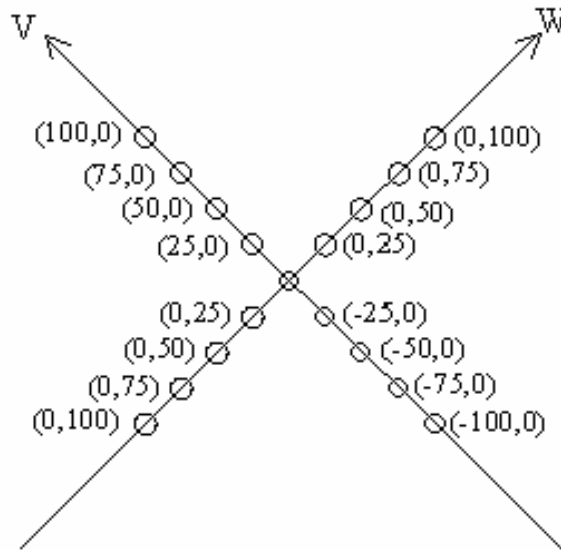


**Figure 5.3: Rotor set-points in intermediate coordinates ( $v_{Trans}, w_{Trans}$ ) for system identification of axes scale (Platform 1)**

The raw data, shown in Figure 5.4 for the case of Platform 1, shows the effective positions ( $v_e, w_e$ ) calculated by the MPM that correspond to the rotor set-points in Figure 5.3.

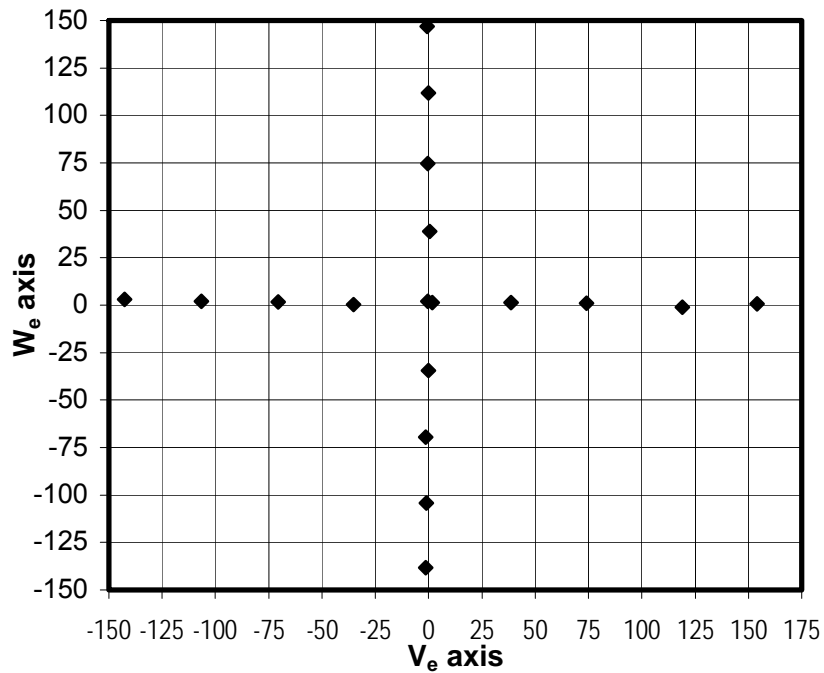


**Figure 5.4: Effective rotor positions calculated by MPM for the rotor set-points of Figure 5.3**

A comparison of the rotor set-points in  $(v_{Trans}, w_{Trans})$  to their corresponding effective offsets showed a linear relationship between the two coordinate systems. Each axis ( $V$  and  $W$ ) was treated independently so that it is possible to have a  $V$  axis scale that differs from the  $W$  axis scale for the same system. An example of the linear relationship is shown in Figure 5.5. Figure 5.5 is a plot of the effective position offset from the effective origin ( $v_e$ ) versus rotor set-point offset from the effective origin ( $v_{Trans}$ ) for the  $V$  axis of Platform 1. A linear fit of the data is shown as well. A best fit line with intercept forced to zero was used to approximate the relationship between the effective offsets and the rotor set-point offsets, the slope of the line represents the system identification of the scale factor and is represented by  $s_v$  and  $s_w$  in the transform.

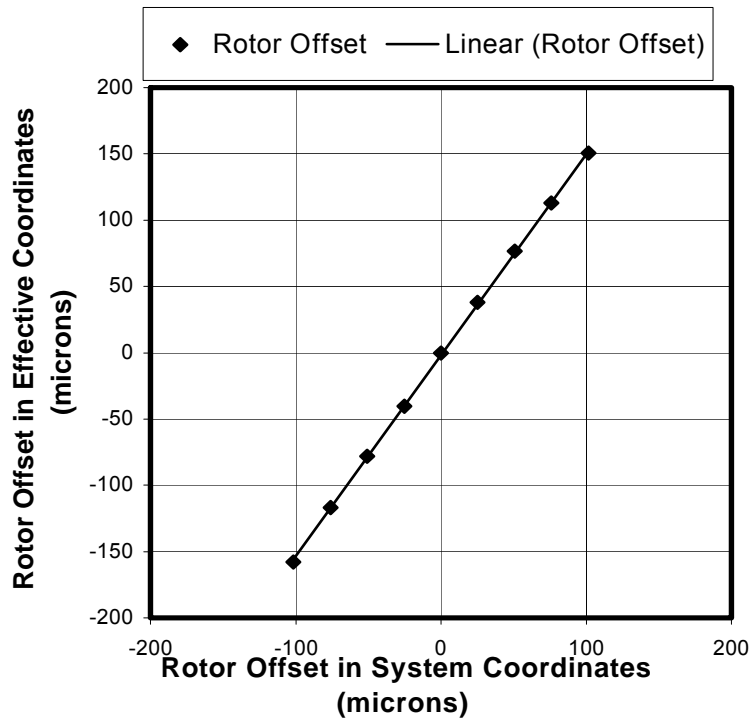


**Figure 5.5: Linear fit of effective rotor offset determined by MPM to the rotor offset in system coordinates for the V axis (Platform 1)**

### 5.3.3 Rotation

During the scaling procedure a relative rotation was discovered. Although the rotor was translated along one axis at a time, the MPM reported non-zero effective offsets for both axes. The rotation effect can be seen in Figure 5.4 at the  $V_e$  axis location of -140. Although the system set-point offset applied to the  $W$  axis was zero, a non-zero effective offset is observed in the  $W_e$  axis. It was further noted that the off-axis effective offsets tended to increase as their corresponding on-axis component increased. An average angle, based on the inverse tangent of the ratio of the off-axis component to the on-axis component was determined for each system. The angle is represented by  $\lambda$  in the transform. In general,  $\lambda$  was determined to be small ( $\sim 2^\circ$ ) so that its' effect on the transformation is negligible. It is included in the transformation for the sake of completeness.

### 5.3.4 Confirmation via Known Applied Load

After the transformation from system coordinates to effective coordinates was determined, the transformed values of rotor position were used in the AMB force model described by Equation 5.6 to calculate the applied load. Force transducers placed beneath the bearing also measured the applied load. Calculated load values were compared to the measured load values as a way to validate the coordinate transformation.

## 5.4 RESULTS

The results of this research are the transformation components for each bearing tested. The transformation components represent a system identification of a bearing and allow use of a characterized version of a simple model (Equation 1.13) to accurately determine bearing force. The results are evaluated by comparing loads calculated from a characterized model to known loads.

### 5.4.1 Transformation Components

The offset, rotation, and scale transformation components for the five AMB systems tested are given in Table 5.3. It can be seen that angular translations tend to be small ( $\sim 2^\circ$ ); they have little effect on the transformation, and for these cases could be neglected. They are included for the sake of completeness.

**Table 5.3: Identified transformation components for five AMB systems**

System	Offset (microns)		Rotation (degrees)	Scale	
	$b_v$	$b_w$	$\lambda$	$s_v$	$s_w$
<b>Platform 1</b>	2	-17	-0.2	1.51	1.51
<b>Platform 2; System 1</b>	8	7	1.9	1.12	1.21
<b>Platform 2; System 2</b>	-15	44	2.2	1.30	1.32
<b>Platform 2; System 3</b>	-27	31	2.2	1.44	1.54
<b>Platform 2; System 4</b>	6	41	2.2	1.32	1.37

### 5.4.2 Comparison of Model Output to Known Applied Load

Bearing load was determined by force transducers positioned under the bearing. Table 5.4 shows the known bearing loads (transducer based), the load calculated using Equation 5.6 with coordinate transformation applied, and the load calculated using Equation 5.6 without the coordinate transformation applied. The calculated load values shown are mean load values. They represent the average of the load values calculated at each of the rotor positions that were used to determine the transform scale. Recall that for the case of Platform 1, eight rotor position set-points were considered per axis,  $\pm 25\mu\text{m}$ ,  $\pm 50\mu\text{m}$ ,  $\pm 75\mu\text{m}$ , and  $\pm 100\mu\text{m}$  relative to the effective origin. In the case of Platform 2 the points considered were  $\pm 25\mu\text{m}$  and  $\pm 50\mu\text{m}$  relative to the effective origin. In the case of Platform 2, System 1, no transducer data was collected. It can be seen that model error is reduced if the differences between the system coordinates and the effective coordinates are accounted for. For the cases in which the transformation is applied, average model error is  $\sim 4\%$  of measured load, for the cases in which the transformation is not applied, average model error is  $\sim 15\%$  of measured load.

**Table 5.4: Calculated loads based on a simple model with and without a coordinate transformation applied**

System	Known Load	Calculated Load (Mean)		% Mean Error	
		Transform Applied	No Transform Applied	Transform Applied	No Transform Applied
<b>Platform 1</b>	1.50	1.59	1.54	6	3
<b>Platform 2; System 1</b>	X	4.06	4.27	x	x
<b>Platform 2; System 2</b>	3.78	3.90	4.44	3	17
<b>Platform 2; System 3</b>	4.15	4.31	3.22	4	22
<b>Platform 2; System 4</b>	3.94	3.87	4.62	2	17

The calculated load data was further analyzed to determine the consistency of the two methods. Table 5.5 shows the standard deviations associated with the load calculations. It can be seen that the load calculations that rely on a coordinate transformation have significantly smaller standard deviations as compared to the load calculations that do not employ a coordinate transformation. For the cases in which the transformation is applied, average standard deviation is ~4% of measured load, for the cases in which the transformation is not applied, average standard deviation is ~22%.

**Table 5.5: Standard deviations of calculated loads based on a simple model with and without a coordinate transformation applied**

System	Known Load	Standard Deviation		Standard Deviation as % of load	
		Transform Applied	No Transform Applied	Transform Applied	No Transform Applied
<b>Platform 1</b>	1.50	0.03	0.47	2	31
<b>Platform 2; System 1</b>	x	0.29	1.10	~7	~27
<b>Platform 2; System 2</b>	3.78	0.12	0.43	3	11
<b>Platform 2; System 3</b>	4.15	0.24	1.27	6	31
<b>Platform 2; System 4</b>	3.94	0.12	0.40	3	10

## **5.5 CONCLUSIONS**

A broadly applicable technique is introduced that allows system identification of the relationship between actual and effective AMB rotor offsets. The relationship between the resulting actual and effective rotor positions can be described by a coordinate transformation. Coordinate transformation components of offset, rotation, and scale are determined through a system identification procedure known as the Multi-Point Method. The technique is unique in that direct knowledge of bearing load is not required for the calibration. In lieu of a direct force measurement, current perturbations are employed to produce coil current data sets that correspond to a common load and rotor position scenario. The data is analyzed according to the Multi-Point Method to provide estimates of bearing load and effective rotor position. System identification is based on the relationship between the true rotor offset as reported by the AMB system, and the estimate of rotor offset based on current perturbation methods. Force models that have

a system identification applied can be used to provide instantaneous force data given instantaneous coil current and rotor position data. Thus, system identification facilitates application of a force model under dynamic conditions.

Considering all of the data, it can be said that the technique produced static force measurements with 2% - 6% mean error, and an associated standard deviation of 2% - 7% or less. If the coordinate transformation was not applied, the model produced static force measurements with 3% - 22% mean error, and an associated standard deviation of 10% - 31%.

## Chapter 6 AMB Based Dynamic Force Measurement – Pilot Study

This chapter and the following chapter are concerned with the use of AMBs to measure dynamic forces. The primary focus is on the measurement of dynamic forces in a radial bearing due to rotating unbalance of the rotor. The dynamic force measurement methods discussed in the following chapter rely on application of the static system identification techniques discussed in the previous chapters. Our goal is to allow for accurate measurement of dynamic AMB forces based on coil current and rotor offset measurements. Attempts to predict dynamic force based on coil currents must account for parasitic effects on coil currents. This chapter outlines a pilot study that was performed in which coil currents and rotor positions corresponding to known dynamic loads were analyzed to determine if a mathematical model for current-based force measurement based on magnetic circuit theory and accounting for current and speed dependent losses was feasible. In order to account for losses a modification to a standard force equation in which measured current is replaced by an expression for “effective current” was proposed. The effective current expression accounts for errors due to both current and speed dependent loss mechanisms.

### **6.1 INTRODUCTION**

A pilot study was performed to see if a mathematical model for current-based force measurement based on magnetic circuit theory and accounting for current and speed dependent losses was feasible. Such a model would need to account for magnetic saturation as well as dynamic effects such as eddy currents. In order to achieve this we proposed a modification to a standard force equation in which measured current is replaced by an expression for “effective current”. The effective current expression accounts for errors due to both current and speed dependent loss mechanisms. A series of tests was devised to aid with model development and validation. The tests were carried out on a laboratory test rotor that was modified to include force transducers so that true bearing load was known. Parameters describing the effective current in the new model were optimized so that variation between the modeled force and the force transducer measurements was minimized. The optimization was based on one initial set

of measurement data consisting of 8 data points. Additional data from a variety of load conditions and bias current conditions was then modeled using the optimized parameters to predict the bearing force. Although this technique requires knowledge that is not typically available (force transducer measurements) the positive results demonstrate that a current-based model based on a limited data set can be made to fit a wide variety of dynamic scenarios.

A system resonance near 3000 RPM made modeling difficult in that region. Neglecting the affected data, the average error between predicted and known forces had a magnitude of 2.8% with a worst case of 6.8%. To put this in context with other research, Fittro et al. (1997) applied an extensively calibrated (5675 data points) reluctance network technique to a radial AMB (Section 1.7.2). The resulting static errors were 1% on average, the dynamic error of the model was not directly measured. Researchers employing Hall probe techniques (Section 1.7.3) have reported data with <1% static error and <3% dynamic error.

Although the study was successful in demonstrating that a mathematical model based solely on current and position data can successfully predict dynamic forces in a magnetic bearing, the pilot study does have limitations. At the time of testing an appropriate base for the system was not available, so that testing was performed with the 8.3kg aluminum base (shown in Figure 4.3 repeated below) resting the floor. The housing of the bearing in question was mounted on two force transducers, it was later determined that these did not provide sufficient stability to the housing allowing the housing to rock during testing. This was aggravated by system resonance near certain rotational speeds. Furthermore, inertial effects of the bearing housing were not accounted for. These limitations were taken into account during the design of the next iteration test rig, discussed in following chapters.

The pilot study, detailed below, was prepared for and presented at the 9<sup>th</sup> International Symposium on Magnetic Bearings (Prins and Kasarda, 2004).

## **6.2 FORCE MODEL MODIFICATION**

The force model shown in Equation 1.13, repeated here for convenience, assumes that all of the measured currents  $i_{upper}$  and  $i_{lower}$  are available for use in generating magnetic flux that is available for force capacity.

$$F = k_{th} \cos \theta \left[ \frac{i_{upper}^2}{(2(g_o - x \cos \theta) + b_{th})^2} - \frac{i_{lower}^2}{(2(g_o + x \cos \theta) + b_{th})^2} \right] \quad (1.13)$$

In the case of a dynamic load there will be a difference between the measured currents and the current that is available for use in generating magnetic flux that is available for force capacity due to parasitic losses such as hysteresis and eddy currents. Therefore, a form of Equation 1.13 that incorporates an “effective” current,  $i_e$  is proposed to offer improved force measurement accuracy. Although we chose not to develop a rigorous physical model of effective current at this time, we did expect that the effective current would be a function of the measured current and the rotor speed. Based on these assumptions we proposed the following equation for determining effective current, based loosely on the expected effects of projected loss sources:

$$i_e = i_m - p_1 i_m - p_2 i_m \omega - p_3 i_m^2 \omega^2 \quad (6.1)$$

where  $i_e$  is the effective current,  $i_m$  is the measured current, and  $\omega$  is the rotor speed. The parameters  $p_1$ ,  $p_2$ , and  $p_3$  are not known *a priori* and were determined for the initial data set by using the known force values provided by the transducers.

### 6.3 EXPERIMENTAL SETUP

Test data for the pilot study was generated using a high-speed laboratory rotor supported by AMBs as shown in Figure 4.3.

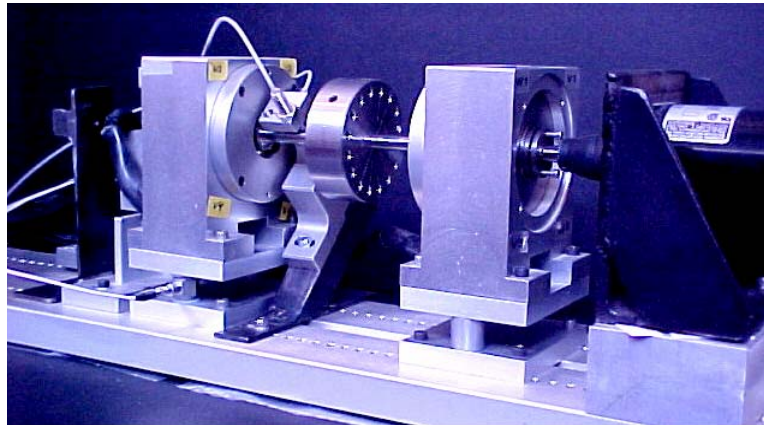


**Figure 4.3: Experimental setup**

The system consists of two eight-pole, 35mm stator inner diameter heteropolar design AMBs with a digital PID controller manufactured by Revolve Magnetic Bearings, Inc. Additional specifications are as follows; 0.381mm nominal air gap, 12lb<sub>f</sub> maximum rated load per bearing, 9.5mm shaft, 200mm bearing span. The outboard bearing was mounted on ICP type force transducers to allow monitoring of the bearing reaction force. Each transducer has a 10lb<sub>f</sub> capacity (PCB Model 208C01). The inboard bearing and motor were mounted on spacers to maintain alignment. This rig allowed us to observe the magnetic bearing control signals and the force transducer output for a variety of system conditions.

As described in detail in Chapter 1, electromagnets within an AMB system are supplied with a bias current, the level of bias current is generally set to one half of the maximum available current. This allows maximum effect of the differential control current. The AMB associated with the test rig has a maximum available current of 3 Amps so that a typical setup would call for a 1.5 Amp bias. Additional bias current scenarios of 1.3 Amps and 1.7 Amps were chosen for their proximity to the typical case.

Data was collected for 120 unique system conditions; the system conditions that were varied were rotational speed, bias current, and dynamic load. Speed was varied from 2000 to 9000 RPM via the motor controller. Bias currents were changed using the AMB controller; bias currents of 1.3, 1.5, and 1.7 Amps were applied. The different dynamic load scenarios were achieved by inserting various unbalance masses into the disk. In addition to the 0g added unbalance mass case, unbalance masses of 0.4g, 0.6g, 0.8g,

and 1.0g were added to the disk to vary the dynamic loading. These conditions and the associated dynamic forces determined by force transducers are summarized in Table 6.1.

**Table 6.1: Summary of rotor test conditions and resulting dynamic load (lb)**

Load Scenario	Bias Current (Amps)	Speed (RPM)							
		2000	3000	4000	5000	6000	7000	8000	9000
<b>Case 1 0g added</b>	<b>1.3</b>	0.42	0.83	1.3	1.6	2.17	2.79	3.15	3.12
	<b>1.5</b>	0.43	0.79	1.26	1.63	2.3	2.98	3.32	3.23
	<b>1.7</b>	0.45	0.74	1.21	1.61	2.4	3.12	3.46	3.3
<b>Case 2 0.4g added</b>	<b>1.3</b>	0.46	0.97	1.56	1.96	2.73	3.53	4.12	4.32
	<b>1.5</b>	0.48	0.91	1.5	1.99	2.9	3.8	4.4	4.52
	<b>1.7</b>	0.49	0.87	1.44	1.97	3.02	3.99	4.61	4.66
<b>Case 3 0.6g added</b>	<b>1.3</b>	0.5	1.04	1.68	2.14	2.95	3.89	4.6	4.92
	<b>1.5</b>	0.49	0.98	1.63	2.18	3.15	4.22	4.94	5.18
	<b>1.7</b>	0.49	0.91	1.55	2.15	3.28	4.43	5.19	5.35
<b>Case 4 0.8g added</b>	<b>1.3</b>	0.54	1.12	1.82	2.37	3.26	4.27	5.14	5.6
	<b>1.5</b>	0.53	1.05	1.76	2.41	3.49	4.64	5.54	5.93
	<b>1.7</b>	0.52	0.98	1.67	2.38	3.64	4.9	5.84	6.16
<b>Case 5 1.0g added</b>	<b>1.3</b>	0.55	1.2	1.95	2.63	3.55	4.66	5.65	6.22
	<b>1.5</b>	0.53	1.12	1.89	2.58	3.8	5.11	6.14	6.66
	<b>1.7</b>	0.52	1.04	1.8	x	2.84	5.43	6.47	6.96

An initial set of data was used to provide input to determine the model parameters shown in Equation 6.1, the technique for determining the parameters is discussed below. The data that makes up the initial set is set in boldface in the table and consists of the 0g added load case (Case 1) operating with bias currents of 1.5 Amps across the full range of speeds (2000 –9000 RPM).

## 6.4 PARAMETER ESTIMATION

The parameters in Equation 6.1 were optimized using an augmented Equation 1.13 where the measured coil currents  $i_{upper}$  and  $i_{lower}$  were replaced by expressions for their respective effective currents based on Equation 6.1. The relevant equations are repeated here for convenience.

$$F = k_{th} \cos \theta \left[ \frac{i_{upper}^2}{(2(g_o - x \cos \theta) + b_{th})^2} - \frac{i_{lower}^2}{(2(g_o + x \cos \theta) + b_{th})^2} \right] \quad (1.13)$$

$$i_e = i_m - p_1 i_m - p_2 i_m \omega - p_3 i_m^2 \omega^2 \quad (6.1)$$

The expression for effective current incorporates three parameters,  $p_1$ ,  $p_2$ , and  $p_3$ , whose values were unknown at the outset. These parameters were determined using an initial data set consisting of constant load and bias current selections at all seven test speeds (0g added load; bias currents of 1.5 Amps; full range of speeds). Measured current ( $i_{m1}$ ,  $i_{m2}$ ) and displacement data ( $g_1$ ,  $g_2$ ) for the initial data set were used as inputs to the

augmented equation so that a force value could be calculated for each selected speed, assuming arbitrary parameter values. Each parameter was then assigned a range of possible values; forces corresponding to every combination of parameter values were calculated for each of the seven speeds in the initial data set. Each calculated force for a given speed was then compared to the force transducer data associated with that speed. The set of parameters  $p_1$ ,  $p_2$ , and  $p_3$  which caused the least percentage error over all seven test points of the initial data set were chosen as the parameters of record to be used in Equation 6.1 for the purpose of modeling the remaining data. The final parameter values are as follows:

$$\begin{aligned} p_1 &= 0.48 \\ p_2 &= -1.6e-5 \\ p_3 &= -3.1e-11 \end{aligned}$$

so that Equation 6.1 becomes:

$$i_e = i_m - (0.48)i_m + (1.6e-5)i_m\omega + (3.1e-11)i_m^2\omega^2 \quad (6.2)$$

A cursory examination of Equation 6.2 shows that this model predicts effective current to *increase* as rotor speed increases. This is counter to expected behavior since eddy currents and hysteresis, which represent a parasitic loss of current, at least initially increase as speed increases (until skin effects are expected to come into play). Equation 6.2 does not reflect expectations; likely due to a faulty proposed initial model (Equation 6.1) forcing overcompensation by the optimization routine to account for current magnitude effects. However, the technique does demonstrate that a variety of dynamic load scenarios can be accurately predicted using a single mathematical model as will be shown in the next section.

## **6.5 EXPERIMENTAL RESULTS**

If measured currents are used directly in the force model instead of effective currents, large errors occur. This is illustrated in Figure 6.1 for all three bias current cases (1.3A, 1.5A, 1.7A) associated with load Case 1 (0g added unbalance).

Figure 6.1 shows that unacceptably large errors occur between unmodified model data and transducer data.

The measured currents and displacements from the 1.5 Amp bias current data set shown in Figure 6.1 as bias Case 2 were used as inputs in the procedure described earlier to determine the parameters  $p_1$ ,  $p_2$ , and  $p_3$  in the effective current equation (Equation 6.1).

Once the parameters were optimized, the force model in Equation 1.13 utilizing the effective current expression in Equation 6.1 was used to determine predicted AMB forces in the remaining data sets (shown in Table 6.1).

An example data set consisting of transducer force data and predicted AMB forces for the load case when unbalance is 0.6g and for three bias current settings of 1.3, 1.5, and 1.7 Amps through a speed range of 2000 – 9000 RPM is presented in Figure 6.2.

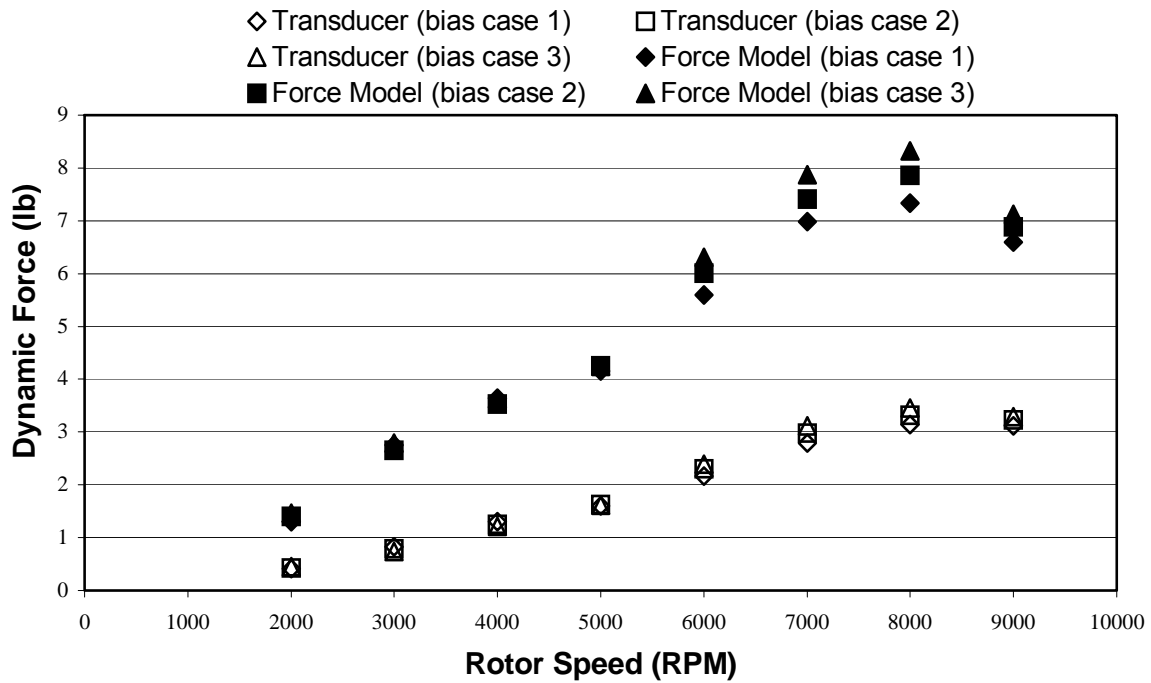


Figure 6.1: Transducer force and AMB force (from an unmodified model; based on total  $i_m$ ) for the 0g added unbalance data set

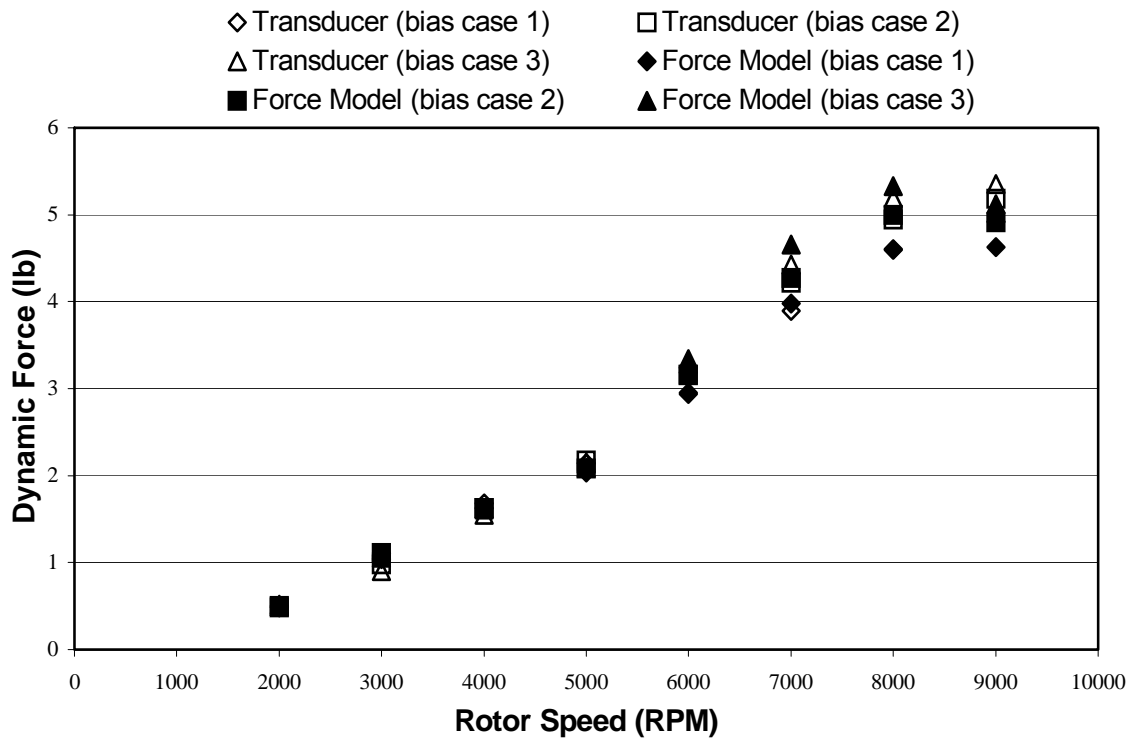
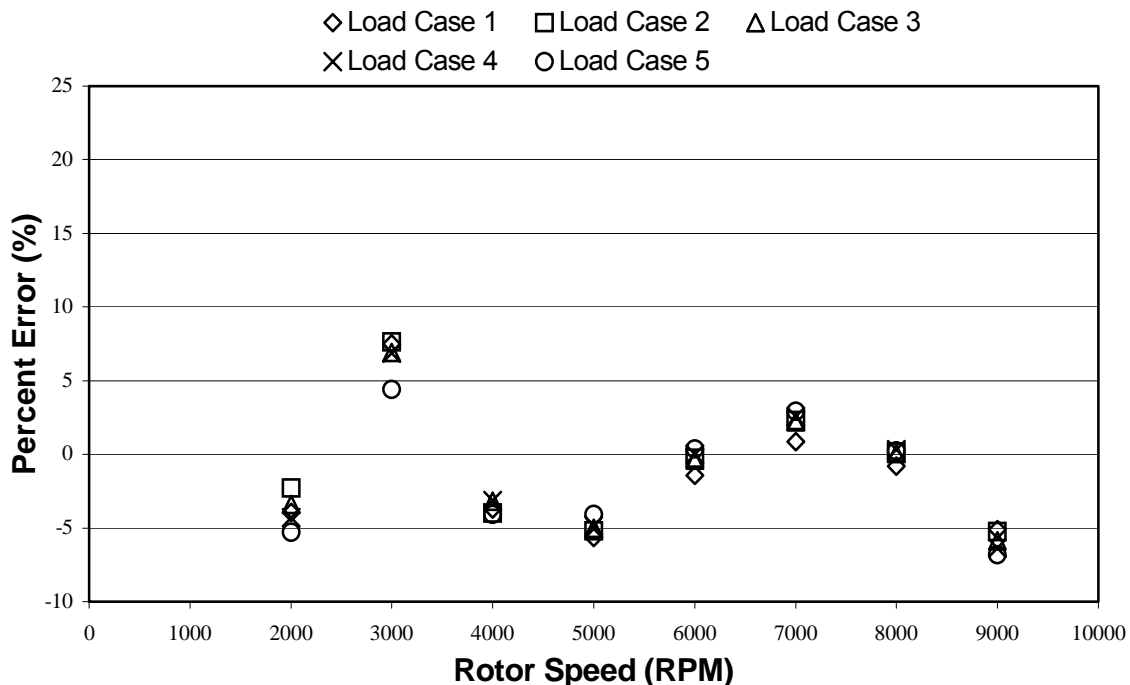


Figure 6.2: Comparison of transducer data and model data (based on  $i_e$ ) for all Bias settings of load Case 3 (0.6g added unbalance)

A fit with an average error of 4.1% and maximum error of 16.8% between the AMB predicted forces and measured transducer data is shown in Figure 6.2 for this load case. The maximum error, in terms of percentage of load, occurs at the 3000 RPM case. If the 3000 RPM speed cases are neglected, the average error is 2.8% with a maximum error of 5.9%. Figure 6.2 demonstrates that an effective current based AMB force model provides a significant improvement in accuracy as compared the force model that relies solely on measured currents.

In order to better judge the effective current model, the error percentages between the transducer readings and the forces determined by the model were calculated for all load cases throughout the speed range. Figure 6.3, Figure 6.4, and Figure 6.5 show the resulting error plots for bias currents of 1.3, 1.5, and 1.7 Amps, respectively. It should be noted that there is a system critical speed at approximately 3000 RPM that appears to be affecting the accuracy at the 3000 RPM cases for all test scenarios.

Errors for all load and operating speed cases for a bias current of 1.3 Amps are shown in Figure 6.3. Except for the 3000 RPM outliers, all of the AMB model force values are within  $\pm 6.8\%$  of the associated transducer values for bias currents of 1.3 Amps. The average error for this case is 3.5%. The worst-case error at 3000 RPM is 7.6%.



**Figure 6.3: Model error for bias Case 1 (1.3 Amps)**

The error trends for the bias current setting of 1.5 Amps for all load and speed cases are shown in Figure 6.4. Except for the 3000 RPM outliers, all of the AMB model force values are within  $\pm 6.8\%$  of the associated transducer values for bias currents of 1.5 Amps. The average error for this case is 2.3%. The worst-case error at 3000 RPM is 13.6%

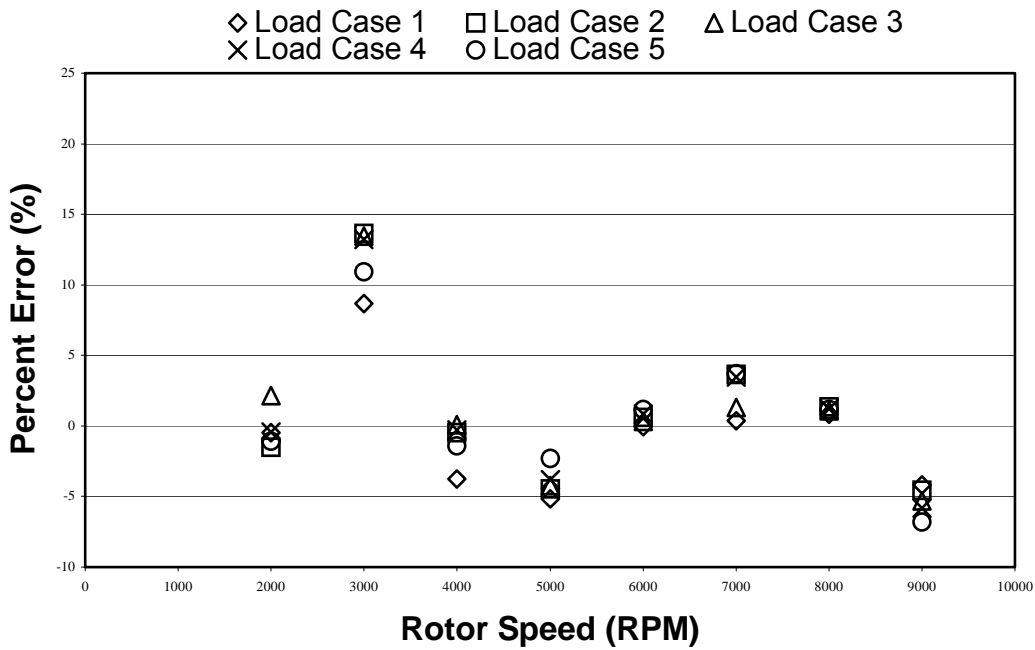


Figure 6.4: Model error for bias Case 2 (1.5 Amps)

The error trends for the bias current setting of 1.7 Amps for all load and speed cases are shown in Figure 6.5. Except for the 3000 RPM outliers, all of the AMB model force values are within  $\pm 6.4\%$  of the associated transducer values for the for bias current of 1.7 Amps. The average error for this case is 3%. The worst-case error at 3000 RPM is 21%.

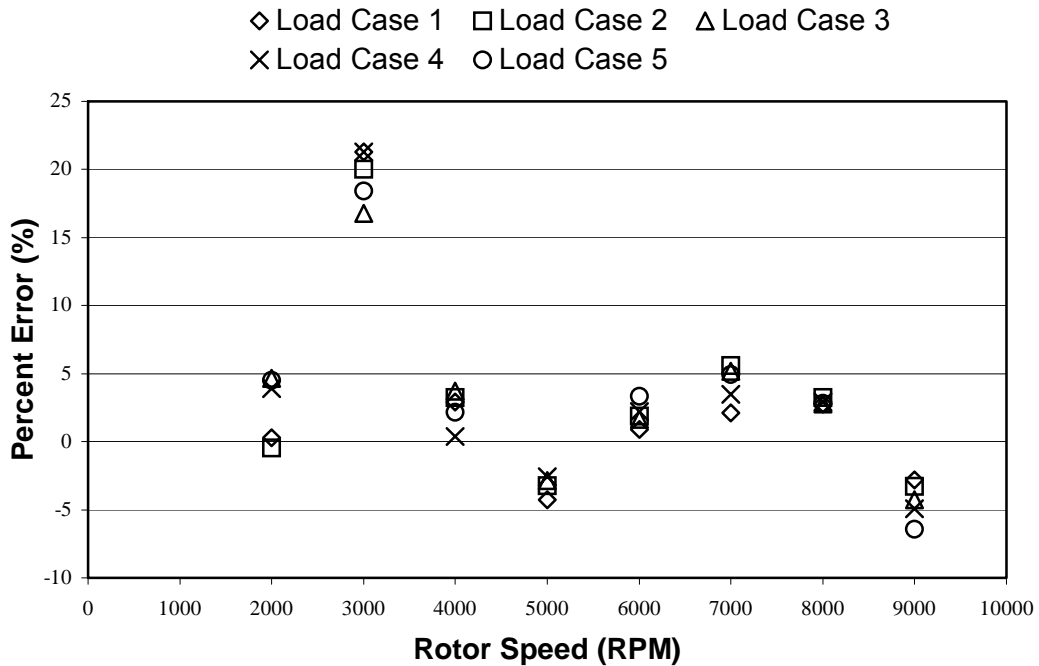


Figure 6.5: Model error for bias Case 3 (1.7 Amps)

As mentioned earlier, it is suspected that a system resonance, possibly related to the way in which the AMB bases are mounted to the transducers, was in play near the 3000 RPM speed. Bias current changes may have contributed to changes in the system stiffness and damping parameters. Such changes could have been enough to cause significant variation in the system response at 3000 RPM, making modeling difficult in that region.

In broad strokes, if all of the data is considered, the average error is 4% and the worst-case error is 21%. If the data associated with 3000 RPM is neglected the average error is reduced to 2.8% and the worst-case error becomes 6.8%. These errors are in line with errors reported by other researchers.

## **6.6 KEY CONCLUSIONS FROM PILOT STUDY**

It has been successfully demonstrated that a mathematical model based solely on current and position data can successfully predict dynamic forces in a magnetic bearing. Although the chosen model does not represent the underlying physical processes, it remains significant that it can predict dynamic forces for multiple speeds and loads and the results shown here lay the foundation for *a priori* determination of an accurate current-based force measurement technique. The model developed here has been shown to fit a range of data that includes variations in speed, bias current, and dynamic load, the errors observed are in line with errors reported by other researchers.

The pilot study also underscores some challenges associated with developing an appropriate test setup. Lessons taken from the pilot study include the need for an inertial base for the system and additional force transducers to better support the bearing. Knowledge of the systems response to excitation in the frequency band associated with the applied shaft rotation is also desirable.

# Chapter 7 Force Measurement Applied to a Rotating System

## 7.1 INTRODUCTION

This chapter is primarily concerned with the collection and analysis of dynamic AMB system data from five different AMBs. The purpose of the data collection was to compare measured bearing forces to bearing forces that were calculated based on different models. The bearings were mounted onto force transducers to facilitate the direct measurement of bearing force. For all five AMBs, the control signal breakout box was used to record coil currents from the upper and lower actuators of each axis, as well as rotor position along each axis. The AMB control signal data was used in two different AMB force models to calculate dynamic force. Force transducer data that was collected during each test was used to audit the calculated values of dynamic force. Figure 7.1 shows a typical AMB system on its test platform.

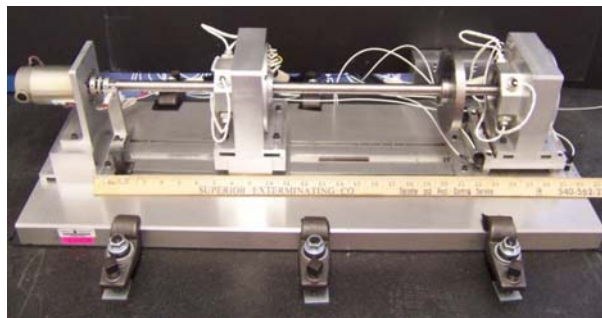


**Figure 7.1: Typical AMB system mounted to test platform**

The amount of dynamic force applied to the bearings was varied by changing the rotational speed of the rotor and the applied unbalance; dynamic force amplitudes varied from 1N – 60N (~0.25 lb<sub>f</sub> - ~13.5 lb<sub>f</sub>). Rotational speeds ranged from 4000–10000 RPM, added unbalance ranged from 0 – 2.25 gram-inches. Data was collected while the rotor was maintained at a continuous speed. Additionally, three AMB bias current settings were used per rotor. The total amount of bias current variation ranged from 0.5 – 0.7

Amps in one set of tests to 1.2 – 2.0 Amps in another set, depending on AMB. The primary goal of the data collection was to provide a library of dynamic AMB system data for use in the development of AMB force models. The entire library consists of over 500 dynamic test points.

Our goal is to allow for accurate measurement of dynamic AMB forces based on coil current and rotor offset measurements. Initially, the aim of this work was to develop modifications to an existing AMB force model to account for dynamic effects associated with eddy currents and hysteresis in magnetic bearings. Tests were run and as expected, errors existed between measured and calculated forces but trends did not indicate that the errors were necessarily due to dynamic effects. It has been determined that the laboratory test rotors used in the study do not achieve high enough surface speeds to realize significant eddy current and hysteresis effects. However, the absence of significant dynamic effects in the tests has led to the development of techniques to characterize rotor position runout and its absolute importance when applying current-based force models to AMBs. Without first characterizing the effect of runout on force measurement, appropriate correction factors for eddy current and hysteresis effects cannot be developed. The effects of eddy currents and hysteresis on AMB force models is discussed further in Appendix A.

### 7.1.1 Force Models

Although dynamic effects are not considered in this chapter, two static force models were applied to the data and their results compared to the measured force provided by the force transducers. The first model is the basic magnetic circuit expression for calculating force in a magnetic bearing. The second model uses the same general force equation but with modifications to the parameters based on system identification techniques developed here.

#### BASIC MAGNETIC CIRCUIT MODEL

Magnetic circuit models are discussed in Chapters 1 and 2. The first model applied to the data is the basic unmodified magnetic circuit model for calculating force in a magnetic bearing using the information from the rotor displacement sensors to account for rotor displacement. Rotor displacement from a nominal location ( $g_o$ ) affects the value used for air gap length as shown in Equation 1.13. Direct application of rotor displacement sensor data represents the approach before the system characterization techniques developed here are applied.

The general form of the magnetic circuit force model is discussed at length in Chapter 1; the equation describing the model is Equation 1.13, repeated below:

$$F = k \cos \theta \left[ \frac{i_{upper}^2}{(2(g_o - x \cos \theta) + b)^2} - \frac{i_{lower}^2}{(2(g_o + x \cos \theta) + b)^2} \right] \quad (1.13)$$

where:

$$k = \mu_o AN^2$$

$\mu_o$  = magnetic permeability of air

$A$  = area of pole face

- $N$  = number of wire turns on actuator coil
- $\theta$  = angle between bearing axis and axis of an individual magnetic pole.
- $i_{upper}$  = coil current in upper actuator
- $i_{lower}$  = coil current lower actuator
- $g_o$  = nominal air gap
- $x$  = rotor displacement along bearing axis
- $b = L_i / \mu_r$  = equivalent air gap due to the flux path through the rotor and stator
- $L_i$  = approximation of flux path through rotor and stator
- $\mu_r$  = the relative permeability of the rotor and stator material (relative to  $\mu_o$ )

In the case of the basic magnetic circuit model, the rotor displacement term,  $x$ , is taken as the rotor displacement value reported by the controller.

### **CHARACTERIZED MAGNETIC CIRCUIT MODEL FROM SYSTEM IDENTIFICATION**

A model that better characterizes the system resulting in more accurate force measurement is possible based on the system identification techniques developed here. This approach characterizes air gap as a function of rotor location, in both a radial and an angular (rotor phase) sense. The characterization accounts for unmodeled effects by characterizing runout in the rotor position sensors as discussed in Chapter 4.

The characterized model is based on the system identification technique known as the Multi-Point Method (MPM). The MPM was initially developed to identify an effective value of static bearing load (Kasarda et al., 2000; Marshall et al. 2001). In Chapter 4, the MPM was applied to AMBs in order to establish the relationship between the rotor position origin as measured by the rotor offset sensors and the rotor position origin inferred by the system model. The rotor position origin inferred by the system model is known as the effective origin. The same technique used to determine the effective origin can also be used to identify a rotor position compensation that accounts for runout.

An AMB controller monitors the signals from the rotor position offset probes. The controller reacts to changes in these signals by applying control current as required to move the rotor to the location for which the position probe signals indicate zero offset. Sensor runout refers to changes in position probe signals that are not related to real changes in the position of the rotor relative to the stator. Changes in the position sensor signal may be due to mechanical runout of the sensor target surface, or electrical runout caused by sub-surface material irregularities in the sensor target (Setiawan et al., 2001). Sensor runout is typically a function of rotation angle and is noticeable at low rotational speeds. The AMB controller reacts to sensor runout by applying control currents as necessary to move the rotor to the location for which the position probe signals indicate zero offset. The controller's reaction has the undesirable effect of creating a rotor orbit as the controller continuously reacts to phantom rotor motion. Two general approaches have been applied to the issue of runout in AMBs; reduction of the runout signal and controller compensation of the runout signal. The first approach, which calls for the reduction of signal runout, requires some combination of improved sensors and sensor targets. The improvements are generally achieved by upgrading the sensor technology or applying special manufacturing techniques. The controller compensation approach is less invasive. Rather than eliminate the runout signal, the runout signal is identified so that it can be compensated. Controller based approaches require additional computing

power to run control algorithms not typically associated with an AMB. Additional discussion of sensor runout is found in Chapter 1.

Another form of runout results from non-collocation between the rotor position sensors and the stator. Typically, the rotor position sensors are axially offset from the stator. In the case of a bowed rotating shaft, if the rotor position stays constant at the location of the position sensors, non-collocation will lead to runout of the portion of the rotor that is aligned with the stator.

In Chapter 4, the MPM was applied at twelve equally spaced rotation angles in order to determine a lookup table of rotation angle dependent values of the effective origin. In the general case, these values could be input to a controller so that runout is compensated. In this research, the runout identified by the MPM was used only in the post-processing of sensor position data.

In Chapter 5, the idea of an effective origin that differs from the system origin is expanded to consider an effective coordinate system that differs from the system coordinates. System coordinates are based on the rotor position reported to the system controller by the rotor offset sensors. The geometric center of the backup bearing and the axes of the rotor offset sensors inherent to an AMB are used to define the system coordinates (i.e. controller set-point for the “center” of the bearing is determined by moving the rotor around in the “rattle space” and determining physical boundaries which are used to define the rotor set point. Effective coordinates are inferred by applying the MPM at several broadly positioned rotor locations throughout the stator volume. The effective rotor positions at these locations, calculated via the MPM, are used to determine an effective coordinate system.

In Chapter 5, the effective rotor position was used in the modeling of static force in a non-rotating system. The results of Chapter 5 show that the resulting model of magnetic force is significantly more accurate than a similar model that relies on system coordinates alone. Specifically, Chapter 5, shows that the technique produced static force measurements with 2% - 6% mean error, and an associated standard deviation of 2% - 7%. If the coordinate transform was not applied, the model produced static force measurements with 3% - 22% mean error, and an associated standard deviation of 10% - 31%. In this chapter, the characterized magnetic circuit model that was used in the modeling of static force in Chapter 5 is applied to the modeling of dynamic force in a rotating system.

The data described in this chapter forms a library of dynamic AMB system data from five different AMBs at a variety of speed, unbalance, and bias current conditions. Furthermore, force transducers mounted underneath the bearing offer a direct measure of dynamic bearing force. The library of data allows us to get quick feedback on the effectiveness of proposed force models.

## **7.2 TEST SETUP**

### ***7.2.1 Test Systems***

The experiments described here were carried out on five separate AMB systems that were based on two rotor platforms as described in detail in Chapter 3. One test setup was used on a test apparatus referred to as Platform 1. The first platform (Platform 1) is a typical high-speed laboratory rotor kit from Revolve Magnetic Bearings and has a 0.015 inch radial gap and 0.005 inch rotor lamination thickness.

Four test setups were tested on Platform 2, they consisted of a common stator with four different rotors. Each rotor gives the system a different combination of nominal air gap and lamination thickness. The second platform (Platform 2) is a custom built magnetic bearing test bed, also built by Revolve Magnetic Bearings. Platform 2 was designed with a common AMB stator and four interchangeable AMB rotors. Each rotor results in a unique combination of nominal air gap and lamination thickness in the AMB system. Platform 2 can be configured as 4 unique systems as follows:

1. 0.010 inch radial gap, 0.005 inch lamination (Arnon 5)
2. 0.030 inch radial gap, 0.005 inch lamination (Arnon 5)
3. 0.010 inch radial gap, 0.014 inch lamination (M19)
4. 0.030 inch radial gap, 0.014 inch lamination (M19)

One of the bearing housings of each of the two platforms was mounted onto force transducers (while the second bearing housing was shimmed appropriately for proper alignment). The force transducers are capable of measuring the dynamic component of bearing load; as such they provide a comparison to verify the accuracy of calculated values of dynamic load. Additional specifications for each test system are found in Chapter 3.

### ***7.2.2 Dynamic effects of Test Systems***

Care was taken to minimize the effect of the test setup structure on the force measurements. The AMB platforms were mounted to a massive (1500 lb<sub>f</sub>) granite base; a thin layer of rubber was placed between the test platform and the granite base to assure broad contact between them. Six clamps placed along the edges of the platform were used to secure the platform to the granite block as shown in Figure 7.1. The procedure provided the platform with solid foundation, however, there was some concern regarding the bearing housing mounting.

#### **BASE DYNAMICS**

The bearing housings were mounted on force transducers so that dynamic loads could be directly measured. Figure 7.1 shows the configuration. It would be preferable to mount the bearing housings directly to a large mass, such as the granite block that is underneath the base of the AMB platform. Introduction of additional structure between the platform base and the bearing housings, such as that required to accommodate the force transducers, can lead to additional system dynamics. A test of the bearing housing's dynamic response was performed in order to observe its dynamic response.

The test consisted of determining the transfer function between a vertical input force (provided by a modal hammer), to the forces measured by the force transducers. Figure 3.17 shows the magnitude and phase plots of the transfer function. It can be seen that the transducer response is quasi-static in the range of ~20 to ~200 Hz. The spikes that are visible at 60Hz and 180Hz are assumed to be due to noise in the AC power source. Since rotor speeds reached during dynamic testing range from 4000 – 10000 RPM (67 – 167 Hz), dynamic effects related to the system structure are neglected in the analysis.

## **7.3 TEST DATA**

For each test setup a balance disk was positioned on the rotor shaft between the support bearings; varying amounts of unbalance load could be applied adding small masses to the disk. The unbalance disks are pre-drilled and tapped along their perimeter to accept set screws, set screws of a variety of lengths and materials were inserted into the tapped holes as a means to add mass to the disk at specific phase locations.

Each system was run up to 10000 RPM prior to collection of AMB data. During such a run up, a Bentley Nevada ADRE system was used to monitor rotor displacements and associated orbits. The data was used to apply mass to the balance disk in an attempt to balance the system. The goal was to collect data from a system that was initially balanced and to add increasing amounts of unbalance.

A typical test of an AMB set up called for AMB data (coil current and rotor position), and force transducer data to be collected for specific settings of rotor speed, bias current, and rotor unbalance. Typically, rotor speeds ranged from 4000 RPM to 10000 RPM, and added unbalance ranged from 0 to 2.25 gram-inches. Bias currents were varied as much as possible while maintaining control of the system over the speed and unbalance ranges. In one extreme case bias currents ranged from only 0.5 – 0.7 Amps, in another extreme case bias currents ranged from 1.2 – 2.0 Amps. In general, less data was collected for the systems with small nominal air gaps because these systems were more difficult to control over a wide range of speeds, unbalances, and bias currents. At low speeds (below 4000 RPM), rotor position orbits exhibited significant irregularity. At the time of testing the source of the irregularity was unknown and initial rotor test speeds were set to 4000RPM. In retrospect, the irregularity was likely due to the controller reacting to runout.

The measured forces reported by the force transducers are shown in Sections 7.3.1 and 7.3.2. These load values will be compared to modeled values of load in later sections. They are shown here as a means to introduce the reader to the dynamic testing. The values shown in the plots below are dynamic force amplitudes, they are based on a curve fit of the sampled data to a sine function; the curve-fit process will be discussed in Section 7.4.

### ***7.3.1 Platform 1***

Only one setup was tested on Platform 1. The characteristics of the rotor associated with the setup are described in Table 7.1.

**Table 7.1: Characteristics of the setup associated with Platform 1**

System	Nominal Air Gap		Rotor Lamination Thickness		Rotor Material
	inches	$\mu\text{m}$	inches	$\mu\text{m}$	
1	0.015	366	0.005	127	Arnon 5

The test conditions applied to Platform 1 are described below.

### PLATFORM 1, SETUP 1

- unbalance mass of 0, 400, 600, 800, and 1000mg (0, 0.48, 0.72, 0.96, and 1.2gm-in.)
- bias currents of 1.3A, 1.5A, and 1.7A
- rotational speeds of 4000, 5000, 6000, 7000, 8000, 9000, and 10000 RPM

These conditions resulted in dynamic load amplitudes ranging from 4N to 35N ( $\sim 1\text{lb}_f$  to  $\sim 8\text{lb}_f$ ). The test conditions and the corresponding load as reported by the force transducers are summarized in Figure 7.2-Figure 7.6. Each figure is a graph of dynamic load amplitude (as measured by the force transducers) versus rotor speed. All of the data in a given figure is associated with one unbalance mass. Each figure contains three data sets, one for each of the three different bias current settings.

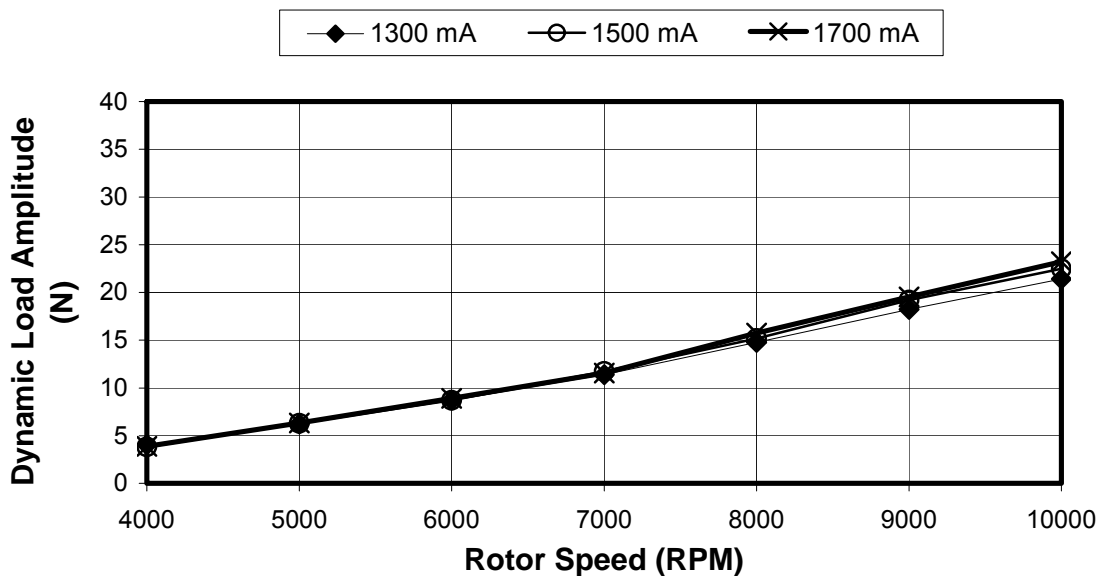


**Figure 7.2: Dynamic load amplitude versus rotor speed. Platform 1, System 1. 0 mg added unbalance. 1.3, 1.5, and 1.7 Amp bias currents**

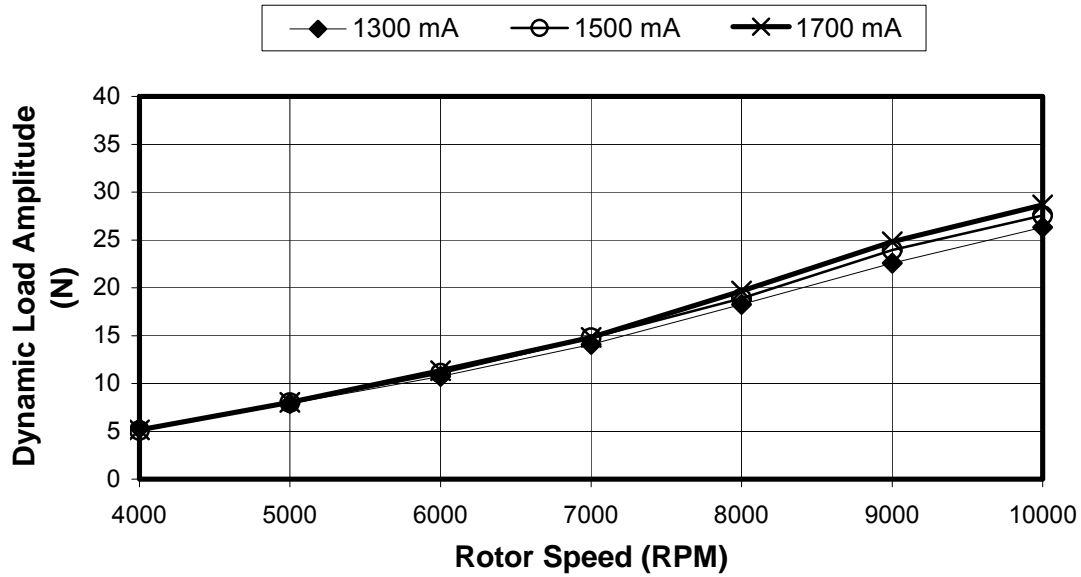


Figure 7.3: Dynamic load amplitude versus rotor speed. Platform 1, System 1. 400 mg (0.48 gm-in) added unbalance. 1.3, 1.5, and 1.7 Amp bias currents

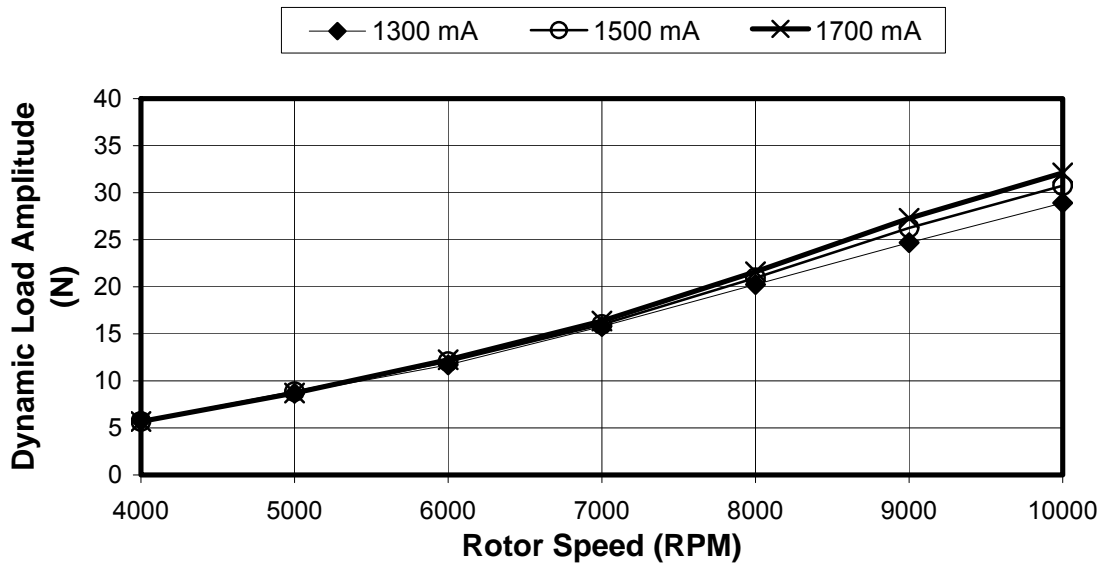


Figure 7.4: Dynamic load amplitude versus rotor speed. Platform 1, System 1. 600 mg (0.72 gm-in) added unbalance . 1.3, 1.5, and 1.7 Amp bias currents

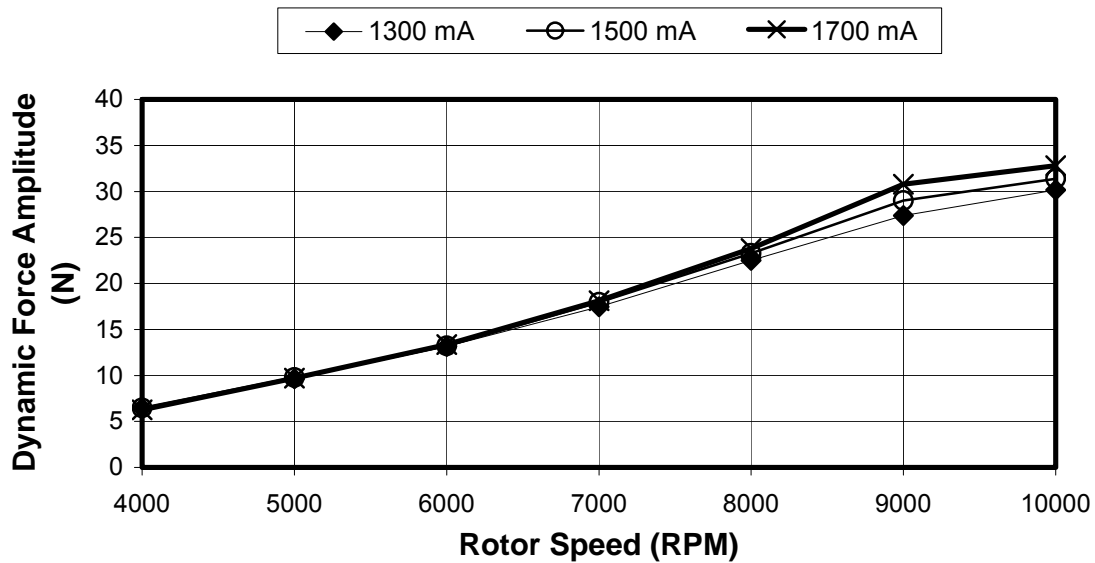


Figure 7.5: Dynamic load amplitude versus rotor speed. Platform 1, System 1. 800 mg (0.96 gm-in) added unbalance. 1.3, 1.5, and 1.7 Amp bias currents

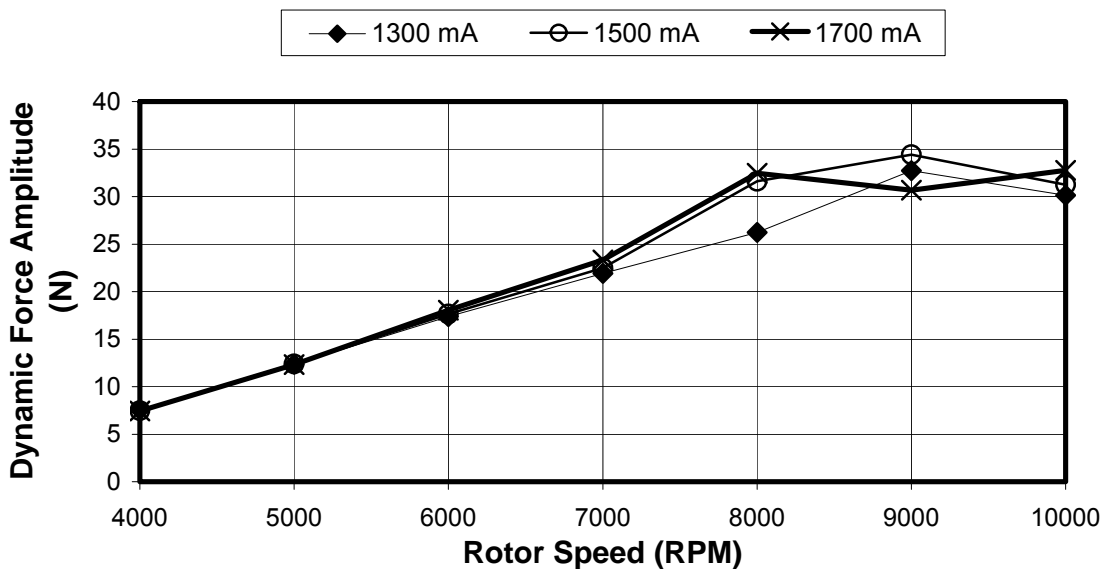


Figure 7.6: Dynamic load amplitude versus rotor speed. Platform 1, System 1. 1000 mg (1.2 gm-in) added unbalance. 1.3, 1.5, and 1.7 Amp bias currents

Figure 7.2-Figure 7.5 show the expected trends that dynamic force increases with speed and with added unbalance. Variation in dynamic force as a function of bias current for any given unbalance load and speed case is generally small (2-3N). More significant variation (~7N) is apparent in figure 7.7 for the 8000 RPM case. The greatest difference occurs between the extremes in bias current, 1.3 Amps and 1.7 Amps. The difference may be explained as a result of variation in system resonance brought on by changes in bearing stiffness and damping characteristics as a function of bias current.

### 7.3.2 Platform 2

Four test setups were tested on Platform 2, they consisted of a common stator with four different rotors. Each rotor gives the system a different combination of nominal air gap and lamination thickness. The characteristics of the four systems are described in Table 7.2.

**Table 7.2: Characteristics of the four systems associated with Platform 2**

System	Nominal Air Gap		Rotor Lamination Thickness		Rotor Material
	inches	$\mu\text{m}$	inches	$\mu\text{m}$	
1	0.010	244	0.005	127	Arnon 5
2	0.030	732	0.005	127	Arnon 5
3	0.010	244	0.014	356	M19
4	0.030	732	0.014	356	M19

The applied test conditions for the four varied somewhat. It was desired to test each system with a wide range of bias current and unbalance conditions. During testing it was found that each system had different limiting values of bias current and unbalance that could be applied while maintaining system stability. In general, the broadest variety of settings that could be applied to each system while maintaining stability was used. The settings for each system are detailed below.

#### PLATFORM 2, SETUP 1

- 0.010 inch nominal gap, 0.005 inch lamination (Arnon 5)
- unbalance mass of 0, 100, 200, 300mg (0, 0.23, 0.45, 0.68gm-in)
- bias currents of 0.5A, 0.6A, and 0.7A
- rotational speeds of 4000, 5000, 6000, 7000, 8000, 9000, and 10000 RPM

These conditions resulted in dynamic load amplitudes ranging from 3N to 60N ( $\sim 0.7\text{lb}_f$  to  $\sim 13.5\text{lb}_f$ ). The test conditions and the corresponding load as reported by the force transducers are summarized in Figure 7.7-Figure 7.10. Each figure is a graph of dynamic load amplitude (as measured by the force transducers) versus rotor speed. All of the data in a given figure is associated with one unbalance mass. Each figure contains three data sets, one for each of the three different bias current settings.

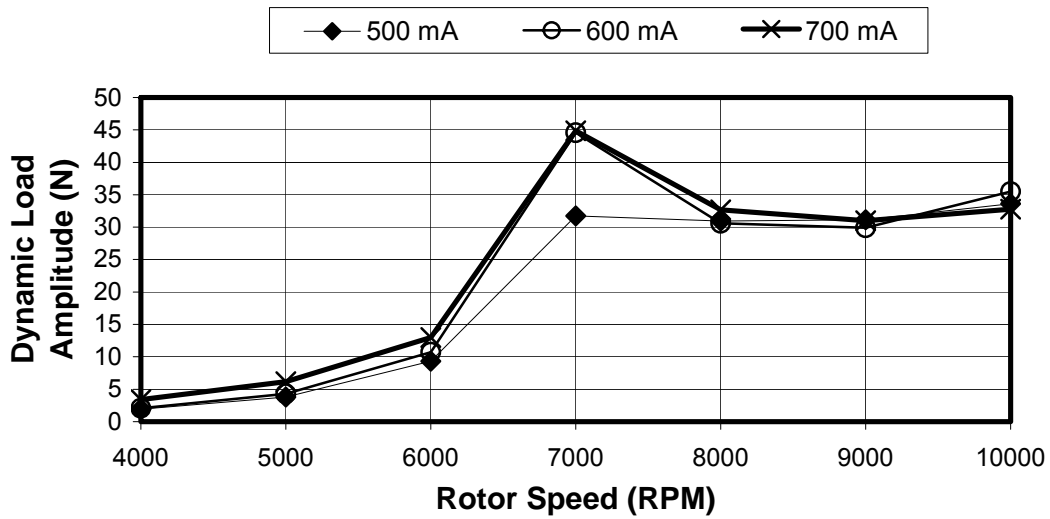


Figure 7.7: Dynamic load amplitude versus rotor speed. Platform 2, System 1. 0 mg added unbalance. 0.5, 0.6, and 0.7 Amp bias currents

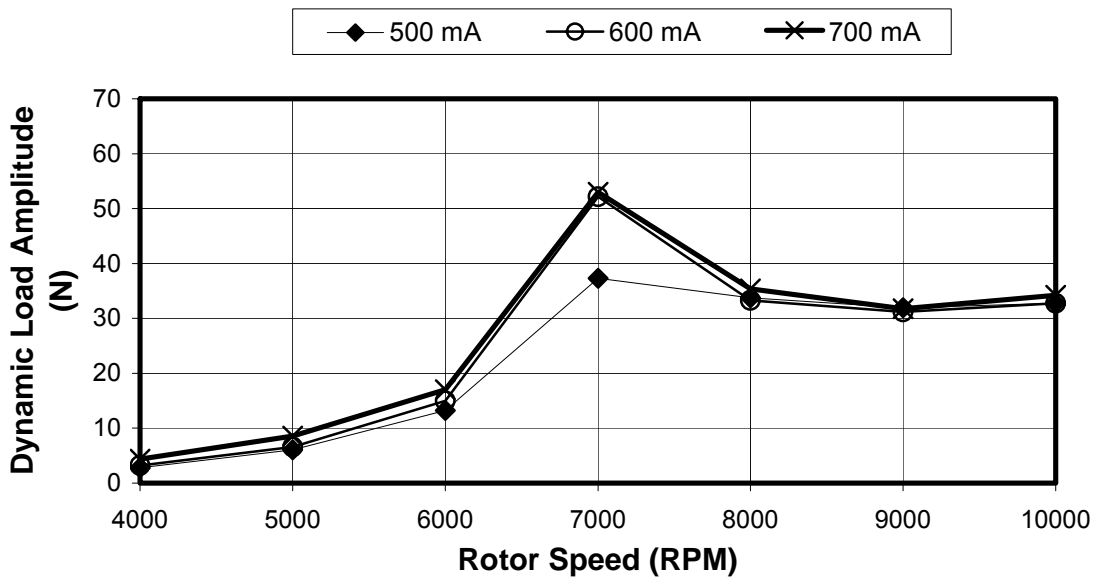
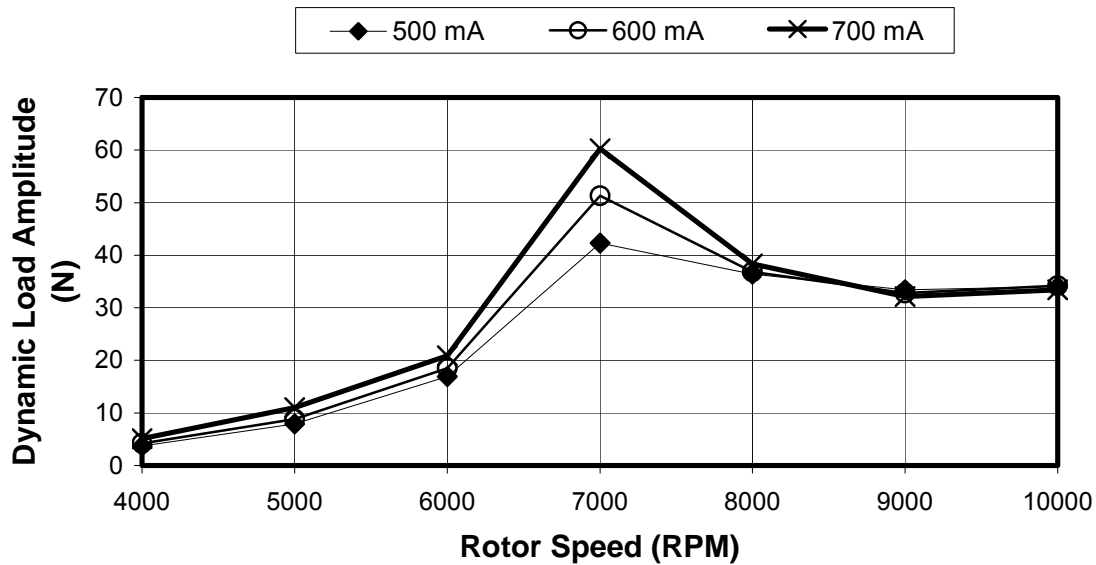
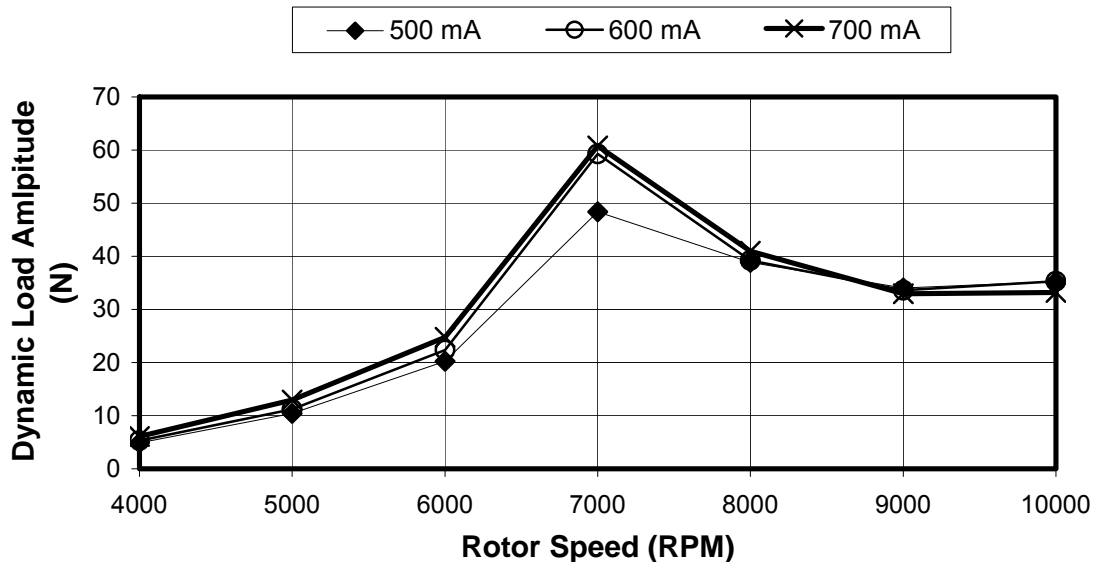


Figure 7.8: Dynamic load amplitude versus rotor speed. Platform 2, Setup 1. 100 mg (0.23 gm-in) added unbalance. 0.5, 0.6, and 0.7 Amp bias currents



**Figure 7.9: Dynamic load amplitude versus rotor speed. Platform 2, Setup 1. 200 mg (0.45 gm-in) added unbalance. 0.5, 0.6, and 0.7 Amp bias currents**



**Figure 7.10: Dynamic load amplitude versus rotor speed. Platform 2, Setup 1. 300 mg (0.68 gm-in) added unbalance. 0.5, 0.6, and 0.7 Amp bias currents**

All of Figure 7.7-Figure 7.10 show that the dynamic force amplitude for each unbalance load case has a distinct peak near 7000 RPM due to a system critical speed near 7000 RPM. Significant variation in dynamic force as a function of bias current is also seen at 7000 RPM. In Figure 7.9, for instance, the dynamic force associated with the lowest and highest bias currents varies by ~20N. The difference may be a result of variation in system critical speed brought on by changes in bearing stiffness and damping characteristics as a function of bias current. A change in bearing stiffness and damping characteristics would have two effects; the system with the smaller damping ratio (likely

the higher bias current case) would experience its critical speed at a higher RPM, and it will have a greater amplification factor.

Remember that although lines are drawn through the points on the graph to aid in distinguishing between data sets, due to the sampling interval the lines do not fully represent the shape of the amplitude plot as a function of speed. All cases are subject to frequency sampling; we chose to observe the system at 1000 RPM intervals, if the critical speed of a particular case occurs between these intervals we will record less than peak force. On the other hand, a different bias current case may achieve its critical speed right at one of the test speeds. Comparison of points from both example cases could lead to misinterpretation of the data.

### PLATFORM 2, SETUP 2

- 0.030 inch nominal gap, 0.005 inch lamination (Arnon 5)
- unbalance mass of 0, 200, 400, 600, 800, and 1000mg (0, 0.45, 0.9, 1.35, 1.8, and 2.25gm-in)
- bias currents of 1.2A, 1.6A, and 2.0A
- rotational speeds of 4000, 5000, 6000, 7000, 8000, 9000, and 10000 RPM

The test conditions resulted in dynamic loads amplitudes ranging from 4N to 32N (~1lb<sub>f</sub> to ~7lb<sub>f</sub>). The test conditions and the corresponding load as reported by the force transducers are summarized in Figure 7.11-Figure 7.16. Each figure is a graph of dynamic load amplitude (as measured by the force transducers) versus rotor speed. All of the data in a given figure is associated with one unbalance mass. Each figure contains three data sets, one for each of the three different bias current settings.

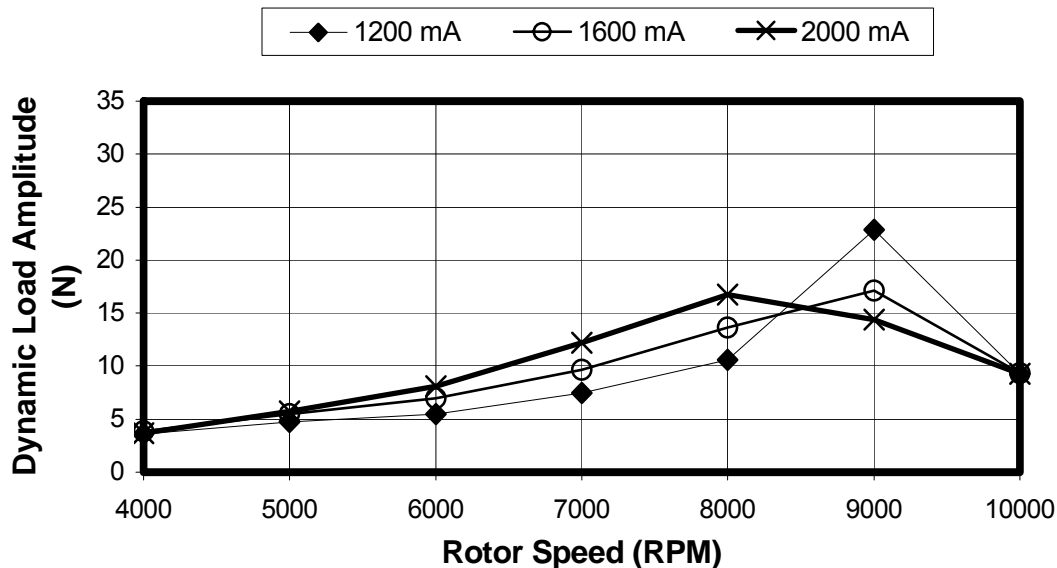


Figure 7.11: Dynamic load amplitude versus rotor speed. Platform 2, Setup 2. 0 mg added unbalance. 1.2, 1.6, and 2.0 Amp bias currents

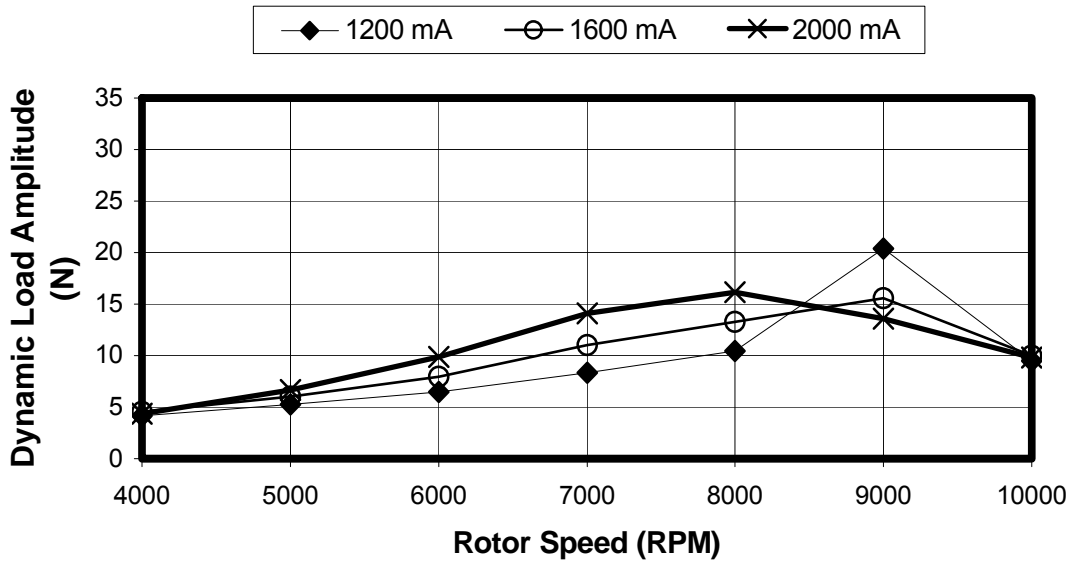


Figure 7.12: Dynamic load amplitude versus rotor speed. Platform 2, Setup 2. 200 mg (0.45 gm-in) added unbalance. 1.2, 1.6, and 2.0 Amp bias currents

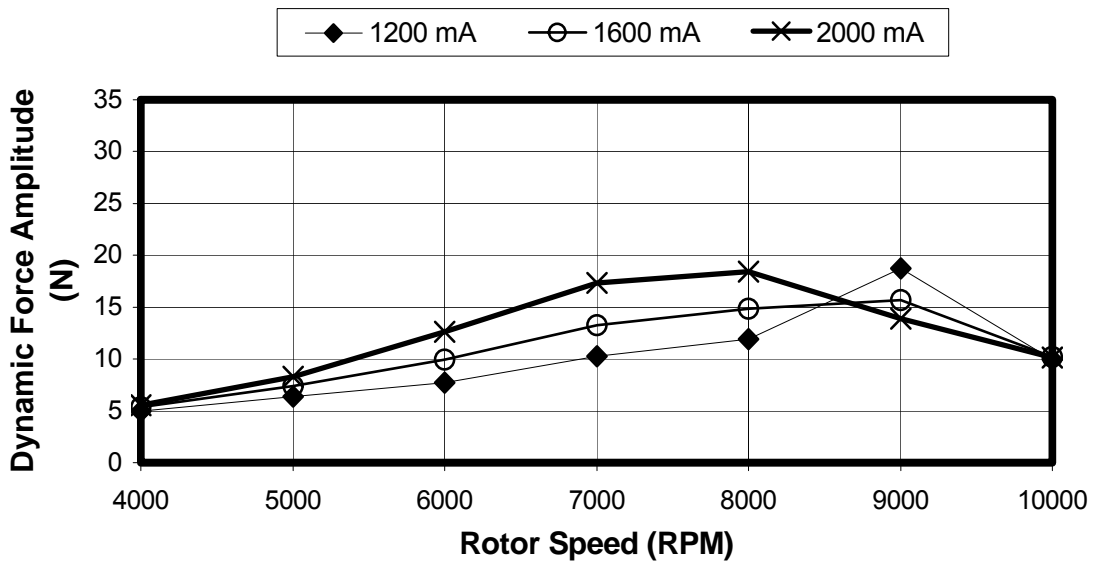


Figure 7.13: Dynamic load amplitude versus rotor speed. Platform 2, Setup 2. 400 mg (0.9 gm-in) added unbalance. 1.2, 1.6, and 2.0 Amp bias currents

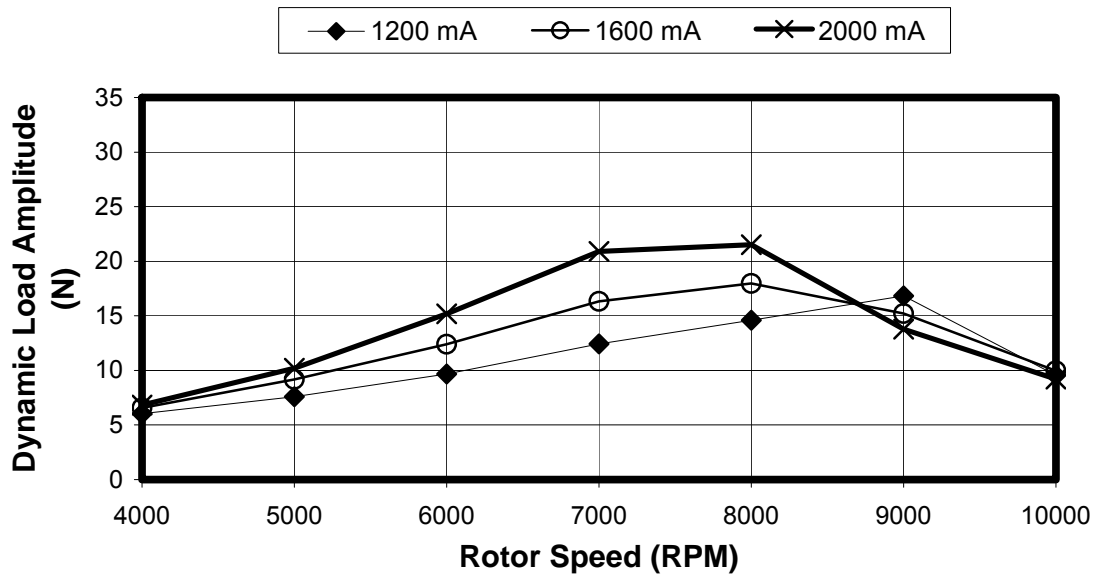


Figure 7.14: Dynamic load amplitude versus rotor speed. Platform 2, Setup 2. 600 mg (1.35 gm-in) added unbalance. 1.2, 1.6, and 2.0 Amp bias currents

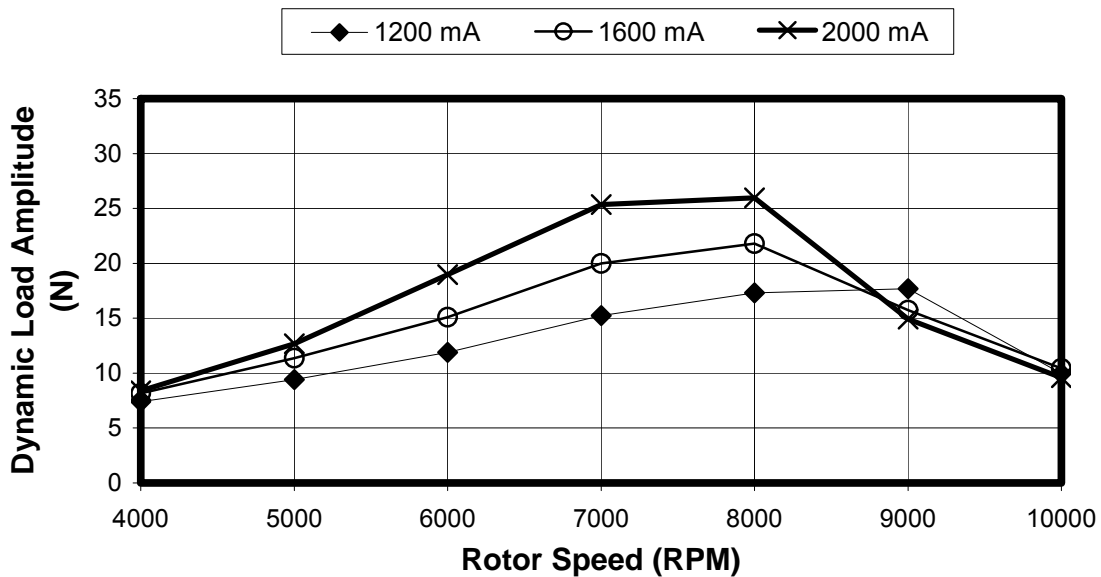
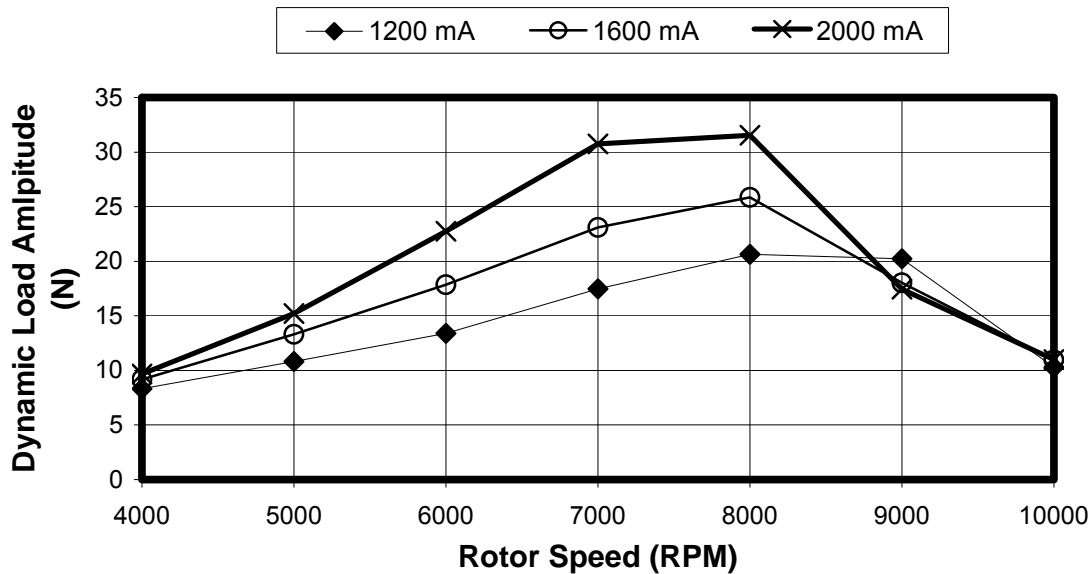


Figure 7.15: Dynamic load amplitude versus rotor speed. Platform 2, Setup 2. 800 mg (1.8 gm-in) added unbalance. 1.2, 1.6, and 2.0 Amp bias currents



**Figure 7.16: Dynamic load amplitude versus rotor speed. Platform 2, Setup 2 1000 mg (2.25m gm-in) added unbalance. 1.2, 1.6, and 2.0 Amp bias currents**

In general, Figure 7.11-Figure 7.16 show that the dynamic force amplitude for each unbalance load case has peak near the 7000-8000 RPM range. For the most part they show a less “peaky” response than Setup 1. In Figure 7.16 the dynamic force associated with the lowest and highest bias currents varies by ~12N. The difference may be a result of variation in system critical speed brought on by changes in bearing stiffness and damping characteristics as a function of bias current. A change in bearing stiffness and damping characteristics would have two effects; the system with the lower damping ratio (likely the higher bias current case) would experience its critical speed at a higher RPM, and it will have a greater amplification factor.

Remember that although lines are drawn through the points on the graph to aid in distinguishing between data sets, due to the sampling interval the lines do not fully represent the shape of the amplitude plot as a function of speed. All cases are subject to frequency sampling; we chose to observe the system at 1000 RPM intervals, if the critical speed of a particular case occurs between these intervals we will record less than peak force. On the other hand, a different bias current case may achieve its critical speed right at one of the test speeds. Comparison of points from both example cases could lead to misinterpretation of the data.

### PLATFORM 2, SETUP 3

- 0.010 inch nominal gap, 0.014 inch lamination (M19)
- unbalance mass of 0, 100, and 200mg (0, 0.23, 0.45 gm-in)
- bias currents of 0.5A, 0.65A, and 0.8A
- rotational speeds of 4000, 5000, 6000, 7000, 8000, 9000, and 10000 RPM

The test conditions resulted in dynamic loads amplitudes ranging from 1N to 44N (~0.25lb<sub>f</sub> to ~10lb<sub>f</sub>). The test conditions and the corresponding load as reported by the force transducers are summarized in Figure 7.17-Figure 7.19. Each figure is a graph of

dynamic load amplitude (as measured by the force transducers) versus rotor speed. All of the data in a given figure is associated with one unbalance mass. Each figure contains multiple data sets, one for each of the different bias current settings.

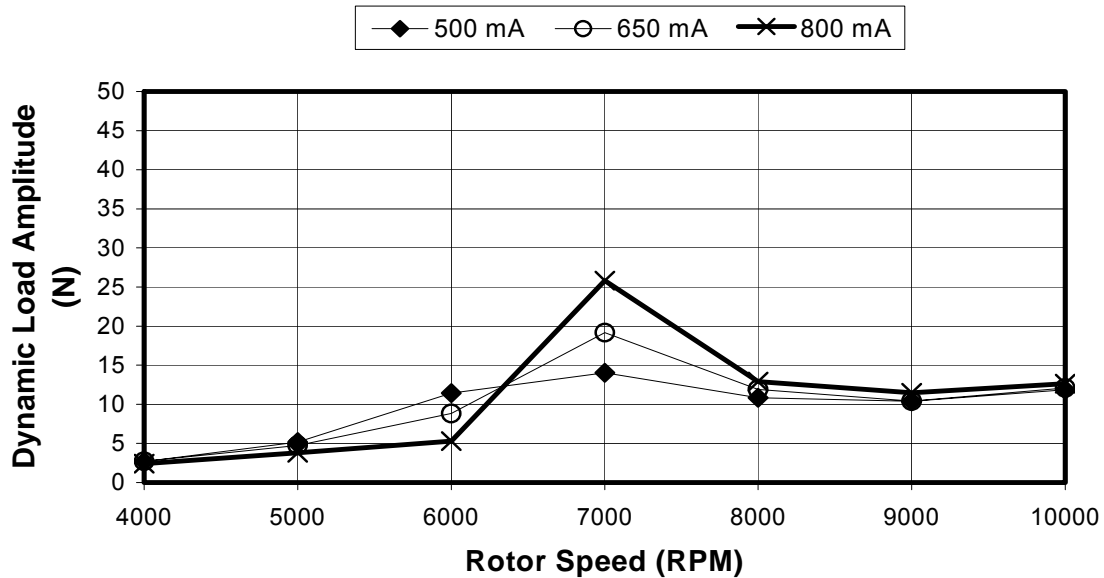


Figure 7.17: Dynamic load amplitude versus rotor speed. Platform 2, Setup 3. 0 mg added unbalance. 0.5, 0.65, and 0.8 Amp bias currents

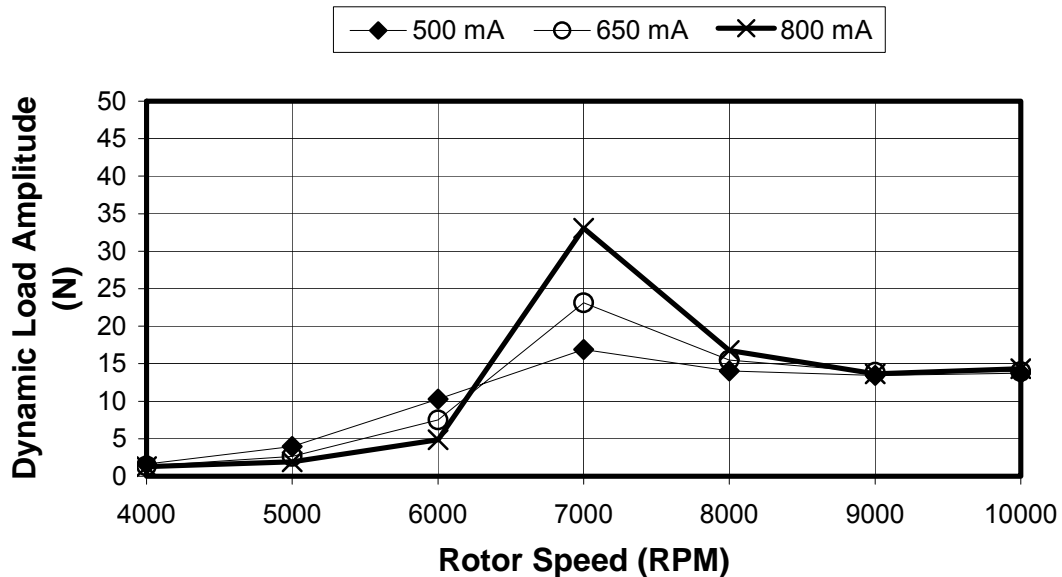
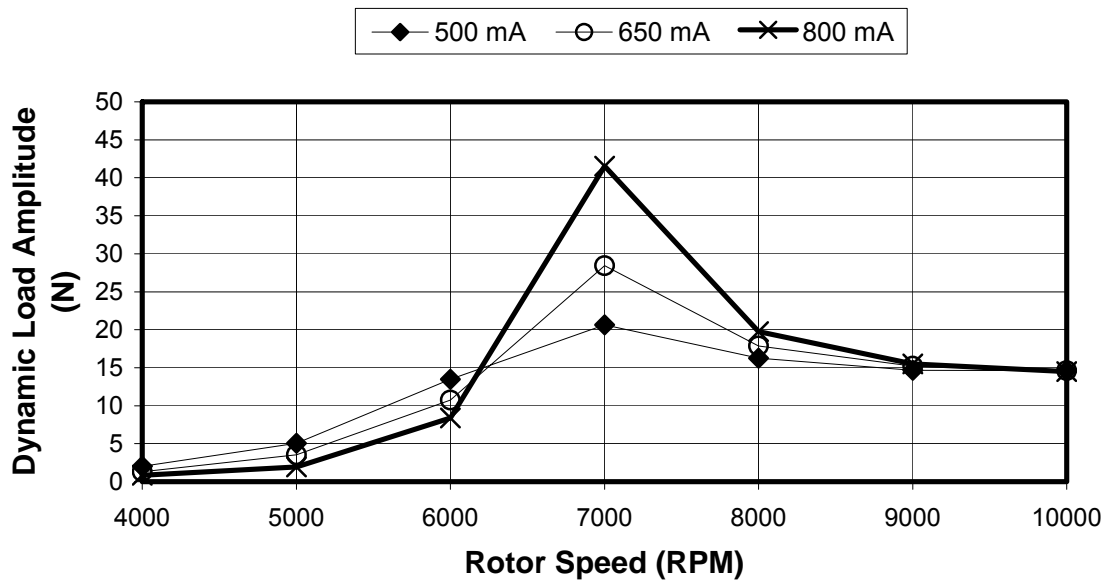


Figure 7.18: Dynamic Load amplitude versus rotor speed. Platform 2, Setup 3. 100 mg (0.23 gm-in) added unbalance. 0.5, 0.65, and 0.8 Amp bias currents



**Figure 7.19: Dynamic load amplitude versus rotor speed. Platform 2, Setup 3. 200 mg (0.45 gm-in) added unbalance. 0.5, 0.65, and 0.8 Amp bias currents**

All of Figure 7.17-Figure 7.19 show that the dynamic force amplitude for each unbalance load case has a distinct peak near 7000 RPM, due to a system critical speed near 7000 RPM. Significant variation in dynamic force as a function of bias current is also seen at 7000 RPM. In Figure 7.19, for instance, the dynamic force associated with the lowest and highest bias currents varies by ~20N. The difference may be a result of variation in system critical speed brought on by changes in bearing stiffness and damping characteristics as a function of bias current. A change in bearing stiffness and damping characteristics would have two effects; the system with the smaller damping ratio (likely the higher bias current case) would experience its critical speed at a higher RPM, and it will have a greater amplification factor.

Remember that although lines are drawn through the points on the graph to aid in distinguishing between data sets, due to the sampling interval the lines do not fully represent the shape of the amplitude plot as a function of speed. All cases are subject to frequency sampling; we chose to observe the system at 1000 RPM intervals, if the critical speed of a particular case occurs between these intervals we will record less than peak force. On the other hand, a different bias current case may achieve its critical speed right at one of the test speeds. Comparison of points from both example cases could lead to misinterpretation of the data.

#### PLATFORM 2, SETUP 4

- 0.030 inch nominal gap, 0.014 inch lamination (M19)
- unbalance mass of 0, 200, 300, 400, 500, 600, 700, and 800 mg (0, 0.45, 0.68, 0.9, 1.13, 1.35, 1.58, 1.8gm-in)
- bias currents of 1.4A, 1.7A, and 2.0A for unbalance mass up to 700 mg
- bias current of 1.5A, 1.6A, and 1.7A for 800 mg unbalance mass
- rotational speeds of 4000, 5000, 6000, 7000, 8000, 9000, and 10000 RPM

The test conditions resulted in dynamic loads amplitudes ranging from 6N to 48N (~1.5lb<sub>f</sub> to ~11lb<sub>f</sub>). The test conditions and the corresponding load as reported by the force transducers are summarized in Figure 7.20 through Figure 7.27. Each figure is a graph of dynamic load amplitude (as measured by the force transducers) versus rotor speed. All of the data in a given figure is associated with one unbalance mass. Each figure contains three data sets, one for each of the three different bias current settings.

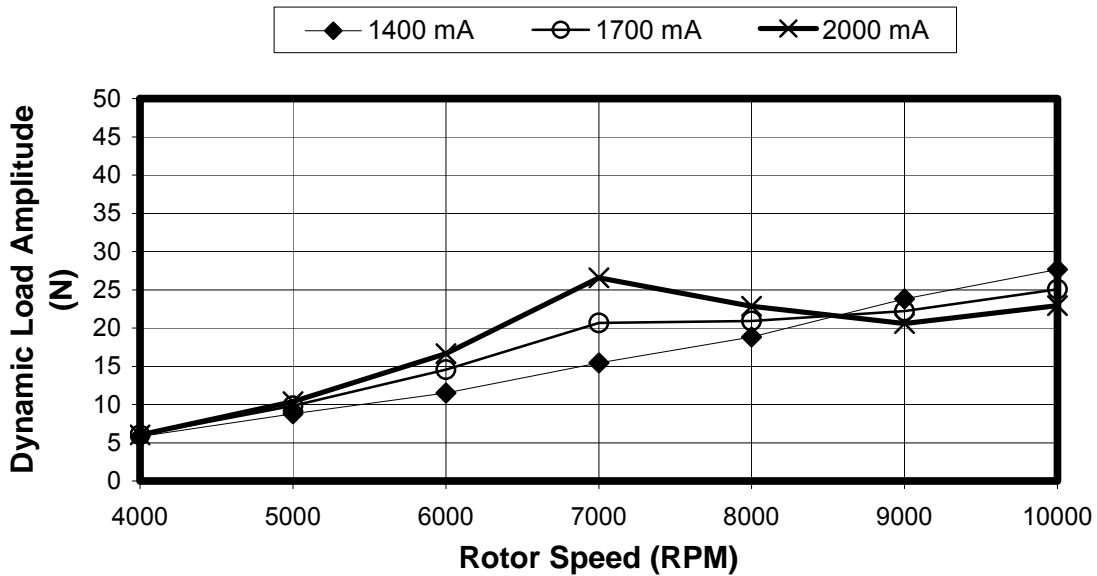


Figure 7.20: Dynamic load amplitude versus rotor speed. Platform 2, Setup 4. 0 mg added unbalance. 1.4, 1.7, and 2.0 Amp bias currents

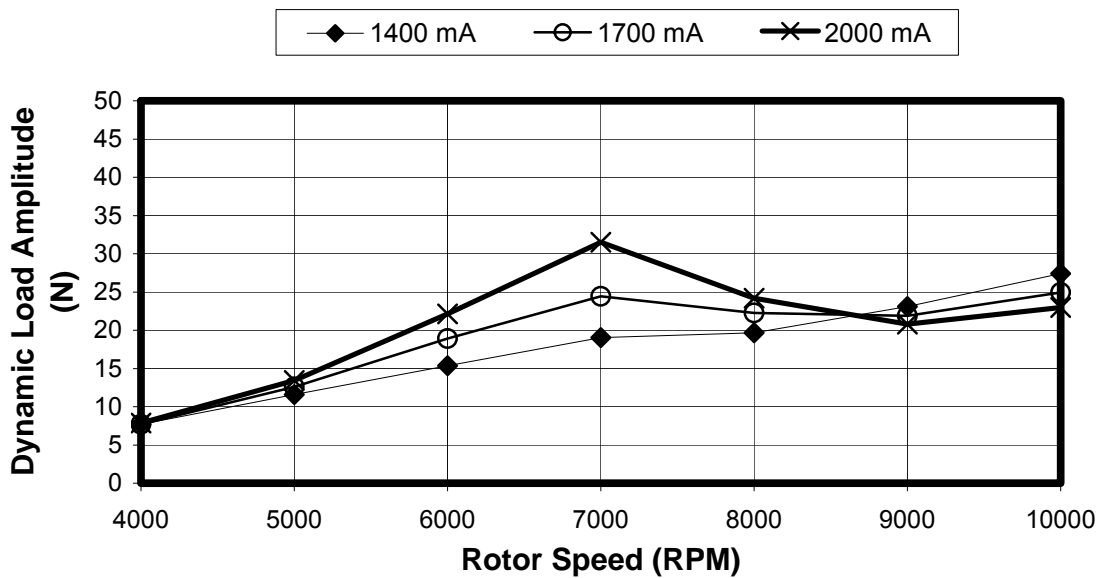


Figure 7.21: Dynamic load amplitude versus rotor speed. Platform 2, Setup 4. 200 mg (0.45 gm-in) added unbalance. 1.4, 1.7, and 2.0 Amp bias currents

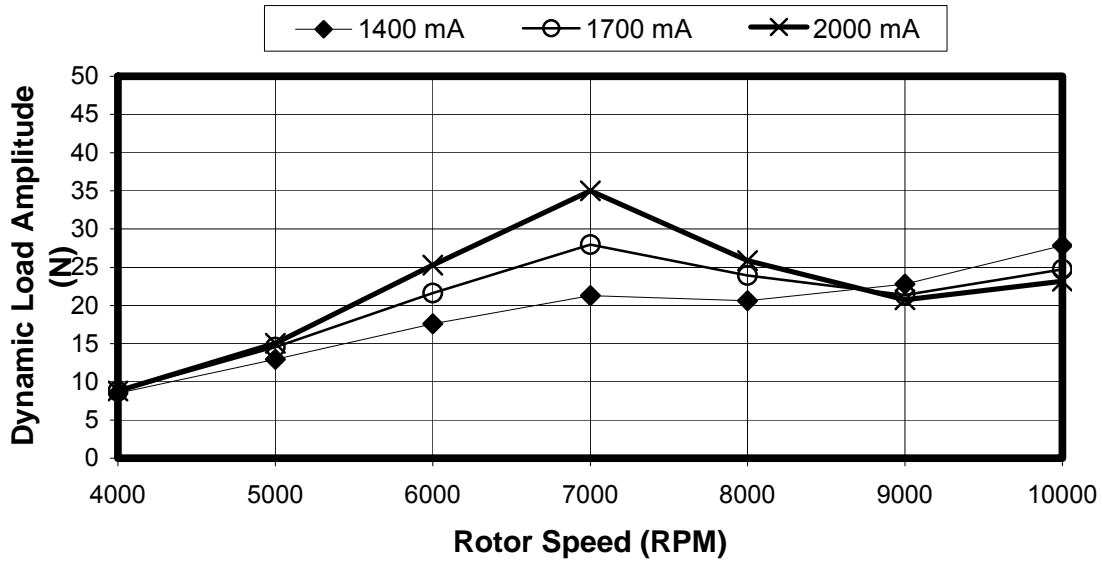


Figure 7.22: Dynamic load amplitude versus rotor speed. Platform 2, Setup 4. 300 mg (0.68 gm-in) added unbalance. 1.4, 1.7, and 2.0 Amp bias currents

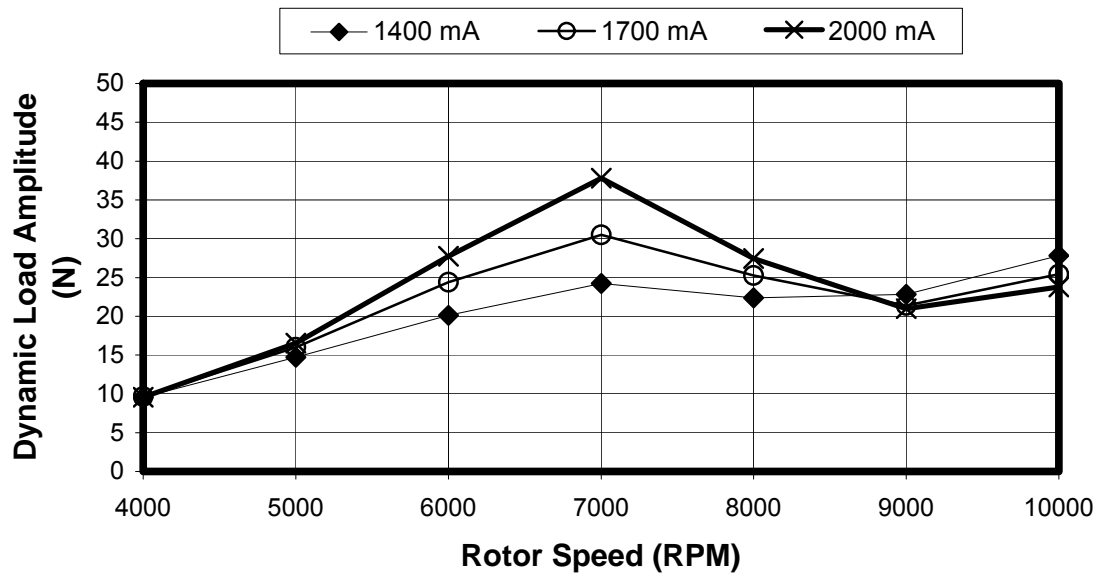


Figure 7.23: Dynamic load amplitude versus rotor speed. Platform 2, Setup 4. 400 mg (0.9 gm-in) added unbalance. 1.4, 1.7, and 2.0 Amp bias currents

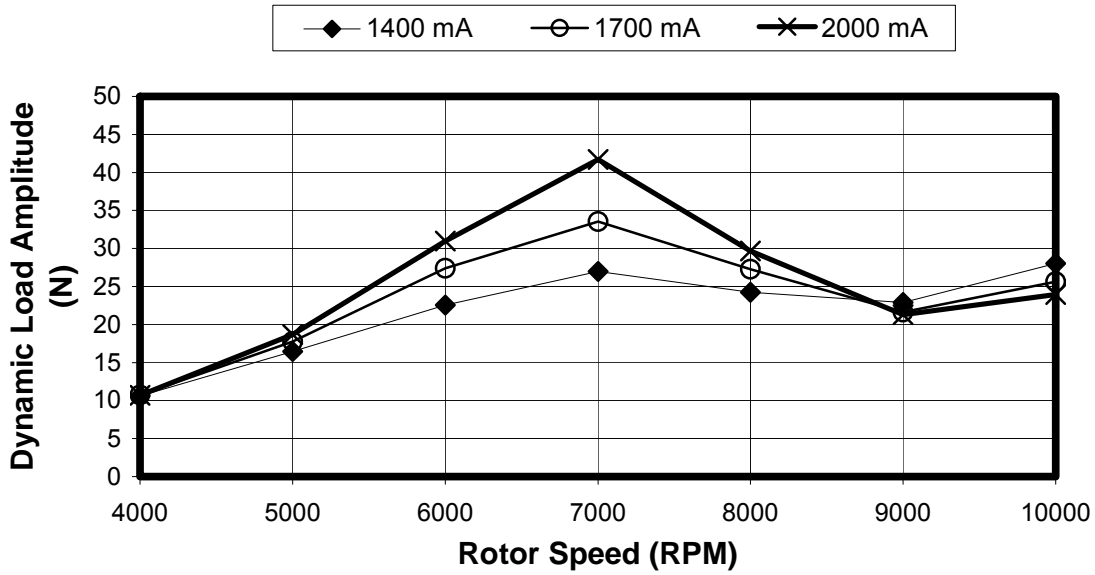


Figure 7.24: Dynamic load amplitude versus rotor speed. Platform 2, Setup 4. 500 mg (1.13 gm-in) added unbalance. 1.4, 1.7, and 2.0 Amp bias currents

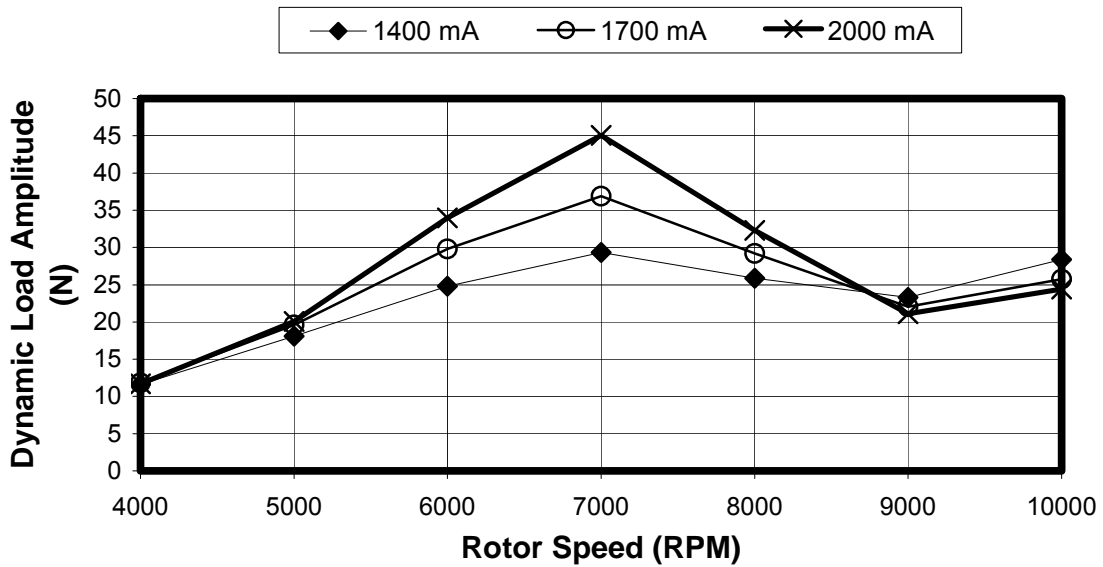
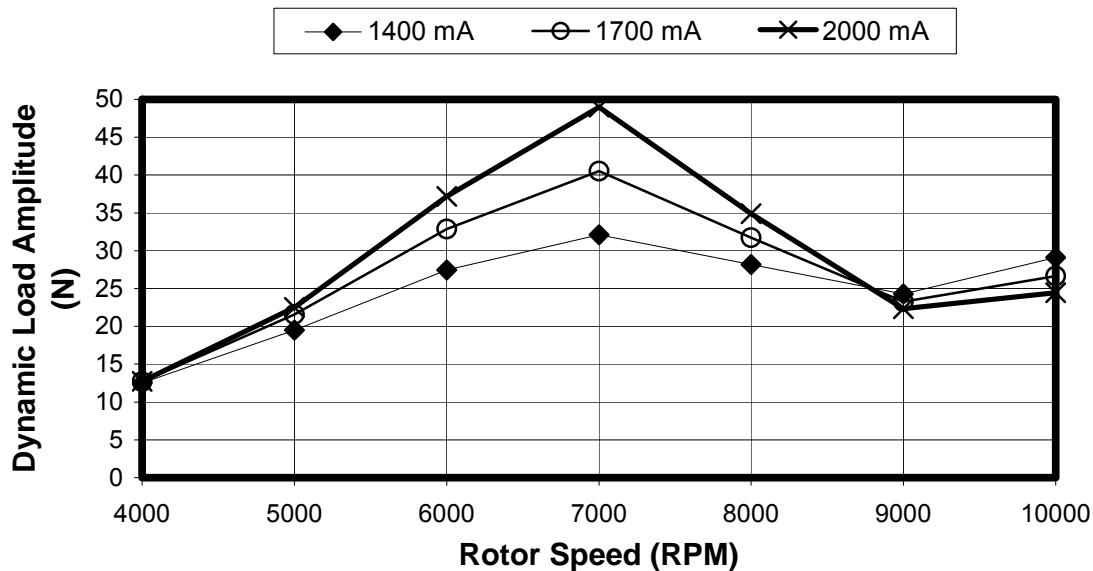
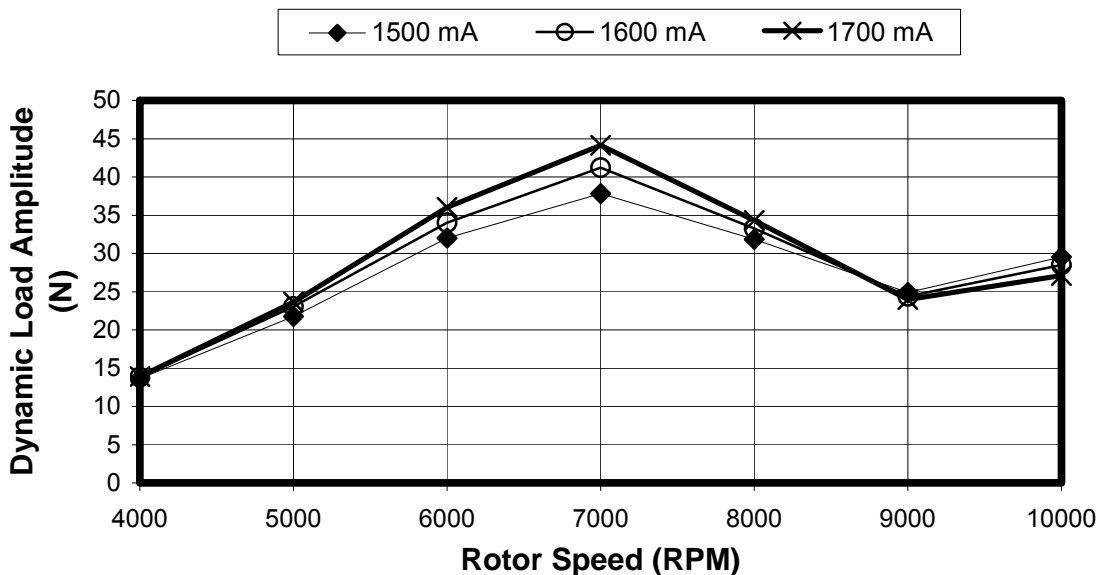


Figure 7.25: Dynamic load amplitude versus rotor speed. Platform 2, Setup 4. 600 mg (1.35 gm-in) added unbalance. 1.4, 1.7, and 2.0 Amp bias currents



**Figure 7.26: Dynamic load amplitude versus rotor speed. Platform 2, Setup 4. 700 mg (1.58 gm-in) added unbalance. 1.4, 1.7, and 2.0 Amp bias currents**



**Figure 7.27: Dynamic load amplitude versus rotor speed. Platform 2, Setup 4. 800 mg (1.8 gm-in) added unbalance. 1.5, 1.6, and 1.7 Amp bias currents**

In general, Figure 7.20-Figure 7.27 show that the dynamic force amplitude for each unbalance load case has a peak near 7000RPM range. For the most part they show a less “peaky” response than Setup 3. In Figure 7.26, the dynamic force associated with the lowest and highest bias currents varies by  $\sim 18N$ . The difference may be a result of variation in system critical speed brought on by changes in bearing stiffness and damping characteristics as a function of bias current. A change in bearing stiffness and damping characteristics would have two effects; the system with the lower damping ratio

(likely the higher bias current case) would experience its critical speed at a higher RPM, and it will have a greater amplification factor.

Remember that although lines are drawn through the points on the graph to aid in distinguishing between data sets, due to the sampling interval the lines do not fully represent the shape of the amplitude plot as a function of speed. All cases are subject to frequency sampling; we chose to observe the system at 1000 RPM intervals, if the critical speed of a particular case occurs between these intervals we will record less than peak force. On the other hand, a different bias current case may achieve its critical speed right at one of the test speeds. Comparison of points from both example cases could lead to misinterpretation of the data.

Considering all of the force amplitude data, the setups with larger nominal air gaps (setups 2 and 4) appear to be less “peaky” than their counterparts. The difference is due to the inverse relationship between AMB stiffness and nominal air gap. The systems with a larger air gap will have a lower stiffness leading to a larger damping ratio which gives the systems their characteristic behavior.

## **7.4 DATA COLLECTION**

AMB system data was collected during operation at the speed, bias current, and added unbalance scenarios for each of the five AMB systems as described above. The observed and recorded data consisted of a keyphasor signal indicating rotor rotation angular location, four coil currents (upper and lower actuator currents for both axes) and two rotor position signals (one for each axis) as reported by the AMB system controller and force transducer signals. Data was collected for one second at a sample rate of 20kHz/channel. Care was taken to allow the system to achieve a steady continuous speed prior to data acquisition for each speed point. Testing was conducted at 1000 RPM interval over a rotor speed range of 4000 RPM to 10000 RPM.

Two processes were performed on the incoming data streams prior to writing them to a file. A low-pass filter was applied to the incoming signals to eliminate higher frequency harmonics. After filtering conversion factors were applied to the incoming voltage signals. The conversion factors served to convert the voltage signals to their associated physical units.

## **7.5 DATA REDUCTION AND ANALYSIS**

After data collection, the files containing AMB system data as well as force transducer data were analyzed. Each file consists of 20000 samples of each of the variables that correspond to a single test. In order to apply a variety of models to the data with some agility, the data needed to be reduced as described below. The collected data was reduced in two ways;

- decimation to a lower frequency
- curve fit to a sine function

The decimation process was applied to raw coil current, rotor position, and transducer signals. The decimated coil current for a given actuator along with the decimated rotor position data for the corresponding axis were then applied to a magnetic circuit model to determine the magnetic flux density associated with the actuator. A flux density calculation was performed for each of the decimated data points. Knowledge of the flux density in an actuator allowed an actuator force to be calculated. A force calculation was performed for each of the decimated flux density points for a given actuator. Upper and lower actuator forces were summed to arrive at an axis force value. Next, the second data reduction was applied; decimated force data was curve fit to a sine function. The curve fit allows for many cycles of data to be described by three parameters; a DC offset, an amplitude, and a phase. The data was reduced to accommodate the analysis of large amounts of data in an efficient manner. Following the curve fit process a vertical force value was determined by summing the force amplitudes associated with both axes and multiplying by the cosine of  $45^\circ$ , the angle between each axis and the vertical direction.

The decimation and curve fitting was also applied to the transducer data.

The data reduction and analysis process will be discussed in general below. To aid understanding, an example that graphically shows the intermediate results of the process is interleaved with the general discussion. The example data is associated with the V-axis of the stator of Platform 2; Setup 3. The specific test case is 0 added unbalance, 0.5 Amps bias, at 6000 RPM.

### **7.5.1 Decimation**

The first reduction step was to decimate the 20kHz data to a lower frequency. The frequency of the decimated data was determined as a function of rotor speed. It was decided to set the decimation frequency such that at least 30 points were in each cycle.

Figure 7.28 and Figure 7.29 contain examples of a “raw” AMB current and rotor position data. The data in these figures is associated with the top actuator of the V-axis for a rotor speed of 6000 RPM. The figure shows 0.1 seconds worth of data. The figures also show the result of decimation, the large red circles show which of the raw data points were kept. Decimation was done at a rate that resulted in at least 30 points per cycle in the reduced data set.

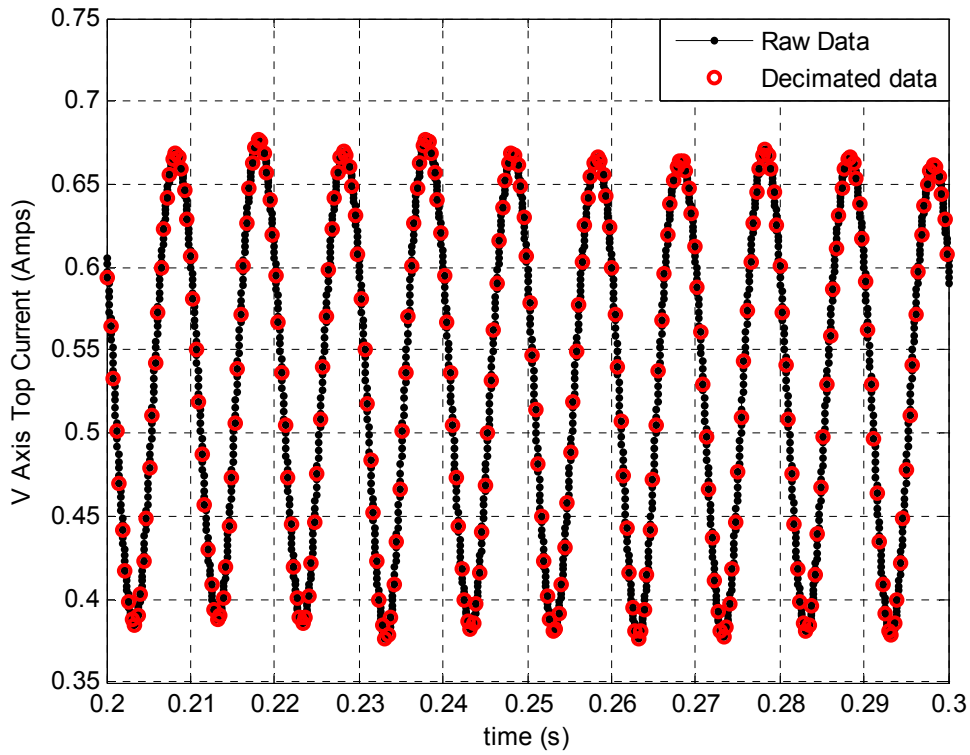


Figure 7.28: Raw and decimated current data

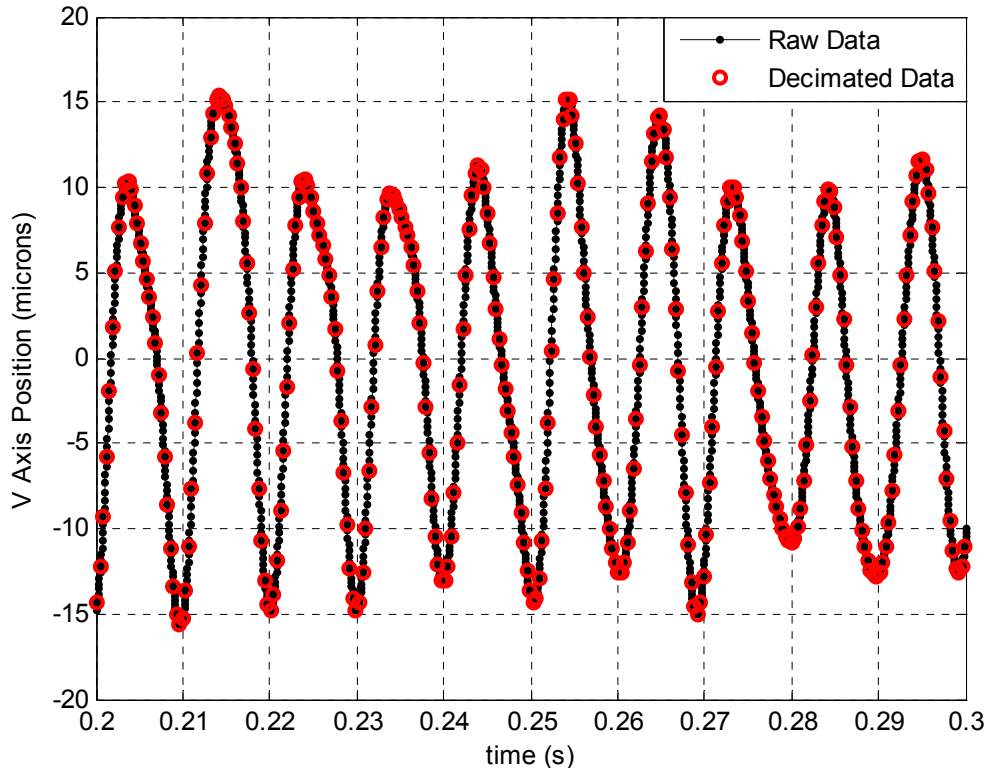


Figure 7.29: Raw and decimated position data

### 7.5.2 Magnetic Circuit Model

The reduced current and position data was used in conjunction with Equation 1.3, repeated here, to calculate a flux density at each of the points in the decimated data set as shown.

$$B = \frac{\mu_o NI}{2g} \quad (1.3)$$

In the equation,  $B$  is magnetic flux density,  $\mu_o$  is the magnetic permeability of air,  $N$  is the number of wire turns in a coil,  $I$  is the coil current, and  $g$  is the length of each air gap. Equation 1.3 is written generically; to make it a specific calculation of magnetic flux for a typical test bearing configuration, consider Figure 1.4, repeated below. The figure shows a typical force axis, consisting of an upper actuator and a lower actuator which act in opposition to each other. In the figure, the coil currents in the upper and lower actuators are noted as  $i_{upper}$  and  $i_{lower}$  respectively. Likewise, the air gaps associated with the upper and lower actuators are noted as  $g_{upper}$  and  $g_{lower}$ . Although the rotor position sensor is not shown in the figure, the axis of the rotor position sensor is shown; offset of the rotor along the sensor axis is noted as  $x$ . Note that the actuator poles are each at an angle  $\theta$  relative to the sensor axis. Additional details regarding the development of Equation 1.3 and its application to an AMB force axis as shown in Figure 1.4 are found in Chapter 1.

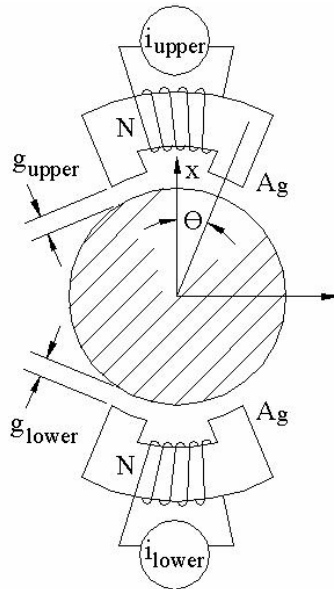


**Figure 1.4: An example of an AMB control axis**

The relationship between rotor position offset as reported by the position sensors ( $x$ ) and the bearing air gap ( $g_{upper}$  or  $g_{lower}$ ) is summarized in Chapter 1 and repeated here (Allaire et al., 1993):

$$g_{upper} = g_o - x \cos \theta \quad (1.7)$$

$$g_{lower} = g_o + x \cos \theta \quad (1.8)$$

Where  $g_{upper}$  and  $g_{lower}$  are the air gaps associated with the upper and lower actuators respectively,  $g_o$  is the nominal bearing clearance,  $x$  is the distance traveled along the bearing axis, and  $\theta$  is the angle between the bearing axis and the axis of an individual

magnetic pole. Considering these definitions and Figure 1.4, Equation 1.3 can be re-written for an upper actuator as:

$$B = \frac{\mu_o N i_{upper}}{2(g_o - x \cos \theta)} \quad (7.1)$$

The flux density calculation shown in Equation 7.1 requires a rotor offset value. The rotor offset value can be taken directly as the rotor position offset as reported by the controller (basic magnetic circuit model), or as some function of the reported position offset (characterized model). The difference in rotor position offset used in each of the models accounts for their differing values of calculated flux density and force.

Equation 7.1 was applied to each of the decimated current and rotor position values shown in Figure 7.28 and Figure 7.29. The calculation resulted in a flux density  $B$  that corresponds to each of the decimated values. The resulting values of flux density are shown in Figure 7.30. Specifically, the figure shows the flux density associated with the stator poles that make up the upper actuator of the V-axis.

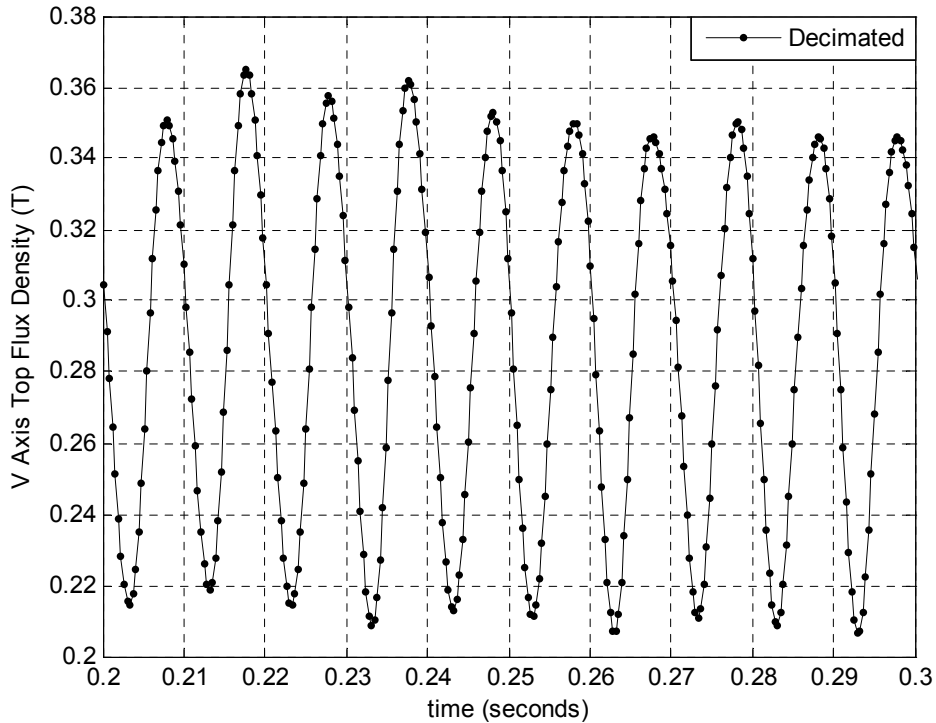


**Figure 7.30: Calculated Flux Density Based on Decimated Current and Position Values in Conjunction With Equation 7.1**

The flux density values shown in Figure 7.30 can be converted to a magnetic force by taking the pole face area,  $A_g$  in Figure 1.2, into account as shown in Equation 1.4, repeated here.

$$F = \frac{B^2 A}{\mu_o} \quad (1.2)$$

In order to allow Equation 1.2 to be directly applied to an AMB actuator that is typical of a test bearing configuration as shown in Figure 1.4, the angle of force action of the individual poles must be accounted for. Since each pole applies force at angles  $\pm\theta$  to the force axis, calculation of the total lift force generated by the actuator requires the pole angle to be taken into account. Considering the pole angle and the expanded magnetic flux term given in Equation 7.1 leads to the lift force developed by an upper actuator.

$$F_{upper} = \cos\theta \frac{\mu_o N^2 i_{upper}^2 A}{2(g_o - x \cos\theta)^2} \quad (7.2)$$

As discussed in Chapter 1, the air gap,  $g_{upper}$  in Equation 7.2, accounts for most of the reluctance in the circuit. However, in order to improve model accuracy, the rotor and stator reluctances can be accounted for by determining their equivalent air gap length. The equivalent air gap length of the iron path is represented as (Baun et al., 1996):

$$b = \frac{L_i}{\mu_r} \quad (1.10)$$

where

$b$  = equivalent air gap due to the flux path through the rotor and stator

$L_i$  = approximation of flux path through rotor and stator

$\mu_r$  = the relative permeability of the rotor and stator material (relative to  $\mu_o$ )

Taking the equivalent air gap length into account leads to Equation 7.3, the final formulation of force in an upper actuator.

$$F_{upper} = \cos\theta \frac{\mu_o N^2 i_{upper}^2 A}{(2(g_o - x \cos\theta) + b)^2} \quad (7.3)$$

Equation 7.3 was applied to the flux densities in the upper actuator of the V-axis that were determined for the decimated current and position values. Recall that these are the flux densities shown in Figure 7.30. The force values in the upper actuator of the V-axis, resulting from application of Equation 7.3 to the flux density data, are shown in Figure 7.31.

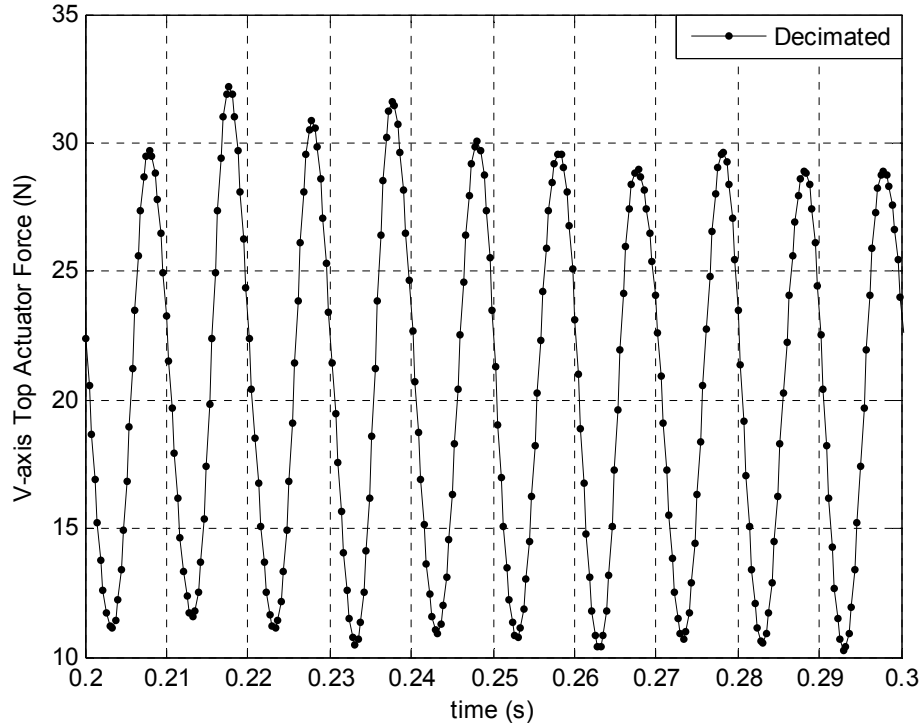


**Figure 7.31: calculated upper actuator force in V-axis based on decimated flux density**

The attractive force developed by the lower actuator of a typical force axis can be determined in a similar way. The development is the same with the exception that air gap length is calculated using Equation 1.8 instead of Equation 1.7. The attractive force developed by a typical lower actuator is described by Equation 7.4.

$$F_{lower} = \cos \theta \frac{\mu_o N^2 i_{lower}^2 A}{(2(g_o + x \cos \theta) + b)^2} \quad (7.4)$$

The force developed by a single axis must take both the upper and lower actuator forces into account by taking the vector sum of the forces of the upper and lower actuators. Since the forces in the upper and lower actuators have opposite sense, their sum is determined by subtracting the force of the lower actuator from the force of the upper actuator. The result is the basic magnetic circuit model as repeated below. The equation was discussed in Chapter 1 and in the introduction to this chapter. Note that the common terms of  $\mu_o$ ,  $N^2$ , and  $A$  have been combined in the constant  $k$ .

$$F = k \cos \theta \left[ \frac{i_{upper}^2}{(2(g_o - x \cos \theta) + b)^2} - \frac{i_{lower}^2}{(2(g_o + x \cos \theta) + b)^2} \right] \quad (1.13)$$

The force given by Equation 1.13 is an axis force. Figure 7.32 shows the upper actuator force that was calculated from Equation 7.3 and previously plotted in Figure 7.31. Also shown in Figure 7.32 is the lower actuator force as calculated by Equation 7.4, as well

as a plot of the difference between the upper and lower actuator forces as calculated by Equation 1.13. The points at which the force values are calculated correspond to the decimated data points. A similar graph could be made for the  $W$ -axis.

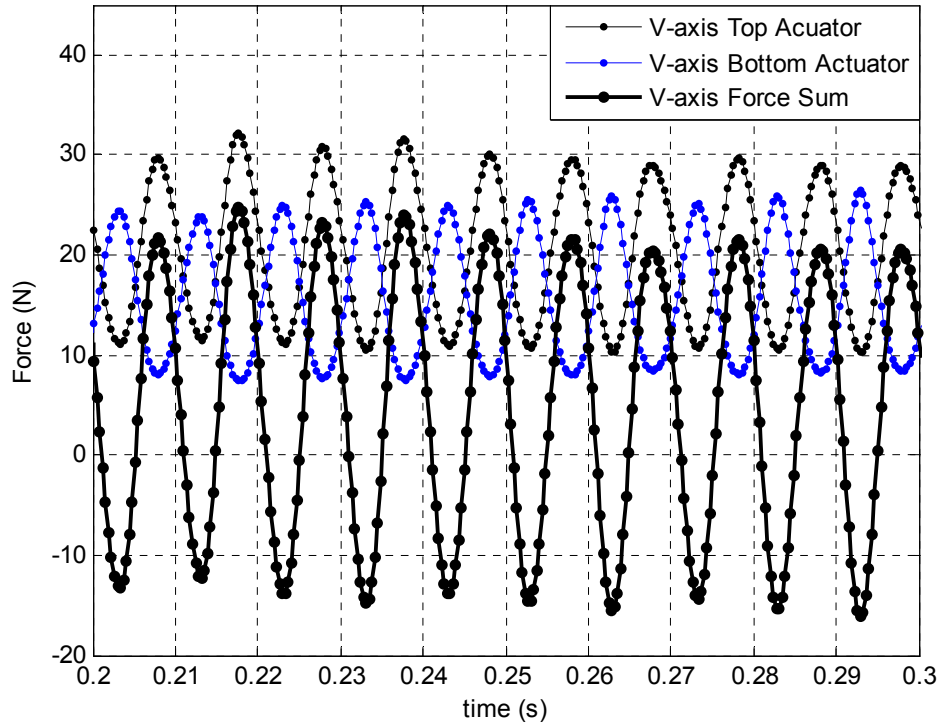


**Figure 7.32: V-axis force calculated from Equation 1.13 (upper actuator force – lower actuator force) and decimated data**

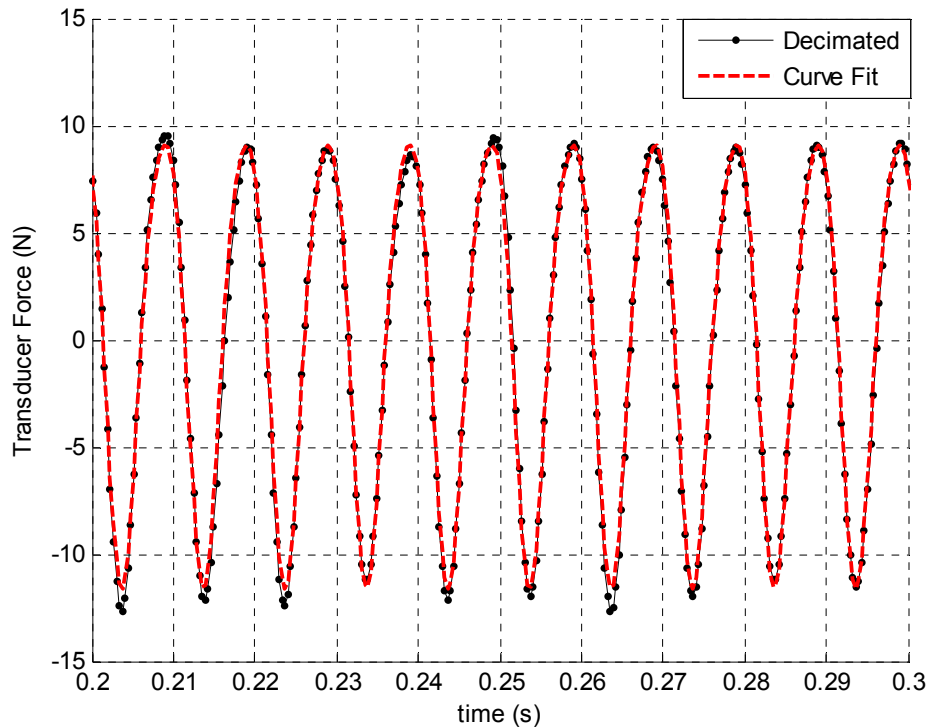
### 7.5.3 Curve Fit

Figure 7.32, above, shows the V-axis force that was calculated from decimated rotor position and coil current data. Also shown in the figure is a sine wave that has been fit to the data. The fit allows the force data to be described by a DC offset, an amplitude, and a phase.

The coil current, rotor position, and force transducer data that was collected for a given test are expected to be periodic since it was collected at a continuous rotor speed. Since the system is harmonically driven due to the synchronous unbalance, the coil current, rotor position, and force transducer data can be well approximated with a trigonometric function. The second reduction step was to fit a representative sample of nineteen cycles to a sine function. The curve fit allowed the nineteen cycles of data to be described by three parameters; a DC offset, an amplitude, and a phase. The curve fit minimizes residual error in a least-squares sense (de Callafon et al., 1996). Forcing the data to fit a specific function results in uncertainty because the collected data does not fit the function perfectly. Relative error between the curve fit and the calculated force data can be seen in Figure 7.32. In following sections, the uncertainty associated with the fit process is shown as error bars located in the error plots associated with each test. The



the decimation as well as the resulting curve fit. Forcing the data to fit a specific function results in added uncertainty because the collected data does not fit the function perfectly. Relative error between the curve fit and the decimated force transducer data can be seen in Figure 7.33. In following sections, the uncertainty associated with the fit process is shown as error bars located in the error plots associated with each test. The uncertainty is further discussed in Appendix B. The data reduction was applied in order to efficiently analyze a large amount of data in a reasonable amount of time.



**Figure 7.33: Decimated data from force transducers and resulting curve fit**

The curve fit process allowed the transducer force from a given test to be described by a DC offset, an amplitude, and a phase. The resulting transducer force amplitude was compared to the calculated vertical force discussed in Section 7.5.4.

## COMPARISON OF MEASURED AND CALCULATED FORCES

AMB system data corresponding to a variety of dynamic loading scenarios was used to calculate force using two different models. The models are described in Chapter 2, the data analysis is discussed in Section 7.5. The results of each model were then compared to the measured force provided by the force transducers.

## 7.6 RESULTS OF FORCE COMPARISON

The results of two force models were compared to the measured force. The first model is the basic magnetic circuit force model of Equation 1.13. The second model has the same form as Equation 1.13, but also accounts for unmodeled system effects via the static characterizations discussed in earlier chapters and reviewed in the introduction.

### 7.6.1 Platform 1 Results

Recall that Platform 1 is a typical high-speed laboratory rotor kit from Revolve Magnetic Bearings and has a 0.015 inch radial gap and 0.005 inch thick rotor laminations. It is described in greater detail in Chapter 3.

The test conditions applied to Platform 1 are described below. Raw force transducer data was presented in Figure 7.2-Figure 7.6 for Platform 1.

#### PLATFORM 1, SYSTEM 1

- 0.015 inch nominal gap, 0.005 inch thick rotor laminations (Arnon 5)
- unbalance mass of 0, 400, 600, 800, and 1000 mg (0, 0.48, 0.72, 0.96, and 1.2 gm-in)
- bias currents of 1.3A, 1.5A, and 1.7A
- rotational speeds of 4000, 5000, 6000, 7000, 8000, 9000, and 10000 RPM

These conditions resulted in dynamic loads amplitudes ranging from 4N to 35N (~1 lb<sub>f</sub> to ~8 lb<sub>f</sub>). Figure 7.34 shows the results of the force measurement via force transducers, the basic magnetic circuit model, and a characterized version of the basic magnetic circuit model as applied to data corresponding to one unbalance case (0 added unbalance). Each of the three subfigures in Figure 7.34 corresponds to one bias current setting as specified in the subfigure heading; the topmost subfigure presents the data from the 1.3 Amp bias cases, the middle subfigure presents the data from the 1.5 Amp bias cases, and the bottom subfigure presents the data from the 1.7 Amp bias cases. The measured and calculated forces are shown in Newtons on the y-axis versus rotor speed in RPM x1000 on the x-axis. A legend is included in each plot; the measured force values from the force transducers are connected by a solid line. The force values calculated from the two models are shown as points only; the basic magnetic circuit model results are represented by a square, and the characterized version of the basic magnetic circuit model results are represented by an asterisk. Although the difference in model results is difficult to determine at the plot scale, it can be seen that the characterized model typically predicts force values that are closer to the measured values than the predictions from the basic model.

Directly following Figure 7.34 is the error plot associated with the same tests; Figure 7.35. The error plot shows the variation of each model from the measured value. A positive error value indicates an over-prediction by the model; a negative value indicates an under-prediction. Using the same legend convention introduced on the force plots, the errors associated with the basic magnetic circuit model results are represented by a square, and the errors associated with the characterized version of the basic magnetic circuit model results are represented by an asterisk. The heading of each subfigure shows a mean error value for both models. The mean error value is based on calculations of error absolute value and is included to give a broad overview of the results in each subfigure.

Also included in the error plots are error bars. The error bars were mentioned in Section 7.5; they represent the error associated with the curve fit. The wide, shaded error bars represent error associated with the transducer curve fit, the line-style error bars

represent error associated with the axis force curve fit associated with the model data. The line style error bars are shown only with the characterized model data to minimize clutter. Curve fit error associated with the basic model can be considered to be the same magnitude as the error associated with the characterized model. Error associated with a given curve fit was calculated as the difference between the fit line and the decimated points. The length of the error bars in the graph represents four standard deviations of the error values ( $\pm 2\sigma$ ). The error is discussed further in Appendix B.

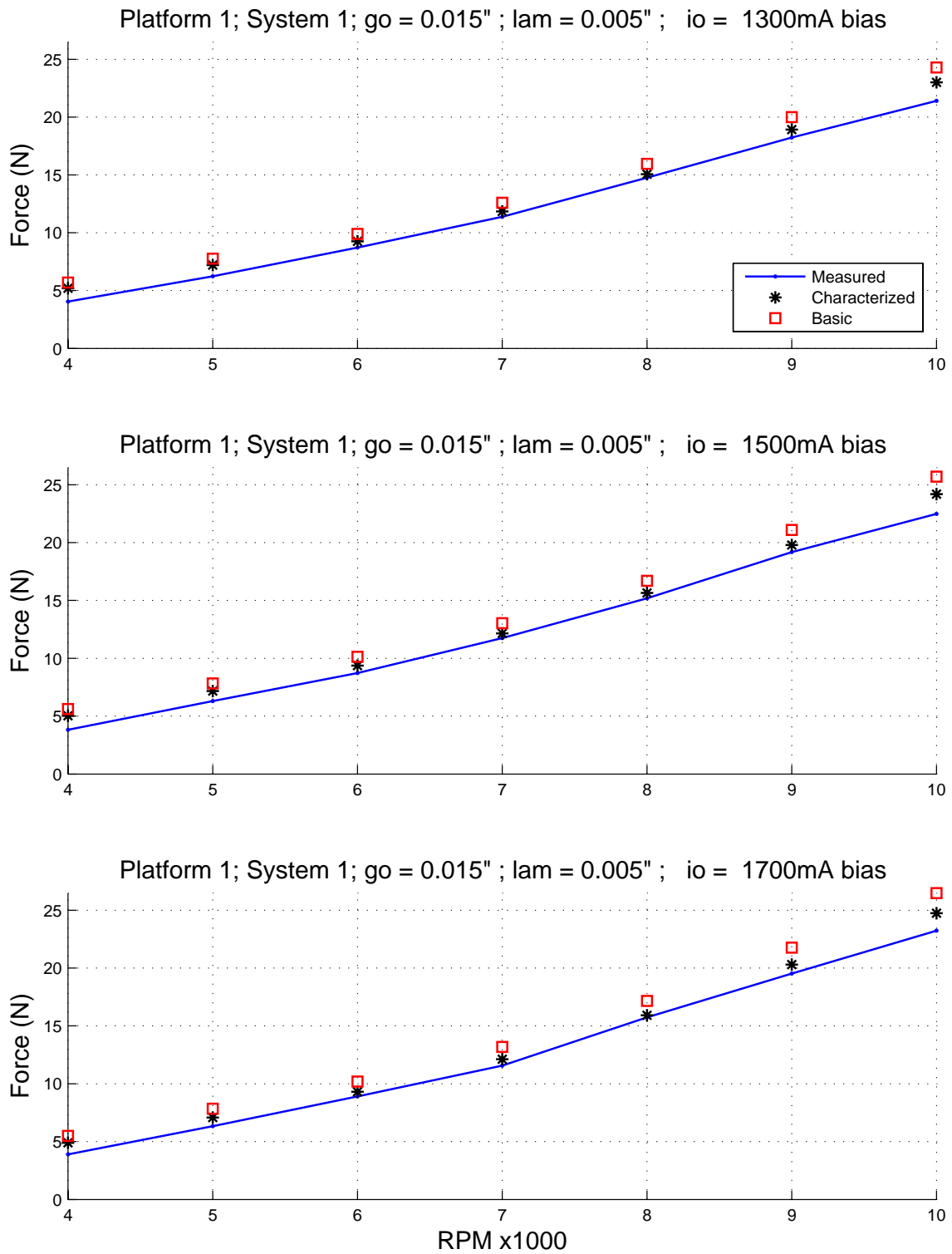


**Figure 7.34: Comparison of measured and calculated forces versus rotor speed. Platform 1 System 1. Added Unbalance: 0 mg**

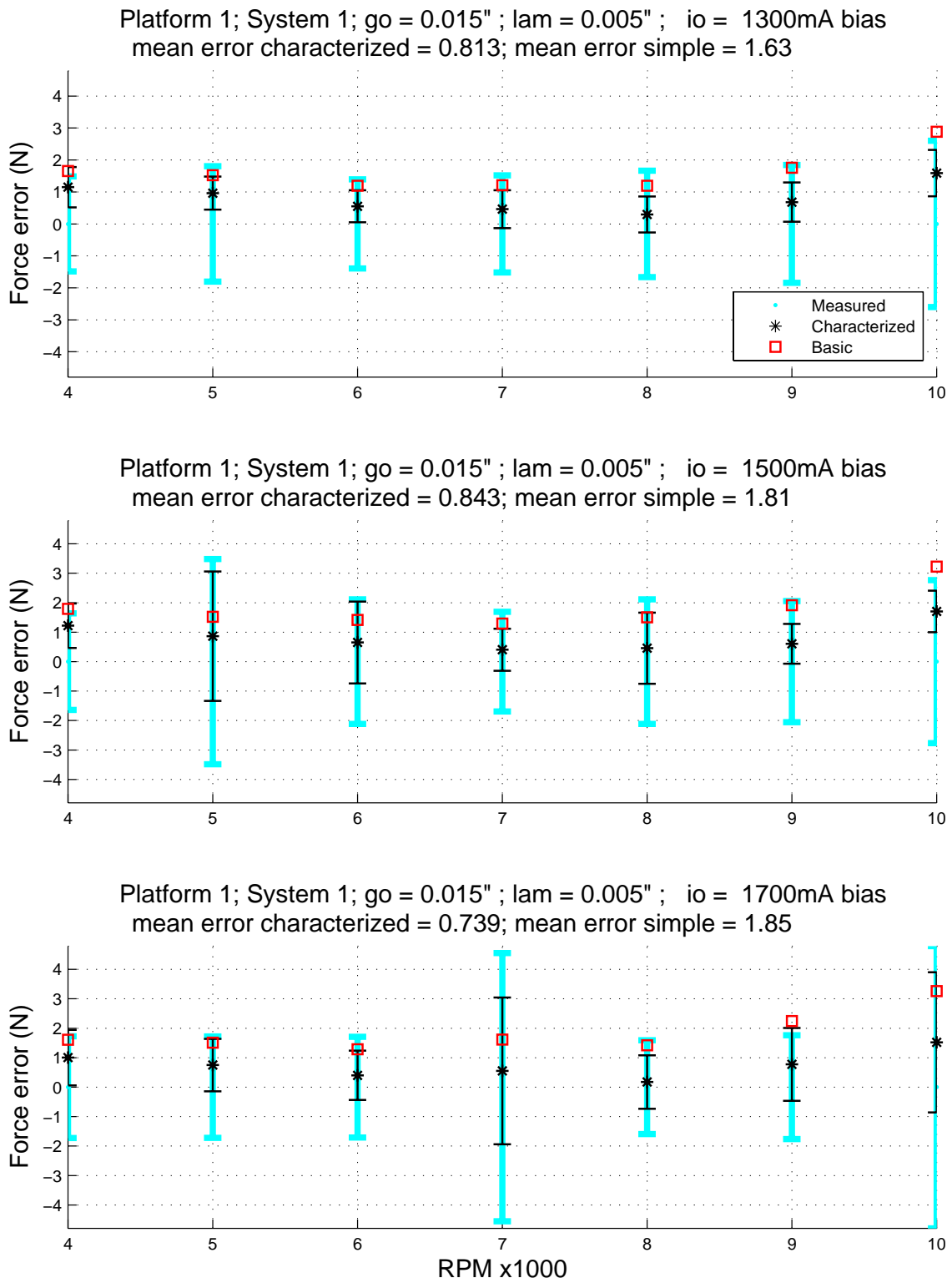
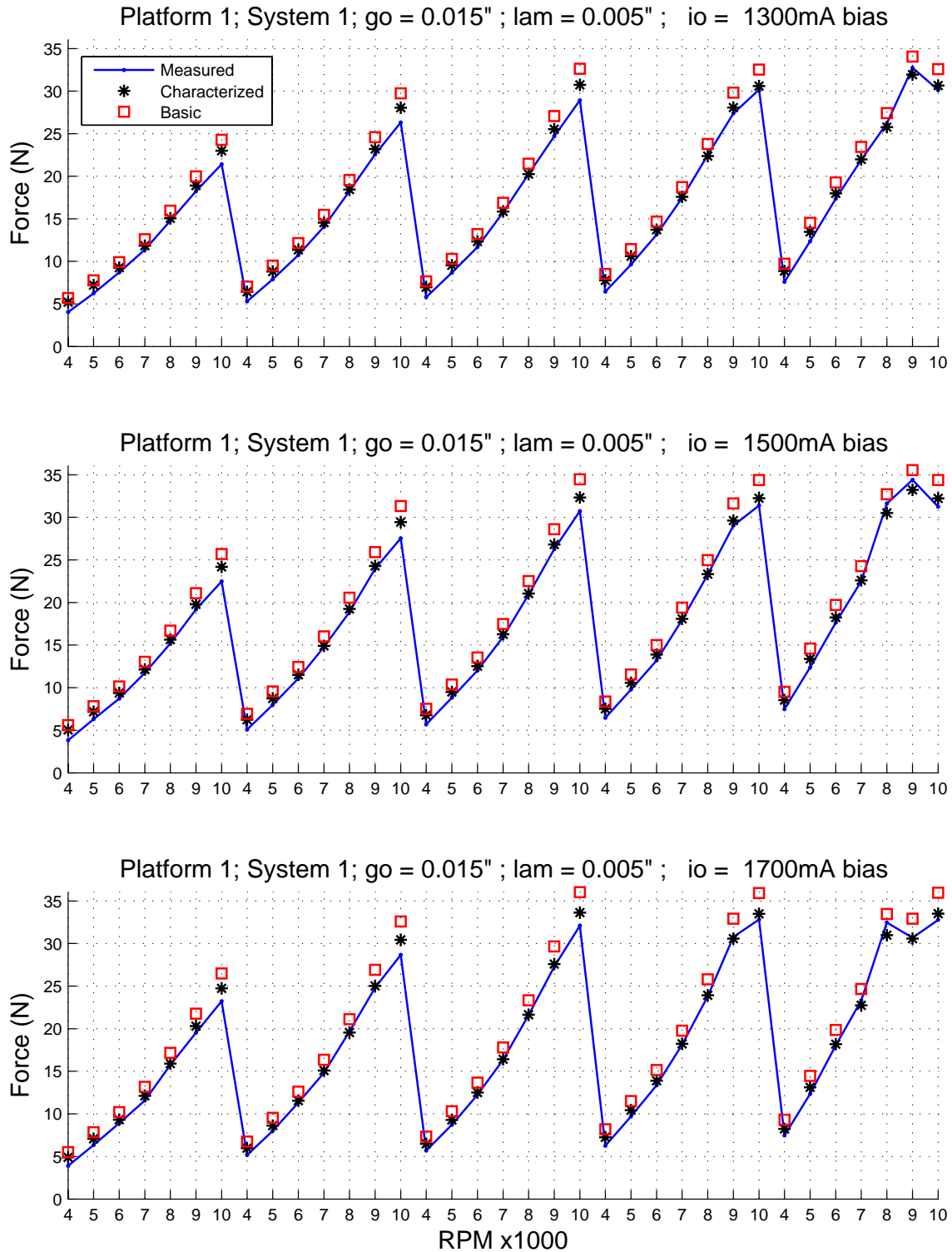


Figure 7.35: Comparison of measured and calculated forces versus rotor speed. Platform 1 System 1. Added Unbalance: 0 mg

Similar presentation of all of the data scenarios on both platforms would require twenty-six force plots and twenty-six error plots similar to Figure 7.34 and Figure 7.35. Such a representation would consume a lot of space and make data comparisons difficult. In order to more efficiently present the data, multiple unbalance load cases will be presented on the same plot. Rather than cluttering one region of the plot with several points corresponding to the same speed, the rotor speed scale repeats itself along the x-axis. Each repeated speed scale section corresponds to a different unbalance case. The unbalance cases that correspond to each speed section are clearly defined in the figure caption. The bias currents are specified in the heading of each subfigure.

The error plots are presented in a similar way. To introduce the presentation method, the data from Figure 7.34 and Figure 7.35 are re-plotted along with the remaining unbalance cases in Figure 7.36 and Figure 7.37.



**Figure 7.36: Comparison of measured and calculated forces versus rotor speed. Platform 1 System 1. Added Unbalance Sections (left to right) 0, 400, 600, 800, and 1000 mg (0, 0.48, 0.72, 0.96, and 1.2 gm-in)**

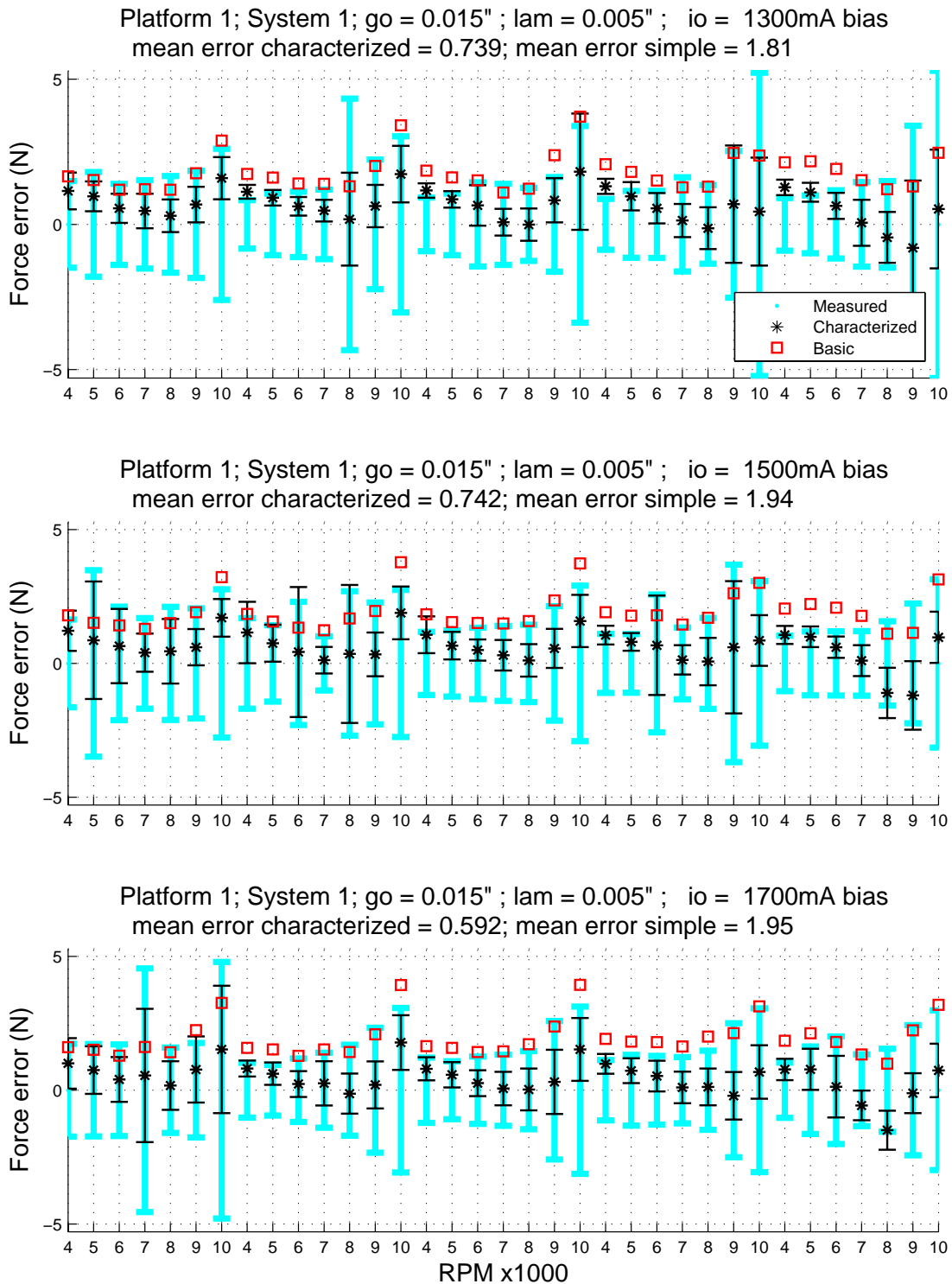


**Figure 7.37: Comparison of errors in calculated force versus rotor speed. Platform 1 System 1. Added Unbalance Sections (left to right) 0, 400, 600, 800, and 1000 mg (0, 0.48, 0.72, 0.96, and 1.2 gm-in)**

The error data from Figure 7.37 is broadly summarized in Table 7.3 in which error data from each model is summarized by a mean value and a maximum value. All of the values given in the table are based on a summary of absolute error values. The table is organized into three regions from left to right. The leftmost region shows the error summary of the basic and characterized models in terms of the measured unit of Newtons. The middle section expresses the error summary as a percent of the corresponding measured force. In the rightmost section, the error summary is expressed as a percentage of the maximum measured force associated with Platform 1 Setup 1. As mentioned, Table 7.3 is a summary of the error data; a complete record is appended to the end of this chapter.

The table shows that the characterized model provides a significantly better estimate of dynamic force than the basic model. The mean error associated with the characterized model is typically ~40% of the mean error associated with the basic model.

**Table 7.3: Summary of force model errors associated with Figure 7.36 and Figure 7.37**

	Error (N)		Error as Percent of Measured Force (%)		Error as Percent of Maximum Measured Force (%)	
	Basic	Characterized	Basic	Characterized	Basic	Characterized
<b>MAXIMUM</b>	3.93	1.89	47.0	32.0	11.4	5.5
<b>MEAN</b>	1.90	0.69	14.4	6.2	5.5	2.0

## 7.6.2 Platform 2 Results

The second platform (Platform 2) is a custom built magnetic bearing test bed, also built by Revolve Magnetic Bearings. Platform 2 was designed with a common stator and four interchangeable rotors. Each rotor has a unique combination of nominal air gap and lamination thickness so that Platform 2 can be configured as 4 unique systems.

1. 0.010 inch radial gap, 0.005 inch lamination (Arnon 5)
2. 0.030 inch radial gap, 0.005 inch lamination (Arnon 5)
3. 0.010 inch radial gap, 0.014 inch lamination (M19)
4. 0.030 inch radial gap, 0.014 inch lamination (M19)

Platform 2 is described in greater detail in Chapter 3.

### PLATFORM 2, SYSTEM 1

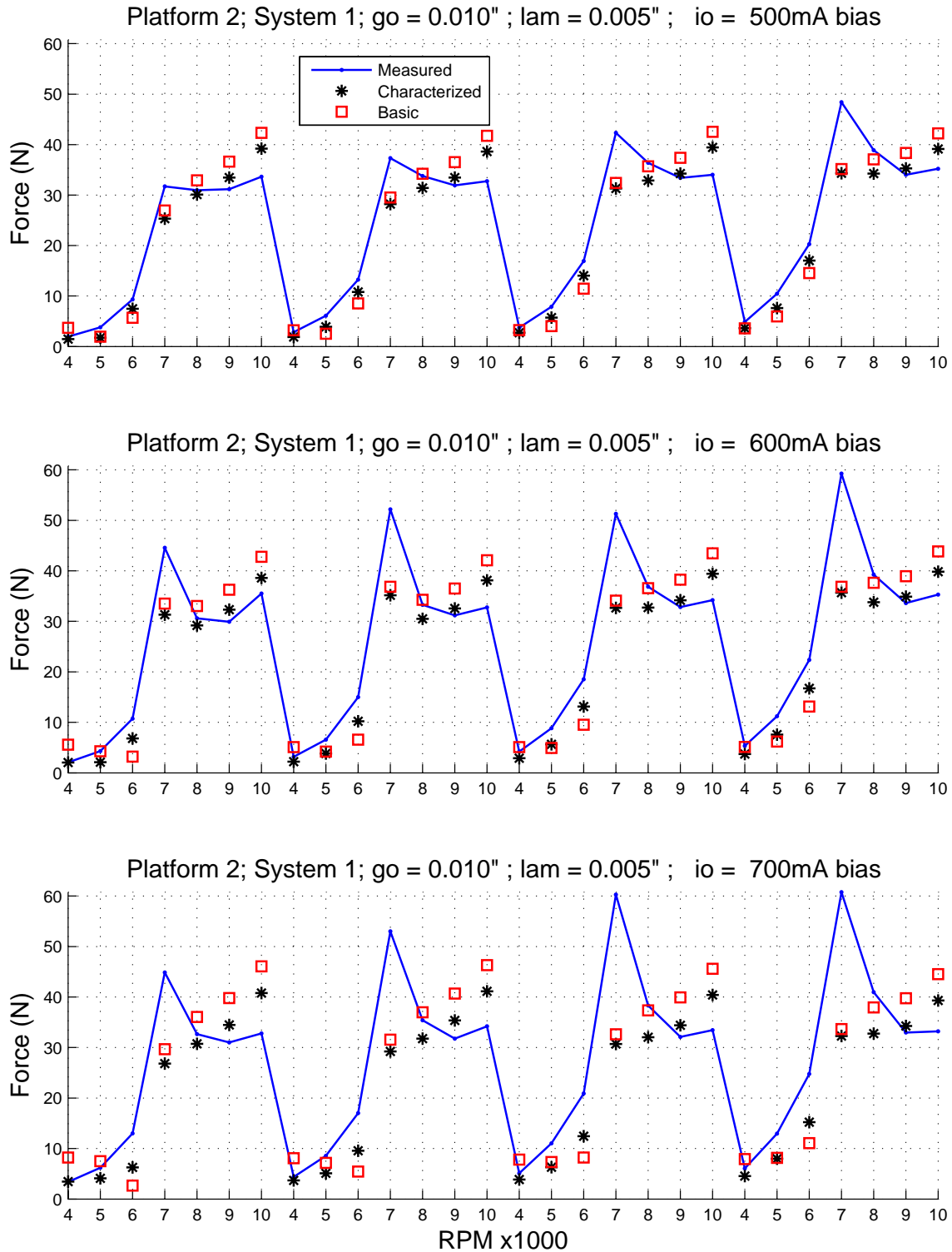
- 0.010 inch nominal gap, 0.005 inch lamination (Arnon 5)
- unbalance mass of 0, 100, 200, 300 mg (0, 0.23, 0.45, 0.68 gm-in)
- bias currents of 0.5A, 0.6A, and 0.7A
- rotational speeds of 4000, 5000, 6000, 7000, 8000, 9000, and 10000 RPM

These conditions resulted in dynamic load amplitudes ranging from 3N to 60N (~0.7l<sub>f</sub> to ~13.5l<sub>f</sub>). Figure 7.38 shows the results of the force measurement via force transducers, the basic magnetic circuit model, and a characterized version of the basic magnetic circuit model. Each of the three subfigures in Figure 7.38 corresponds to one bias current setting as noted in the subfigure heading; the topmost subfigure presents the

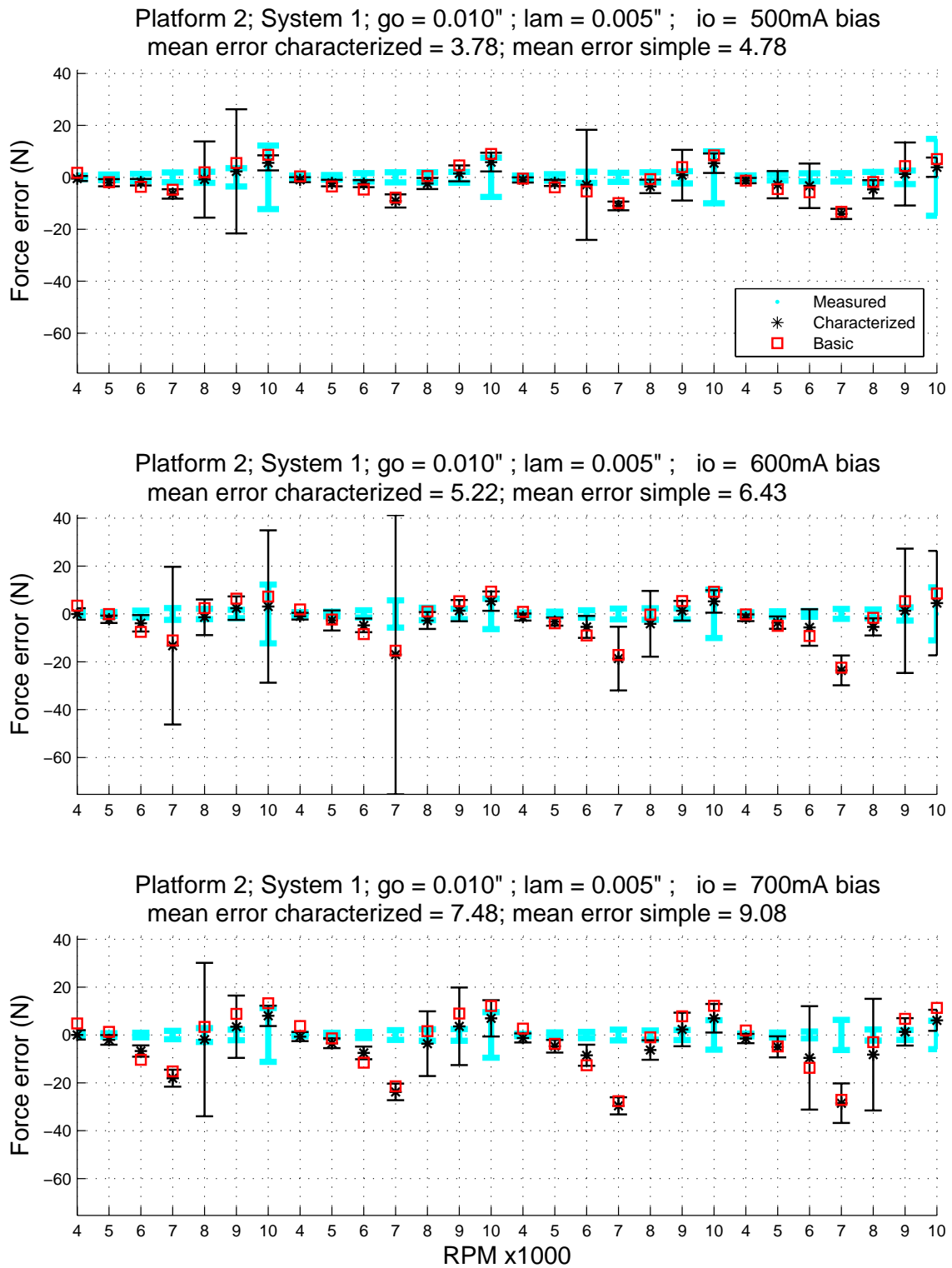
data from the 0.5 Amp bias cases, the middle subfigure presents the data from the 0.6 Amp bias cases, and the bottom subfigure presents the data from the 0.7 Amp bias cases. The measured and calculated forces are shown in Newtons on the y-axis versus rotor speed in RPM x1000 on the x-axis. A legend is included in each plot; the measured force values from the force transducers are connected by a solid line. The force values calculated from the two models are shown as points only; the basic magnetic circuit model results are represented by a square, and the characterized version of the basic magnetic circuit model results are represented by an asterisk. It can be seen that the characterized model tracks the measured force in the <7000 RPM speed range than the basic model does. Neither model does well at tracking the measured force near the 7000 RPM critical speed. Above the critical speed, both models show similar trends, however, the model trends do not track the trend seen in the measured data.

Figure 7.39 shows the errors associated with the simple model and the characterized model as compared to the transducer reported values. Also shown are error bars that correspond to  $\pm 2\sigma$  uncertainty introduced by the parameterization of the data discussed in Sections 7.5.3 and 7.5.5. The wide, shaded error bars represent error associated with the transducer curve fit, the line-style error bars represent error associated with the axis force curve fit associated with the model data. The line style error bars are shown only with the characterized model data to minimize clutter. Curve fit error associated with the basic model can be considered to be the same magnitude as the error associated with the characterized model.

Error associated with a given curve fit was calculated as the difference between the fit line and the decimated points. The length of the error bars in the graph represents four standard deviations of the error values ( $\pm 2\sigma$ ). The error is discussed further in Appendix B.



**Figure 7.38: Comparison of measured and calculated forces versus rotor speed. Platform 2 System 1. Added Unbalance (left to right) 0, 100, 200 and 300mg (0, 0.23, 0.45, 0.68 gm-in)**



**Figure 7.39: Comparison of errors in calculated force versus rotor speed. Platform 2 System 1. Added Unbalance (left to right) 0, 100, 200 and 300mg (0, 0.23, 0.45, 0.68 gm-in)**

The error data from Figure 7.39 is broadly summarized in Table 7.4 in which error data from each model is summarized by a mean value and a maximum value. All of the values given in the table are based on a summary of absolute error values. The table is organized into three regions from left to right. The leftmost region shows the error summary of the basic and characterized models in terms of the measured unit of Newtons. The middle section expresses the error summary as a percent of the corresponding measured force. In the rightmost section, the error summary is expressed as a percentage of the maximum measured force associated with Platform 2 Setup 1. As mentioned, Table 7.4 is a summary of the error data; a complete record is appended to the end of this chapter.

The table shows that the characterized model provides a somewhat better estimate of dynamic force than the basic model. The mean error associated with the characterized model is typically ~80% of the mean error associated with the basic model in terms of the measured units. When taking the measured load value into consideration, the characterized model errors are ~65% of the mean errors associated with the basic model. The improvement is due to the low-speed force estimates, recall that the characterized model tracked the measured values well at speeds <7000 RPM, where loads are small. Small load values are sensitive to errors that are expressed in terms of measured force.

**Table 7.4: Summary of force model errors associated with Platform 2, Setup 1 as shown in Figure 7.38 and Figure 7.39.**

	Error (N)		Error as Percent of Measured Force (%)		Error as Percent of Maximum Measured Force (%)	
	Basic	Characterized	Basic	Characterized	Basic	Characterized
<b>MAXIMUM</b>	27.65	29.59	167.8	54.6	45.5	48.7
<b>MEAN</b>	6.71	5.45	32.9	22.8	11.7	9.4

## PLATFORM 2, SYSTEM 2

- 0.030 inch nominal gap, 0.005 inch lamination (Arnon 5)
- unbalance mass of 0, 200, 400, 600, 800, and 1000 mg (0, 0.45, 0.9, 1.35, 1.8, and 2.25 gm-in)
- bias currents of 1.2A, 1.6A, and 2.0A
- rotational speeds of 4000, 5000, 6000, 7000, 8000, 9000, and 10000 RPM

These conditions resulted in dynamic load amplitudes ranging from 4N to 32N (~1lb<sub>f</sub> to ~7lb<sub>f</sub>). Figure 7.40 shows the results of the force measurement via force transducers, the basic magnetic circuit model, and a characterized version of the basic magnetic circuit model. Each of the three subfigures in Figure 7.38 corresponds to the bias current setting noted in the subfigure heading; the topmost subfigure presents the data from the 1.2 Amp bias cases, the middle subfigure presents the data from the 1.6 Amp bias cases, and the bottom subfigure presents the data from the 2.0 Amp bias cases. The measured and calculated forces are shown in Newtons on the y-axis versus rotor speed in RPM x1000 on the x-axis. A legend is included in each plot; the measured

force values from the force transducers are connected by a solid line. The force values calculated from the two models are shown as points only; the basic magnetic circuit model results are represented by a square, and the characterized version of the basic magnetic circuit model results are represented by an asterisk.

It can be seen that both models typically predict the trends seen in the measured force values for Platform 2 System 2. It is of interest that both models also track the measured force near the critical speeds,  $\sim 9000$  RPM for the low bias cases and  $\sim 8000$  RPM at the highest bias case. At 10000 RPM, model accuracy degrades with increased bias current.

Figure 7.41 shows the errors associated with the simple model and the characterized model as compared to the transducer reported values. Also shown are error bars that correspond to  $\pm 2\sigma$  uncertainty introduced by the parameterization of the data discussed in Sections 7.5.3 and 7.5.5. The wide, shaded error bars represent error associated with the transducer curve fit, the line-style error bars represent error associated with the axis force curve fit associated with the model data. The line style error bars are shown only with the characterized model data to minimize clutter. Curve fit error associated with the basic model can be considered to be the same magnitude as the error associated with the characterized model. Error associated with a given curve fit was calculated as the difference between the fit line and the decimated points. The length of the error bars in the graph represents four standard deviations of the error values ( $\pm 2\sigma$ ). The error is discussed further in Appendix B.

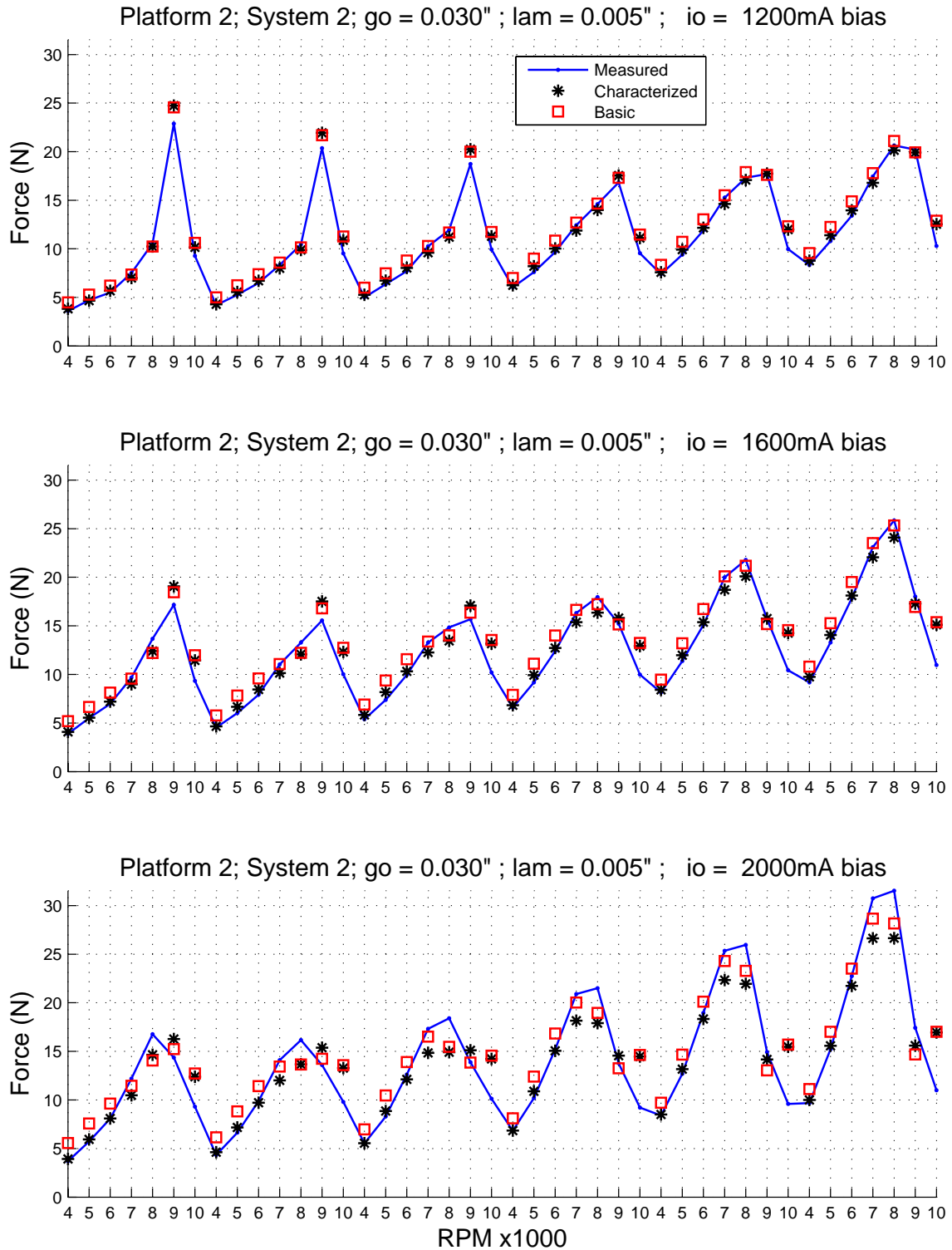


**Figure 7.40: Comparison of Measured and Calculated Forces versus Rotor Speed. Platform 2 System 2. Added Unbalance (left to right) 0, 200, 400, 600, 800, and 1000mg (0, 0.45, 0.9, 1.35, 1.8, and 2.25 gm-in)**

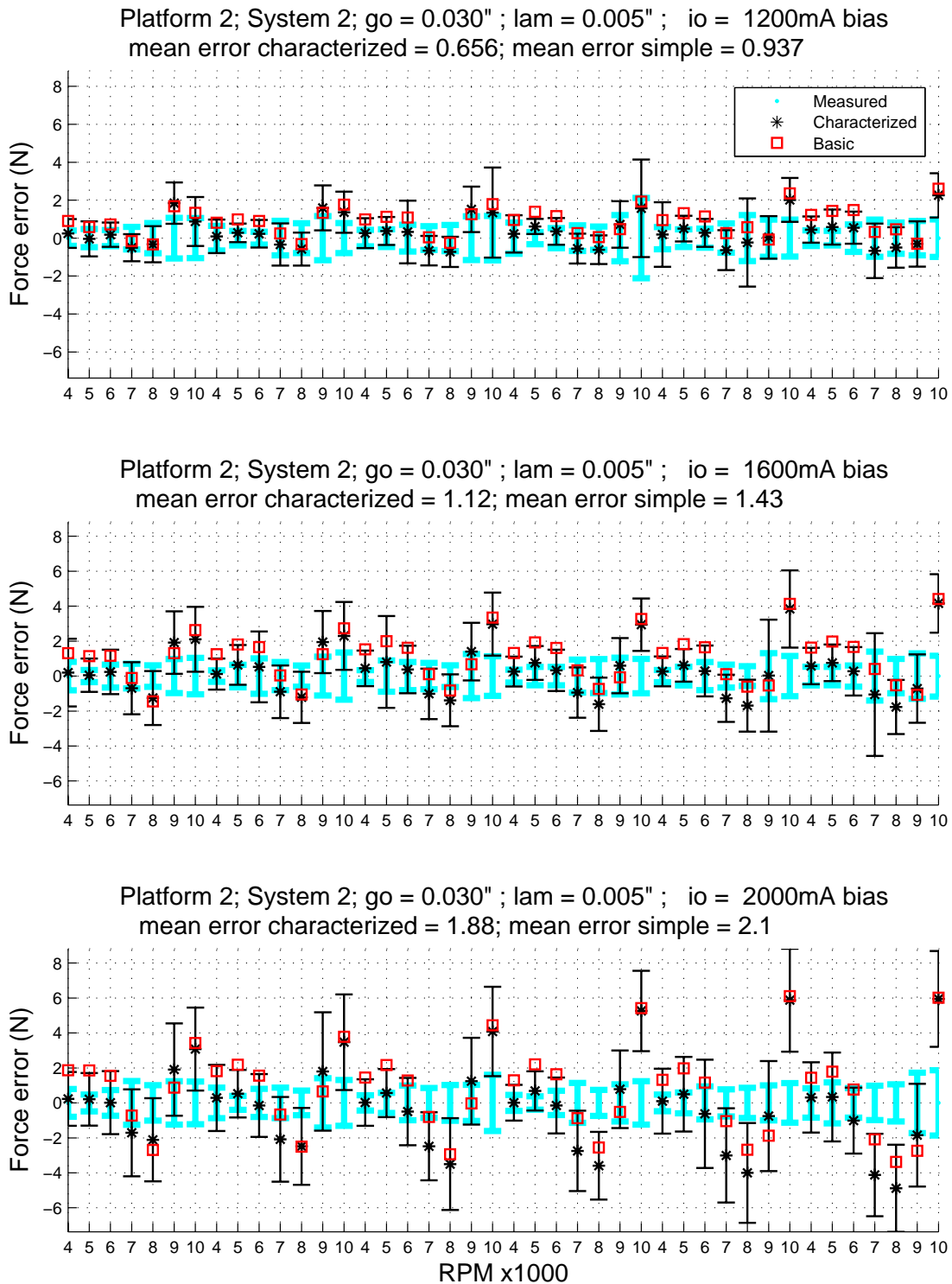


**Figure 7.41: Comparison of Errors in Calculated Force versus Rotor Speed. Platform 2 System 2. Added Unbalance (left to right) 0, 200, 400, 600, 800, and 1000gm (0, 0.45, 0.9, 1.35, 1.8, and 2.25 gm-in)**

The error data from Figure 7.41 is broadly summarized in Table 7.5 in which error data from each model is summarized by a mean value and a maximum value. All of the values given in the table are based on a summary of absolute error values. The table is organized into three regions from left to right. The leftmost region shows the error summary of the basic and characterized models in terms of the measured unit of Newtons. The middle section expresses the error summary as a percent of the corresponding measured force. In the rightmost section, the error summary is expressed as a percentage of the maximum measured force associated with Platform 2 Setup 2. As mentioned, Table 7.5 is a summary of the error data; a complete record is appended to the end of this chapter.

The table shows that the characterized model provides a somewhat better estimate of dynamic force than the basic model. The mean error associated with the characterized model is typically ~80% of the mean error associated with the basic model in terms of the measured units. When taking the measured load value into consideration, the characterized model errors are ~65% of the mean errors associated with the basic model. The improvement is likely due to the better low-speed force estimates where forces tend to be small. Small loads values are sensitive to errors that are expressed in terms of measured force.

**Table 7.5: Summary of force model errors associated with Platform 2, Setup 2 as shown in Figure 7.40 and Figure 7.41.**

	Error (N)		Error as Percent of Measured Force (%)		Error as Percent of Maximum Measured Force (%)	
	Basic	Characterized	Basic	Characterized	Basic	Characterized
<b>MAXIMUM</b>	6.10	5.88	63.6	61.2	19.4	18.6
<b>MEAN</b>	1.43	1.15	15.5	9.7	4.6	3.7

### PLATFORM 2, SYSTEM 3

- 0.010 inch nominal gap, 0.014 inch lamination (M19)
- unbalance mass of 0, 100, and 200mg (0, 0.23, 0.45 gm-in)
- bias currents of 0.5A, 0.65A, and 0.8A
- rotational speeds of 4000, 5000, 6000, 7000, 8000, 9000, and 10000 RPM

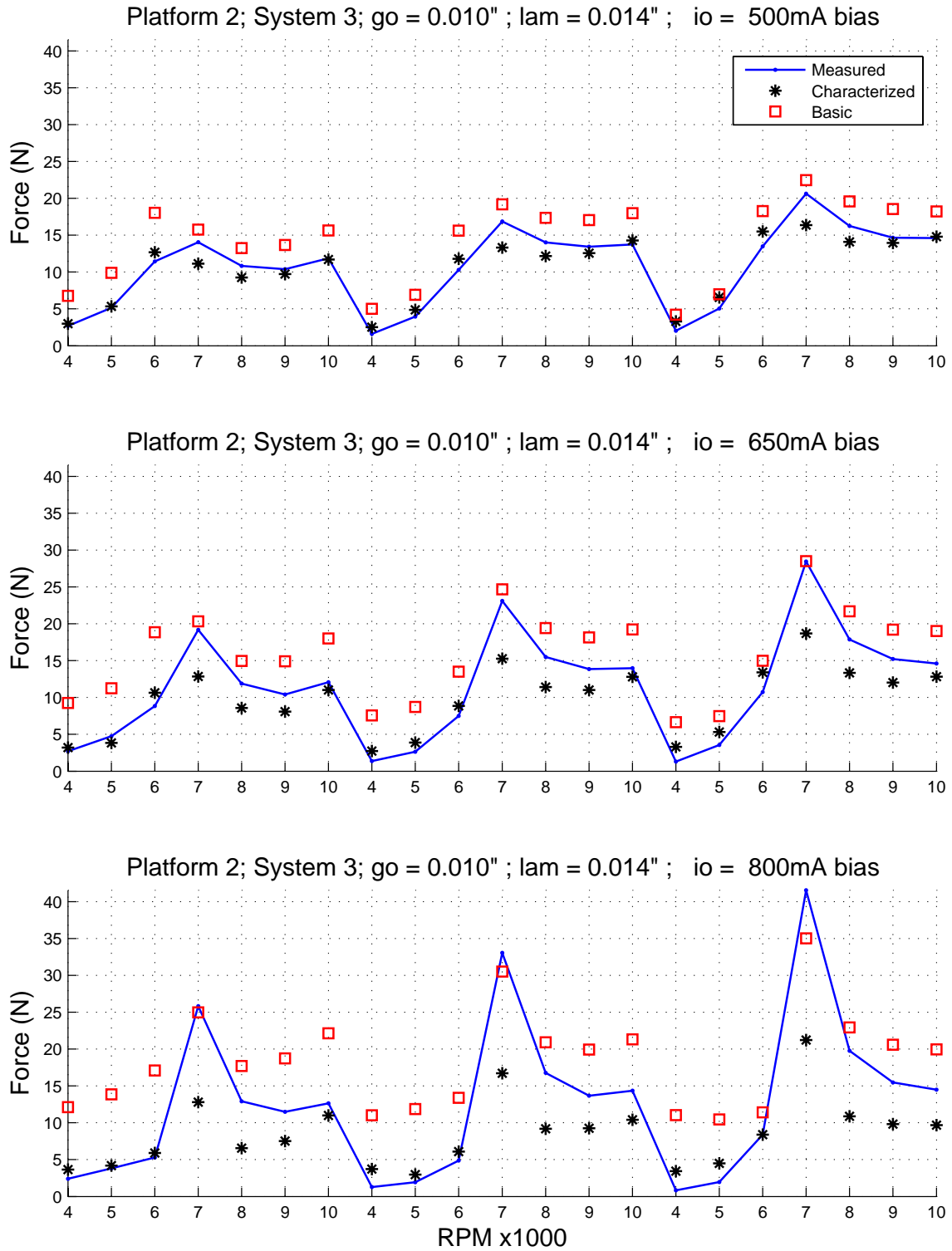
The test conditions resulted in dynamic loads amplitudes ranging from 1N to 44N (~0.25lb<sub>f</sub> to ~10lb<sub>f</sub>). Figure 7.42 shows the results of the force measurement via force transducers, the basic magnetic circuit model, and a characterized version of the basic magnetic circuit model. Each of the three subfigures in Figure 7.38 corresponds to one bias current setting as shown in the subfigure heading; the topmost subfigure presents the data from the 0.5 Amp bias cases, the middle subfigure presents the data from the 0.65 Amp bias cases, and the bottom subfigure presents the data from the 0.8 Amp bias cases. The measured and calculated forces are shown in Newtons on the y-axis versus rotor speed in RPM x1000 on the x-axis. A legend is included in each plot; the measured force values from the force transducers are connected by a solid line. The force values calculated from the two models are shown as points only; the basic

magnetic circuit model results are represented by a square, and the characterized version of the basic magnetic circuit model results are represented by an asterisk.

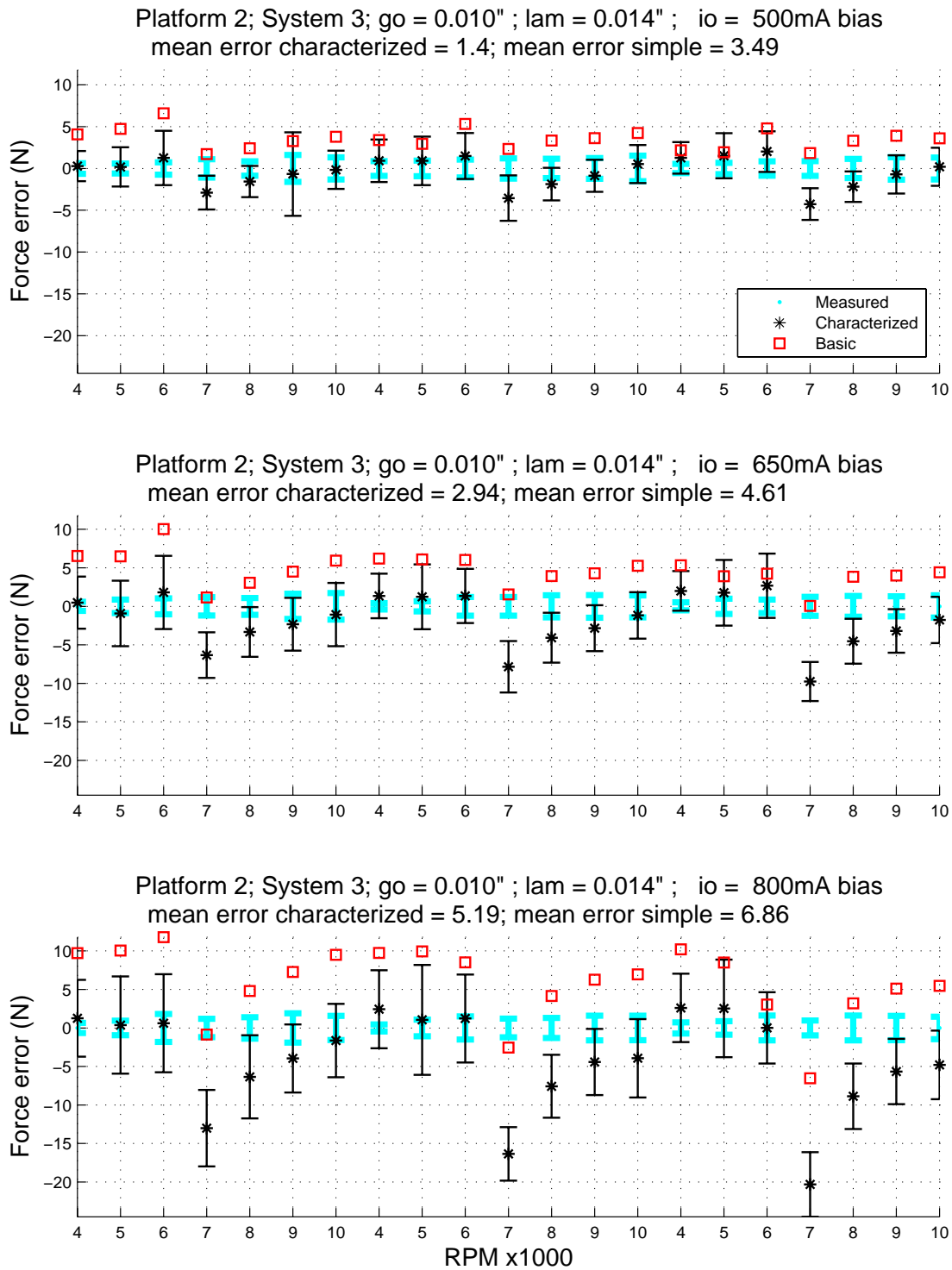
It can be seen that although both models predict the trends in measured force, the characterized model does a significantly better job in the lower speed region (<7000 RPM) below the critical speed. Above 7000 RPM the accuracy of both models varies with bias current level. The worst case error for the characterized model occurs in the highest bias case near the critical speed.

Figure 7.43 shows the errors associated with the simple model and the characterized model as compared to the transducer reported values. Also shown are error bars that correspond to  $\pm 2\sigma$  uncertainty introduced by the parameterization of the data discussed in Sections 7.5.3 and 7.5.5. The wide, shaded error bars represent error associated with the transducer curve fit, the line-style error bars represent error associated with the axis force curve fit associated with the model data. The line style error bars are shown only with the characterized model data to minimize clutter. Curve fit error associated with the basic model can be considered to be the same magnitude as the error associated with the characterized model.

Error associated with a given curve fit was calculated as the difference between the fit line and the decimated points. The length of the error bars in the graph represents four standard deviations of the error values ( $\pm 2\sigma$ ). The error is discussed further in Appendix B.



**Figure 7.42: Comparison of measured and calculated forces vs rotor speed. Platform 2 System 3. Added Unbalance (left to right) 0, 100, and 200mg (0, 0.23, 0.45 gm-in)**



**Figure 7.43: Comparison of errors in calculated force versus rotor speed. Platform 2 System 3. Added Unbalance (left to right) 0, 100, and 200mg (0, 0.23, 0.45 gm-in)**

The error data from Figure 7.43 is broadly summarized in Table 7.6 in which error data from each model is summarized by a mean value and a maximum value. All of the

values given in the table are based on a summary of absolute error values. The table is organized into three regions from left to right. The leftmost region shows the error summary of the basic and characterized models in terms of the measured unit of Newtons. The middle section expresses the error summary as a percent of the corresponding measured force. In the rightmost section, the error summary is expressed as a percentage of the maximum measured force associated with Platform 2 Setup 3. As mentioned, Table 7.6 is a summary of the error data; a complete record is appended to the end of this chapter.

The table shows that the characterized model provides a significantly better estimate of dynamic force than the basic model. Considering the direct error measurement in the leftmost column, it can be seen that the mean error associated with the characterized model is typically ~60% of the mean error associated with the basic model. When the error is taken as a percent of measured force, the error associated with the characterized model is typically ~30% of the error associated with the basic model. The improvement implies that the basic model is significantly handicapped in the lower force range, where error percentages can be large. Significant low-speed error associated with the basic model can be seen in Figure 7.42 and Figure 7.43.

**Table 7.6: Summary of force model errors associated with Figure 7.42 and Figure 7.43.**

	Error (N)		Error as Percent of Measured Force (%)		Error as Percent of Maximum Measured Force (%)	
	Basic	Characterized	Basic	Characterized	Basic	Characterized
<b>MAXIMUM</b>	11.80	20.32	1237	315	38	49
<b>MEAN</b>	4.99	3.18	122	37	14	9

#### PLATFORM 2, SYSTEM 4

- 0.030 inch nominal gap, 0.014 inch lamination (M19)
- unbalance mass of 0, 200, 300, 400, 500, 600, 700, and 800 mg (0, 0.45, 0.68, 0.9, 1.13, 1.35, 1.58, 1.8 gm-in)
- bias currents of 1.4A, 1.7A, and 2.0A for unbalance mass up to 700 mg
- bias current of 1.5A, 1.6A, and 1.7A for 800 mg unbalance mass
- rotational speeds of 4000, 5000, 6000, 7000, 8000, 9000, and 10000 RPM

The test conditions resulted in dynamic loads amplitudes ranging from 6N to 48N (~1.5l<sub>f</sub> to ~11l<sub>f</sub>). Figure 7.44 shows the results of the force measurement via force transducers, the basic magnetic circuit model, and a characterized version of the basic magnetic circuit model. Each of the three subfigures in Figure 7.44 corresponds to one bias current setting as given in the subfigure heading; the topmost subfigure presents the data from the 1.5 Amp bias cases, the middle subfigure presents the data from the 1.6 Amp bias cases, and the bottom subfigure presents the data from the 1.7 Amp bias cases. The measured and calculated forces are shown in Newtons on the y-axis versus rotor speed in RPM x1000 on the x-axis. A legend is included in each plot; the measured force values from the force transducers are connected by a solid line. The force values calculated from the two models are shown as points only; the basic

magnetic circuit model results are represented by a square, and the characterized version of the basic magnetic circuit model results are represented by an asterisk. Both models track the measured trends reasonably well in Platform 2 Setup 4 case. Error values are at a maximum near the critical speed. The trend becomes stronger as bias current is increased.

Figure 7.45 shows the errors associated with the simple model and the characterized model as compared to the transducer reported values. Also shown are error bars that correspond to  $\pm 2\sigma$  uncertainty introduced by the parameterization of the data discussed in Section 7.5. The wide, shaded error bars represent error associated with the transducer curve fit, the line-style error bars represent error associated with the axis force curve fit associated with the model data. The line style error bars are shown only with the characterized model data to minimize clutter. Curve fit error associated with the basic model can be considered to be the same magnitude as the error associated with the characterized model.

Error associated with a given curve fit was calculated as the difference between the fit line and the decimated points. The length of the error bars in the graph represents four standard deviations of the error values ( $\pm 2\sigma$ ). The error is discussed further in Appendix B.

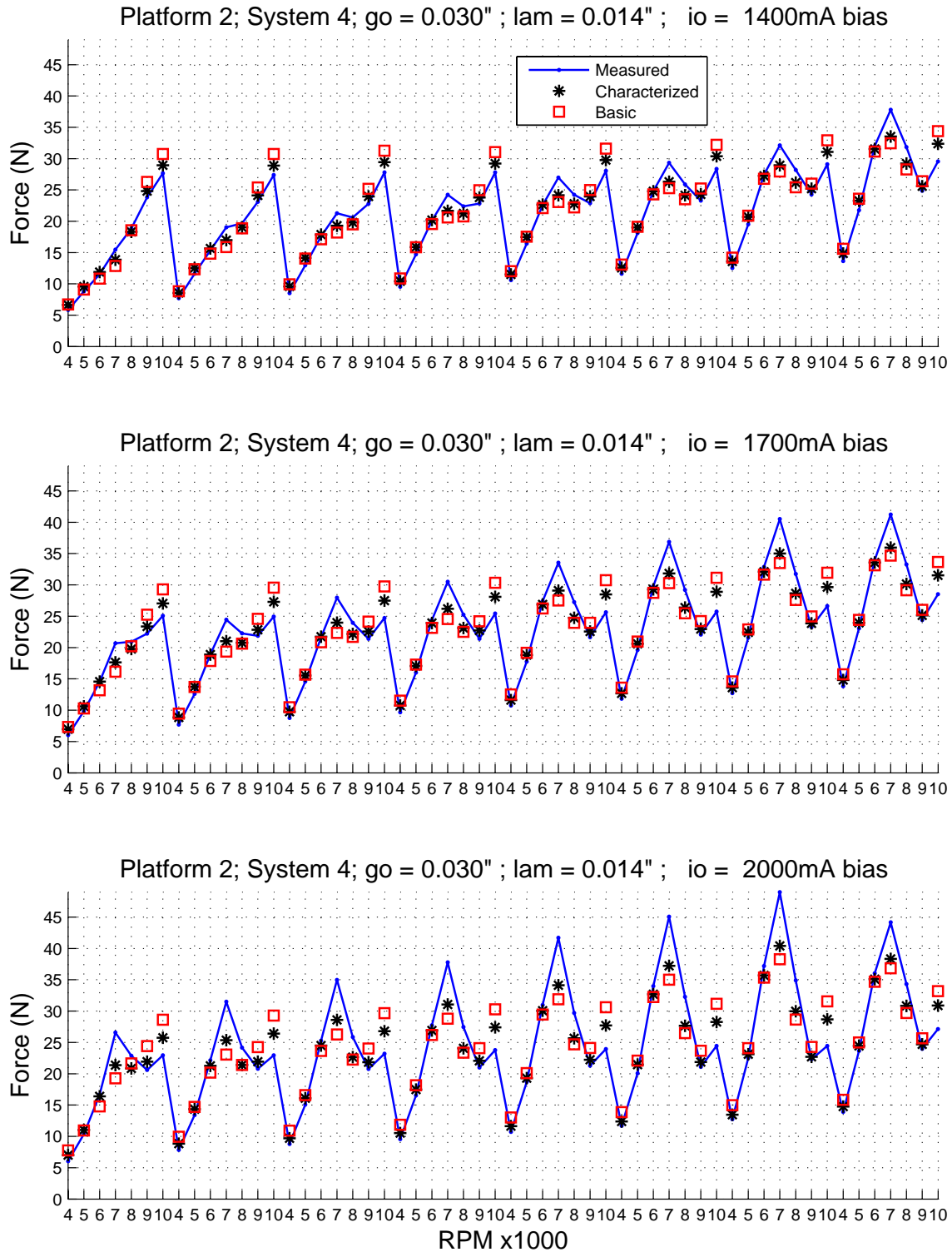
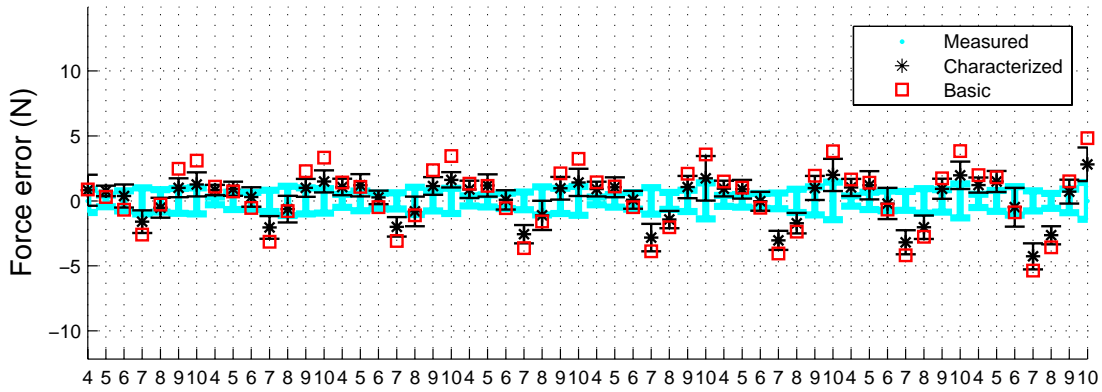
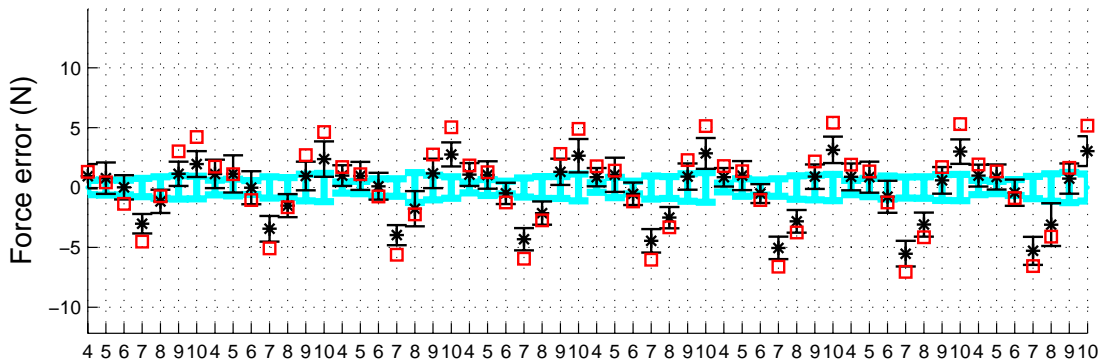


**Figure 7.44: Comparison of measured and calculated forces vs rotor speed. Platform 2 System 4. Added Unbalance (left to right) 0, 200, 300, 400, 500, 600, 700, and 800mg (0, 0.45, 0.68, 0.9, 1.13, 1.35, 1.58, 1.8 gm-in)**

Platform 2; System 4;  $g_o = 0.030''$  ;  $\lambda_m = 0.014''$  ;  $i_o = 1400\text{mA}$  bias  
 mean error characterized = 1.3; mean error simple = 2.05



Platform 2; System 4;  $g_o = 0.030''$  ;  $\lambda_m = 0.014''$  ;  $i_o = 1700\text{mA}$  bias  
 mean error characterized = 1.8; mean error simple = 2.87



Platform 2; System 4;  $g_o = 0.030''$  ;  $\lambda_m = 0.014''$  ;  $i_o = 2000\text{mA}$  bias  
 mean error characterized = 2.51; mean error simple = 3.94

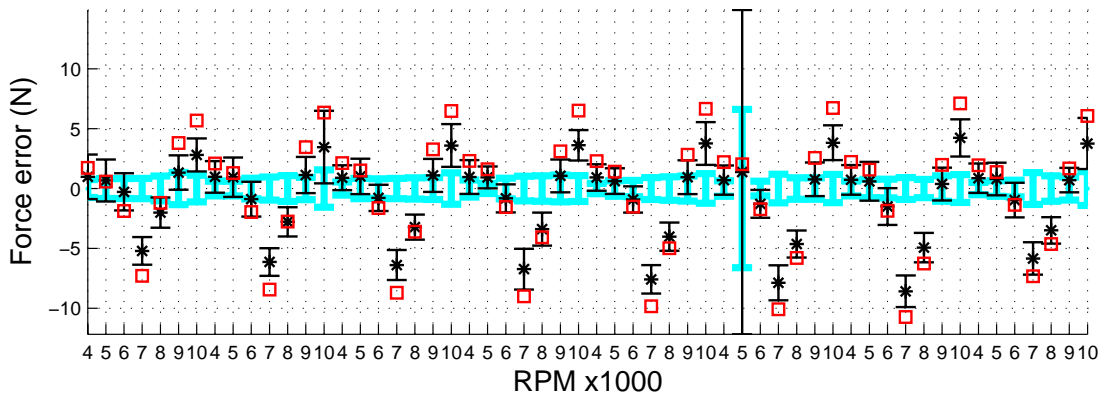


**Figure 7.45: Comparison of errors in calculated force versus rotor speed. Platform 2 System 4. Added Unbalance (left to right) 0, 200, 300, 400, 500, 600, 700, and 800mg (0, 0.45, 0.68, 0.9, 1.13, 1.35, 1.58, 1.8 gm-in)**

The error data from Figure 7.45 is broadly summarized in Table 7.7 in which error data from each model is summarized by a mean value and a maximum value. All of the values given in the table are based on a summary of absolute error values. The table is organized into three regions from left to right. The leftmost region shows the error summary of the basic and characterized models in terms of the measured unit of Newtons. The middle section expresses the error summary as a percent of the corresponding measured force. In the rightmost section, the error summary is expressed as a percentage of the maximum measured force associated with Platform 2 Setup 4. As mentioned, Table 7.7 is a summary of the error data; a complete record is appended to the end of this chapter.

The table shows that the characterized model provides a significantly better estimate of dynamic force than the basic model. Considering the direct error measurement in the leftmost column, it can be seen that the mean error associated with the characterized model is typically ~60% of the mean error associated with the basic model.

**Table 7.7: Summary of force model errors associated with Figure 7.44 and Figure 7.45.**

	Error (N)		Error as Percent of Measured Force (%)		Error as Percent of Maximum Measured Force (%)	
	Basic	Characterized	Basic	Characterized	Basic	Characterized
<b>MAXIMUM</b>	9.83	7.86	28.59	19.52	20.06	16.05
<b>MEAN</b>	2.78	1.63	13.41	6.92	5.83	3.43

### 7.6.3 Summary of Results

Differences in model accuracy appears to be most pronounced at the lowest speeds, generally below the critical speed. The characterized model offers significantly better accuracy below the critical speed. The most likely explanation is that the model was statically characterized, and the low speeds most closely represent the system state during the characterization.

As speed increases, particularly in the case of setups 1 and 3, model accuracy suffers. Due to their narrow air gaps, setups 1 and 3 are expected to be more sensitive to eddy current effects. It is possible that these effects, which are not accounted for in either model, are causing the discrepancy between the modeled and measured values in these cases. Another possible explanation, which will be discussed in Section 7.7.1, is that uncertainty in the runout correction may be causing the discrepancy.

A broad view of the results from all of the tests discussed in Section 7.6 is shown in Table 7.8; essentially a summary of Table 7.3-Table 7.7. The error data from both models is summarized by a mean value and a maximum value. All of the values given in the table are based on a summary of absolute error values. The table is organized into three regions from left to right. The leftmost region shows the error summary of the basic and characterized models in terms of the measured unit of Newtons. The middle section expresses the error summary as a percent of the corresponding measured force.

In the rightmost section, the error summary is expressed as a percentage of the maximum measured force associated with the Platform and Setup associated with the test. Table 7.8 is a broad summary of the error data; a complete record is appended to the end of this chapter.

It can be seen that the characterized model offers improved accuracy over the simple model for each test setup. In terms of estimated force values, errors associated with the characterized model are typically ~70% of the error magnitudes associated with the basic model. From a percent of measured load standpoint, errors associated with the characterized model are typically ~40% of the error magnitudes associated with the basic model.

**Table 7.8: Mean errors associated with characterized model and simple model for each test along with mean error in terms of max load**

Platform	Setup	Error (N)		Error as Percent of Measured Force (%)		Error as Percent of Maximum Measured Force (%)	
		Basic	Characterized	Basic	Characterized	Basic	Characterized
1	1	1.90	0.69	14.4	6.2	5.5	2.0
2	1	6.71	5.53	32.9	20.1	11.7	9.6
	2	1.43	1.15	15.5	9.7	4.6	3.7
	3	4.99	3.18	122	37	14	9
	4	2.78	1.71	13.4	8.2	5.8	3.6
<b>MEAN</b>		3.6	2.5	39.6	16.2	8.4	5.7

## **7.7 EFFECT OF CHARACTERIZATION ON MODEL RESULTS**

As stated in the previous section, the characterized model offers significant accuracy improvements as compared to the basic model for each test setup. In terms of estimated force values, errors associated with the characterized model are typically ~70% of the error magnitudes associated with the basic model. From a percent of measured load standpoint, errors associated with the characterized model are typically ~40% of the error magnitudes associated with the basic model. The separation in model performance is most pronounced when taken in terms of percent of measured force. The difference implies that the characterized model outperforms the basic model particularly at small force values, where the error calculation is most sensitive to absolute error. The error plots in Figure 7.39, Figure 7.41, Figure 7.43, and Figure 7.45 corroborate this. It is believed that runout aspect of the characterization plays a large role in the accuracy improvement.

### ***7.7.1 Significance of Runout Correction***

Recall that the runout correction was based on twelve applications of the MPM. The MPM was applied at twelve equally spaced rotation angles (30° separation) in order to

determine a lookup table of rotation angle dependent values of the effective origin. The  $30^\circ$  separation between runout correction sites may be considered coarse. Furthermore, an exact angular location was not enforced on the shaft; some “floating” ( $\pm 5^\circ$ ) of the shaft was noted during application of the different MPM bias currents. In order to bound the significance that angular errors may have on the results of the characterized model, a simulated perturbation was applied to the runout correction table corresponding to the setup that exhibited the worst error in terms of percent of measured load for the characterized model; Platform 2, Setup 3. It is shown below that a perturbation of  $20^\circ$  between the MPM based runout correction and the rotor angle results in significant improvement of the characterized force model. Note that a  $20^\circ$  perturbation is less than the MPM sampling angle of  $30^\circ$ .

Figure 7.46 and Figure 7.47 are similar to Figure 7.42 and Figure 7.43 except for the change in characterized model results due to the shift in runout correction. From a comparison of Figure 7.46 to Figure 7.42 and likewise comparison of Figure 7.47 to Figure 7.43 it can be seen that the artificially perturbed runout characterization provides improved results at both low and high speeds, regardless of bias current. However the model does not track the measured value at 7000 RPM, near the critical speed, particularly for the higher bias current cases.

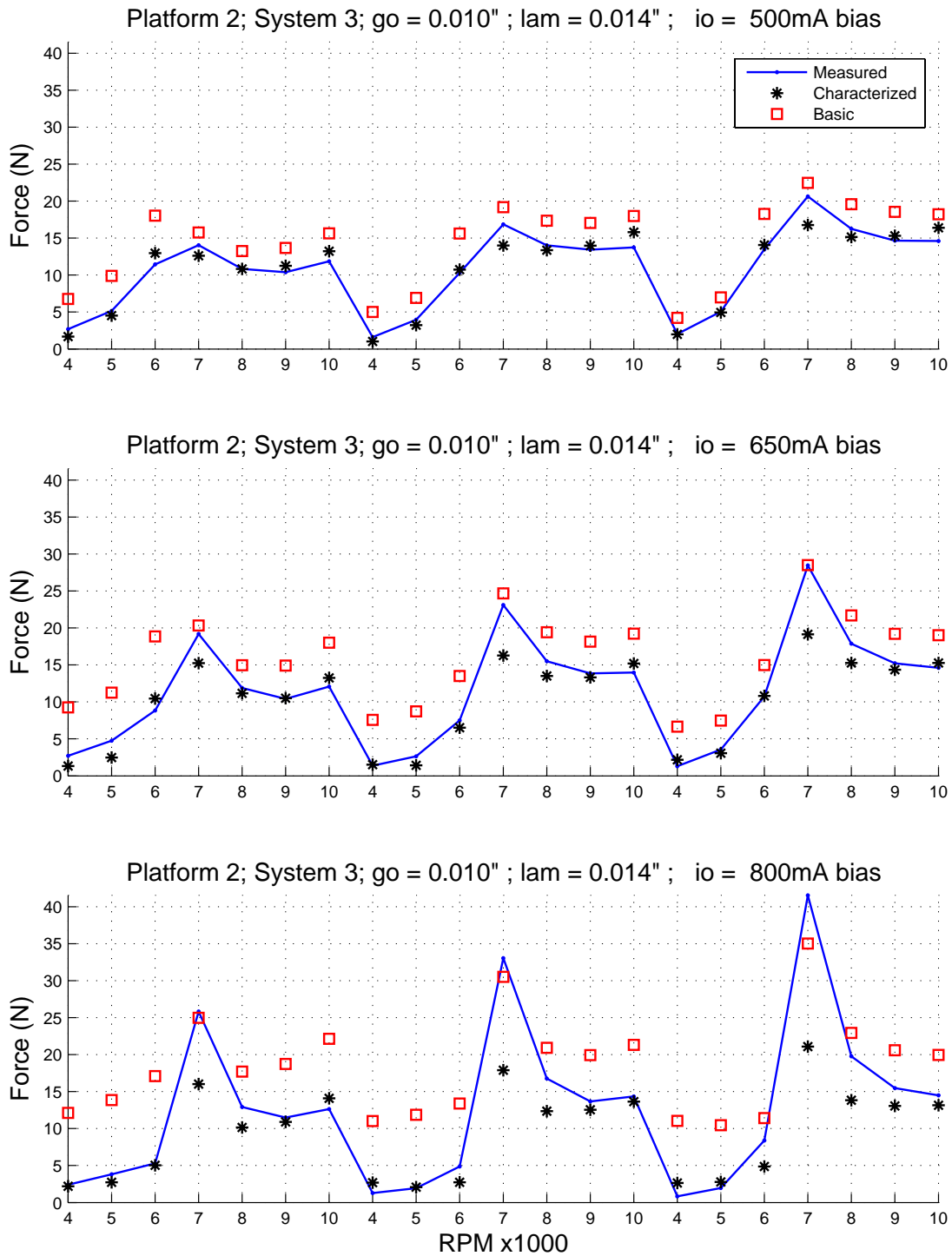


**Figure 7.46: Comparison of Measured and Calculated Forces vs Rotor Speed; (perturbed model). Platform 2 System 3. Added Unbalance (left to right) 0, 100, and 200mg (0, 0.23, 0.45 gm-in)**

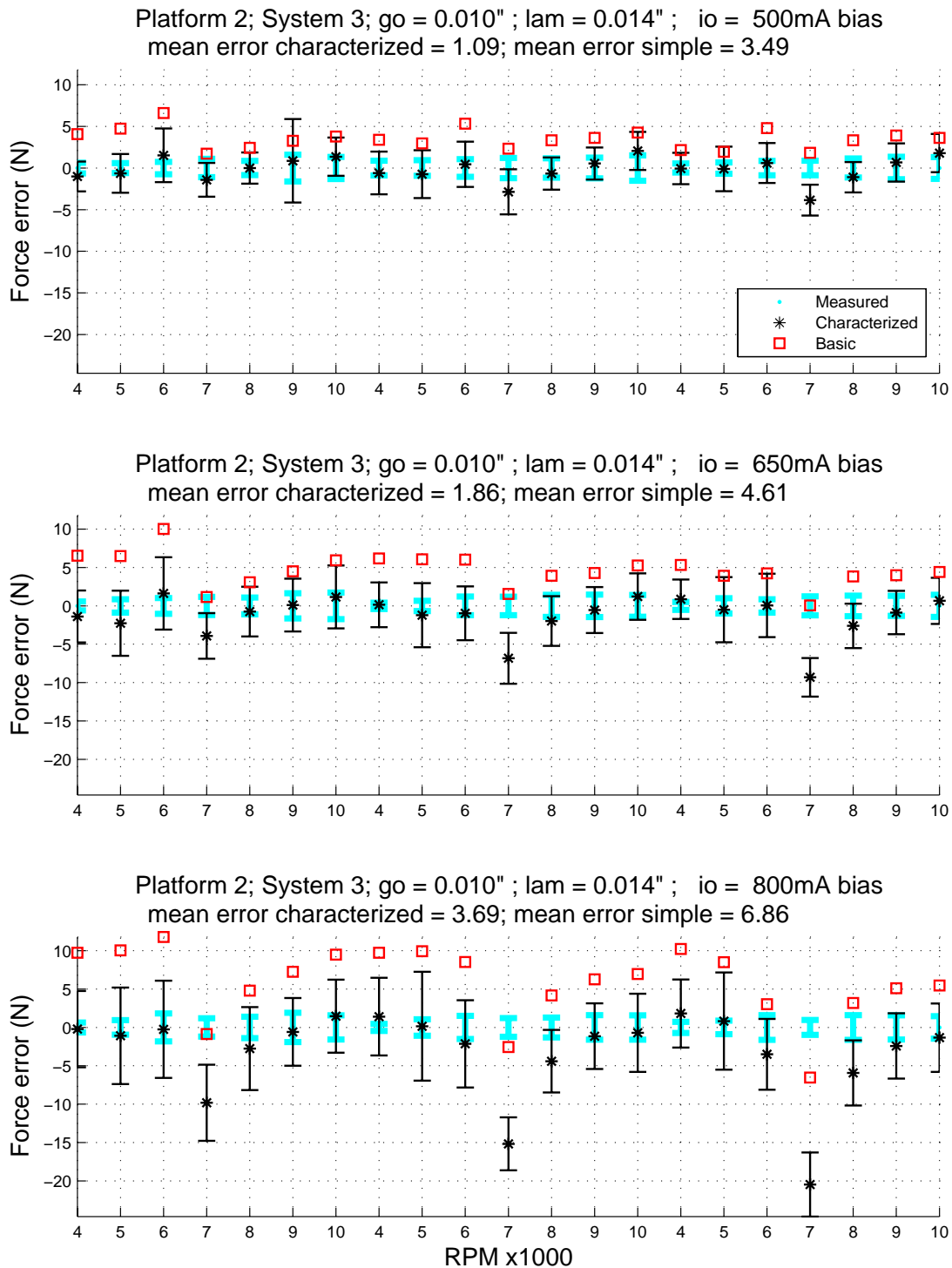


**Figure 7.47: Comparison of Errors in Calculated Force versus Rotor Speed; (perturbed model). Platform 2 System 3. Added Unbalance (left to right) 0, 100, and 200mg (0, 0.23, 0.45 gm-in)**

Table 7.9 broadly summarizes the error plot of Figure 7.47, and also shows the results associated with the original characterized model. A complete record of the results of the simulation are appended to this chapter.

**Table 7.9: Summary of basic, characterized, and perturbed force model errors associated with Figure 7.42, Figure 7.43, Figure 7.46 and Figure 7.47.**

	Error (N)			Error as Percent of Measured Force (%)			Error as Percent of Maximum Measured Force (%)		
	Simple	Characterized	20 Degree Simulated Phase Shift	Simple	Characterized	20 Degree Simulated Phase Shift	Simple	Characterized	20 Degree Simulated Phase Shift
<b>MAXIMUM</b>	11.80	20.32	20.47	1237	315	220	38	49	49
<b>MEAN</b>	4.99	3.18	2.21	122	37	23	14	9	6

The results, summarized in Table 7.9, show that a 20° shift between the MPM data and its associated rotor angle has a significant effect on the results of the characterized model. The errors associated with the perturbed model are ~60% - 70% of the errors associated with the unperturbed, characterized model. The difference in error demonstrates a strong correlation between static characterization and force model accuracy. Furthermore, it underscores the requirement that a comprehensive static calibration must be applied prior to attempting a dynamic force measurement. The effects of dynamic phenomena such as eddy current and hysteresis cannot be inferred until static effects such as runout are first compensated.

## **7.8 CONCLUSION**

This chapter introduces a library of dynamic AMB data that can be used in the development of an AMB force model that accounts for effects observed in a rotating system. The data library consists of dynamic AMB system data from five different AMBs. AMB coil current and rotor position data was collected while the supported rotor was rotating. Rotational speeds ranged from 4000–10000 RPM, data was collected while the rotor was maintained at a continuous speed. System conditions other than rotational speed were varied as well; the collected data includes scenarios in which various levels of unbalance and bias current were applied. The primary goal of the data collection was to provide a library of dynamic AMB system data for use in the development of an AMB force model that can be applied to forces observed in a rotating system. To this end, force transducers were mounted underneath the bearing housing to provide a measurement of the dynamic forces experienced by the bearing. The force transducer data can be used to audit force models.

Dynamic effects on force measurement, such as eddy current and hysteresis, are not considered in this chapter, however, two static force models were applied to the data and their results compared to the measured force provided by the force transducers. The models that were applied to the data include a basic force model that directly applies the AMB system data of coil current and rotor position, and a characterized version of the model in which a transform based on the MPM is applied to the rotor position. A broad view of these results shows that the characterized model outperforms the simple model in every case. In terms of estimated force values, errors associated with the characterized model are typically ~70% of the error magnitudes associated with the basic model. From a percent of measured load standpoint, errors associated with the characterized model are typically ~40% of the error magnitudes associated with the basic model.

It is believed that the runout aspect of the characterization plays a large role in the accuracy improvement. In order to bound the significance that angular errors introduced during runout characterization may have on the results of the characterized model, a simulated perturbation was applied to the runout correction table corresponding to one of the test rotors. The errors associated with the perturbed model are shown to be ~60% - 70% of the errors associated with the unperturbed, characterized model. The difference demonstrates a strong correlation between static runout characterization and force model accuracy. Furthermore, it underscores the requirement that a comprehensive static calibration must be applied prior to attempting a dynamic force measurement. The effects of dynamic phenomena such as eddy current and hysteresis cannot be determined until static effects such as runout are first compensated.

## Chapter 8 Conclusions and Recommendations

In broad terms, the experiments that were performed as part of this research can be put into one of two classifications: static or dynamic. Static experiments were performed on the AMB experimental systems without shaft rotation and with the motor uncoupled from the shaft. The motivation behind the static experiments was to identify system parameters that can be applied in conjunction with a simple AMB force model to generate a characterized model with improved force measurement accuracy. Dynamic experiments were performed with the added element of a shaft rotation. The motivation behind the dynamic experiments was to observe how the accuracy of the force measurement based on the characterized model varied as other system parameters such as rotational speed, bias current, and unbalance load were varied. For comparison, a non-characterized model was also applied to the dynamic force measurement. The force measurement results from each model were compared to measured values of force provided by force transducers.

The conclusions are summarized here, additional details can be found below.

### **A magnetic circuit force model that relies on measurement of coil current and rotor position can be characterized to increase model accuracy**

- System Identification allows the model to be characterized without knowledge of bearing load
- Characterization can be applied as a function of shaft rotation angle to account for runout
- Force measurement errors associated with characterized model are ~30% less than force measurement errors associated with basic model
- Force measurement errors associated with characterized model are ~60% less than force measurement errors associated with basic model if taken as a percentage of measured load

### **Characterization methods developed here provide useful diagnostics for field tuning of AMBs**

- Effective origin

- Runout

## **8.1 TEST SYSTEMS**

The experiments described here were carried out on 5 separate AMB systems that were based on two platforms. The first platform (Platform 1) is a typical high-speed laboratory rotor kit from Revolve Magnetic Bearings and has a 0.015in. radial gap and 0.014in. rotor laminations. One system was tested on this platform. The second platform (Platform 2) is a custom built magnetic bearing test bed, also built by Revolve Magnetic Bearings. This platform was designed with a common stator and four interchangeable rotors. Each rotor has a unique combination of nominal air gap and lamination thickness. In this way, Platform 2 can be configured as 4 unique systems.

1. 0.010 inch radial gap, 0.005 inch lamination (Arnon 5)
2. 0.030 inch radial gap, 0.005 inch lamination (Arnon 5)
3. 0.010 inch radial gap, 0.014 inch lamination (M19)
4. 0.030 inch radial gap, 0.014 inch lamination (M19)

Additional specifications for each test system are found in Chapter 3.

## **8.2 STATIC CHARACTERIZATION**

The static characterization developed here has three components; location of the effective origin, determining the change in the effective origin as a function of shaft rotation angle to account for runout, and a coordinate transform. Each of the static characterizations are based on a system identification technique known as the Multi-Point Method (MPM). The MPM is a perturbation technique that when applied to a non-rotating, statically loaded AMB in conjunction with a basic magnetic circuit based model can be used to identify bearing load as well as an infer an “effective” rotor position.

### ***8.2.1 Effective origin***

The effective origin is the position at which the MPM force model behaves as if the rotor is at position (0,0). Identification of this location is the first step in characterizing the model as it establishes the origin of the effective coordinates.

### ***8.2.2 Runout Identification***

The effective origin identification can be applied for a range of shaft rotation angles. Each rotational position of the shaft will result in a different calculated value of the effective origin due to runout. Sensor runout, due to surface or sub-surface anomalies in the sensor target, causes changes in position probe signals that are not related to real changes in the position of the rotor. Another form of runout results from non-collocation between the rotor position sensors and the stator. Typically, the rotor position sensors are axially offset from the stator. In the case of a bowed rotating shaft, if the rotor

position stays constant at the location of the position sensors, non-collocation will lead to runout of the portion of the rotor that is aligned with the stator.

The AMB controller reacts to runout as it would react to a real change in rotor position; control currents are applied as necessary to move the rotor to the location for which the position probe signals indicate zero offset. MPM based runout identification can be used to compensate the rotor position sensor input in order to eliminate the controllers response to the runout signal.

### **8.2.3 Coordinate Transform**

Application of the MPM at a variety of rotor position reveals that the effective positions determined by the MPM are not in agreement with the rotor position reported by the rotor position sensors. A coordinate transform was introduced to generalize the relationship between effective rotor position determined through perturbation and the rotor position reported by the controller. The coordinate transformation provides a way to estimate the effective rotor position based on instantaneous system measurements. In this way force measurements with roughly the same accuracy as MPM based force measurements can be made “on the fly” since the MPM force value can be directly calculated given an estimated effective rotor location. This was a key step to application of an MPM based force measurement technique to the measurement of dynamic forces.

When the coordinate transform technique was applied to non-rotating systems that were supporting static loads, force measurements could be with 2% - 6% mean error, and an associated standard deviation of 2% - 7%. If the coordinate transformation was not applied, the model produced static force measurements with 3% - 22% mean error, and an associated standard deviation of 10% - 31%.

## **8.3 FORCE MEASUREMENT IN ROTATING SYSTEMS**

Two static force models were applied to the data and their results compared to the measured force provided by the force transducers. The models that were applied to the data include a basic force model that directly applies the AMB system data of coil current and rotor position, and a characterized version of the model in which a transform based on the MPM is applied to the rotor position. A broad view of these results shows that the characterized model outperforms the basic model in every case. In terms of estimated force values, errors associated with the characterized model are typically ~70% of the error magnitudes associated with the basic model. From a percent of measured load standpoint, errors associated with the characterized model are typically ~40% of the error magnitudes associated with the basic model.

It is believed that the runout aspect of the characterization plays a large role in the accuracy improvement. In order to bound the significance that angular errors introduced during runout characterization may have on the results of the characterized model, a simulated perturbation was applied to the runout correction table corresponding to one of the test rotors. The errors associated with the perturbed model are shown to be ~60% - 70% of the errors associated with the unperturbed, characterized model. This demonstrates a strong correlation between static runout characterization and force

model accuracy. Furthermore, it underscores the requirement that a comprehensive static calibration must be applied prior to attempting a dynamic force measurement. The effects of dynamic phenomena such as eddy current and hysteresis cannot be determined until static effects such as runout are first compensated.

## **8.4 FUTURE WORK AND RECOMMENDATIONS**

The work to date has been iterative; initial static work with the MPM was followed by a dynamic force measurement pilot study. Following the pilot study, a series of static characterizations were formulated, these were recently applied to dynamic load cases. The future work in this area should continue to follow this pattern.

### ***8.4.1 Recommendations for Static Testing***

- address runout with greater precision
- increase angular density of MPM application
- apply a mass to balance disk bottom to minimize angular float
- broader testing of static characterization methods
- dense rotor position location matrix through wide range of volume
- compare results to results of other current-based models
- reluctance method
- other method that does not assume a lumped gap
- explore a different formulation of static characterization
- current “coordinate transformation” approach is a convenient analogy to a real, physical phenomenon
- attempt a correction as a function of pole face area similar to the Joe Imlach’s fringing factor (Imlach et al., 2000)

### ***8.4.2 Recommendations for Dynamic Testing***

- rotate bearing housing 45° to eliminate cross-coupling of  $V$ -axis with  $W$ -axis
- apply signal injection to non-rotating bearing as a means to characterize dynamic effects from non-rotational sources
- initially concentrate on narrow air gap bearings such as Platform 2 Setups 1 and 3
- greatest potential for improvement relative to recent tests
- most likely to exhibit dynamic flux generation effects
- find out if errors from recent test are due to uncertainty in static characterization or something else

### ***8.4.3 Global Recommendations***

Future research should explore avenues to apply the static characterization techniques, particularly the effective origin and runout characterizations, to bearings that are currently in service or that more closely resemble bearings that are currently in service.

Such experience can be used as a guide to direct how to best make the techniques broadly applicable as well as confirm or deny the real value of the techniques.

## References

- Aenis, M., and Nordmann, R. (2000), "Active Magnetic Bearings for Fault Detection in a Centrifugal Pump," *7<sup>th</sup> International Symposium on Magnetic Bearings*, Zurich, Switzerland.
- Allaire, P.E., Maslen, E.H., Humphris, R.R., Knospe, C.R., and Lewis, D.W. (1993), "Magnetic Bearings", *STLE Handbook of Tribology and Lubrication*, Volume III, R. Booser (Editor).
- Allaire, P.E., Fittro, R.L., and Maslen, E.H. (1995), "Measured Force/Current Relations in Solid Magnetic Thrust Bearings", *International Gas Turbine and Aeroengine Congress and Exposition*, Houston, TX, ASME Paper 95-GT-400.
- Baun, D.O. and Flack, R.D. (1999), "A Plexiglas Research Pump with Calibrated Magnetic Bearings/Load Cells for Radial and Axial Hydraulic Force Measurement", *Journal of Fluids Engineering* 121.
- Baun, D.O., Fittro, R.L., and Maslen, E. H. (1996), "Force Versus Current and Air Gap Calibration of a Double Acting Magnetic Thrust Bearing", *International Gas Turbine and Aeroengine Congress and Exhibition*, Birmingham, UK, ASME Paper 96-GT-121.
- de Callafon, R.A., de Roover, D., Van den Hof, P.M.J. (1996), "Multivariable Least Squares Frequency Domain Identification using Polynomial Matrix Fraction Descriptions", *Proceedings of the 35<sup>th</sup> Conference on Decision and Control*, Kobe, Japan.
- Department of Electrical Engineering, Massachusetts Institute of Technology (1943), *Magnetic Circuits and Transformers*, John Wiley and Sons Inc, New York, NY.
- Fittro, R.L., Baun, D.O., Maslen, E.H., and Allaire, P.E. (1997), "Calibration of an 8-Pole Radial Magnetic Actuator", *International Gas Turbine and Aeroengine Congress and Exposition*, Orlando, FL, ASME Paper 97-GT-18.
- Gahler, C. and Forch, P. (1994), "A Precise Magnetic Bearing Exciter For Rotordynamic Experiments", *4<sup>th</sup> International Symposium on Magnetic Bearings*, ETH Zurich.
- Goodwin, G.C. and Payne, R.L. (1977), *Dynamic System Identification: Experiment Design and Data Analysis*, Academic Press Inc, New York, NY.
- Hammond, P. (1978), *Electromagnetism for Engineers*, Pergamon Press Inc, Elmsford, NY.

- Hsia, T.C., (1977), *System Identification*, Lexington Books, D.C. Heath and Company, Lexington, MA.
- Imlach, J., Kasarda, M.E.F., and Balaji, P.A. (2000), "Enhancements to AMB Force Measurement Procedures for Application to a Rocket Thrust Measurement System", *International Gas Turbine and Aeroengine Congress and Exhibition*, Munich, Germany, ASME Paper 2000-GT-414.
- Jansen, R.H., Wagner, R.C., Duffy, K.P., Hervol, D.S., Storozuk, R.J., Dever, T.P., Anzalone, S.M., Trudell, J.J., and Konno, K.E. (2002), "Redesign of Glenn Research Center D1 Flywheel Module", *37<sup>th</sup> Intersociety Energy Conversion Engineering Conference*, IEEE Electron Devices Society, Washington, D.C.
- Kasarda, M.E.F., Imlach, J., and Balaji, P.A. (2000), "The Concurrent Use of Magnetic Bearings for Rotor Support and Force Sensing for the Nondestructive Evaluation of Manufacturing Processes", *SPIE's 7<sup>th</sup> International Symposium on Smart Structures and Materials*, Newport Beach, CA.
- Kasarda, M.E.F. (1997), *The Measurement and Characterization of Power Losses in High Speed Magnetic Bearings*, PhD dissertation, University of Virginia, VA.
- Kim, C.-S. and Lee, C.-W. (1997), "In Situ Runout Identification in Active Magnetic Bearing System by Extended Influence Coefficient Method", *IEEE/ASME Transactions on Mechatronics* 2(1).
- Knopf, E. and Nordmann, R. (2001), "Identification of the Dynamic Characteristics of Turbulent Journal Bearings", *8<sup>th</sup> ISROMAC*, Honolulu, HI.
- Knopf, E., and Nordmann, R. (1998), "Active Magnetic Bearing for the Identification of Dynamic Characteristics of Fluid Bearings – Calibration Results", *Proceedings of the Sixth International Symposium on Magnetic Bearings*, Cambridge, MA, pp. 52-61.
- Marshall, J.T., Kasarda, M.E.F., and Imlach, J. (2001), "A Multi-Point Measurement Technique for the Enhancement of Force Measurement With Active Magnetic Bearings", *Proceedings of TURBOEXPO2001*, ASME TURBO EXPO 2001, New Orleans, LA.
- Meeker, D.C., Maslen, E.H., and Noh, M.D (1996), "An Augmented Circuit Model for Magnetic Bearings Including Eddy Currents, Fringing, and Leakage", *IEEE Transactions on Magnetics* 32(4).
- Moffat, R.J. (1988), "Describing the Uncertainties in Experimental Results", *Experimental Thermal and Fluid Science* 1, pp. 3-17.
- Namuerikawa, T., Shinozuka, W., and Fujita, M. (2004), "Disturbance and Initial State Uncertainty Attenuation Control for Magnetic Bearings", *9<sup>th</sup> International Symposium on Magnetic Bearings*, Lexington, KY.
- Plonus, M.A. (1978), *Applied Electromagnetics*, McGraw Hill Inc, New York, NY.
- Prins, R.J., Kasarda, M.E.F., and Bates Prins, S.C. (2005), "A System Identification Technique Using Bias Current Perturbation for Determining Radial Magnetic Center of Active Magnetic Bearings", Submitted to *ASME Journal of Vibration and Acoustics*.
- Prins, R.J. and Kasarda, M.E.F. (2004), "Investigation of Current-Based Dynamic Force Measurement with Active Magnetic Bearings", *9<sup>th</sup> International Symposium on Magnetic Bearings*, Lexington, KY.
- Rippy, M., Proto Laminations Inc., Santa Fe Springs, CA 90670.
- Schroder, P., Green, B., Grum, N., and Fleming, P.J. (2001), "On-line evolution of robust control systems: an industrial active magnetic bearing application", *Control Engineering Practice* 9(1), pp. 37-49.

- Schweitzer, G., Bleuler, H., and Traxler, A. (1993), *Active Magnetic Bearings*, Verlag der Fachvereine, Zurich, Switzerland.
- Serway, R.A. (1986), *Physics for Scientists and Engineers with Modern Physics*, 2<sup>nd</sup> Edition, Saunders College Publishing, Philadelphia, PA.
- Setiawan, J.D., Mukherjee, R., and Maslen, E.H. (2001), "Adaptive Compensation of Sensor Runout of Magnetic Bearings With Uncertain Parameters: Theory and Experiments", *Journal of Dynamic Systems, Measurement, and Control* 123.
- Sortore, C., Allaire, P., Maslen, E., Humphris, R., and Studer, P. (1990), "Permanent Magnet Biased Magnetic Bearings Design, Construction, and Testing", *Second International Symposium on Magnetic Bearings*, Tokyo, Japan, pp. 175-182.
- Various authors, (1996), "Special Issue on Magnetic Bearing Control", *IEEE Transactions on Control System Technology* 4(5).
- Vining, G.G. (1998), *Statistical Methods for Engineers*, Duxbury Press, Brooks/Cole Publishing, Pacific Grove, CA.
- Wu, F. (2001), "Switching LPV Control Design for Magnetic Bearing Systems", *Proceedings of the 2001 IEEE International Conference on Control Applications*, Mexico City, Mexico.
- Zutavern, Z.S. and Childs, D.W. (2004), "Fiber-Optic Strain Gauge Calibration And Dynamic Flexibility Transfer Function Identification in Magnetic Bearings", *9<sup>th</sup> International Symposium on Magnetic Bearings*, Lexington, KY.

## Appendix A Mechanisms that Affect Force Measurement in Rotating Systems

The general case of bearing loads in rotating machinery includes dynamic forces. Dynamic forces due to rotating unbalance cause the rotor to move in an orbit that is synchronous with the speed of rotation. Consider a single axis of an AMB, as shown in Figure 1.4 repeated below, for the case of a cyclic orbit. Shaft orbit implies that the air gaps of  $g_{upper}$  and  $g_{lower}$ , will vary with time. The controller will respond to the position perturbation resulting in time varying values of  $i_{upper}$  and  $i_{lower}$ . Variation of coil currents leads to hysteresis, eddy current, and skin effect. The effects of a time varying flux can be read about in detail in MIT (1943), Plonus (1978), Hammond (1978), Serway (1986) and Kasarda (1997). The following sections are included to provide a brief synopsis of such effects.

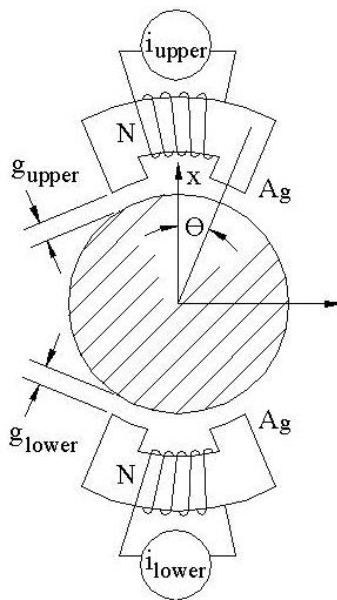
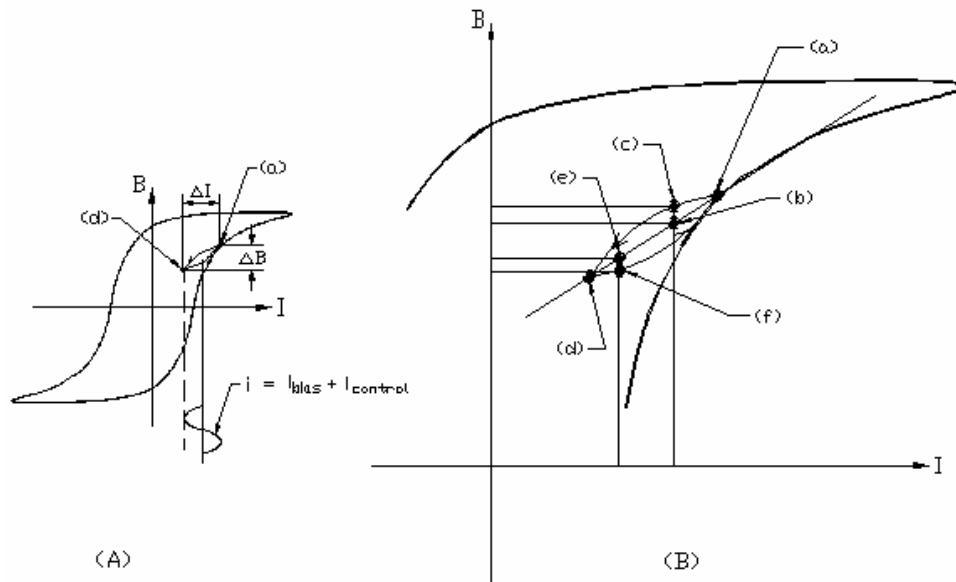


Figure 1.4: Typical AMB force axis

## A.1 HYSTERESIS

The time varying electric field applied to the core material as a result of fluctuation of the coil currents  $i_{upper}$  and  $i_{lower}$  results in a time varying magnetic flux density as shown in Figure A.1. The figure shows a typical magnetization curve for a core material; magnetic flux density  $B$  is a function of applied coil current  $i$ . In the case of a dynamic load, the current  $i$  will vary as represented by the sinusoidal current shown in the figure. The cyclic current causes a cyclic flux density. However, the reversal of current results in a hysteresis loop as shown in the figure. The area encompassed by the hysteresis loop represents energy that is lost due to a varying coil current.

Study of hysteresis effects is traditionally related to transformers, generators, electric motors, and other equipment used to generate or convert electric power. For these cases, hysteresis effects are considered a net power loss since energy is lost every cycle.



**Figure A.1: Hysteresis due to cyclic coil current**

Examination of Figure A.1 shows that from a dynamic force measurement perspective, hysteresis could lead to either an over-prediction or an under-prediction of flux density  $B$ , leading to either an over-prediction or an under-prediction of force. For instance, assume that the current cycle shown in the figure and described as  $i$  is the coil current associated with an upper actuator such as that depicted by Figure 1.4. Such a current cycle would be observed in the case of a dynamic load. Point (a), represents the moment in time that maximum current  $i$  and maximum flux density  $B$  occur. Current  $i$  is reduced as time advances. Point (b) represents the theoretical value of flux density a short time later; point (c) represents the true flux density at the same time instant by taking hysteresis into account. It can be seen that the true value of flux density is greater than the theoretical flux density. This means that a force calculation that does not account for hysteresis will under-predict the true force value for this scenario.

On the other hand, consider a similar situation later in the current cycle. Point (d), represents the moment in time that minimum current  $i$  and minimum flux density  $B$  occur. Current  $i$  is increased as time advances. Point (e) represents the theoretical value of flux density a short time later; point (f) represents the true flux density at the same time instant by taking hysteresis into account. It can be seen that the true value of flux density is less than the theoretical flux density in this case. This means that a force calculation that does not account for hysteresis will over-predict the true force value for this scenario.

## **A.2 EDDY CURRENT**

Recall that variation in rotor position and the resulting variation in coil current contribute to variation in the magnetic flux density in the air gap (Equation A.1).

$$B = \frac{\mu_o NI}{g} \quad (\text{A.1})$$

Faraday's law, shown in Equation A.2, states that variation in magnetic flux results in a voltage gradient.

$$\varepsilon = -\frac{d\phi}{dt} \quad (\text{A.2})$$

In a magnetic bearing, variation in the magnetic flux within the core material will cause a voltage gradient within the core. The voltage gradient will result in a current flow through the core material in accordance with Ohm's law.

$$\varepsilon = i_e R \quad (\text{A.3})$$

The current generated in this way is known as an eddy current. Direct calculation of eddy current requires a value of material resistance,  $R$ . In the case of a wire, the resistance depends on the wire material resistivity  $\rho$ , the wire length  $L$ , and the cross sectional area of the wire  $A$ .

$$R = \frac{\rho L}{A} \quad (\text{A.4})$$

Material resistance models exist for the calculation of eddy currents (Hammond, MIT). A typical model is shown in Figure A.2. A changing magnetic flux  $d\phi/dt$  is applied to a plate of material with resistivity  $\rho$ . The plate has dimensions of  $w$  wide,  $C$  long, and  $t$  thick. To determine the total resistance to eddy current, first consider the resistance of a narrow band of material of thickness  $dx$  and as long as the plate,  $C$ . The current path length of the band is  $\sim 2w$  if material thickness is neglected. The resistance  $dR$  of this band of material can be calculated from Equation A.4.

$$dR = \frac{\rho 2w}{C dx} \quad (\text{A.5})$$

From Equations A.3 and A.5 an equation for  $di_e$  can be written.

$$di_e = \frac{\varepsilon}{dR} = \frac{\varepsilon C dx}{2\rho w} \quad (\text{A.6})$$

Equation A.6 can then be integrated to account for the total eddy current in the material.

$$i_e = \int_0^{t/2} \frac{\epsilon C}{2\rho w} dx = \frac{\epsilon C}{2\rho w} \int_0^{t/2} dx = \epsilon \frac{Ct}{4\rho w} \tag{A.7}$$

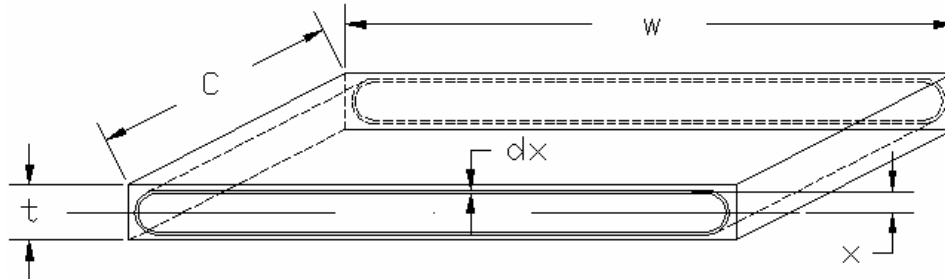


**Figure A.2: Model of eddy current path**

Due to their circulating nature, eddy currents act to generate an additional flux. The magnitude of the additional flux can be calculated from the model described by Equation A.1. The direction of the flux that is generated by eddy current is found from Lenz’s law. Lenz’s law states that changes to an applied flux will produce a voltage gradient whose polarity will produce a current that generates a magnetic flux in opposition to the change in applied flux.

As an example, consider a bar of material in a field of magnetic flux  $\phi$  as shown in Figure A.3. For both bars shown, the direction of the flux is into the page as indicated by the arrow and the ‘x’s on the face of the bars, The bar on the left (a) is experiencing an increase to the applied flux, the bar on the right (b) is experiencing a decrease in applied flux. If the magnetic flux  $\phi$  is increasing at a rate  $\frac{d\phi}{dt}$  in bar (a), the resulting voltage gradient predicted by Faraday’s law will produce eddy current that will in turn generate an additional flux. According to Lenz’s law, the additional flux will be opposite in sense to the flux gradient  $\frac{d\phi}{dt}$ , which in case (a) is also opposite to the direction of the applied flux field. In case (b), the applied flux is decreasing at a rate  $\frac{d\phi}{dt}$ . In this case Lenz’s law determines that the additional flux generated by the eddy current will have the same sense as the applied flux.

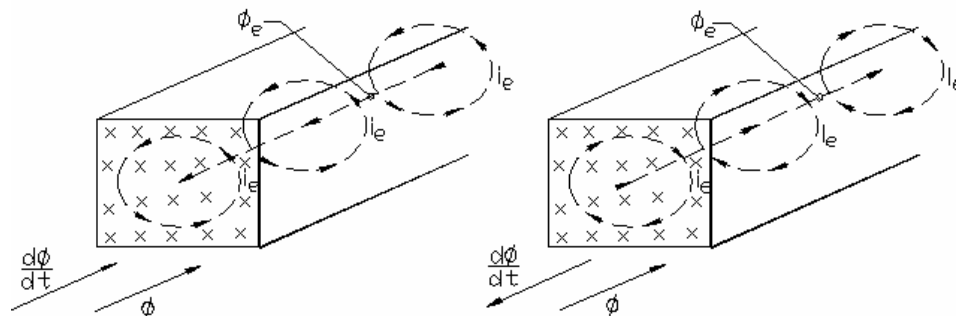


**Figure A.3: Direction of flux generated by eddy current  $i_e$  (Lenz’s Law)**

The implication to AMB based force measurement is that a simple calculation of flux that does not account for eddy currents will be in error. In some cases the simple calculation will over-predict the flux value such as in (a), in other cases the simple calculation will under-predict the flux value such as in (b).

Study of eddy current effects is traditionally related to transformers, generators, electric motors, and other equipment used to generate or convert electric power. For these cases, eddy current effects are considered a net loss, since they always oppose the direction of  $d\phi/dt$ . It is important to note that they can either reduce or increase the magnetic flux in the circuit; from an instantaneous force measurement standpoint they can represent a gain or a loss

### **A.3 SKIN EFFECT**

Skin effect, is typically discussed in terms of high frequency signal transmission lines and cables (Plonus, 1978). Skin effect refers to the tendency of eddy current magnitude to decrease exponentially at locations progressively further from a materials surface. The skin depth,  $\delta$ , is the depth at which the eddy current has decreased by a factor of  $1/e$ . Skin depth is a function of magnetic field frequency and can be calculated from the following equation.

$$\delta = \frac{1}{(\pi f \mu_o \sigma)^{1/2}} \quad (\text{A.8})$$

where:

$f$  = magnetic field frequency

$\mu_o$  = permeability of free space

$\sigma$  = conductivity of host material (=  $1/\rho$  where  $\rho$  = resistivity)

The highest frequency applied in this research was 167 Hz (10000RPM), the rotor/stator material with the least resistivity (Arnon5) has a resistivity of  $40\mu\Omega\cdot\text{cm}$  ( $0.4\mu\Omega\cdot\text{m}$ ) leading to a conductivity of  $2.5\text{e}6$ . These values are substituted into Equation A.8 below.

$$\delta = \frac{1}{(\pi f \mu_o \sigma)^{1/2}} = \frac{1}{(\pi \cdot 167 \cdot 4\pi \cdot 10^{-7} \cdot 2.5 \cdot 10^6)^{1/2}} = \frac{1}{40.6} = 0.024\text{m} \approx 1''$$

This result shows that the smallest skin depth encountered in this research is roughly 70 times greater than the lamination thickness of 0.014in. Due to the large skin depths at our operation frequencies, skin effect is not expected to impact our measurements.

## Appendix B Uncertainty Analysis

### **B.1 UNCERTAINTY IN BRIEF**

“Uncertainty Analysis” is the study of components that contribute to variation between a measurement and its true value. Uncertainty is generally described as a range or tolerance about a measured value. Calculations that rely on multiple measurements accrue uncertainty as a function of the individual uncertainties associated with each measured term. The basic techniques used here for determining an aggregate uncertainty are taken from ‘Describing the Uncertainties in Experimental Results’ (Moffat, 1988). Moffat suggests setting uncertainty values such that the odds are 20:1 that the measurement will fall within the uncertainty limits. This is equivalent to applying a 95% confidence interval, or  $\pm 2$  standard deviations ( $\pm 2\sigma$ ). In the work of Moffat, uncertainty is described as having two components, fixed and random. The fixed component accounts for terms that are being used as constants, but may be in error by some amount. A relevant example for this research may be the assumed value for the relative permeability of the electro-magnetic core material,  $\mu_r$ . This type of error is also referred to as bias error. The random error component accounts for errors that arise from sampling a signal. For this research a relevant example is the measurement of the coil current. Such errors are also referred to as precision errors and can be estimated using statistical methods.

Moffat also outlines methods for determining the uncertainty in a result that is a function of multiple parameters, each of which has associated fixed and random error. The first method involves taking the partial derivative of the result with respect to each input parameter. This technique provides a ‘sensitivity coefficient’ for each input term. The overall uncertainty of the result can be calculated by multiplying each sensitivity coefficient by the uncertainty associated with its input term. These results are conglomerated into a final uncertainty using a root sum square approach. The sensitivity coefficient method is mentioned because it is familiar to many engineers. Although this technique is elegant it does not lend itself well to more complex situations.

For a more complex situation, Moffat recommends using the same computer code used to perform data analysis to determine uncertainties. In this case, nominal or representative input terms are perturbed individually in order to observe their effect on the value of the result. The amount of perturbation of a given term corresponds to the

amount of error associated with that term so that the observed effect on the final result will be the amount of error due to the uncertainty in the perturbed term. The overall uncertainty is taken as the root sum square of the result variations introduced by the perturbations.

## **B.2 OVERVIEW OF CALCULATIONS REQUIRED FOR FORCE MEASUREMENT**

Calculations of AMB force are developed from a magnetic circuit model in Chapter 1. The equation used to describe this model is repeated below.

$$F = \mu_o AN^2 \cos \theta \left( \frac{i_{upper}^2}{(2(g_o - x \cos \theta) + b)^2} - \frac{i_{lower}^2}{(2(g_o + x \cos \theta) + b)^2} \right) \quad (1.13)$$

In Equation 1.13, certain values that are assumed to be constant have been “bundled” for simplicity, they are:

$$b = \frac{L_i}{\mu_r} \quad (1.12)$$

where:

$\mu_o$  = magnetic permeability of air

$A$  = area of pole face

$N$  = number of wire turns on actuator coil

$\theta$  = angle between bearing axis and axis of an individual magnetic pole.

$i_{upper}$  = coil current in upper actuator

$i_{lower}$  = coil current lower actuator

$g_o$  = nominal air gap

$x$  = rotor displacement along bearing axis

$b = L_i / \mu_r$  = equivalent air gap due to the flux path through the rotor and stator

$L_i$  = approximation of flux path through rotor and stator

$\mu_r$  = the relative permeability of the rotor and stator material (relative to  $\mu_o$ )

In general, the terms in Equation 1.13 are either constants or are directly measured. The exception is the  $x$  term. This term is used to describe the position of the rotor as an offset from some origin. The value of  $x$  for any specific rotor location can be determined via system identification. In this research, a characterization of the system identification is developed that allows values of  $x$  to be estimated without the requirement of an individual system identification. The characterization of  $x$  acts as a coordinate transformation. Development of the coordinate transformation requires several individual system identifications of rotor position. During this process the rotor is translated to specific positions within the stator volume.

In order to account for the uncertainty in the force measurement, we must first account for the uncertainty in the coordinate transformation. In order to account for uncertainty in the coordinate transformation, we must first account for uncertainty in the individual system identifications of rotor position,  $x$ .

### **B.2.1 Identification of Rotor Position**

The system identification of  $x$  is based on Equation 2.6. Further discussion of the development of Equation 2.6 is found in Chapter 2.

$$x = \frac{1}{\cos \theta} \left[ \frac{2g_o + b}{i_{lower,1}^2 - i_{lower,2}^2 - i_{upper,1}^2 + i_{upper,2}^2} \right] * \left[ \frac{i_{lower,1}^2 - i_{lower,2}^2 + i_{upper,1}^2 - i_{upper,2}^2}{2} \pm \sqrt{(i_{lower,1}^2 - i_{lower,2}^2)(i_{upper,1}^2 - i_{upper,2}^2)} \right] \quad (2.6)$$

From Equation 2.6 it can be seen that the value of  $x$  is based on measured values ( $i_{lower,1}$ ,  $i_{lower,2}$ ,  $i_{upper,1}$ ,  $i_{upper,2}$ ), system constants ( $L_i$ ,  $g_o$ ,  $\theta$ ), and a material property ( $\mu_r$ ). The uncertainty in a single rotor position identification is based on uncertainty in these terms.

### **B.2.2 Development of Characterization of Rotor Position Identification**

The system identification method is used to identify an effective value of rotor offset,  $x$ . If the system identification of rotor position is applied at several well chosen rotor locations, a generalization of the relationship between the identified rotor locations and the rotor locations reported by the system sensors can be established. This is discussed at length in Chapter 2 and Chapter 5. The generalized relationship has the form of a coordinate transformation. The transformation consists of an origin offset, an axes rotation, and an axes scale. Each portion of the transformation contains some uncertainty.

### **B.2.3 Force Calculated from Characterized Model**

Equation 1.13 is used to calculate the force developed by an AMB. In the characterized version of Equation 1.13, the rotor position term,  $x$ , is based on the characterization of the rotor position identification. The uncertainty in the force measurement is based on uncertainty in the rotor position identification as well as uncertainty of the remaining terms.

### **B.2.4 Test Setups**

The force model described above was applied to test data from multiple test setups on two test platforms. The outcome of the uncertainty equation varies with test setup; the uncertainties associated with three representative test setups will be calculated below. The three test setups correspond to Platform 1 Setup 1, Platform 2 Setups 1 and 3, and Platform 2 Setups 2 and 4. Uncertainty in Platform 2 Setups 1 and 3, are grouped together because the setups share a common nominal air gap. Likewise for Platform 2 Setups 2 and 4.

### **B.3 UNCERTAINTY IN IDENTIFICATION OF ROTOR POSITION**

The system identification of rotor position  $x$  is based on Equation 2.6, which stems from the Multi-Point Method (MPM). Further discussion of the development of Equation 2.6 is found in Chapter 2.

The uncertainty in the identified value of  $x$  depends on the uncertainty in each of its constituent terms. These uncertainties and their sources are discussed below.

#### ***B.3.1 Uncertainty in Constituent Terms in MPM Calculation***

##### ***$i_{lower,1}$ , $i_{lower,2}$ , $i_{upper,1}$ , $i_{upper,2}$ (Coil Currents)***

The coil currents contribute two types of uncertainty to the calculation, a fixed uncertainty (or bias) due to calibration, and a random uncertainty due to sampling. The values determined here apply to both bearing platforms.

An auxiliary 'breakout box' provided by the system manufacturer provides a voltage signal that is proportional to the various controller currents. These signals are sampled by the data acquisition system to get measurements of the currents in the upper and lower coils of each actuator. Because the measured signal is linearly proportional to the current (and not the current value itself) a linear calibration must be applied to the measured voltage to convert it to current. The calibration is a source of fixed uncertainty in the current measurement. The amount of uncertainty can be estimated through observation of the controller reported current values and the data acquisition reported current values. These observations show that the calibration is good to 0.01 Amps. This is considered to be a  $3\sigma$  value so that the  $2\sigma$  value to be used as the fixed uncertainty value is 0.0067 Amps.

Due to sampling, there is also a random uncertainty component. The observed current data showed a consistent standard deviation of 0.005 Amps, so that the  $2\sigma$  value is 0.010 Amps. However, in the case of an MPM based measurement such as that used to identify the rotor position term, this value is based on a minimum of 20000 samples and represents an estimate of the population standard deviation. In order to estimate the standard deviation of the means ( $\sigma_m$ ), this value must be adjusted per the following equation

$$\sigma_m = \frac{\sigma}{\sqrt{n}} = \frac{0.005}{\sqrt{20000}} = 0.000035 \quad (\text{B.1})$$

where  $\sigma$  is the observed standard deviation, and  $n$  is the sample size (Vining, 1998). This causes the  $2\sigma$  uncertainty value to be 0.00007 Amps for the MPM.

##### ***$g_o$ (Nominal Air Gap)***

The nominal value for rotor air gap is a design parameter that is typically provided by the manufacturer. In the case of the first platform it is  $0.015 \pm 0.001$  inches. The tolerance is considered to be a  $3\sigma$  value so that the  $2\sigma$  value to be used as the fixed uncertainty value is 0.00066 inches. The same tolerance is applied to calculations associated with the second platform.

There is no random component associated with this term.

#### **$L_i$ (Mean Flux Path Length)**

For the smaller bearing platform (Platform 1) the mean path length of the magnetic flux has a nominal value of 2.87 inches. This value is an assumption based on magnetic theory and cannot be easily verified. Therefore a relatively large fixed error of 0.287 inches (10%) will be assigned to it, this translates to a  $2\sigma$  uncertainty of 0.191 inches.

For the larger bearing platform (Platform 2) the mean path length of the magnetic flux has a nominal value of 4.8 inches. This value is an assumption based on magnetic theory and cannot be easily verified. Therefore a relatively large fixed error of 0.48 inches (10%) will be assigned to it, this translates to a  $2\sigma$  uncertainty of 0.32 inches.

There is no random component associated with this term.

#### **$\mu_r$ (Magnetic Permeability)**

The stator cores are built from M19 silicon steel, the rotors are built from either M19 or Arnon 5. The bearing manufacturer reports that these materials have a relative magnetic permeability of 3000, the nominal value for this material. A conversation with Mark Rippey of Proto Laminations, Inc (Rippey) revealed that magnetic permeability is not a controlled specification of this material. Mark observed that in his experience magnetic permeability could vary by up to 20% from the nominal value. Based on this information, a total error of  $\pm 600$  (20%) fixed error will be assumed. This translates to an estimated  $2\sigma$  error of 400 that is applicable to both platforms.

There is no random component associated with this term.

#### **$\theta$ (Stator Axis Angle)**

The bearing manufacturer reports a tolerance of  $\pm 0.5^\circ$  for this dimension. This translates to an estimated  $2\sigma$  fixed error of  $0.33^\circ$  for both platforms.

There is no random component associated with this term.

### ***B.3.2 Uncertainty of Position Determined by MPM - Results***

The uncertainties values given above can be used to perturb Equation 2.6. This is done by running the analysis program with all parameters set to nominal values except for the perturbed parameter. The perturbed parameter is set to its nominal value  $\pm$  its  $2\sigma$  error value. The program is run for each extreme condition, nominal value  $+2\sigma$  error and nominal value  $-2\sigma$  error, and the resulting changes in the calculated value of  $x$  are noted. The larger variation in calculated value (from either  $+2\sigma$  or  $-2\sigma$ ) is taken as the resulting uncertainty of record associated with the perturbed parameter.

The resulting values of fixed and random error along with their effects on the calculated position  $x$  are tabulated below. Table B.1 shows the effect of the perturbations for the AMB system associated with Platform 1, Table B.2 shows the effect of the perturbations for the AMB system associated with Platform 2 that have a 0.010in nominal air gap, and Table B.3 shows the effect of the perturbations for the AMB system associated with Platform 2 that have a 0.030in nominal air gap.

The tables show that the largest contributor to uncertainty is associated with the fixed error of the current measurements. Recall that this error is related to calibration of the signal “breakout box”. Calibration precision is limited due to the precision of the current readout. In any event, it can be seen that the largest position uncertainty is less than 5 microns or ~0.0002 inches.

**Table B.1: Uncertainty in Equation 2.6 and its Effect on Identified Rotor Location (Platform 1)**

Term	Uncertainty of Terms		Uncertainty of Position Calculation in $\mu\text{m}$	
	Fixed Error	Random Error	Fixed Error	Random Error
$g_o$	0.00067 in	0	2.00E-02	0
$b_{th}$	$L_i$	0.191 in	8.00E-04	0
	$\mu_r$	400	2.00E-03	0
$\theta$	0.33°	0	1.00E-03	0
$i_{upper,1}$	0.0067 Amps	0.00007 Amps	2	0.04
$i_{lower,1}$	0.0067 Amps	0.00007 Amps	1	0.02
$i_{upper,2}$	0.0067 Amps	0.00007 Amps	2.8	0.06
$i_{lower,2}$	0.0067 Amps	0.00007 Amps	2	0.04
<b>RSS</b>			4.10	0.08
<b>Total Uncertainty</b>			4.10	

**Table B.2: Uncertainty in Equation 4 and its Effect on Identified Rotor Location (Platform 2, 0.010” Nominal Gap)**

Term	Uncertainty of Terms		Uncertainty of Position Calculation in $\mu\text{m}$	
	Fixed Error	Random Error	Fixed Error	Random Error
$g_o$	0.00067 in	0	1.00E-01	0
$b_{th}$	$L_i$	0.32 in	1.00E-02	0
	$\mu_r$	400	2.00E-02	0
$\theta$	0.33°	0	1.00E-02	0
$i_{upper,1}$	0.0067 Amps	0.00007 Amps	1.2	0.03
$i_{lower,1}$	0.0067 Amps	0.00007 Amps	0.7	0.02
$i_{upper,2}$	0.0067 Amps	0.00007 Amps	2	0.04
$i_{lower,2}$	0.0067 Amps	0.00007 Amps	1.7	0.04
<b>RSS</b>			2.97	0.07
<b>Total Uncertainty</b>			2.97	

## **B.4 UNCERTAINTY IN CHARACTERIZATION OF ROTOR POSITION IDENTIFICATION**

If the system identification of rotor position is applied at several well chosen rotor locations, a generalization of the relationship between the identified rotor locations and the rotor locations reported by the system sensors can be established. This is discussed at length in Chapter 2 and Chapter 5. The generalized relationship has the form of a coordinate transformation. The transformation consists of an origin offset, an axes rotation, and an axes scale. Each portion of the transformation contains some uncertainty.

**Table B.3: Uncertainty in Equation 2.6 and its Effect on Identified Rotor Location (Platform 2, 0.030" Nominal Gap)**

Term	Uncertainty of Terms		Uncertainty of Position Calculation in m	
	Fixed Error	Random Error	Fixed Error	Random Error
$g_o$	0.00067 in	0	6.00E-02	0
$b_{th}$	$L_i$	0.32 in	2.00E-03	0
	$\mu_r$	400	1.00E-02	0
$\theta$	0.33°	0	1.00E-02	0
$i_{upper,1}$	0.0067 Amps	0.00007 Amps	1.4	0.03
$i_{lower,1}$	0.0067 Amps	0.00007 Amps	0.6	0.01
$i_{upper,2}$	0.0067 Amps	0.00007 Amps	2.2	0.05
$i_{lower,2}$	0.0067 Amps	0.00007 Amps	1.9	0.04
<b>RSS</b>			3.28	0.07
<b>Total Uncertainty</b>			3.28	

### ***B.4.1 Uncertainty of “Origin Offset” Portion of Coordinate Transformation***

Origin offset values are confirmed by direct application of the MPM. The uncertainty associated with this term of the transformation is the same as the uncertainty in rotor position offset determined in Section B.3.

### ***B.4.2 Uncertainty of Axes Rotation Portion of Coordinate Transformation***

The rotation angle accounts for angular displacement of the effective axes relative to the system coordinate axes. In order to determine the angular displacement between a system coordinate axis and its corresponding axis in effective coordinates, the rotor is positioned at specific locations along the system coordinate axis. At each point, the MPM is used to determine the corresponding effective position. A best-fit line is applied to the effective positions; the angular displacement between the best-fit line and the system coordinate axis is considered the angular offset for that axis. This is repeated for the remaining system axis, the average of the two angular offsets is the axes rotation angle of record.

The position uncertainty due to the MPM, discussed in the previous section, provides the basis of the axes rotation angle uncertainty tabulated in Table B.4. The rotor was moved to four positions along each axis;  $\pm 25\mu\text{m}$  and  $\pm 50\mu\text{m}$ . The effect that position error has on rotation angle error can be determined from the previously calculated MPM position uncertainties.

Table B.4 shows the angular uncertainties for each platform and nominal gap combination. The second column of Table B.4 shows the position uncertainties associated with each platform and nominal gap, these are the MPM position uncertainty values determined in the previous section. Column three shows the amount of angular error associated with a best-fit line if one of the  $\pm 25\mu\text{m}$  points has an error equal to its position uncertainty. Column four shows the amount of angular error associated with a best-fit line if one of the  $\pm 50\mu\text{m}$  points has an error equal to its position uncertainty. The last column shows the aggregate angular uncertainty associated with the rotation portion of the transform, this a root sum square of the uncertainties at  $\pm 25\mu\text{m}$  and  $\pm 50\mu\text{m}$ . It can be seen that the uncertainty associated with rotation ranges from about  $2^\circ$  to  $3^\circ$ .

**Table B.4: Angular Uncertainty of Axes Rotation Angle due to Position Uncertainty**

System	Position Uncertainty ( $\mu\text{m}$ )	Angular Uncertainty at 2 degrees		
		+/- 25 $\mu\text{m}$	+/- 50 $\mu\text{m}$	Aggregate
<b>Platform 1</b>	4.1	0.9	1.9	3.0
<b>Platform 2, 0.010" Nominal Gap</b>	2.97	0.7	1.4	2.2
<b>Platform 2, 0.030" Nominal Gap</b>	3.28	0.8	1.5	2.4

### ***B.4.3 Uncertainty of Axes Scale Portion of Coordinate Transformation***

A scale factor is determined for each axis to account for differences between the scale of the system coordinates relative to the effective coordinates. In order to determine the scale factor for a particular axis, the rotor is positioned at specific locations along that system coordinate axis. At each point, the MPM is used to determine the corresponding effective position. The scale factor is based on the ratio between the effective position and the system coordinate position. The average scale factor considering all points on an axis is taken as the scale factor for that axis. The same points that were used to determine axes rotation,  $\pm 25\mu\text{m}$  and  $\pm 50\mu\text{m}$ , were used in the scale factor calculations.

The position uncertainty due to the MPM, discussed previously, provides the basis of the scale factor uncertainties, tabulated in Table B.5. The second column of Table B.5 shows the position uncertainties associated with each platform and nominal gap, these are the MPM position values determined previously. Column three shows the amount of scale error if one of the  $\pm 25\mu\text{m}$  points has an error equal to its position uncertainty. Column four shows the amount of scale error if one of the  $\pm 50\mu\text{m}$  points has an error equal to its position uncertainty. The last column shows the aggregate scale uncertainty associated with the scale portion of the transform, this a root sum square of the uncertainties at  $\pm 25\mu\text{m}$  and  $\pm 50\mu\text{m}$ . It can be seen that the uncertainty associated with

the transform scale is roughly 0.05. Although the uncertainty of the axes scale portion of the transform is a constant, its effect on the uncertainty in the characterized value of  $x$  will increase as rotor offset increases.

#### **B.4.4 Aggregate Uncertainty of Entire Transformation**

The entire transformation consists of an offset, axes rotation, and scale. This allows position data to be mapped from system coordinates to effective coordinates. The above sections describe the amount of position uncertainty associated with the offset, the amount of angular uncertainty associated with the rotation, and the amount of scale uncertainty. The overall uncertainty of the transform can be determined from this information. Since the relevant units of the transform are position based, the overall uncertainty will be given as a position uncertainty.

**Table B.5: Uncertainty of Scale Factor due to Position Uncertainty**

System	Position Uncertainty ( $\mu\text{m}$ )	Scale Uncertainty for a Scale factor of 1.3		
		+/- 25 $\mu\text{m}$	+/- 50 $\mu\text{m}$	Aggregate
<b>Platform 1</b>	4.1	0.040	0.020	0.063
<b>Platform 2, 0.010" Nominal Gap</b>	2.97	0.030	0.015	0.047
<b>Platform 2, 0.030" Nominal Gap</b>	3.28	0.034	0.017	0.054

A position in system coordinates is mapped to effective coordinates via a transform. The data that was used to create the transform has uncertainty associated with it so that the transform itself also has uncertainty. For a point  $(v,w)$  the transform is given by the following:

- Translation:  $v_T = v + b_v$ ,  $w_T = w + b_w$ ; where  $b_v$  and  $b_w$  are the translation offsets for each axis and  $v_T$  and  $w_T$  are the transformed coordinates.
- Rotation:  $v_T = v \cos \theta - w \sin \theta$ ,  $w_T = v \sin \theta + w \cos \theta$ ; where  $\theta$  is the angular offset.
- Scale:  $v_T = v * s_v$ ,  $w_T = w * s_w$ ; where  $s_v$  and  $s_w$  are the scaling factors for each axis.

Consider the uncertainty accrued by the  $v$  coordinate of the point  $(v,w)$  as it is transformed to  $(v_T,w_T)$ . The translation, rotation, and scale uncertainties associated with the  $v$  coordinate are  $b_{vU}$ ,  $\theta_U$ , and  $s_{vU}$  respectively. The uncertainty  $T_U$  of the transform is calculated as:

$$T_U = \sqrt{(b_{vU})^2 + (v * (1 - \cos \theta_U))^2 + (v * s_{vU})^2} \quad (\text{B.2})$$

It can be seen that the total uncertainty of the transform depends not only on the uncertainty terms, but also on rotor position. This is due to the rotation and scaling terms. In general, the greater the rotor position offset from the origin, the greater the fixed uncertainty of the transform. For the case of magnetic center,  $v = 0$  and the uncertainty in  $x$  is the uncertainty in the MPM as discussed in Section B.3.

The effect of position offset is explored by considering two scenarios,  $v = 25$  mm and  $v = 50$  mm. The effect of these offsets on the uncertainties associated with three different test setups is tabulated in Table B.6.

## **B.5 UNCERTAINTY OF FORCE MEASUREMENT**

Aggregate uncertainty of the calculated force can be determined from the uncertainty associated with each of its constituents. Calculations of AMB force are developed from a magnetic circuit model in Chapter 1. A brief description of each term in the model is given in Section B.2

Equations 1.13 and 1.12 contain measured values ( $i_{upper}$  and  $i_{lower}$ ), system constants ( $A$ ,  $N$ ,  $\theta$ ,  $L_i$ ,  $g_o$ ), a material constant ( $\mu_o$ ), a physical constants ( $\mu_r$ ), as well as a term determined via system identification, ( $x$ ). Each term has an individual uncertainties. The uncertainty associated with the force measurement is determined by analyzing the effect of the uncertainty in each individual term.

### ***B.5.1 Uncertainty of Force Equation Constituents***

The uncertainties associated with  $i_{upper}$ ,  $i_{lower}$ ,  $\theta$ ,  $L_i$ ,  $g_o$ , and  $\mu_r$  are given in Section 3.1 of this appendix, and are repeated below along with the uncertainties of the remaining terms. The uncertainty associated with  $x$  is discussed in Section 0 of this appendix.

#### ***i<sub>upper</sub>*, *i<sub>lower</sub>* Coil Currents**

The coil currents contribute two types of uncertainty to the calculation, a fixed uncertainty (or bias) due to calibration, and a random uncertainty due to sampling. The values determined here apply to both bearing platforms.

An auxiliary 'breakout box' provided by the system manufacturer provides a voltage signal that is proportional to the various controller currents. These signals are sampled by the data acquisition system to get measurements of the currents in the upper and lower coils of each actuator. Because the measured signal is linearly proportional to the current (and not the current value itself) a linear calibration must be applied to the measured voltage to convert it to current. The calibration is a source of fixed uncertainty in the current measurement. The amount of uncertainty can be estimated through observation of the controller reported current values and the data acquisition reported current values. These observations show that the calibration is good to 0.01 Amps. This is considered to be a  $3\sigma$  value so that the  $2\sigma$  value to be used as the fixed uncertainty value is 0.0067 Amps.

Due to sampling, there is also a random uncertainty component. The observed current data showed a consistent standard deviation of 0.005 Amps, so that the  $2\sigma$  value is 0.010 Amps. However, in the case of an MPM based measurement such as that used to identify the rotor position term, this value is based on a minimum of 20000 samples and represents an estimate of the population standard deviation. In order to estimate the standard deviation of the means ( $\sigma_m$ ), this value must be adjusted per Equation B.1. This causes the  $2\sigma$  uncertainty value to be 0.00007 Amps for the MPM

**$g_o$  (Nominal Air Gap)**

The nominal value for rotor air gap is a design parameter that is typically provided by the manufacturer. In the case of the first platform it is  $0.015 \pm 0.001$  inches. The tolerance is considered to be a  $3\sigma$  value so that the  $2\sigma$  value to be used as the fixed uncertainty value is 0.00066 inches. The same tolerance is applied to calculations associated with the second platform.

There is no random component associated with this term.

 **$L_i$  (Mean Flux Path Length)**

For the smaller bearing platform (Platform 1) the mean path length of the magnetic flux has a nominal value of 2.87 inches. This value is an assumption based on magnetic theory and cannot be easily verified. Therefore a relatively large fixed error of 0.287 inches (10%) will be assigned to it, this translates to a  $2\sigma$  uncertainty of 0.191 inches.

For the larger bearing platform (Platform 2) the mean path length of the magnetic flux has a nominal value of 4.8 inches. This value is an assumption based on magnetic theory and cannot be easily verified. Therefore a relatively large fixed error of 0.48 inches (10%) will be assigned to it, this translates to a  $2\sigma$  uncertainty of 0.32 inches.

There is no random component associated with this term.

 **$\mu_o$  (Magnetic Permeability of Free Space)**

The magnetic permeability of free space is a physical constant; no uncertainties will be associated with it in this study.

 **$\mu_r$  (Magnetic Permeability of Laminate Cores)**

The stator cores are built from M19 silicon steel, the rotors are built from either M19 or Arnon 5. The bearing manufacturer reports that these materials have a relative magnetic permeability of 3000, the nominal value for this material. A conversation with Mark Rippy of Proto Laminations, Inc (Rippy) revealed that magnetic permeability is not a controlled specification of this material. Mark observed that in his experience magnetic permeability could vary by up to 20% from the nominal value. Based on this information, a total error of  $\pm 600$  (20%) fixed error will be assumed. This translates to an estimated  $2\sigma$  error of 400 that is applicable to both platforms.

There is no random component associated with this term.

 **$\theta$  (Stator Axis Angle)**

The bearing manufacturer reports a tolerance of  $\pm 0.5^\circ$  for this dimension. This translates to an estimated  $2\sigma$  fixed error of  $0.33^\circ$  for both platforms.

There is no random component associated with this term.

 **$N$** 

The number of wire turns per coil is an important factor in the manufacturing of electromagnetic actuators and its value is a well-known design parameter. From this perspective, it seems unlikely that the manufacturing process would allow it to vary.

However, for the sake of completeness, a fixed uncertainty component of 1 turn will be considered. For Platform 1,  $N = 228$ , for Platform 2,  $N = 248$ . There is no random component associated with this term.

### A

The pole face area is also a well-known design parameter that is subject to manufacturing tolerance. The manufacturer typically provides its nominal value.

In the case of Platform 1, the nominal dimensions of the pole are given as 0.207in x 0.496in; with a tolerance of  $\pm 0.005$ in on each dimension. This equates to a worst-case fixed error of:  $\sqrt{0.005^2 + 0.005^2} = 0.0071\text{in}^2$  for the area measurement. It is assumed that this value is a  $3\sigma$  value, the corresponding  $2\sigma$  value of  $0.0047\text{in}^2$  will be as the fixed error. There is no random component associated with this term.

In the case of Platform 2, its nominal dimensions are given as 0.530in x 0.875in; with a tolerance of  $\pm 0.005$ in on each dimension. This equates to a worst-case fixed error of:  $\sqrt{0.005^2 + 0.005^2} = 0.0071\text{in}^2$  for the area measurement. It is assumed that this value is a  $3\sigma$  value, the corresponding  $2\sigma$  value of  $0.0047\text{in}^2$  will be as the fixed error. There is no random component associated with this term.

Of the terms discussed above, the measured terms,  $i_{upper}$ ,  $i_{lower}$ , and  $x$  have both fixed and random uncertainties associated with them. The amount of random uncertainty is a function of sampling. The sampling method applied to the measured terms varies depending on which implementation of the force measurement is applied.

### B.5.2 Sampling Effects on Force Measurement

Force is calculated by three different methods in this research, each using the same model, but different ways of measuring certain terms within the model. In particular, the coil current values used in an MPM calculation are based on several thousand individual samples; this dramatically reduces the sampling error in coil current for the MPM cases. During a typical implementation of force measurement, the coil current value used in Equation 1.13 will be based on a single sample. The uncertainty in the offset values of rotor position,  $x$ , also vary with the different force measurement methods; in the MPM, force uncertainty is not applicable since it is not used in the force identification. Table B.6 summarizes the different uncertainties associated with each type of force measurement method. It can be seen from the table that the uncertainty in the coil current term is  $\sim 140$  times larger when it does not benefit from sampling.

**Table B.6: Sampling associated with different force measurement methods**

Force Calculation Method	Samples		$2\sigma$ Uncertainty	
	Current	Position	Current	Position
<b>MPM</b>	20000	-	0.00007	-
<b>Characterized Model (Static)</b>	1	1	0.010	position dependent
<b>Characterized Model (Dynamic)</b>	1	1	0.010	position dependent

### B.5.3 Force Measurement Uncertainty Associated with the MPM

The force measurement uncertainty associated with the MPM was determined in the same way as position uncertainty in the MPM was determined in Section B.3.2. Each of the terms in Equation 1.13 was perturbed by their estimated individual  $2\sigma$  uncertainty values. Their individual uncertainties and uncertainty sources are listed in Section B.5.1.

The resulting values of fixed and random error along with their effects on the calculated force  $F$  are tabulated below. Table shows the effect of the perturbations for the AMB system associated with Platform 1, Table shows the effect of the perturbations for the AMB system associated with Platform 2 that have a 0.010in nominal air gap, and Table B.9 shows the effect of the perturbations for the AMB system associated with Platform 2 that have a 0.030in nominal air gap.

The tables show that the largest uncertainty is associated with the setups from Platform 2 that have the narrow air gap (0.010in). This is due their greater sensitivity to uncertainty in air gap; a given air gap uncertainty represents a more significant portion of their total air gap. For instance, the  $2\sigma$  uncertainty shown in the table represents 7% of the air gap for the 0.010in nominal gap case, but only ~2% of the air gap for the 0.030in nominal gap case.

**Table B.7: Uncertainty in Equation 1.13 and its Effect on Calculated Force (Platform 1)**

Term	Uncertainty of Terms		Uncertainty of Force Calculation in lb <sub>f</sub>	
	Fixed Error	Random Error	Fixed Error	Random Error
$g_o$	0.00067 in	0	1.00E-03	0
$b_{th}$	$L_i$	0.191 in	5.80E-03	0
	$\mu_r$	400	1.03E-02	0
$\theta$	0.33°	0	3.40E-03	0
$\mu_o$	0	0	0.00E+00	0
$A$	0.0047	0	6.40E-02	0
$i_{upper}$	0.0067 Amps	0.00007	0.0493	0.0005
$i_{lower}$	0.0067 Amps	0.00007	0.0402	0.0003
$x$	-	-	0	0
<b>RSS</b>			<b>0.09</b>	<b>0.001</b>
<b>Total Uncertainty</b>			<b>0.09</b>	

**Table B.8: Uncertainty in Equation 1.13 and its Effect on Calculated Force  
(Platform 2, 0.010" Nominal Gap)**

Term	Uncertainty of Terms		Uncertainty of Force Calculation in $lb_f$	
	Fixed Error	Random Error	Fixed Error	Random Error
$g_o$	0.00067 in	0	4.20E-01	0
$b_{th}$	$L_i$	0.32 in	0	3.60E-02
	$\mu_r$	400	0	6.70E-02
$\theta$	0.33°	0	9.00E-03	0
$\mu_o$	0	0	0.00E+00	0
$A$	0.0047 in <sup>2</sup>	0	3.90E-03	0
$i_{upper}$	0.0067 Amps	0.00007	0.1	0.001
$i_{lower}$	0.0067 Amps	0.00007	0.05	0.0005
$x$	-	-	0	0
<b>RSS</b>			<b>0.44</b>	<b>0.001</b>
<b>Total Uncertainty</b>			<b>0.44</b>	

**Table B.9: Uncertainty in Equation 1.13 and its Effect on Calculated Force  
(Platform 2, 0.030" Nominal Gap)**

Term	Uncertainty of Terms		Uncertainty of Force Calculation in $lb_f$	
	Fixed Error	Random Error	Fixed Error	Random Error
$g_o$	0.00067 in	0	1.75E-01	0
$b_{th}$	$L_i$	0.32 in	0	1.43E-02
	$\mu_r$	400	0	2.60E-02
$\theta$	0.33°	0	1.00E-03	0
$\mu_o$	0	0	0.00E+00	0
$A$	0.0047 in <sup>2</sup>	0	4.00E-02	0
$i_{upper}$	0.0067 Amps	0.00007	0.03	0.0004
$i_{lower}$	0.0067 Amps	0.00007	0.016	0.0002
$x$	-	-	0	0
<b>RSS</b>			<b>0.18</b>	<b>0.000</b>
<b>Total Uncertainty</b>			<b>0.18</b>	

#### ***B.5.4 Force Measurement Uncertainty Associated with the Characterized Model (Static)***

The force measurement uncertainty associated with the characterized model was determined in the same way that force uncertainty in the MPM was determined in the previous section. Each of the terms in Equation 1.13 was perturbed by their estimated

individual  $2\sigma$  uncertainty values. Their individual uncertainties and uncertainty sources are listed in Section B.5.1.

The resulting values of fixed and random error along with their effects on the calculated force  $F$  are tabulated below for the case in which there is no rotor offset from magnetic center. Table B.10 shows the effect of the perturbations for the AMB system associated with Platform 1, Table B.11 shows the effect of the perturbations for the AMB system associated with Platform 2 that have a 0.010in nominal air gap, and Table B.12 shows the effect of the perturbations for the AMB system associated with Platform 2 that have a 0.030in nominal air gap.

The tables show that force uncertainty is greater for the characterized model than for the MPM. This is because the MPM relies on 20000 samples of coil current, and the characterized model relies on just one sample of coil current.

Furthermore, uncertainty in rotor position due to uncertainty in the coordinate transform increases the uncertainty in the force measurement. This effect becomes more pronounced as the rotor is moved further from its origin due to axes rotation and axes scaling effects.

The tables show that application of the characterized model introduces more uncertainty than is associated with the MPM, this is mostly due to the current sampling effect on the uncertainty. This has the most pronounced effect on Platform 1. The uncertainty associated with the setups of Platform 2 increase also, but not as significantly. For instance, the uncertainty for Platform 1 more than doubles while the uncertainty associated with Platform 2 increases by 20% or less.

**Table B.10: Uncertainty in Equation 1.13 and its Effect on Calculated Force (Platform 1)**

Term	Uncertainty of Terms		Uncertainty of Force Calculation in $lb_f$	
	Fixed Error	Random Error	Fixed Error	Random Error
$g_o$	0.00067 in	0	9.72E-02	0
$b_{th}$	$L_i$	0.191 in	4.30E-03	0
	$\mu_r$	400	7.70E-03	0
$\theta$	0.33°	0	2.50E-03	0
$\mu_o$	0	0	0.00E+00	0
$A$	0.0047	0	4.77E-02	0
$i_{upper}$	0.0067 Amps	0.01	0.032	0.0478
$i_{lower}$	0.0067 Amps	0.01	0.0273	0.0408
$x$	4.1 $\mu$ m (0.00016in)	4.1 $\mu$ m (0.00016in)	0.14	0.14
<b>RSS</b>			<b>0.18</b>	<b>0.15</b>
<b>Total Uncertainty</b>			<b>0.24</b>	

**Table B.11: Uncertainty in Equation 1.13 and its Effect on Calculated Force  
(Platform 2, 0.010" Nominal Gap)**

Term	Uncertainty of Terms		Uncertainty of Force Calculation in $lb_f$	
	Fixed Error	Random Error	Fixed Error	Random Error
$g_o$	0.00067 in	0	3.10E-01	0
$b_{th}$	$L_i$	0.32 in	0	2.66E-02
	$\mu_r$	400	0	4.79E-02
$\theta$	0.33°	0	6.80E-03	0
$\mu_o$	0	0	0.00E+00	0
$A$	0.0047 in <sup>2</sup>	0	2.84E-02	0
$i_{upper}$	0.0067 Amps	0.01	0.134	0.2
$i_{lower}$	0.0067 Amps	0.01	0.103	0.154
$x$	3 $\mu$ m (0.00012in)	3 $\mu$ m (0.00012in)	0.225	0.225
<b>RSS</b>			<b>0.42</b>	<b>0.34</b>
<b>Total Uncertainty</b>			<b>0.54</b>	

Uncertainty in rotor position due to uncertainty in the coordinate transform increases the uncertainty in the force measurement. This effect becomes more pronounced as the rotor is moved further from its origin due to axes rotation and axes scaling effects. Tables B.13-B.15 show the uncertainties in force measurement related to a rotor position that is 25 $\mu$ m from magnetic center, Tables B.16-18 show the uncertainties in force measurement related to a rotor position that is 50 $\mu$ m from magnetic center.

**Table B.12: Uncertainty in Equation 1.13 and its Effect on Calculated Force  
(Platform 2, 0.030" Nominal Gap)**

Term	Uncertainty of Terms		Uncertainty of Force Calculation in $lb_f$	
	Fixed Error	Random Error	Fixed Error	Random Error
$g_o$	0.00067 in	0	1.24E-01	0
$b_{th}$	$L_i$	0.32 in	0	1.00E-02
	$\mu_r$	400	0	1.80E-02
$\theta$	0.33°	0	7.00E-03	0
$\mu_o$	0	0	0.00E+00	0
$A$	0.0047 in <sup>2</sup>	0	2.90E-02	0
$i_{upper}$	0.0067 Amps	0.01	0.046	0.069
$i_{lower}$	0.0067 Amps	0.01	0.033	0.049
$x$	3.3 $\mu$ m (0.00013in)	3.3 $\mu$ m (0.00013in)	0.076	0.076
<b>RSS</b>			<b>0.16</b>	<b>0.11</b>
<b>Total Uncertainty</b>			<b>0.20</b>	

The tables show that uncertainty increases as distance from magnetic center increases. This is predicted by Equation B.2. The setup associated with Platform 1 is the least affected, its uncertainty increases by ~8% at the 50 mm location. The Platform 2 setups with 0.030in gap are significantly affected; their uncertainty increases by 30% at the 50 mm location. The Platform 2 setups with 0.010in gap are less affected; their uncertainty increases by 15% at the 50 mm location. In terms of actual uncertainty, Platform 1 and the Platform 2 0.030in nominal gap cases have the same maximum uncertainty of 0.26 lb<sub>f</sub> (1.15N). The 0.010in nominal gap setups of Platform 2 have a maximum uncertainty of 0.62 lb<sub>f</sub> (2.75N).

**Table B.13: Uncertainty in Equation 1.13 and its Effect on Calculated Force (25 $\mu$ m Offset) (Platform 1)**

Term	Uncertainty of Terms		Uncertainty of Force Calculation in lbf	
	Fixed Error	Random Error	Fixed Error	Random Error
$g_o$	0.00067 in	0	9.05E-02	0
$b_{th}$	$L_i$	0.191 in	4.60E-03	0
	$\mu_r$	400	8.40E-03	0
$\theta$	0.33°	0	1.70E-03	0
$\mu_o$	0	0	0.00E+00	0
$A$	0.0047	0	3.22E-02	0
$i_{upper}$	0.0067 Amps	0.01	0.033	0.05
$i_{lower}$	0.0067 Amps	0.01	0.0264	0.0395
$x$	4.1 $\mu$ m (0.00016in)	4.4 $\mu$ m (0.00017in)	0.14	0.15
<b>RSS</b>			<b>0.18</b>	<b>0.16</b>
<b>Total Uncertainty</b>			<b>0.24</b>	

**Table B.14: Uncertainty in Equation 1.13 and its Effect on Calculated Force (25 $\mu$ m Offset) (Platform 2, 0.010" Nominal Gap)**

Term	Uncertainty of Terms		Uncertainty of Force Calculation in lb <sub>f</sub>	
	Fixed Error	Random Error	Fixed Error	Random Error
$g_o$	0.00067 in	0	3.20E-01	0
$b_{th}$	$L_i$	0.32 in	2.89E-02	0
	$\mu_r$	400	5.00E-02	0
$\theta$	0.33°	0	5.00E-03	0
$\mu_o$	0	0	0.00E+00	0
$A$	0.0047 in <sup>2</sup>	0	2.00E-02	0
$i_{upper}$	0.0067 Amps	0.01	0.144	0.216
$i_{lower}$	0.0067 Amps	0.01	0.1	0.148
$x$	3 $\mu$ m (0.00012in)	3.2 $\mu$ m (0.00013in)	0.23	0.256
<b>RSS</b>			<b>0.44</b>	<b>0.37</b>
<b>Total Uncertainty</b>			<b>0.57</b>	

### B.5.5 Force Measurement Uncertainty Associated with the Characterized Model (Dynamic)

The uncertainty effects in the characterized model described by Equation 1.13 are the same in dynamic scenarios as they are in static scenarios. However, axis forces that were based on Equation 1.13 were also subject to a curve fit as part of the data reduction. The data reduction was applied in order to efficiently analyze a large amount of data in a reasonable amount of time.

**Table B.15: Uncertainty in Equation 1.13 and its Effect on Calculated Force (25 $\mu$ m Offset) (Platform 2, 0.030" Nominal Gap)**

Term	Uncertainty of Terms		Uncertainty of Force Calculation in lbf	
	Fixed Error	Random Error	Fixed Error	Random Error
$g_o$	0.00067 in	0	1.31E-01	0
$b_{th}$	$L_i$	0.32 in	0	7.80E-03
	$\mu_r$	400	0	1.40E-02
$\theta$	0.33°	0	5.50E-03	0
$\mu_o$	0	0	0.00E+00	0
$A$	0.0047 in <sup>2</sup>	0	2.25E-02	0
$i_{upper}$	0.0067 Amps	0.01	0.0477	0.071
$i_{lower}$	0.0067 Amps	0.01	0.036	0.0487
$x$	3.3 $\mu$ m (0.00013in)	3.6 $\mu$ m (0.00014in)	0.0779	0.085
<b>RSS</b>			<b>0.17</b>	<b>0.12</b>
<b>Total Uncertainty</b>			<b>0.21</b>	

**Table B.16: Uncertainty in Equation 1.13 and its Effect on Calculated Force (50 $\mu$ m Offset) (Platform 1)**

Term	Uncertainty of Terms		Uncertainty of Force Calculation in lbf	
	Fixed Error	Random Error	Fixed Error	Random Error
$g_o$	0.00067 in	0	9.80E-02	0
$b_{th}$	$L_i$	0.191 in	0	5.00E-03
	$\mu_r$	400	0	9.00E-03
$\theta$	0.33°	0	9.00E-04	0
$\mu_o$	0	0	0.00E+00	0
$A$	0.0047	0	1.78E-02	0
$i_{upper}$	0.0067 Amps	0.01	0.035	0.052
$i_{lower}$	0.0067 Amps	0.01	0.025	0.038
$x$	4.1 $\mu$ m (0.00016in)	5.1 $\mu$ m (0.0002in)	0.143	0.179
<b>RSS</b>			<b>0.18</b>	<b>0.19</b>
<b>Total Uncertainty</b>			<b>0.26</b>	

Finding a best-fit curve for the axis force data introduced additional error because the fit curve does not perfectly describe the data. Differences between the actual data and the curve fit are shown as error bars in the error plots that are in Chapter 7. The error bars are drawn such that they represent plus and minus two standard deviations ( $\pm 2\sigma$ ) of the error incurred by the fit. Here, the plus and minus two standard deviations ( $\pm 2\sigma$ ) errors are plotted again in Figures B.1, B.3, B.5, B.7 and B.9. Plots of the uncertainty as a percent of the measured force are given in Figures B.2, B.4, B.6, B.8 and B.10. The uncertainty values for the basic and characterized models are considered to be the same.

## **B.6 TRANSDUCER UNCERTAINTY**

The plots show that uncertainty in the transducer values is generally below 10% of the measured load value, although a worst case of ~30% does exist. It should be noted that this case corresponds to an actual uncertainty of ~0.1lb<sub>f</sub> or ~0.5N, so that the large percent error is due to a small measured force value. In absolute terms, the transducer uncertainty tends to be less than 0.25 lb<sub>f</sub> or 1N.

### **Model Uncertainty**

For Platform 1, and for the 0.030in nominal air gap setups associated with Platform 2, the model uncertainty associated with the curve fit tends to be less than 10%. This corresponds to actual uncertainties of generally less than 0.25 lb<sub>f</sub> or 1N. Discounting one outlier, the remaining uncertainties are never greater than 0.38 lb<sub>f</sub> or 1.7N.

**Table B.17: Uncertainty in Equation 1.13 and its Effect on Calculated Force (50 $\mu$ m Offset) (Platform 2, 0.010" Nominal Gap)**

Term	Uncertainty of Terms		Uncertainty of Force Calculation in lb <sub>f</sub>	
	Fixed Error	Random Error	Fixed Error	Random Error
$g_o$	0.00067 in	0	3.56E-01	0
$b_{th}$	$L_i$	0.32 in	3.00E-02	0
	$\mu_r$	400	6.00E-02	0
$\theta$	0.33°	0	3.00E-03	0
$\mu_o$	0	0	0.00E+00	0
$A$	0.0047 in <sup>2</sup>	0	1.50E-02	0
$i_{upper}$	0.0067 Amps	0.01	0.155	0.2329
$i_{lower}$	0.0067 Amps	0.01	0.0946	0.1418
$x$	3 $\mu$ m (0.00012in)	3.8 $\mu$ m (0.00015in)	0.24	0.3
<b>RSS</b>			<b>0.47</b>	<b>0.41</b>
<b>Total Uncertainty</b>			<b>0.62</b>	

**Table B.18: Uncertainty in Equation 1.13 and its Effect on Calculated Force (50 $\mu$ m Offset) (Platform 2, 0.030" Nominal Gap)**

Term	Uncertainty of Terms		Uncertainty of Force Calculation in lb <sub>f</sub>	
	Fixed Error	Random Error	Fixed Error	Random Error
$g_o$	0.00067 in	0	1.29E-01	0
$b_{th}$	$L_i$	0.32 in	0	1.07E-02
	$\mu_r$	400	0	1.89E-02
$\theta$	0.33°	0	6.00E-03	0
$\mu_o$	0	0	0.00E+00	0
$A$	0.0047 in <sup>2</sup>	0	2.50E-02	0
$i_{upper}$	0.0067 Amps	0.01	0.074	0.098
$i_{lower}$	0.0067 Amps	0.01	0.057	0.07
$x$	3.3 $\mu$ m (0.00013in)	4.3 $\mu$ m (0.00017in)	0.1	0.128
<b>RSS</b>			<b>0.19</b>	<b>0.18</b>
<b>Total Uncertainty</b>			<b>0.26</b>	

The model uncertainties associated with the 0.010in nominal air gap setups have significantly worse uncertainties. In these cases, uncertainties of 20% are common, with a worst case greater than 100%. Corresponding actual uncertainties for Platform 2 Setup 3 tend to be in the range of 0.17 lb<sub>f</sub> (0.75N) to 0.56 lb<sub>f</sub> (2.5N). In the case of Platform 1 Setup 1, uncertainties tend to be in the range of 0.25 lb<sub>f</sub> (5N) to 1.25 lb<sub>f</sub> (5N). Worst case uncertainty, corresponding to the worst case from a percent standpoint, is roughly to 6.7 lb<sub>f</sub> (30N).

## **B.7 COMMENT ON CURVE FIT UNCERTAINTY**

In some cases, the curve fit clearly adds significant modeling uncertainty, particularly in the case of the 0.010in nominal air gap setups. However, the typical uncertainty added by the curve fit is outweighed by the increased speed at which a large amount of data can be processed. Although a cycle-by-cycle analysis would eliminate the uncertainty due to the curve fit, the time required to do this would not be justified. We do not expect that the trends in the model comparison or the conclusions of this research would change due to a cycle-by-cycle analysis.

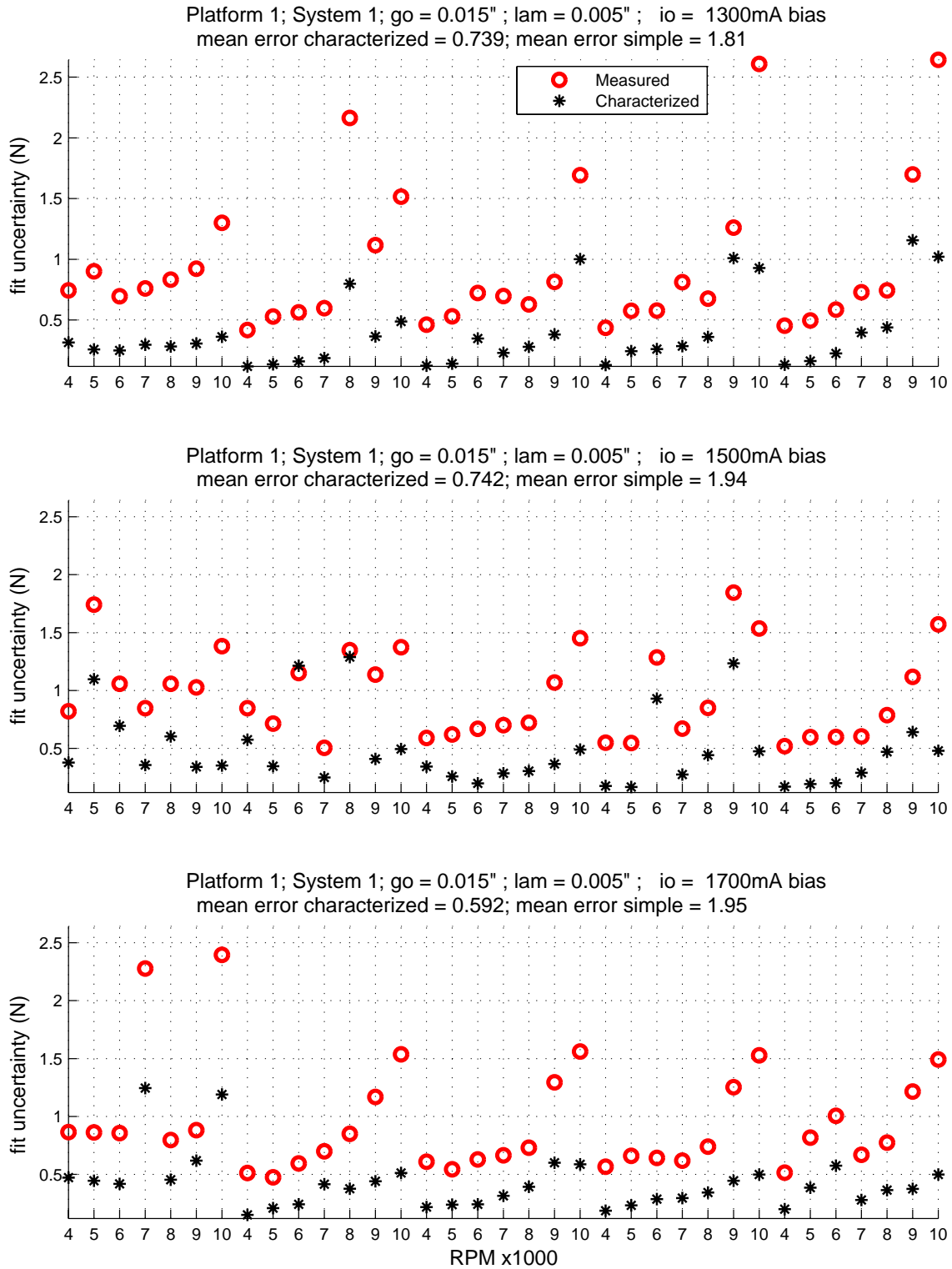


**Figure B.1: Comparison of curve fit uncertainty versus Rotor Speed. Platform 1 System 1. Added Unbalance Sections (left to right) 0, 400, 600, 800, and 1000 mg (0, 0.48, 0.72, 0.96, and 1.2 gm-in)**

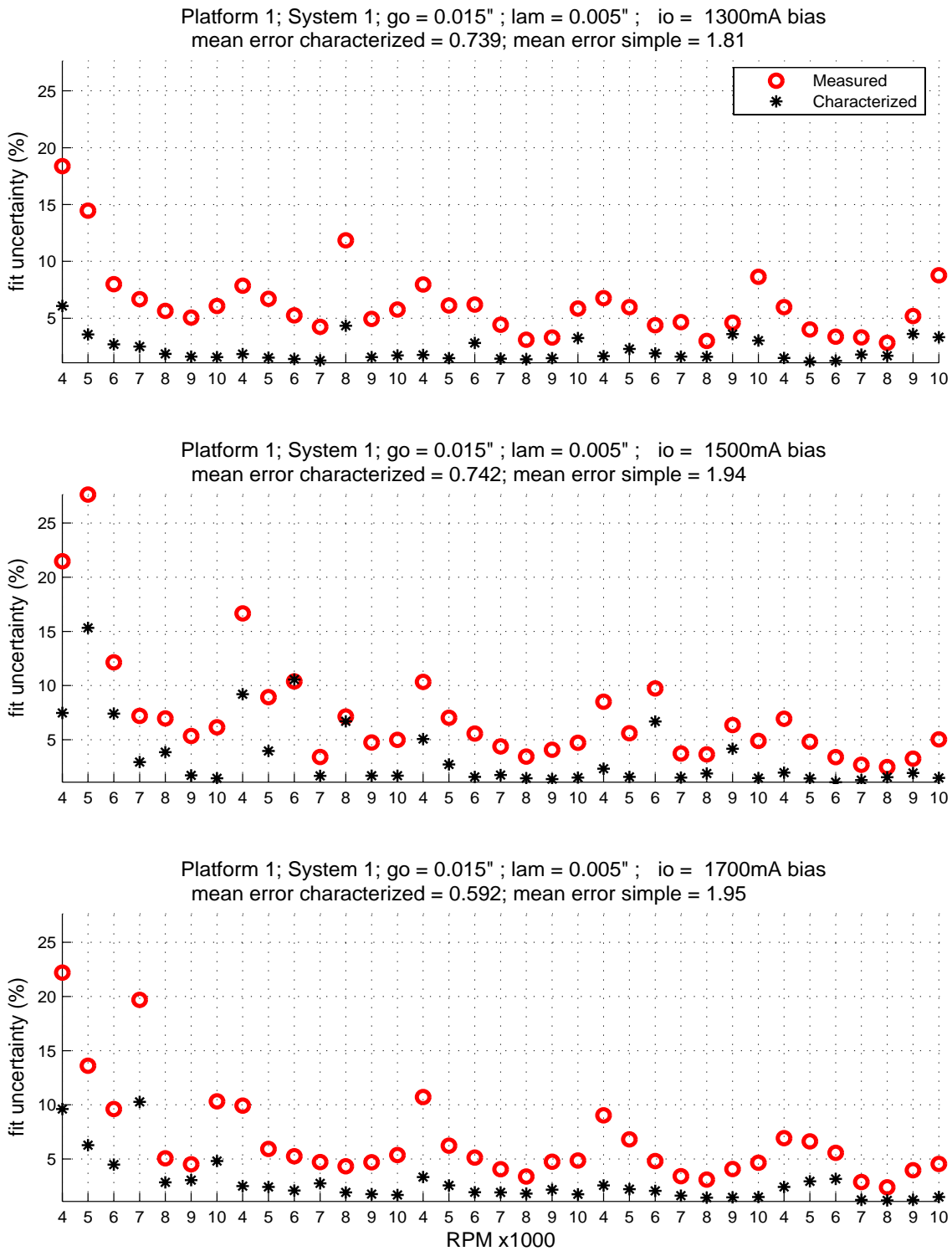


**Figure B.2: Comparison of curve fit uncertainty versus Rotor Speed as a percent of measured load. Platform 1 System 1. Added Unbalance Sections (left to right) 0, 400, 600, 800, and 1000 mg (0, 0.48, 0.72, 0.96, and 1.2 gm-in)**

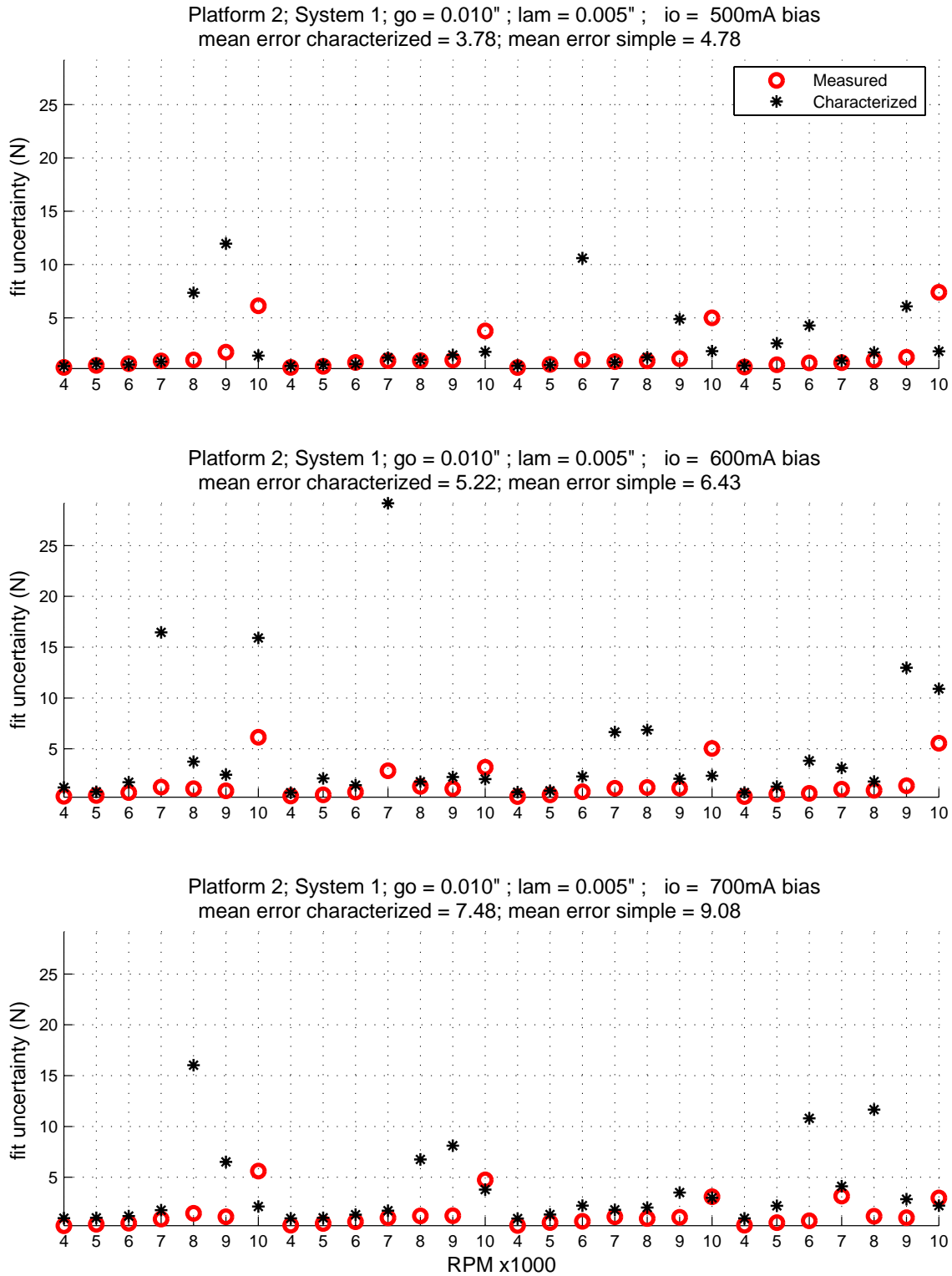


**Figure B.3: Comparison of curve fit uncertainty versus Rotor Speed. Platform 2 System 1. Added Unbalance (left to right) 0, 100, 200 and 300mg (0, 0.23, 0.45, 0.68 gm-in)**

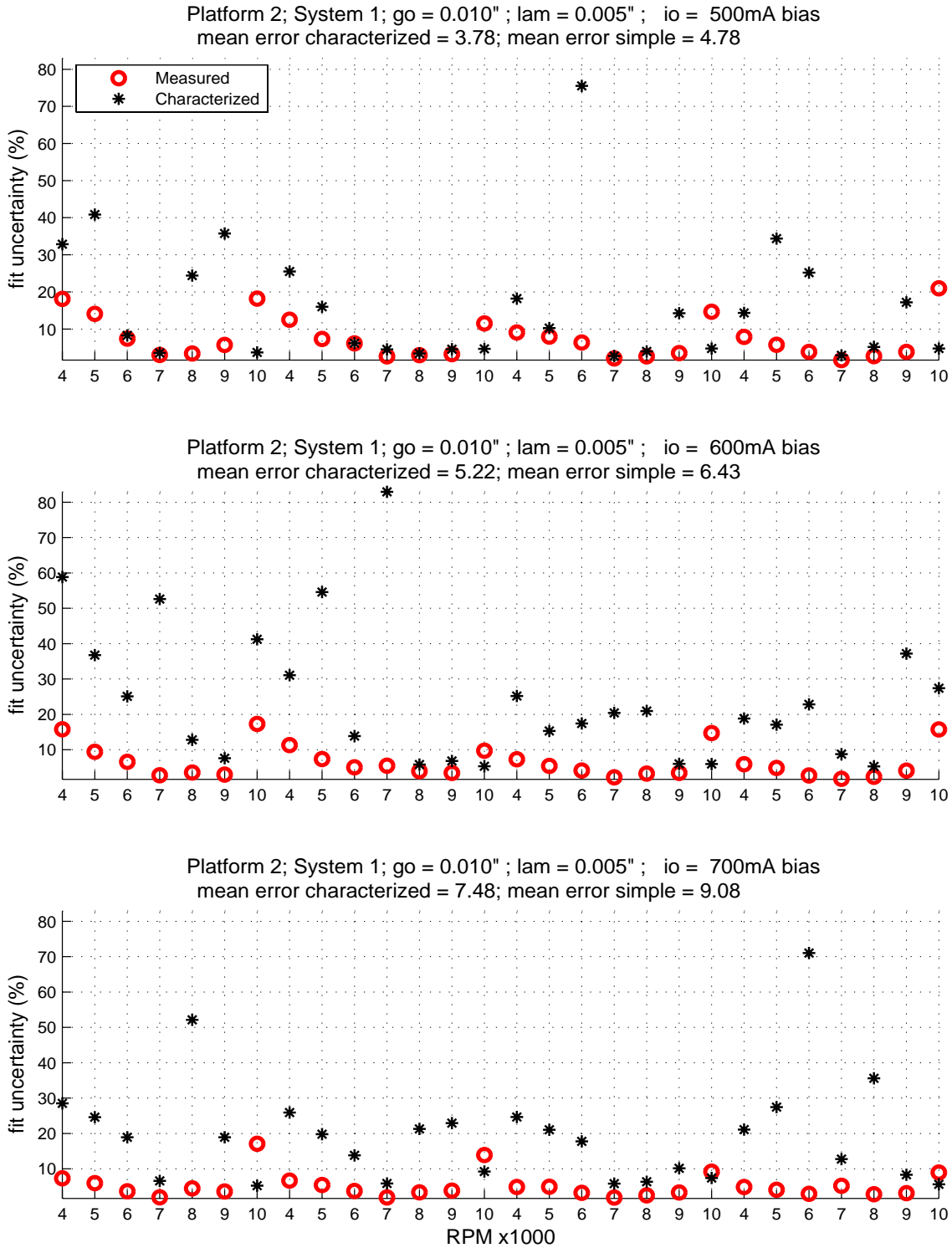


**Figure B.4: Comparison of curve fit uncertainty versus Rotor Speed as a percent of measured load. Platform 2 System 1. Added Unbalance (left to right) 0, 100, 200 and 300mg (0, 0.23, 0.45, 0.68 gm-in)**

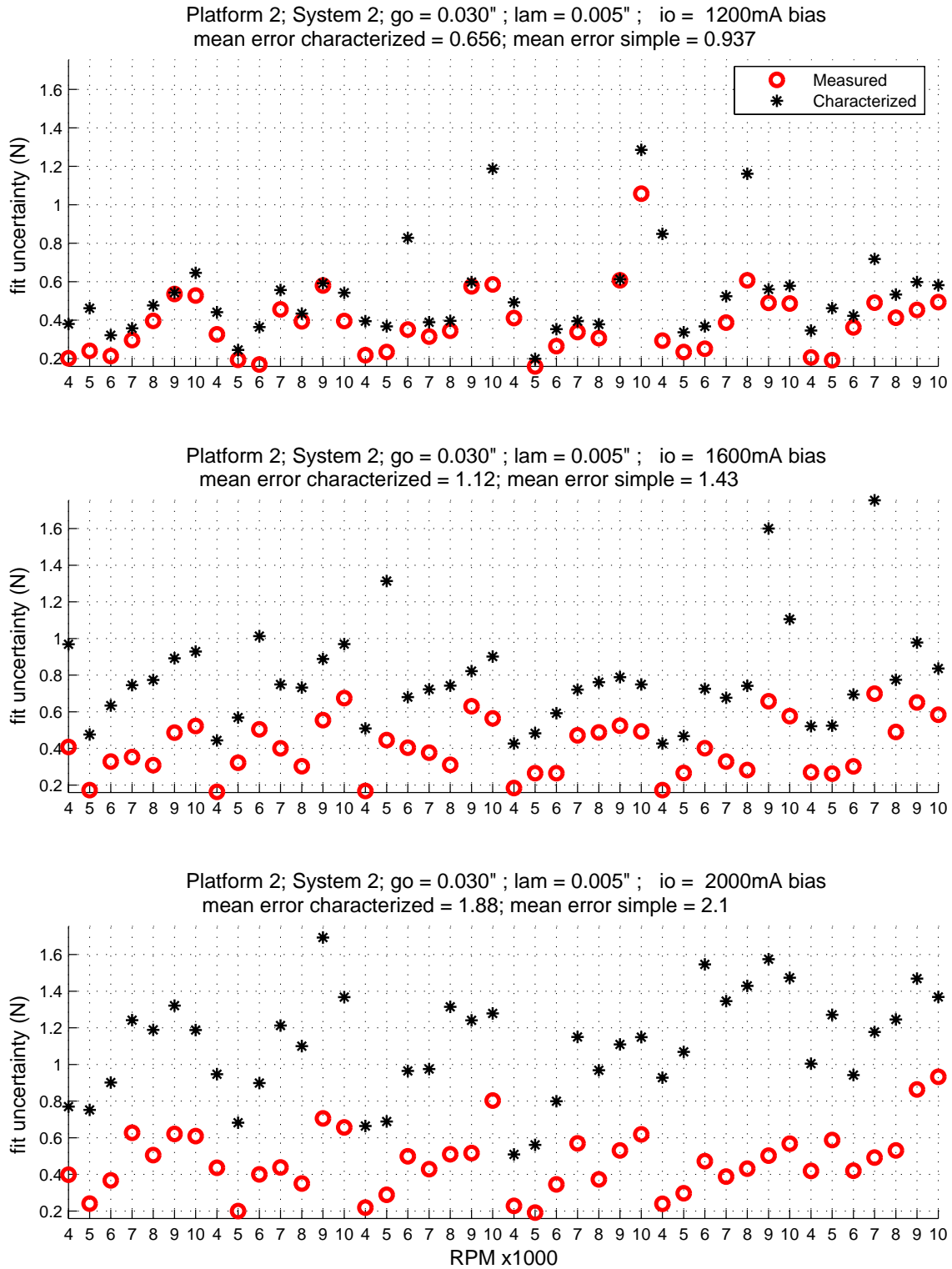


**Figure B.5: Comparison of curve fit uncertainty versus Rotor Speed. Platform 2 System 2. Added Unbalance (left to right) 0, 200, 400, 600, 800, and 1000mg (0, 0.45, 0.9, 1.35, 1.8, and 2.25 gm-in)**

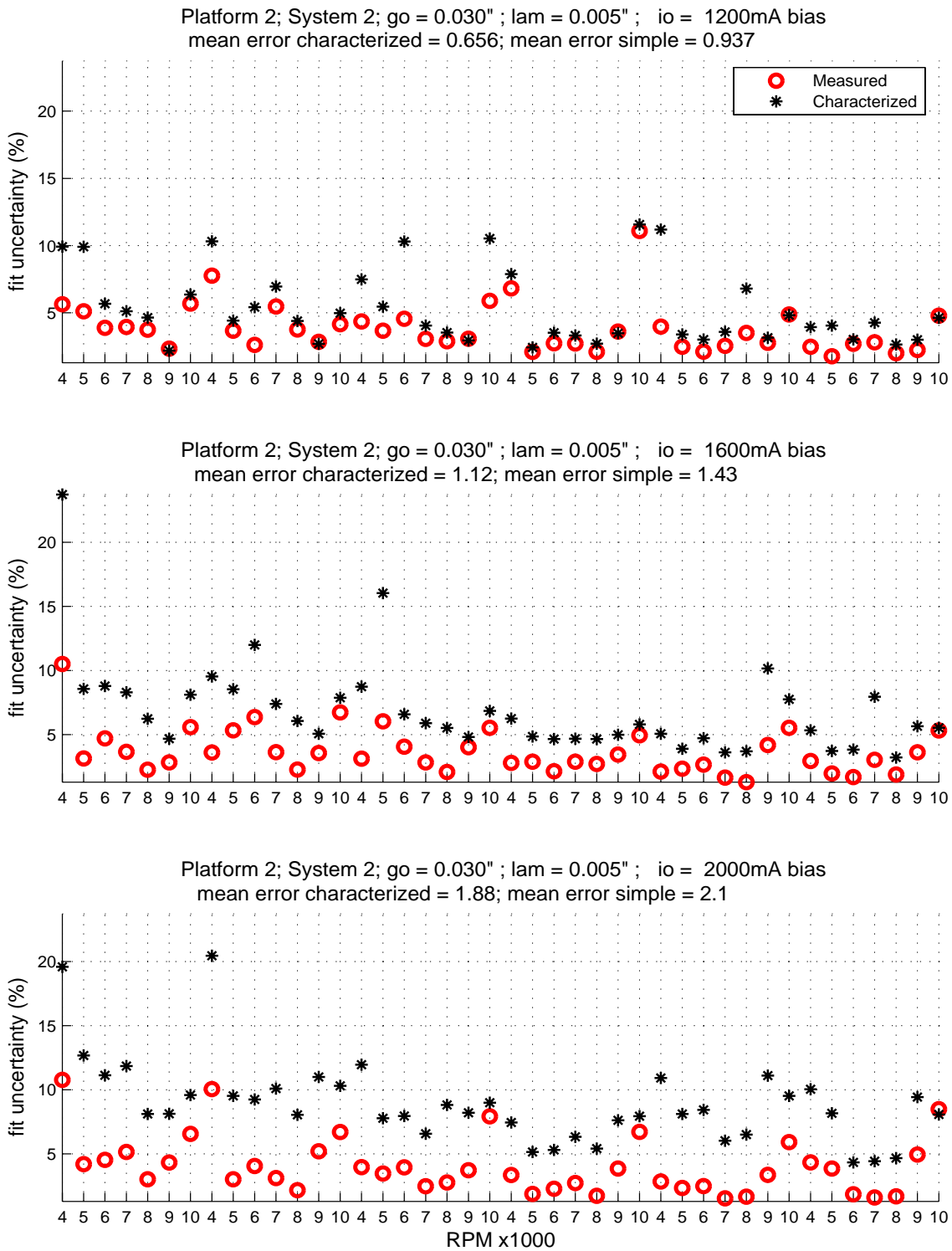


**Figure B.6: Comparison of curve fit uncertainty versus Rotor Speed as a percent of measured load. Platform 2 System 2. Added Unbalance (left to right) 0, 200, 400, 600, 800, and 1000mg (0, 0.45, 0.9, 1.35, 1.8, and 2.25 gm-in)**

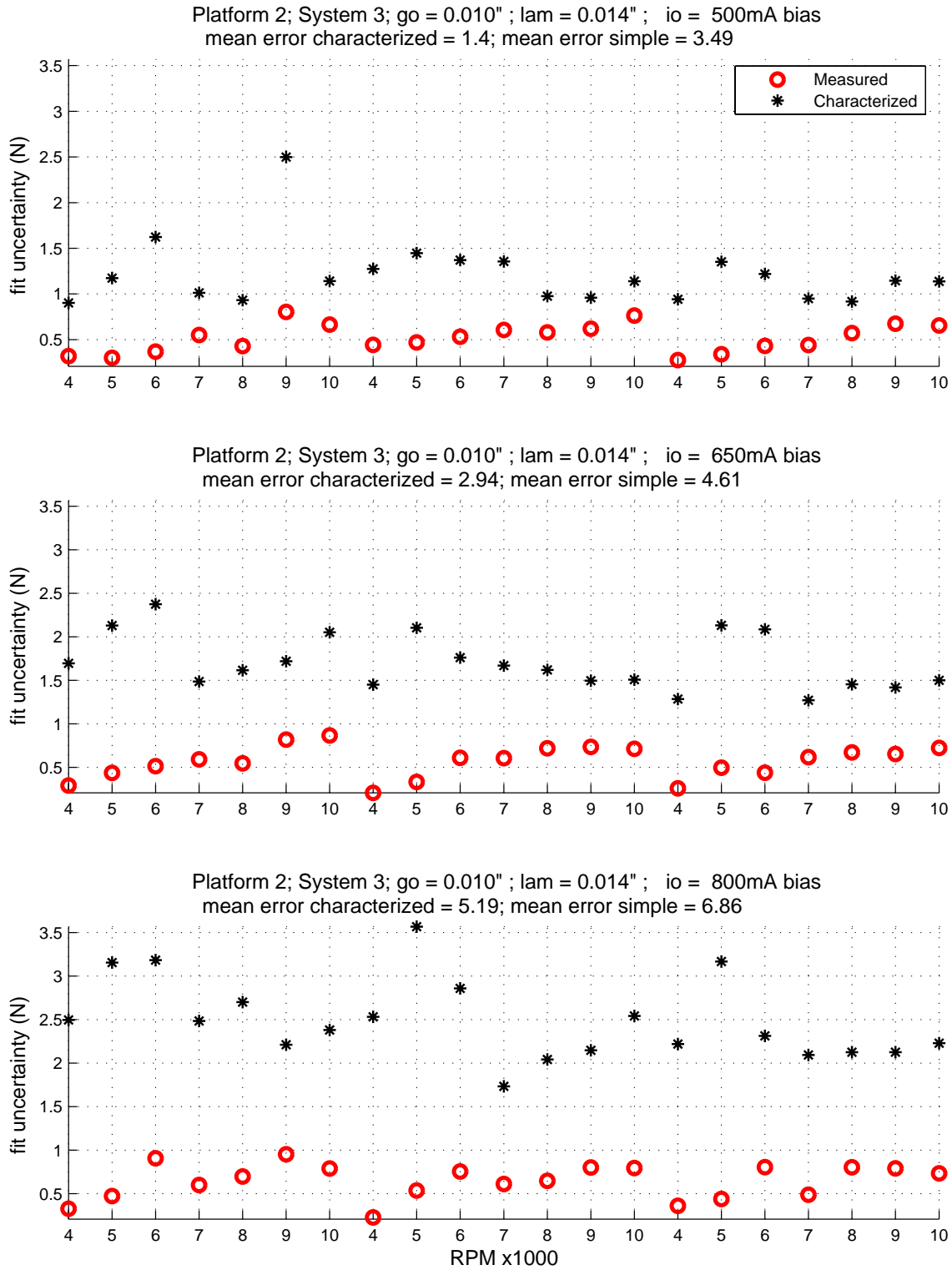


**Figure B.7: Comparison of curve fit uncertainty versus Rotor Speed. Platform 2 System 3. Added Unbalance (left to right) 0, 100, and 200mg (0, 0.23, 0.45 gm-in)**

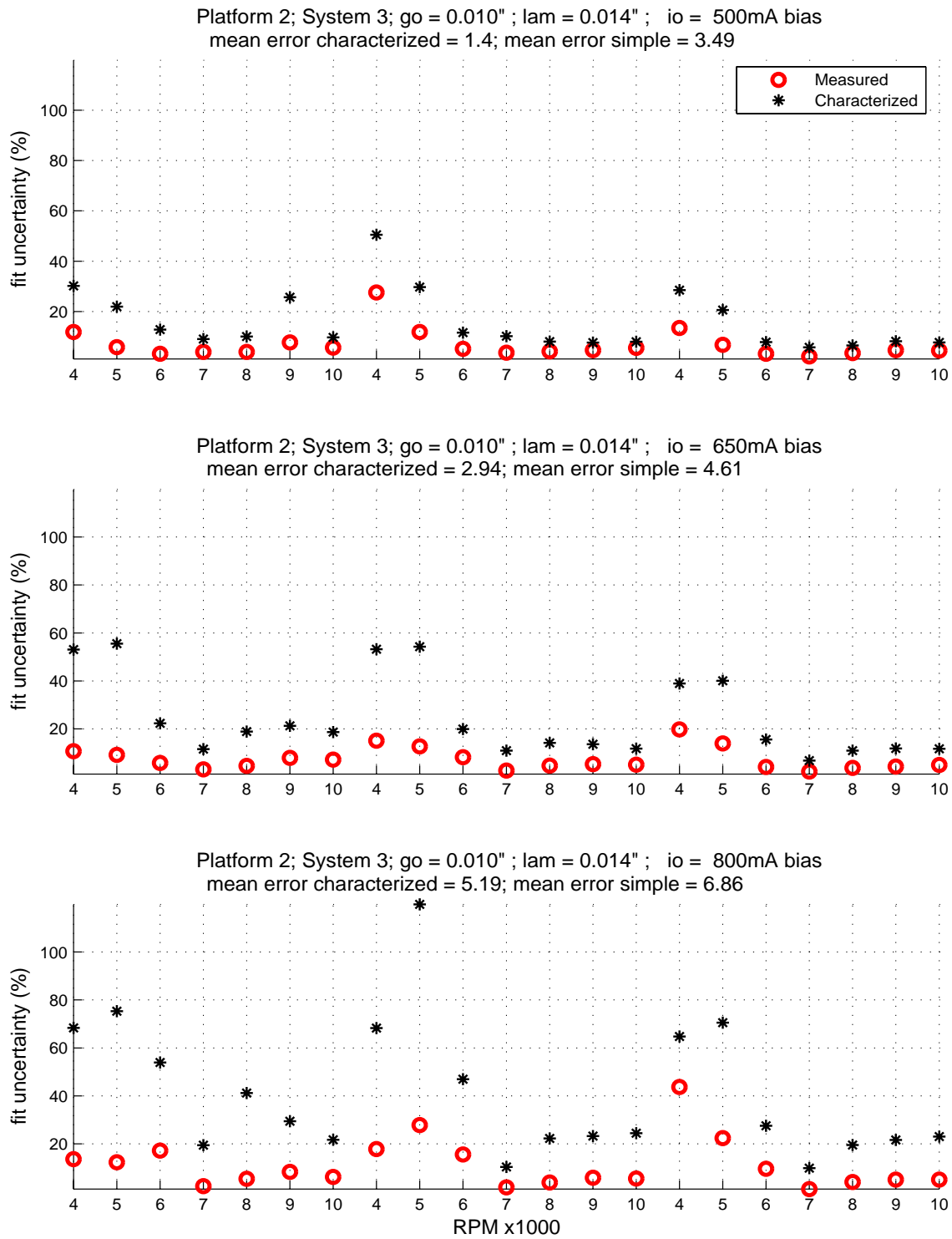


**Figure B.8: Comparison of curve fit uncertainty versus Rotor Speed as a percent of measured load. Platform 2 System 3. Added Unbalance (left to right) 0, 100, and 200mg (0, 0.23, 0.45 gm-in)**

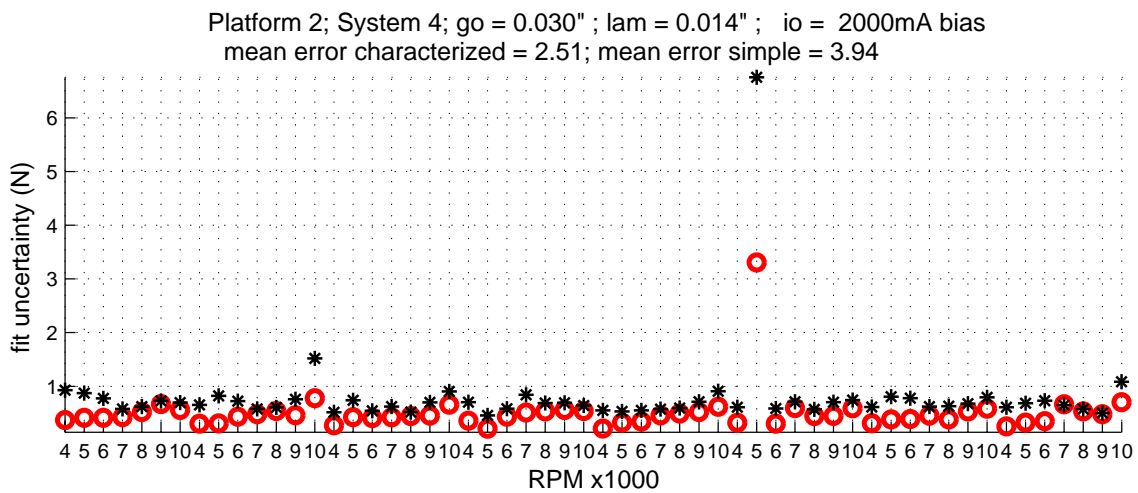
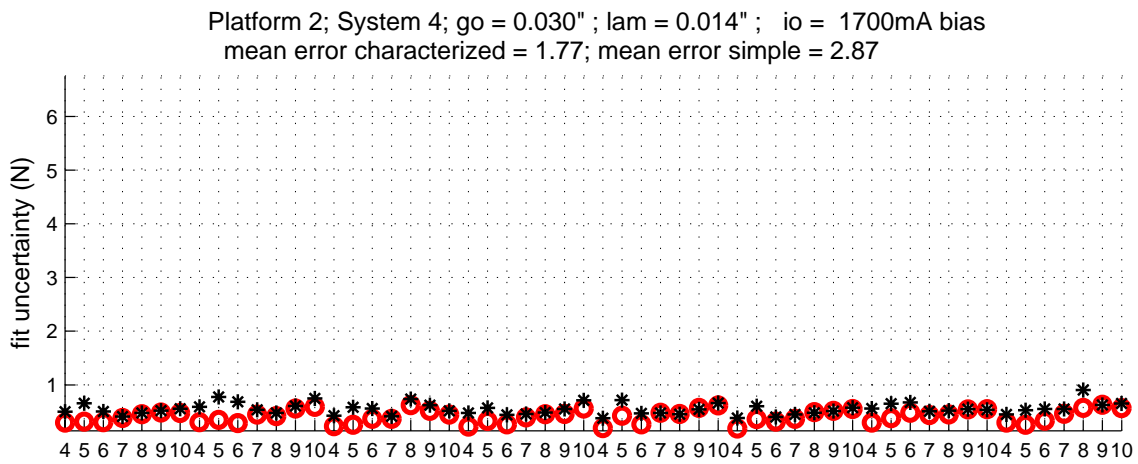
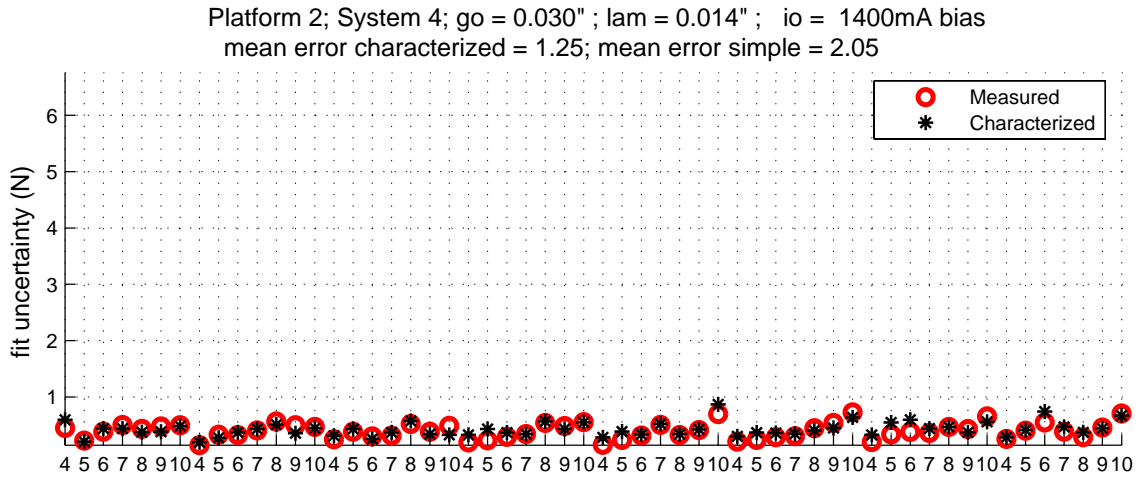


**Figure B.9: Comparison of curve fit uncertainty versus Rotor Speed. Platform 2 System 4. Added Unbalance (left to right) 0, 200, 300, 400, 500, 600, 700, and 800mg (0, 0.45, 0.68, 0.9, 1.13, 1.35, 1.58, 1.8 gm-in)**

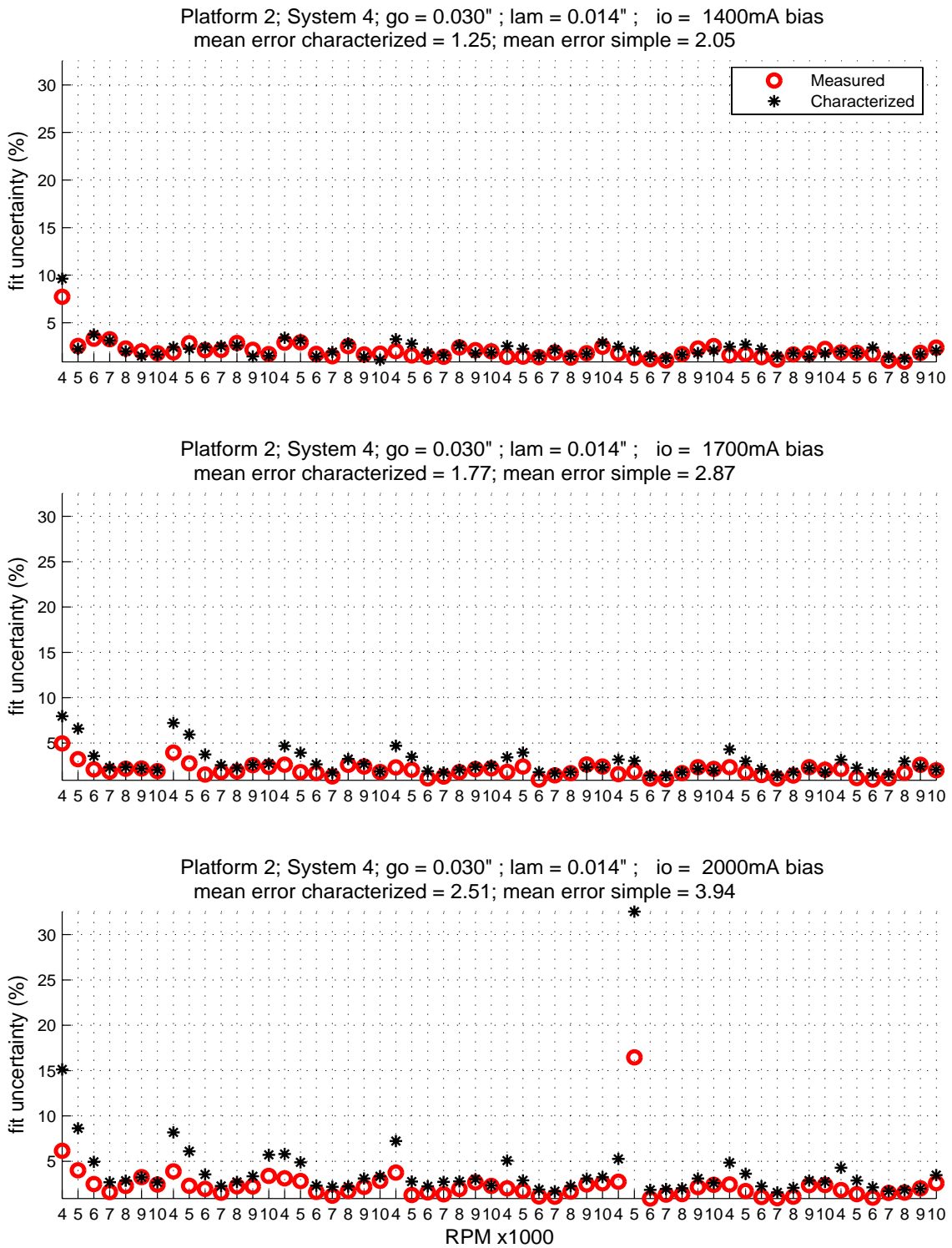


**Figure B.10: Comparison of curve fit uncertainty versus Rotor Speed as a percent of measured load. Platform 2 System 4. Added Unbalance (left to right) 0, 200, 300, 400, 500, 600, 700, and 800mg (0, 0.45, 0.68, 0.9, 1.13, 1.35, 1.58, 1.8 gm-in)**

## Appendix C Dynamic Force Measurement Results: Raw Data

Table C.1: Platform 1 SetUp 1

Added Unbalance (mg)	Rotor Speed (RPM)	Bias Current (Amps)	Dynamic Force Amplitude ( $N$ )			Error ( $N$ )		Error as Percent of Measured Force (%)		Error as Percent of Maximum Measured Force (%)	
			Meas'd	Basic	Char.	Basic	Char.	Basic	Char.	Basic	Char.
0	4000	1.3	4.05	5.70	5.20	1.65	1.15	40.8	28.4	4.8	3.3
		1.5	3.82	5.61	5.04	1.79	1.22	47.0	32.0	5.2	3.5
		1.7	3.89	5.50	4.90	1.61	1.00	41.3	25.7	4.7	2.9
	5000	1.3	6.23	7.76	7.20	1.52	0.96	24.4	15.5	4.4	2.8
		1.5	6.30	7.82	7.16	1.52	0.86	24.1	13.7	4.4	2.5
		1.7	6.33	7.84	7.08	1.51	0.75	23.8	11.9	4.4	2.2
	6000	1.3	8.71	9.90	9.26	1.19	0.55	13.7	6.3	3.5	1.6
		1.5	8.72	10.14	9.37	1.42	0.65	16.3	7.4	4.1	1.9
		1.7	8.91	10.20	9.31	1.29	0.40	14.5	4.5	3.7	1.2
	7000	1.3	11.38	12.59	11.84	1.21	0.46	10.6	4.0	3.5	1.3
		1.5	11.74	13.03	12.14	1.29	0.40	11.0	3.4	3.8	1.2
		1.7	11.57	13.18	12.12	1.61	0.55	13.9	4.8	4.7	1.6
	8000	1.3	14.76	15.96	15.06	1.19	0.30	8.1	2.0	3.5	0.9
		1.5	15.19	16.69	15.64	1.50	0.46	9.9	3.0	4.4	1.3
		1.7	15.74	17.16	15.91	1.42	0.17	9.0	1.1	4.1	0.5
	9000	1.3	18.23	19.99	18.92	1.76	0.68	9.6	3.7	5.1	2.0
		1.5	19.18	21.10	19.79	1.91	0.61	10.0	3.2	5.6	1.8
		1.7	19.52	21.77	20.30	2.25	0.77	11.5	4.0	6.5	2.2
	10000	1.3	21.41	24.29	23.00	2.88	1.59	13.5	7.4	8.4	4.6
		1.5	22.48	25.70	24.18	3.22	1.70	14.3	7.6	9.4	5.0
		1.7	23.22	26.48	24.75	3.26	1.52	14.0	6.6	9.5	4.4

Added Unbalance (mg)	Rotor Speed (RPM)	Bias Current (Amps)	Dynamic Force Amplitude (N)			Error (N)		Error as Percent of Measured Force (%)		Error as Percent of Maximum Measured Force (%)		
			Meas'd	Basic	Char.	Basic	Char.	Basic	Char.	Basic	Char.	
<b>400</b>	<b>4000</b>	<b>1.3</b>	5.30	7.04	6.42	1.73	1.12	32.7	21.1	5.0	3.3	
		<b>1.5</b>	5.08	6.93	6.24	1.85	1.15	36.4	22.6	5.4	3.3	
		<b>1.7</b>	5.16	6.74	5.97	1.58	0.81	30.6	15.7	4.6	2.4	
	<b>5000</b>	<b>1.3</b>	7.88	9.49	8.80	1.61	0.92	20.4	11.6	4.7	2.7	
		<b>1.5</b>	8.00	9.56	8.75	1.56	0.75	19.6	9.4	4.5	2.2	
		<b>1.7</b>	8.01	9.53	8.63	1.52	0.62	19.0	7.7	4.4	1.8	
	<b>6000</b>	<b>1.3</b>	10.74	12.14	11.35	1.41	0.62	13.1	5.8	4.1	1.8	
		<b>1.5</b>	11.08	12.42	11.51	1.34	0.43	12.1	3.8	3.9	1.2	
		<b>1.7</b>	11.32	12.60	11.55	1.28	0.23	11.3	2.0	3.7	0.7	
	<b>7000</b>	<b>1.3</b>	14.08	15.48	14.55	1.40	0.47	9.9	3.4	4.1	1.4	
		<b>1.5</b>	14.79	16.02	14.91	1.24	0.12	8.4	0.8	3.6	0.4	
		<b>1.7</b>	14.83	16.35	15.09	1.52	0.26	10.3	1.7	4.4	0.7	
	<b>8000</b>	<b>1.3</b>	18.25	19.56	18.43	1.31	0.18	7.2	1.0	3.8	0.5	
		<b>1.5</b>	18.88	20.56	19.24	1.68	0.35	8.9	1.9	4.9	1.0	
		<b>1.7</b>	19.68	21.11	19.55	1.43	-0.13	7.3	-0.6	4.2	-0.4	
	<b>9000</b>	<b>1.3</b>	22.58	24.59	23.21	2.01	0.63	8.9	2.8	5.8	1.8	
		<b>1.5</b>	23.95	25.91	24.29	1.96	0.34	8.2	1.4	5.7	1.0	
		<b>1.7</b>	24.82	26.91	25.02	2.09	0.20	8.4	0.8	6.1	0.6	
	<b>10000</b>	<b>1.3</b>	26.32	29.73	28.05	3.41	1.73	13.0	6.6	9.9	5.0	
		<b>1.5</b>	27.55	31.33	29.44	3.78	1.89	13.7	6.9	11.0	5.5	
		<b>1.7</b>	28.66	32.58	30.44	3.93	1.78	13.7	6.2	11.4	5.2	
	<b>600</b>	<b>4000</b>	<b>1.3</b>	5.80	7.65	6.96	1.85	1.17	31.9	20.1	5.4	3.4
			<b>1.5</b>	5.70	7.53	6.77	1.83	1.07	32.2	18.8	5.3	3.1
			<b>1.7</b>	5.69	7.33	6.49	1.65	0.80	28.9	14.1	4.8	2.3
<b>5000</b>		<b>1.3</b>	8.67	10.29	9.54	1.62	0.86	18.7	9.9	4.7	2.5	
		<b>1.5</b>	8.83	10.37	9.49	1.54	0.66	17.5	7.5	4.5	1.9	
		<b>1.7</b>	8.72	10.30	9.29	1.58	0.58	18.1	6.6	4.6	1.7	
<b>6000</b>		<b>1.3</b>	11.69	13.20	12.34	1.52	0.65	13.0	5.6	4.4	1.9	
		<b>1.5</b>	12.03	13.54	12.53	1.51	0.50	12.6	4.2	4.4	1.5	
		<b>1.7</b>	12.24	13.67	12.51	1.43	0.27	11.6	2.2	4.1	0.8	
<b>7000</b>		<b>1.3</b>	15.77	16.87	15.84	1.10	0.07	7.0	0.5	3.2	0.2	
		<b>1.5</b>	15.97	17.46	16.27	1.49	0.30	9.3	1.9	4.3	0.9	
		<b>1.7</b>	16.35	17.80	16.41	1.45	0.06	8.9	0.4	4.2	0.2	
<b>8000</b>		<b>1.3</b>	20.25	21.48	20.24	1.23	-0.01	6.1	0.0	3.6	0.0	
		<b>1.5</b>	20.94	22.52	21.05	1.58	0.11	7.5	0.5	4.6	0.3	
		<b>1.7</b>	21.61	23.33	21.64	1.72	0.03	7.9	0.1	5.0	0.1	
<b>9000</b>		<b>1.3</b>	24.69	27.07	25.52	2.38	0.83	9.6	3.4	6.9	2.4	
		<b>1.5</b>	26.26	28.61	26.82	2.35	0.56	9.0	2.1	6.8	1.6	
		<b>1.7</b>	27.28	29.66	27.59	2.38	0.31	8.7	1.1	6.9	0.9	
<b>10000</b>		<b>1.3</b>	28.93	32.63	30.74	3.71	1.81	12.8	6.3	10.8	5.3	

Added Unbalance (mg)	Rotor Speed (RPM)	Bias Current (Amps)	Dynamic Force Amplitude (N)			Error (N)		Error as Percent of Measured Force (%)		Error as Percent of Maximum Measured Force (%)		
			Meas'd	Basic	Char.	Basic	Char.	Basic	Char.	Basic	Char.	
		1.5	30.74	34.47	32.32	3.73	1.58	12.2	5.2	10.9	4.6	
		1.7	32.11	36.04	33.63	3.93	1.52	12.3	4.7	11.4	4.4	
		1.3	6.45	8.52	7.76	2.07	1.31	32.1	20.3	6.0	3.8	
800	4000	1.5	6.46	8.37	7.52	1.91	1.06	29.6	16.4	5.6	3.1	
		1.7	6.26	8.18	7.25	1.92	0.98	30.7	15.7	5.6	2.9	
		1.3	9.63	11.44	10.60	1.81	0.97	18.8	10.0	5.3	2.8	
	5000	1.5	9.78	11.56	10.58	1.78	0.80	18.2	8.2	5.2	2.3	
		1.7	9.70	11.51	10.42	1.81	0.73	18.7	7.5	5.3	2.1	
		1.3	13.15	14.66	13.71	1.51	0.55	11.5	4.2	4.4	1.6	
	6000	1.5	13.21	15.00	13.88	1.80	0.67	13.6	5.1	5.2	2.0	
		1.7	13.35	15.15	13.88	1.80	0.53	13.5	4.0	5.2	1.5	
		1.3	17.46	18.73	17.59	1.27	0.13	7.3	0.8	3.7	0.4	
	7000	1.5	17.95	19.41	18.08	1.46	0.13	8.1	0.7	4.2	0.4	
		1.7	18.13	19.76	18.23	1.63	0.10	9.0	0.6	4.7	0.3	
		1.3	22.49	23.79	22.36	1.30	-0.13	5.8	-0.6	3.8	-0.4	
	8000	1.5	23.27	24.97	23.34	1.70	0.07	7.3	0.3	5.0	0.2	
		1.7	23.80	25.80	23.93	2.00	0.12	8.4	0.5	5.8	0.4	
		1.3	27.37	29.83	28.07	2.46	0.70	9.0	2.5	7.1	2.0	
	9000	1.5	29.02	31.64	29.63	2.62	0.60	9.0	2.1	7.6	1.7	
		1.7	30.78	32.91	30.57	2.13	-0.21	6.9	-0.7	6.2	-0.6	
		1.3	30.16	32.53	30.60	2.37	0.44	7.9	1.5	6.9	1.3	
	10000	1.5	31.38	34.39	32.24	3.01	0.85	9.6	2.7	8.7	2.5	
		1.7	32.81	35.94	33.49	3.13	0.68	9.5	2.1	9.1	2.0	
		1.3	7.59	9.72	8.86	2.14	1.27	28.2	16.8	6.2	3.7	
	1000	4000	1.5	7.48	9.52	8.54	2.05	1.06	27.4	14.2	5.9	3.1
			1.7	7.45	9.30	8.23	1.85	0.78	24.8	10.4	5.4	2.3
			1.3	12.36	14.54	13.47	2.17	1.10	17.6	8.9	6.3	3.2
5000		1.5	12.39	14.61	13.39	2.21	0.99	17.9	8.0	6.4	2.9	
		1.7	12.34	14.46	13.12	2.12	0.78	17.2	6.3	6.2	2.3	
		1.3	17.36	19.27	18.00	1.91	0.63	11.0	3.7	5.5	1.8	
6000		1.5	17.63	19.72	18.24	2.08	0.61	11.8	3.4	6.1	1.8	
		1.7	18.05	19.85	18.18	1.80	0.13	10.0	0.7	5.2	0.4	
		1.3	21.92	23.44	21.98	1.52	0.05	6.9	0.2	4.4	0.2	
7000		1.5	22.49	24.27	22.60	1.78	0.10	7.9	0.5	5.2	0.3	
		1.7	23.32	24.65	22.75	1.34	-0.57	5.7	-2.4	3.9	-1.6	
		1.3	26.22	27.43	25.77	1.21	-0.45	4.6	-1.7	3.5	-1.3	
8000		1.5	31.61	32.72	30.51	1.11	-1.10	3.5	-3.5	3.2	-3.2	
		1.7	32.47	33.46	30.97	0.99	-1.49	3.0	-4.6	2.9	-4.3	
		1.3	32.74	34.05	31.94	1.30	-0.81	4.0	-2.5	3.8	-2.3	
9000		1.5	34.41	35.55	33.21	1.14	-1.19	3.3	-3.5	3.3	-3.5	

Added Unbalance (mg)	Rotor Speed (RPM)	Bias Current (Amps)	Dynamic Force Amplitude ( <i>N</i> )			Error ( <i>N</i> )		Error as Percent of Measured Force (%)		Error as Percent of Maximum Measured Force (%)		
			Meas'd	Basic	Char.	Basic	Char.	Basic	Char.	Basic	Char.	
	<b>10000</b>	<b>1.7</b>	30.68	32.92	30.57	2.23	-0.11	7.3	-0.4	6.8	-0.3	
		<b>1.3</b>	30.12	32.58	30.65	2.46	0.53	8.2	1.8	7.5	1.6	
		<b>1.5</b>	31.25	34.39	32.23	3.14	0.98	10.0	3.1	9.6	3.0	
		<b>1.7</b>	32.77	35.97	33.51	3.19	0.74	9.7	2.3	9.7	2.3	
						<b>MAXIMUM</b>	<b>3.93</b>	<b>1.89</b>	<b>47.0</b>	<b>32.0</b>	<b>11.4</b>	<b>5.5</b>
						<b>MEAN</b>	<b>1.90</b>	<b>0.69</b>	<b>14.4</b>	<b>6.2</b>	<b>5.5</b>	<b>2.0</b>

**Table C.2: Platform 2 SetUp 1**

Added Unbalance (mg)	Rotor Speed (RPM)	Bias Current (Amps)	Dynamic Force Amplitude (N)			Error (N)		Error as Percent of Measured Force (%)		Error as Percent of Maximum Measured Force (%)		
			Meas'd	Basic	Char.	Basic	Char.	Basic	Char.	Basic	Char.	
<b>0</b>	<b>4000</b>	<b>0.5</b>	1.93	3.68	1.45	1.75	-0.48	91.0	-24.8	2.9	-0.8	
		<b>0.6</b>	2.08	5.57	2.04	3.49	-0.04	167.8	-2.1	5.7	-0.1	
		<b>0.7</b>	3.39	8.23	3.43	4.84	0.04	142.8	1.2	8.0	0.1	
	<b>5000</b>	<b>0.5</b>	3.80	1.94	1.73	-1.86	-2.07	-48.9	-54.6	-3.1	-3.4	
		<b>0.6</b>	4.31	4.29	2.09	-0.02	-2.21	-0.4	-51.4	0.0	-3.6	
		<b>0.7</b>	6.18	7.50	4.11	1.32	-2.07	21.4	-33.5	2.2	-3.4	
	<b>6000</b>	<b>0.5</b>	9.33	5.70	7.47	-3.64	-1.86	-39.0	-19.9	-6.0	-3.1	
		<b>0.6</b>	10.72	3.22	6.80	-7.50	-3.92	-70.0	-36.6	-12.3	-6.4	
		<b>0.7</b>	12.98	2.65	6.28	-10.33	-6.70	-79.6	-51.6	-17.0	-11.0	
	<b>7000</b>	<b>0.5</b>	31.73	26.95	25.34	-4.78	-6.39	-15.1	-20.1	-7.9	-10.5	
		<b>0.6</b>	44.57	33.51	31.30	-11.06	-13.27	-24.8	-29.8	-18.2	-21.8	
		<b>0.7</b>	44.87	29.69	26.82	-15.18	-18.05	-33.8	-40.2	-25.0	-29.7	
	<b>8000</b>	<b>0.5</b>	30.97	32.92	30.11	1.95	-0.85	6.3	-2.8	3.2	-1.4	
		<b>0.6</b>	30.60	33.02	29.18	2.43	-1.42	7.9	-4.6	4.0	-2.3	
		<b>0.7</b>	32.66	36.07	30.75	3.41	-1.91	10.5	-5.8	5.6	-3.1	
	<b>9000</b>	<b>0.5</b>	31.15	36.64	33.46	5.49	2.31	17.6	7.4	9.0	3.8	
		<b>0.6</b>	29.92	36.28	32.33	6.36	2.41	21.2	8.0	10.5	4.0	
		<b>0.7</b>	31.00	39.81	34.46	8.81	3.47	28.4	11.2	14.5	5.7	
	<b>10000</b>	<b>0.5</b>	33.62	42.31	39.19	8.69	5.57	25.8	16.6	14.3	9.2	
		<b>0.6</b>	35.50	42.77	38.60	7.27	3.09	20.5	8.7	12.0	5.1	
		<b>0.7</b>	32.79	46.06	40.79	13.28	8.00	40.5	24.4	21.8	13.2	
	<b>100</b>	<b>4000</b>	<b>0.5</b>	2.82	3.21	1.89	0.39	-0.94	13.7	-33.2	0.6	-1.5
			<b>0.6</b>	3.19	5.08	2.23	1.90	-0.96	59.6	-30.0	3.1	-1.6
			<b>0.7</b>	4.37	8.09	3.70	3.72	-0.67	85.1	-15.3	6.1	-1.1
<b>5000</b>		<b>0.5</b>	6.08	2.54	3.88	-3.55	-2.20	-58.3	-36.2	-5.8	-3.6	
		<b>0.6</b>	6.56	4.21	3.84	-2.36	-2.72	-35.9	-41.5	-3.9	-4.5	
		<b>0.7</b>	8.56	7.16	5.11	-1.41	-3.45	-16.4	-40.3	-2.3	-5.7	
<b>6000</b>		<b>0.5</b>	13.23	8.53	10.79	-4.70	-2.44	-35.5	-18.4	-7.7	-4.0	
		<b>0.6</b>	15.00	6.57	10.22	-8.42	-4.77	-56.2	-31.8	-13.9	-7.9	
		<b>0.7</b>	17.02	5.44	9.55	-11.58	-7.47	-68.0	-43.9	-19.0	-12.3	
<b>7000</b>		<b>0.5</b>	37.32	29.53	28.21	-7.79	-9.11	-20.9	-24.4	-12.8	-15.0	
		<b>0.6</b>	52.18	36.85	35.17	-15.33	-17.01	-29.4	-32.6	-25.2	-28.0	
		<b>0.7</b>	52.99	31.56	29.22	-21.44	-23.77	-40.4	-44.9	-35.3	-39.1	
<b>8000</b>		<b>0.5</b>	33.76	34.23	31.39	0.47	-2.37	1.4	-7.0	0.8	-3.9	
		<b>0.6</b>	33.26	34.29	30.51	1.03	-2.75	3.1	-8.3	1.7	-4.5	
		<b>0.7</b>	35.39	37.00	31.78	1.61	-3.61	4.5	-10.2	2.6	-5.9	
<b>9000</b>		<b>0.5</b>	31.93	36.51	33.45	4.58	1.52	14.3	4.7	7.5	2.5	
		<b>0.6</b>	31.17	36.50	32.55	5.32	1.37	17.1	4.4	8.8	2.3	
		<b>0.7</b>	31.75	40.69	35.37	8.94	3.62	28.2	11.4	14.7	6.0	

Added Unbalance (mg)	Rotor Speed (RPM)	Bias Current (Amps)	Dynamic Force Amplitude (N)			Error (N)		Error as Percent of Measured Force (%)		Error as Percent of Maximum Measured Force (%)		
			Meas'd	Basic	Char.	Basic	Char.	Basic	Char.	Basic	Char.	
10000	10000	0.5	32.75	41.73	38.61	8.99	5.86	27.5	17.9	14.8	9.6	
		0.6	32.75	42.08	38.10	9.33	5.35	28.5	16.3	15.4	8.8	
		0.7	34.19	46.33	41.15	12.14	6.96	35.5	20.3	20.0	11.4	
200	4000	0.5	3.72	3.26	2.72	-0.46	-0.99	-12.4	-26.7	-0.8	-1.6	
		0.6	4.20	5.10	2.89	0.89	-1.31	21.3	-31.2	1.5	-2.2	
		0.7	5.11	7.81	3.85	2.70	-1.26	52.9	-24.7	4.4	-2.1	
	5000	0.5	7.89	4.04	5.73	-3.85	-2.16	-48.8	-27.4	-6.3	-3.6	
		0.6	8.84	4.91	5.66	-3.93	-3.18	-44.5	-36.0	-6.5	-5.2	
		0.7	11.02	7.34	6.31	-3.68	-4.71	-33.4	-42.7	-6.1	-7.8	
	6000	0.5	16.90	11.45	14.03	-5.45	-2.87	-32.2	-17.0	-9.0	-4.7	
		0.6	18.53	9.54	13.13	-8.99	-5.40	-48.5	-29.1	-14.8	-8.9	
		0.7	20.89	8.23	12.43	-12.66	-8.46	-60.6	-40.5	-20.8	-13.9	
	7000	0.5	42.31	32.40	31.32	-9.91	-10.99	-23.4	-26.0	-16.3	-18.1	
		0.6	51.29	34.10	32.64	-17.18	-18.64	-33.5	-36.3	-28.3	-30.7	
		0.7	60.29	32.64	30.70	-27.65	-29.59	-45.9	-49.1	-45.5	-48.7	
	8000	0.5	36.38	35.71	32.87	-0.67	-3.51	-1.8	-9.6	-1.1	-5.8	
		0.6	36.85	36.56	32.72	-0.30	-4.13	-0.8	-11.2	-0.5	-6.8	
		0.7	38.32	37.37	32.05	-0.95	-6.26	-2.5	-16.3	-1.6	-10.3	
	9000	0.5	33.41	37.36	34.24	3.95	0.83	11.8	2.5	6.5	1.4	
		0.6	32.82	38.23	34.16	5.41	1.34	16.5	4.1	8.9	2.2	
		0.7	32.12	39.92	34.42	7.80	2.30	24.3	7.2	12.8	3.8	
	10000	0.5	34.02	42.52	39.44	8.50	5.43	25.0	16.0	14.0	8.9	
		0.6	34.20	43.46	39.42	9.26	5.22	27.1	15.3	15.2	8.6	
		0.7	33.43	45.59	40.41	12.16	6.97	36.4	20.9	20.0	11.5	
	300	4000	0.5	4.87	3.58	3.63	-1.29	-1.24	-26.5	-25.5	-2.1	-2.0
			0.6	5.33	5.12	3.71	-0.21	-1.62	-3.9	-30.3	-0.3	-2.7
			0.7	6.06	7.91	4.55	1.85	-1.50	30.6	-24.8	3.0	-2.5
		5000	0.5	10.45	5.94	7.61	-4.50	-2.84	-43.1	-27.2	-7.4	-4.7
			0.6	11.20	6.20	7.56	-5.00	-3.64	-44.6	-32.5	-8.2	-6.0
			0.7	12.94	8.14	7.99	-4.80	-4.95	-37.1	-38.3	-7.9	-8.2
		6000	0.5	20.27	14.53	17.00	-5.74	-3.27	-28.3	-16.1	-9.4	-5.4
			0.6	22.36	13.13	16.72	-9.23	-5.64	-41.3	-25.2	-15.2	-9.3
			0.7	24.78	11.07	15.21	-13.71	-9.57	-55.3	-38.6	-22.6	-15.7
7000		0.5	48.40	35.14	34.31	-13.27	-14.10	-27.4	-29.1	-21.8	-23.2	
		0.6	59.26	36.83	35.68	-22.42	-23.57	-37.8	-39.8	-36.9	-38.8	
		0.7	60.78	33.66	32.29	-27.12	-28.49	-44.6	-46.9	-44.6	-46.9	
8000		0.5	38.89	37.07	34.26	-1.81	-4.62	-4.7	-11.9	-4.4	-11.3	
		0.6	39.23	37.62	33.80	-1.61	-5.43	-4.1	-13.8	-3.9	-13.3	
		0.7	40.95	37.95	32.77	-3.00	-8.18	-7.3	-20.0	-7.3	-20.0	
9000		0.5	34.03	38.35	35.30	4.32	1.27	12.7	3.7	12.2	3.6	

Added Unbalance (mg)	Rotor Speed (RPM)	Bias Current (Amps)	Dynamic Force Amplitude ( <i>N</i> )			Error ( <i>N</i> )		Error as Percent of Measured Force (%)		Error as Percent of Maximum Measured Force (%)	
			Meas'd	Basic	Char.	Basic	Char.	Basic	Char.	Basic	Char.
		<b>0.6</b>	33.60	38.94	34.89	5.34	1.29	15.9	3.8	15.1	3.6
		<b>0.7</b>	32.96	39.75	34.27	6.78	1.31	20.6	4.0	19.2	3.7
	<b>10000</b>	<b>0.5</b>	35.23	42.22	39.12	6.99	3.89	19.8	11.0	19.8	11.0
		<b>0.6</b>	35.30	43.84	39.83	8.54	4.53	24.2	12.8	24.2	12.8
		<b>0.7</b>	33.20	44.54	39.33	11.35	6.13	34.2	18.5	34.2	18.5
				<b>MAXIMUM</b>	<b>27.65</b>	<b>29.59</b>	<b>167.8</b>	<b>54.6</b>	<b>45.5</b>	<b>48.7</b>	
			<b>MEAN</b>	<b>6.71</b>	<b>5.45</b>	<b>32.9</b>	<b>22.8</b>	<b>11.7</b>	<b>9.4</b>		

**Table C.3: Platform 2 SetUp 2**

Added Unbalance (mg)	Rotor Speed (RPM)	Bias Current (Amps)	Dynamic Force Amplitude (N)			Error (N)		Error as Percent of Measured Force (%)		Error as Percent of Maximum Measured Force (%)	
			Meas'd	Basic	Char.	Basic	Char.	Basic	Char.	Basic	Char.
<b>0</b>	<b>4000</b>	<b>1.2</b>	3.58	4.48	3.83	0.90	0.25	25.1	6.9	3.5	1.0
		<b>1.6</b>	3.88	5.20	4.08	1.31	0.20	33.8	5.1	4.2	0.6
		<b>2.0</b>	3.70	5.57	3.93	1.87	0.23	50.6	6.3	5.9	0.7
	<b>5000</b>	<b>1.2</b>	4.70	5.28	4.67	0.58	-0.04	12.3	-0.8	2.2	-0.1
		<b>1.6</b>	5.50	6.64	5.55	1.14	0.05	20.7	0.9	4.4	0.2
		<b>2.0</b>	5.73	7.58	5.94	1.85	0.21	32.4	3.6	7.1	0.8
	<b>6000</b>	<b>1.2</b>	5.49	6.21	5.67	0.72	0.18	13.2	3.3	2.8	0.7
		<b>1.6</b>	6.97	8.14	7.21	1.17	0.24	16.7	3.4	4.5	0.9
		<b>2.0</b>	8.08	9.63	8.09	1.55	0.01	19.2	0.1	6.0	0.0
	<b>7000</b>	<b>1.2</b>	7.50	7.35	6.99	-0.15	-0.51	-2.1	-6.8	-0.6	-2.0
		<b>1.6</b>	9.68	9.57	8.98	-0.11	-0.70	-1.1	-7.2	-0.4	-2.7
		<b>2.0</b>	12.19	11.46	10.48	-0.73	-1.71	-6.0	-14.0	-2.4	-5.6
	<b>8000</b>	<b>1.2</b>	10.56	10.24	10.24	-0.33	-0.32	-3.1	-3.1	-1.1	-1.1
		<b>1.6</b>	13.66	12.21	12.41	-1.45	-1.25	-10.6	-9.2	-4.7	-4.1
		<b>2.0</b>	16.76	14.07	14.65	-2.69	-2.11	-16.1	-12.6	-8.5	-6.7
	<b>9000</b>	<b>1.2</b>	22.89	24.57	24.73	1.68	1.85	7.4	8.1	5.3	5.9
		<b>1.6</b>	17.15	18.46	19.06	1.31	1.92	7.7	11.2	4.2	6.1
		<b>2.0</b>	14.36	15.23	16.27	0.87	1.91	6.1	13.3	2.8	6.0
<b>10000</b>	<b>1.2</b>	9.28	10.61	10.15	1.33	0.88	14.4	9.4	4.2	2.8	
	<b>1.6</b>	9.34	11.97	11.45	2.63	2.10	28.1	22.5	8.3	6.7	
	<b>2.0</b>	9.30	12.73	12.38	3.43	3.08	36.8	33.1	10.9	9.8	
<b>200</b>	<b>4000</b>	<b>1.2</b>	4.19	5.00	4.28	0.81	0.09	19.4	2.2	2.6	0.3
		<b>1.6</b>	4.54	5.79	4.66	1.25	0.12	27.5	2.6	4.0	0.4
		<b>2.0</b>	4.34	6.15	4.63	1.81	0.28	41.8	6.6	5.7	0.9
	<b>5000</b>	<b>1.2</b>	5.27	6.25	5.55	0.98	0.28	18.7	5.3	3.1	0.9
		<b>1.6</b>	6.03	7.83	6.67	1.81	0.64	30.0	10.6	5.7	2.0
		<b>2.0</b>	6.64	8.82	7.16	2.19	0.53	32.9	8.0	6.9	1.7
	<b>6000</b>	<b>1.2</b>	6.48	7.39	6.71	0.91	0.23	14.0	3.5	2.9	0.7
		<b>1.6</b>	7.92	9.58	8.45	1.66	0.53	21.0	6.7	5.3	1.7
		<b>2.0</b>	9.87	11.43	9.72	1.56	-0.15	15.8	-1.5	5.0	-0.5
	<b>7000</b>	<b>1.2</b>	8.34	8.58	8.00	0.25	-0.34	2.9	-4.1	0.8	-1.1
		<b>1.6</b>	11.03	11.08	10.14	0.04	-0.90	0.4	-8.1	0.1	-2.8
		<b>2.0</b>	14.10	13.43	12.01	-0.67	-2.09	-4.7	-14.8	-2.1	-6.6
	<b>8000</b>	<b>1.2</b>	10.45	10.14	9.87	-0.31	-0.58	-3.0	-5.6	-1.0	-1.8
		<b>1.6</b>	13.28	12.23	12.07	-1.05	-1.21	-7.9	-9.1	-3.3	-3.8
		<b>2.0</b>	16.16	13.66	13.68	-2.50	-2.49	-15.5	-15.4	-7.9	-7.9
	<b>9000</b>	<b>1.2</b>	20.35	21.69	21.95	1.34	1.59	6.6	7.8	4.2	5.0
		<b>1.6</b>	15.56	16.81	17.51	1.25	1.95	8.0	12.5	4.0	6.2
		<b>2.0</b>	13.59	14.24	15.38	0.65	1.80	4.8	13.2	2.1	5.7

Added Unbalance (mg)	Rotor Speed (RPM)	Bias Current (Amps)	Dynamic Force Amplitude (N)			Error (N)		Error as Percent of Measured Force (%)		Error as Percent of Maximum Measured Force (%)		
			Meas'd	Basic	Char.	Basic	Char.	Basic	Char.	Basic	Char.	
<b>10000</b>	<b>10000</b>	<b>1.2</b>	9.52	11.28	10.88	1.76	1.36	18.5	14.3	5.6	4.3	
		<b>1.6</b>	10.02	12.75	12.32	2.73	2.30	27.2	22.9	8.6	7.3	
		<b>2.0</b>	9.80	13.58	13.27	3.78	3.47	38.6	35.5	12.0	11.0	
<b>400</b>	<b>4000</b>	<b>1.2</b>	5.00	5.99	5.26	0.99	0.26	19.8	5.2	3.1	0.8	
		<b>1.6</b>	5.38	6.91	5.82	1.53	0.44	28.4	8.3	4.8	1.4	
		<b>2.0</b>	5.53	6.98	5.55	1.45	0.02	26.1	0.4	4.6	0.1	
	<b>5000</b>	<b>1.2</b>	6.35	7.48	6.73	1.12	0.38	17.6	5.9	3.6	1.2	
		<b>1.6</b>	7.38	9.37	8.19	2.00	0.81	27.0	11.0	6.3	2.6	
		<b>2.0</b>	8.30	10.46	8.86	2.17	0.56	26.1	6.8	6.9	1.8	
	<b>6000</b>	<b>1.2</b>	7.71	8.80	8.03	1.09	0.32	14.1	4.2	3.5	1.0	
		<b>1.6</b>	9.94	11.57	10.33	1.62	0.38	16.3	3.8	5.1	1.2	
		<b>2.0</b>	12.61	13.90	12.12	1.28	-0.49	10.2	-3.9	4.1	-1.6	
	<b>7000</b>	<b>1.2</b>	10.25	10.30	9.59	0.05	-0.66	0.5	-6.4	0.1	-2.1	
		<b>1.6</b>	13.27	13.39	12.26	0.11	-1.02	0.8	-7.7	0.4	-3.2	
		<b>2.0</b>	17.32	16.52	14.84	-0.80	-2.48	-4.6	-14.3	-2.5	-7.9	
	<b>8000</b>	<b>1.2</b>	11.93	11.68	11.20	-0.25	-0.72	-2.1	-6.1	-0.8	-2.3	
		<b>1.6</b>	14.85	14.03	13.46	-0.82	-1.39	-5.5	-9.3	-2.6	-4.4	
		<b>2.0</b>	18.41	15.47	14.91	-2.94	-3.50	-16.0	-19.0	-9.3	-11.1	
	<b>9000</b>	<b>1.2</b>	18.74	20.00	20.25	1.26	1.52	6.7	8.1	4.0	4.8	
		<b>1.6</b>	15.68	16.36	17.08	0.68	1.40	4.3	8.9	2.2	4.4	
		<b>2.0</b>	13.87	13.85	15.12	-0.03	1.24	-0.2	8.9	-0.1	3.9	
	<b>10000</b>	<b>1.2</b>	9.94	11.73	11.28	1.79	1.35	18.0	13.6	5.7	4.3	
		<b>1.6</b>	10.20	13.54	13.17	3.34	2.97	32.8	29.1	10.6	9.4	
		<b>2.0</b>	10.13	14.57	14.21	4.44	4.08	43.8	40.3	14.1	12.9	
	<b>600</b>	<b>4000</b>	<b>1.2</b>	6.03	6.99	6.25	0.96	0.22	16.0	3.7	3.1	0.7
			<b>1.6</b>	6.58	7.90	6.84	1.33	0.26	20.1	3.9	4.2	0.8
			<b>2.0</b>	6.83	8.12	6.84	1.29	0.01	18.8	0.2	4.1	0.0
<b>5000</b>		<b>1.2</b>	7.60	8.99	8.21	1.39	0.62	18.3	8.1	4.4	2.0	
		<b>1.6</b>	9.17	11.10	9.92	1.93	0.75	21.0	8.2	6.1	2.4	
		<b>2.0</b>	10.19	12.40	10.88	2.21	0.69	21.7	6.8	7.0	2.2	
<b>6000</b>		<b>1.2</b>	9.67	10.83	10.03	1.16	0.35	12.0	3.7	3.7	1.1	
		<b>1.6</b>	12.40	14.01	12.73	1.61	0.33	12.9	2.6	5.1	1.0	
		<b>2.0</b>	15.20	16.84	15.05	1.64	-0.14	10.8	-1.0	5.2	-0.5	
<b>7000</b>		<b>1.2</b>	12.43	12.69	11.88	0.27	-0.55	2.1	-4.4	0.8	-1.7	
		<b>1.6</b>	16.32	16.64	15.37	0.33	-0.95	2.0	-5.8	1.0	-3.0	
		<b>2.0</b>	20.90	20.03	18.15	-0.87	-2.75	-4.2	-13.1	-2.8	-8.7	
<b>8000</b>		<b>1.2</b>	14.60	14.65	13.99	0.05	-0.61	0.3	-4.2	0.2	-1.9	
		<b>1.6</b>	17.96	17.23	16.35	-0.74	-1.61	-4.1	-9.0	-2.3	-5.1	
		<b>2.0</b>	21.51	18.96	17.91	-2.55	-3.60	-11.9	-16.7	-8.1	-11.4	
<b>9000</b>	<b>1.2</b>	16.82	17.30	17.55	0.48	0.72	2.8	4.3	1.5	2.3		

Added Unbalance (mg)	Rotor Speed (RPM)	Bias Current (Amps)	Dynamic Force Amplitude (N)			Error (N)		Error as Percent of Measured Force (%)		Error as Percent of Maximum Measured Force (%)		
			Meas'd	Basic	Char.	Basic	Char.	Basic	Char.	Basic	Char.	
		1.6	15.21	15.14	15.80	-0.07	0.59	-0.4	3.9	-0.2	1.9	
		2.0	13.78	13.26	14.56	-0.52	0.78	-3.8	5.7	-1.6	2.5	
		10000	1.2	9.54	11.47	11.11	1.93	1.57	20.2	16.4	6.1	5.0
		10000	1.6	9.97	13.24	12.91	3.27	2.94	32.8	29.5	10.4	9.3
			2.0	9.22	14.64	14.47	5.42	5.26	58.8	57.1	17.2	16.7
			800	4000	1.2	7.39	8.34	7.58	0.95	0.19	12.9	2.6
1.6	8.15	9.47	8.42		1.32	0.27	16.2	3.3	4.2	0.9		
2.0	8.40	9.72	8.50		1.32	0.10	15.7	1.2	4.2	0.3		
5000	5000	1.2	9.41		10.72	9.91	1.32	0.50	14.0	5.3	4.2	1.6
		1.6	11.37		13.20	11.98	1.83	0.62	16.1	5.4	5.8	2.0
		2.0	12.68		14.66	13.18	1.98	0.50	15.6	3.9	6.3	1.6
6000	6000	1.2	11.89	13.03	12.17	1.15	0.28	9.6	2.3	3.6	0.9	
		1.6	15.09	16.73	15.38	1.65	0.29	10.9	1.9	5.2	0.9	
		2.0	18.96	20.12	18.33	1.16	-0.62	6.1	-3.3	3.7	-2.0	
7000	7000	1.2	15.25	15.52	14.62	0.27	-0.63	1.7	-4.1	0.8	-2.0	
		1.6	19.99	20.10	18.71	0.11	-1.27	0.6	-6.4	0.4	-4.0	
		2.0	25.35	24.31	22.35	-1.04	-3.00	-4.1	-11.8	-3.3	-9.5	
8000	8000	1.2	17.31	17.89	17.08	0.58	-0.23	3.3	-1.4	1.8	-0.7	
		1.6	21.78	21.18	20.10	-0.60	-1.69	-2.8	-7.8	-1.9	-5.4	
		2.0	25.95	23.28	21.95	-2.68	-4.00	-10.3	-15.4	-8.5	-12.7	
9000	9000	1.2	17.70	17.62	17.74	-0.08	0.04	-0.4	0.2	-0.2	0.1	
		1.6	15.72	15.18	15.75	-0.54	0.03	-3.4	0.2	-1.7	0.1	
		2.0	14.92	13.05	14.17	-1.88	-0.76	-12.6	-5.1	-6.0	-2.4	
10000	10000	1.2	9.97	12.33	11.98	2.36	2.01	23.7	20.2	7.5	6.4	
		1.6	10.42	14.55	14.26	4.13	3.84	39.7	36.9	13.1	12.2	
		2.0	9.60	15.70	15.47	6.10	5.88	63.6	61.2	19.4	18.6	
1000	4000	1.2	8.33	9.56	8.78	1.23	0.45	14.7	5.4	3.9	1.4	
		1.6	9.18	10.81	9.76	1.62	0.58	17.7	6.3	5.1	1.8	
		2.0	9.68	11.12	9.99	1.44	0.31	14.9	3.2	4.6	1.0	
	5000	5000	1.2	10.81	12.24	11.39	1.43	0.58	13.2	5.4	4.5	1.8
			1.6	13.30	15.27	14.05	1.97	0.76	14.8	5.7	6.3	2.4
			2.0	15.22	17.01	15.57	1.79	0.34	11.7	2.2	5.7	1.1
	6000	6000	1.2	13.40	14.89	13.96	1.48	0.55	11.0	4.1	4.7	1.7
			1.6	17.84	19.51	18.11	1.67	0.27	9.3	1.5	5.3	0.9
			2.0	22.75	23.51	21.74	0.77	-1.01	3.4	-4.4	2.4	-3.2
	7000	7000	1.2	17.46	17.79	16.79	0.33	-0.67	1.9	-3.8	1.0	-2.1
			1.6	23.11	23.52	22.06	0.41	-1.05	1.8	-4.6	1.3	-3.3
			2.0	30.75	28.66	26.62	-2.08	-4.12	-6.8	-13.4	-6.6	-13.1
8000	8000	1.2	20.64	21.11	20.15	0.46	-0.49	2.2	-2.4	1.5	-1.6	
		1.6	25.86	25.33	24.09	-0.53	-1.76	-2.1	-6.8	-1.7	-5.6	

Added Unbalance (mg)	Rotor Speed (RPM)	Bias Current (Amps)	Dynamic Force Amplitude (N)			Error (N)		Error as Percent of Measured Force (%)		Error as Percent of Maximum Measured Force (%)		
			Meas'd	Basic	Char.	Basic	Char.	Basic	Char.	Basic	Char.	
	9000	2.0	31.54	28.16	26.66	-3.38	-4.88	-10.7	-15.5	-10.7	-15.5	
		1.2	20.22	19.92	19.91	-0.29	-0.31	-1.5	-1.5	-1.5	-1.5	
		1.6	18.02	16.94	17.31	-1.08	-0.71	-6.0	-3.9	-6.0	-3.9	
	10000	2.0	17.43	14.69	15.58	-2.74	-1.85	-15.7	-10.6	-15.7	-10.6	
		1.2	10.29	12.90	12.54	2.61	2.25	25.3	21.9	23.7	20.5	
		1.6	10.96	15.37	15.11	4.41	4.16	40.3	37.9	40.1	37.8	
			2.0	11.00	17.01	16.95	6.01	5.95	54.7	54.1	54.7	54.1
						<b>MAXIMUM</b>	<b>6.10</b>	<b>5.88</b>	<b>63.6</b>	<b>61.2</b>	<b>19.4</b>	<b>18.6</b>
						<b>MEAN</b>	<b>1.43</b>	<b>1.15</b>	<b>15.5</b>	<b>9.7</b>	<b>4.6</b>	<b>3.7</b>

**Table C.4: Platform 2 SetUp 3**

Added Unbalance (mg)	Rotor Speed (RPM)	Bias Current (Amps)	Dynamic Force Amplitude (N)			Error (N)		Error as Percent of Measured Force (%)		Error as Percent of Maximum Measured Force (%)	
			Meas'd	Basic	Char.	Basic	Char.	Basic	Char.	Basic	Char.
<b>0</b>	<b>4000</b>	<b>0.50</b>	2.70	6.77	1.68	4.07	-1.01	150.8	-37.6	9.8	-2.4
		<b>0.65</b>	2.72	9.25	1.33	6.53	-1.39	240.6	-51.0	15.7	-3.3
		<b>0.80</b>	2.40	12.13	2.19	9.73	-0.21	405.6	-8.8	23.4	-0.5
	<b>5000</b>	<b>0.50</b>	5.16	9.90	4.52	4.74	-0.65	91.7	-12.5	11.4	-1.6
		<b>0.65</b>	4.76	11.25	2.49	6.50	-2.27	136.6	-47.7	15.6	-5.5
		<b>0.80</b>	3.81	13.86	2.73	10.05	-1.09	263.6	-28.5	24.2	-2.6
	<b>6000</b>	<b>0.50</b>	11.44	18.03	12.96	6.59	1.53	57.6	13.3	15.9	3.7
		<b>0.65</b>	8.83	18.85	10.45	10.02	1.62	113.5	18.4	24.1	3.9
		<b>0.80</b>	5.28	17.08	5.04	11.80	-0.25	223.4	-4.7	28.4	-0.6
	<b>7000</b>	<b>0.50</b>	14.04	15.77	12.62	1.73	-1.42	12.3	-10.1	4.2	-3.4
		<b>0.65</b>	19.17	20.32	15.25	1.15	-3.92	6.0	-20.5	2.8	-9.4
		<b>0.80</b>	25.82	24.97	16.01	-0.85	-9.81	-3.3	-38.0	-2.0	-23.6
	<b>8000</b>	<b>0.50</b>	10.83	13.25	10.82	2.42	-0.01	22.3	-0.1	5.8	0.0
		<b>0.65</b>	11.89	14.96	11.15	3.07	-0.74	25.8	-6.2	7.4	-1.8
		<b>0.80</b>	12.91	17.69	10.15	4.79	-2.76	37.1	-21.4	11.5	-6.6
	<b>9000</b>	<b>0.50</b>	10.40	13.67	11.26	3.27	0.87	31.4	8.3	7.9	2.1
		<b>0.65</b>	10.40	14.91	10.51	4.51	0.10	43.4	1.0	10.9	0.3
		<b>0.80</b>	11.48	18.74	10.90	7.26	-0.58	63.3	-5.1	17.5	-1.4
<b>10000</b>	<b>0.50</b>	11.86	15.65	13.22	3.79	1.36	32.0	11.5	9.1	3.3	
	<b>0.65</b>	12.08	18.01	13.24	5.93	1.16	49.1	9.6	14.3	2.8	
	<b>0.80</b>	12.63	22.12	14.10	9.50	1.47	75.2	11.6	22.9	3.5	
<b>100</b>	<b>4000</b>	<b>0.50</b>	1.61	5.00	1.01	3.40	-0.59	211.7	-37.0	8.2	-1.4
		<b>0.65</b>	1.38	7.57	1.52	6.19	0.14	448.3	10.0	14.9	0.3
		<b>0.80</b>	1.28	11.01	2.69	9.73	1.41	762.1	110.4	23.4	3.4
	<b>5000</b>	<b>0.50</b>	3.96	6.92	3.23	2.96	-0.74	74.6	-18.6	7.1	-1.8
		<b>0.65</b>	2.63	8.71	1.42	6.08	-1.22	230.7	-46.1	14.6	-2.9
		<b>0.80</b>	1.92	11.87	2.08	9.94	0.16	516.7	8.1	23.9	0.4
	<b>6000</b>	<b>0.50</b>	10.30	15.63	10.74	5.32	0.44	51.7	4.3	12.8	1.1
		<b>0.65</b>	7.49	13.51	6.52	6.02	-0.97	80.3	-13.0	14.5	-2.3
		<b>0.80</b>	4.86	13.38	2.72	8.52	-2.14	175.3	-44.0	20.5	-5.1
	<b>7000</b>	<b>0.50</b>	16.87	19.20	14.01	2.33	-2.86	13.8	-17.0	5.6	-6.9
		<b>0.65</b>	23.11	24.66	16.28	1.56	-6.83	6.7	-29.5	3.8	-16.4
		<b>0.80</b>	33.06	30.50	17.88	-2.55	-15.17	-7.7	-45.9	-6.1	-36.5
	<b>8000</b>	<b>0.50</b>	14.03	17.36	13.36	3.34	-0.67	23.8	-4.7	8.0	-1.6
		<b>0.65</b>	15.49	19.42	13.51	3.93	-1.98	25.4	-12.8	9.5	-4.8
		<b>0.80</b>	16.76	20.92	12.36	4.16	-4.40	24.8	-26.3	10.0	-10.6
	<b>9000</b>	<b>0.50</b>	13.44	17.06	13.98	3.62	0.54	26.9	4.0	8.7	1.3
		<b>0.65</b>	13.86	18.15	13.32	4.29	-0.54	31.0	-3.9	10.3	-1.3
		<b>0.80</b>	13.67	19.93	12.53	6.26	-1.14	45.8	-8.3	15.1	-2.7

Added Unbalance (mg)	Rotor Speed (RPM)	Bias Current (Amps)	Dynamic Force Amplitude (N)			Error (N)		Error as Percent of Measured Force (%)		Error as Percent of Maximum Measured Force (%)			
			Meas'd	Basic	Char.	Basic	Char.	Basic	Char.	Basic	Char.		
10000	10000	0.50	13.75	18.00	15.81	4.25	2.05	30.9	14.9	10.2	4.9		
		0.65	13.97	19.23	15.18	5.27	1.22	37.7	8.7	12.7	2.9		
		0.80	14.35	21.30	13.65	6.95	-0.70	48.4	-4.9	16.7	-1.7		
200	4000	0.50	2.04	4.21	1.98	2.16	-0.06	106.0	-3.0	5.2	-0.1		
		0.65	1.31	6.64	2.18	5.33	0.87	407.7	66.5	12.8	2.1		
		0.80	0.83	11.04	2.65	10.22	1.82	1236.7	220.2	24.6	4.4		
	5000	0.50	5.05	6.99	4.95	1.94	-0.10	38.5	-2.0	4.7	-0.2		
		0.65	3.56	7.47	3.05	3.91	-0.50	110.1	-14.1	9.4	-1.2		
		0.80	1.96	10.46	2.79	8.50	0.83	434.2	42.4	20.5	2.0		
	6000	0.50	13.48	18.28	14.08	4.80	0.60	35.6	4.4	11.5	1.4		
		0.65	10.73	14.97	10.79	4.23	0.06	39.5	0.6	10.2	0.1		
		0.80	8.38	11.41	4.88	3.04	-3.50	36.3	-41.8	7.3	-8.4		
	7000	0.50	20.64	22.47	16.78	1.83	-3.86	8.9	-18.7	4.4	-9.3		
		0.65	28.44	28.50	19.14	0.06	-9.31	0.2	-32.7	0.1	-22.4		
		0.80	41.55	35.01	21.08	-6.53	-20.47	-15.7	-49.3	-15.7	-49.3		
	8000	0.50	16.27	19.59	15.16	3.32	-1.11	20.4	-6.8	16.8	-5.6		
		0.65	17.87	21.70	15.26	3.83	-2.60	21.5	-14.6	19.4	-13.2		
		0.80	19.75	22.94	13.83	3.19	-5.92	16.1	-30.0	16.1	-30.0		
	9000	0.50	14.66	18.57	15.32	3.91	0.67	26.7	4.5	25.2	4.3		
		0.65	15.21	19.20	14.34	4.00	-0.87	26.3	-5.7	25.8	-5.6		
		0.80	15.48	20.59	13.06	5.11	-2.42	33.0	-15.6	33.0	-15.6		
	10000	0.50	14.61	18.22	16.40	3.61	1.79	24.7	12.3	24.7	12.3		
		0.65	14.60	19.02	15.26	4.42	0.66	30.3	4.5	30.3	4.5		
		0.80	14.48	19.95	13.15	5.48	-1.33	37.8	-9.2	37.8	-9.2		
							<b>MAXIMUM</b>	<b>11.80</b>	<b>20.47</b>	<b>1236.7</b>	<b>220.2</b>	<b>37.8</b>	<b>49.3</b>
							<b>MEAN</b>	<b>4.99</b>	<b>2.21</b>	<b>121.7</b>	<b>22.8</b>	<b>14.2</b>	<b>6.3</b>

**Table C.5: Platform 2 SetUp 4**

Added Unbalance (mg)	Rotor Speed (RPM)	Bias Current (Amps)	Dynamic Force Amplitude (N)			Error (N)		Error as Percent of Measured Force (%)		Error as Percent of Maximum Measured Force (%)		
			Meas'd	Basic	Char.	Basic	Char.	Basic	Char.	Basic	Char.	
0	4000	1.4	5.82	6.70	6.17	0.89	0.36	15.2	6.2	2.1	0.9	
		1.7	6.02	7.32	6.31	1.30	0.29	21.6	4.8	3.1	0.7	
		2.0	6.03	7.76	6.13	1.73	0.10	28.6	1.6	4.1	0.2	
	5000	1.4	8.78	9.09	9.13	0.30	0.34	3.4	3.9	0.7	0.8	
		1.7	9.85	10.27	9.97	0.43	0.12	4.3	1.2	1.0	0.3	
		2.0	10.36	10.95	10.12	0.59	-0.23	5.7	-2.3	1.4	-0.6	
	6000	1.4	11.52	10.85	11.64	-0.67	0.12	-5.9	1.0	-1.6	0.3	
		1.7	14.54	13.18	14.10	-1.36	-0.44	-9.3	-3.0	-3.3	-1.1	
		2.0	16.66	14.78	15.66	-1.88	-1.00	-11.3	-6.0	-4.5	-2.4	
	7000	1.4	15.46	12.87	14.00	-2.59	-1.46	-16.7	-9.5	-6.2	-3.5	
		1.7	20.67	16.15	17.84	-4.52	-2.83	-21.9	-13.7	-10.8	-6.8	
		2.0	26.56	19.27	21.62	-7.29	-4.94	-27.4	-18.6	-17.5	-11.9	
	8000	1.4	18.85	18.56	18.78	-0.28	-0.06	-1.5	-0.3	-0.6	-0.1	
		1.7	20.92	20.20	20.44	-0.73	-0.48	-3.5	-2.3	-1.6	-1.1	
		2.0	22.85	21.65	21.76	-1.20	-1.09	-5.3	-4.8	-2.7	-2.4	
	9000	1.4	23.81	26.28	25.19	2.47	1.39	10.4	5.8	5.5	3.1	
		1.7	22.23	25.25	23.88	3.02	1.64	13.6	7.4	6.7	3.6	
		2.0	20.60	24.41	22.58	3.81	1.98	18.5	9.6	8.4	4.4	
	10000	1.4	27.66	30.75	29.01	3.09	1.36	11.2	4.9	6.9	3.0	
		1.7	25.07	29.29	27.20	4.21	2.13	16.8	8.5	9.4	4.7	
		2.0	22.94	28.62	26.01	5.68	3.07	24.8	13.4	12.6	6.8	
	200	4000	1.4	7.72	8.81	8.10	1.10	0.38	14.2	4.9	2.4	0.8
			1.7	7.71	9.44	8.21	1.74	0.50	22.5	6.5	3.9	1.1
			2.0	7.85	9.94	8.00	2.09	0.14	26.6	1.8	4.6	0.3
5000		1.4	11.61	12.34	12.08	0.73	0.47	6.3	4.1	1.6	1.0	
		1.7	12.59	13.70	13.07	1.11	0.48	8.8	3.8	2.5	1.1	
		2.0	13.41	14.70	13.45	1.29	0.04	9.6	0.3	2.9	0.1	
6000		1.4	15.36	14.82	15.30	-0.54	-0.05	-3.5	-0.3	-1.2	-0.1	
		1.7	18.91	17.87	18.32	-1.04	-0.59	-5.5	-3.1	-2.3	-1.3	
		2.0	22.15	20.18	20.42	-1.96	-1.73	-8.9	-7.8	-4.4	-3.8	
7000		1.4	19.03	15.88	16.97	-3.15	-2.06	-16.5	-10.8	-7.0	-4.6	
		1.7	24.44	19.36	20.99	-5.08	-3.45	-20.8	-14.1	-11.3	-7.7	
		2.0	31.49	23.06	25.34	-8.43	-6.15	-26.8	-19.5	-18.7	-13.6	
8000		1.4	19.65	18.86	19.43	-0.79	-0.22	-4.0	-1.1	-1.6	-0.5	
		1.7	22.26	20.62	21.37	-1.65	-0.90	-7.4	-4.0	-3.4	-1.8	
		2.0	24.17	21.41	22.26	-2.76	-1.91	-11.4	-7.9	-5.6	-3.9	
9000		1.4	23.11	25.40	24.54	2.29	1.43	9.9	6.2	4.7	2.9	
		1.7	21.86	24.57	23.39	2.70	1.52	12.4	7.0	5.5	3.1	
		2.0	20.79	24.24	22.64	3.45	1.85	16.6	8.9	7.0	3.8	

Added Unbalance (mg)	Rotor Speed (RPM)	Bias Current (Amps)	Dynamic Force Amplitude (N)			Error (N)		Error as Percent of Measured Force (%)		Error as Percent of Maximum Measured Force (%)		
			Meas'd	Basic	Char.	Basic	Char.	Basic	Char.	Basic	Char.	
	10000	1.4	27.40	30.73	29.00	3.33	1.60	12.2	5.8	6.8	3.3	
		1.7	24.92	29.56	27.48	4.64	2.56	18.6	10.3	9.5	5.2	
		2.0	22.95	29.29	26.64	6.34	3.69	27.6	16.1	12.9	7.5	
300	4000	1.4	8.52	9.93	9.14	1.41	0.62	16.5	7.3	2.9	1.3	
		1.7	8.76	10.47	9.14	1.71	0.38	19.6	4.3	3.5	0.8	
		2.0	8.79	10.91	8.88	2.12	0.09	24.1	1.0	4.3	0.2	
	5000	1.4	12.96	14.04	13.70	1.08	0.74	8.4	5.7	2.2	1.5	
		1.7	14.56	15.67	14.87	1.11	0.31	7.6	2.1	2.3	0.6	
		2.0	15.07	16.58	15.19	1.51	0.12	10.0	0.8	3.1	0.2	
	6000	1.4	17.59	17.11	17.48	-0.48	-0.11	-2.7	-0.6	-1.0	-0.2	
		1.7	21.61	20.86	21.11	-0.76	-0.50	-3.5	-2.3	-1.5	-1.0	
		2.0	25.27	23.65	23.60	-1.62	-1.67	-6.4	-6.6	-3.3	-3.4	
	7000	1.4	21.27	18.19	19.20	-3.09	-2.08	-14.5	-9.8	-6.3	-4.2	
		1.7	27.94	22.33	23.87	-5.61	-4.07	-20.1	-14.6	-11.5	-8.3	
		2.0	34.98	26.27	28.45	-8.71	-6.52	-24.9	-18.7	-17.8	-13.3	
	8000	1.4	20.60	19.50	20.17	-1.11	-0.43	-5.4	-2.1	-2.3	-0.9	
		1.7	23.95	21.71	22.73	-2.24	-1.21	-9.3	-5.1	-4.6	-2.5	
		2.0	25.86	22.26	23.45	-3.60	-2.41	-13.9	-9.3	-7.4	-4.9	
	9000	1.4	22.80	25.16	24.39	2.36	1.59	10.3	7.0	4.8	3.2	
		1.7	21.39	24.14	23.16	2.76	1.77	12.9	8.3	5.6	3.6	
		2.0	20.75	24.02	22.62	3.27	1.87	15.8	9.0	6.7	3.8	
	10000	1.4	27.81	31.26	29.54	3.45	1.73	12.4	6.2	7.0	3.5	
		1.7	24.72	29.75	27.67	5.03	2.95	20.3	11.9	10.3	6.0	
		2.0	23.19	29.67	27.08	6.48	3.88	27.9	16.7	13.2	7.9	
	400	4000	1.4	9.54	10.87	9.99	1.32	0.45	13.9	4.7	2.7	0.9
			1.7	9.66	11.51	10.13	1.85	0.47	19.1	4.9	3.8	1.0
			2.0	9.55	11.86	9.74	2.31	0.19	24.2	2.0	4.7	0.4
5000		1.4	14.70	15.86	15.41	1.16	0.71	7.9	4.9	2.4	1.5	
		1.7	16.01	17.28	16.39	1.27	0.38	7.9	2.4	2.6	0.8	
		2.0	16.54	18.16	16.59	1.62	0.05	9.8	0.3	3.3	0.1	
6000		1.4	20.11	19.56	19.78	-0.55	-0.33	-2.8	-1.6	-1.1	-0.7	
		1.7	24.38	23.13	23.28	-1.25	-1.11	-5.1	-4.5	-2.6	-2.3	
		2.0	27.72	26.18	26.00	-1.54	-1.72	-5.6	-6.2	-3.1	-3.5	
7000		1.4	24.23	20.60	21.55	-3.63	-2.68	-15.0	-11.1	-7.4	-5.5	
		1.7	30.49	24.55	26.02	-5.94	-4.47	-19.5	-14.7	-12.1	-9.1	
		2.0	37.78	28.78	30.84	-9.00	-6.94	-23.8	-18.4	-18.4	-14.2	
8000		1.4	22.37	20.79	21.59	-1.58	-0.78	-7.1	-3.5	-3.2	-1.6	
		1.7	25.25	22.51	23.64	-2.75	-1.61	-10.9	-6.4	-5.6	-3.3	
		2.0	27.44	23.37	24.82	-4.07	-2.62	-14.8	-9.5	-8.3	-5.3	
9000		1.4	22.83	24.95	24.26	2.11	1.43	9.3	6.3	4.3	2.9	

Added Unbalance (mg)	Rotor Speed (RPM)	Bias Current (Amps)	Dynamic Force Amplitude (N)			Error (N)		Error as Percent of Measured Force (%)		Error as Percent of Maximum Measured Force (%)		
			Meas'd	Basic	Char.	Basic	Char.	Basic	Char.	Basic	Char.	
		1.7	21.41	24.20	23.33	2.80	1.92	13.1	9.0	5.7	3.9	
		2.0	20.99	24.09	22.85	3.10	1.86	14.8	8.9	6.3	3.8	
		1.4	27.80	31.04	29.36	3.23	1.56	11.6	5.6	6.6	3.2	
	10000	1.7	25.42	30.33	28.27	4.90	2.85	19.3	11.2	10.0	5.8	
		2.0	23.78	30.28	27.68	6.50	3.90	27.3	16.4	13.3	8.0	
		1.4	10.59	12.01	11.06	1.43	0.48	13.5	4.5	2.9	1.0	
500	4000	1.7	10.74	12.51	11.01	1.77	0.28	16.5	2.6	3.6	0.6	
		2.0	10.71	13.01	10.86	2.30	0.15	21.5	1.4	4.7	0.3	
		1.4	16.44	17.54	17.01	1.10	0.57	6.7	3.5	2.3	1.2	
	5000	1.7	17.74	19.15	18.14	1.41	0.40	8.0	2.3	2.9	0.8	
		2.0	18.68	20.10	18.43	1.42	-0.25	7.6	-1.3	2.9	-0.5	
		1.4	22.57	22.09	22.23	-0.48	-0.34	-2.1	-1.5	-1.0	-0.7	
	6000	1.7	27.39	26.23	26.21	-1.16	-1.18	-4.2	-4.3	-2.4	-2.4	
		2.0	30.96	29.45	29.14	-1.51	-1.83	-4.9	-5.9	-3.1	-3.7	
		1.4	26.96	23.08	24.00	-3.88	-2.96	-14.4	-11.0	-7.9	-6.0	
	7000	1.7	33.54	27.51	28.88	-6.03	-4.65	-18.0	-13.9	-12.3	-9.5	
		2.0	41.71	31.89	33.85	-9.83	-7.86	-23.6	-18.9	-20.1	-16.1	
		1.4	24.23	22.20	23.09	-2.03	-1.13	-8.4	-4.7	-4.1	-2.3	
	8000	1.7	27.25	23.93	25.21	-3.32	-2.04	-12.2	-7.5	-6.8	-4.2	
		2.0	29.68	24.70	26.37	-4.98	-3.32	-16.8	-11.2	-10.2	-6.8	
		1.4	22.88	24.97	24.42	2.09	1.54	9.1	6.7	4.3	3.1	
	9000	1.7	21.65	23.94	23.19	2.29	1.54	10.6	7.1	4.7	3.2	
		2.0	21.29	24.12	23.07	2.83	1.78	13.3	8.4	5.8	3.6	
		1.4	28.04	31.61	29.91	3.57	1.87	12.7	6.7	7.3	3.8	
	10000	1.7	25.63	30.75	28.71	5.12	3.08	20.0	12.0	10.5	6.3	
		2.0	23.93	30.60	27.99	6.66	4.06	27.8	17.0	13.6	8.3	
		1.4	11.60	13.09	12.11	1.49	0.51	12.9	4.4	3.0	1.0	
	600	4000	1.7	11.81	13.61	12.08	1.80	0.27	15.2	2.3	3.7	0.6
			2.0	11.68	13.88	11.63	2.20	-0.05	18.8	-0.4	4.5	-0.1
			1.4	18.11	19.12	18.52	1.02	0.42	5.6	2.3	2.1	0.8
5000		1.7	19.59	20.96	19.92	1.37	0.33	7.0	1.7	2.8	0.7	
		2.0	20.07	22.10	20.76	2.03	0.69	10.1	3.4	4.1	1.4	
		1.4	24.82	24.29	24.35	-0.52	-0.47	-2.1	-1.9	-1.1	-1.0	
6000		1.7	29.78	28.74	28.60	-1.04	-1.17	-3.5	-3.9	-2.1	-2.4	
		2.0	33.97	32.24	31.77	-1.73	-2.21	-5.1	-6.5	-3.5	-4.5	
		1.4	29.34	25.29	26.13	-4.05	-3.20	-13.8	-10.9	-8.3	-6.5	
7000		1.7	36.87	30.27	31.59	-6.61	-5.28	-17.9	-14.3	-13.5	-10.8	
		2.0	45.07	35.00	36.86	-10.08	-8.21	-22.4	-18.2	-20.6	-16.8	
		1.4	25.88	23.52	24.44	-2.36	-1.44	-9.1	-5.6	-4.8	-2.9	
8000	1.7	29.21	25.46	26.82	-3.75	-2.39	-12.8	-8.2	-7.7	-4.9		

Added Unbalance (mg)	Rotor Speed (RPM)	Bias Current (Amps)	Dynamic Force Amplitude (N)			Error (N)		Error as Percent of Measured Force (%)		Error as Percent of Maximum Measured Force (%)		
			Meas'd	Basic	Char.	Basic	Char.	Basic	Char.	Basic	Char.	
	9000	2.0	32.27	26.48	28.30	-5.79	-3.97	-17.9	-12.3	-11.8	-8.1	
		1.4	23.30	25.24	24.78	1.94	1.48	8.3	6.3	4.0	3.0	
		1.7	22.06	24.22	23.61	2.17	1.56	9.8	7.1	4.4	3.2	
	10000	2.0	21.10	23.66	22.72	2.55	1.62	12.1	7.7	5.2	3.3	
		1.4	28.37	32.19	30.51	3.82	2.14	13.5	7.6	7.8	4.4	
		1.7	25.74	31.15	29.11	5.40	3.36	21.0	13.1	11.0	6.9	
		4000	2.0	24.44	31.16	28.58	6.72	4.15	27.5	17.0	13.7	8.5
			1.4	12.53	14.18	13.14	1.64	0.61	13.1	4.8	3.4	1.2
			1.7	12.70	14.61	13.02	1.90	0.31	15.0	2.5	3.9	0.6
700	5000	2.0	12.75	14.98	12.72	2.23	-0.02	17.5	-0.2	4.6	0.0	
		1.4	19.50	20.90	20.22	1.40	0.73	7.2	3.7	2.9	1.5	
		1.7	21.56	22.90	21.77	1.34	0.21	6.2	1.0	2.7	0.4	
	6000	2.0	22.50	24.07	22.25	1.57	-0.25	7.0	-1.1	3.2	-0.5	
		1.4	27.44	26.77	26.78	-0.67	-0.66	-2.4	-2.4	-1.4	-1.3	
		1.7	32.88	31.63	31.42	-1.25	-1.45	-3.8	-4.4	-2.5	-3.0	
	7000	2.0	37.19	35.33	34.75	-1.85	-2.44	-5.0	-6.6	-3.8	-5.0	
		1.4	32.12	27.93	28.73	-4.18	-3.39	-13.0	-10.6	-8.5	-6.9	
		1.7	40.52	33.48	34.72	-7.04	-5.81	-17.4	-14.3	-14.4	-11.9	
8000	2.0	48.99	38.27	40.02	-10.73	-8.97	-21.9	-18.3	-21.9	-18.3		
	1.4	28.19	25.43	26.41	-2.76	-1.78	-9.8	-6.3	-6.3	-4.0		
	1.7	31.73	27.59	29.03	-4.15	-2.71	-13.1	-8.5	-9.4	-6.1		
9000	2.0	34.90	28.63	30.56	-6.26	-4.34	-17.9	-12.4	-14.2	-9.8		
	1.4	24.26	26.01	25.69	1.74	1.43	7.2	5.9	3.9	3.2		
	1.7	23.25	24.96	24.52	1.71	1.26	7.3	5.4	3.9	2.9		
10000	2.0	22.32	24.29	23.57	1.97	1.26	8.8	5.6	4.5	2.8		
	1.4	29.11	32.94	31.24	3.83	2.13	13.1	7.3	8.7	4.8		
	1.7	26.63	31.93	29.88	5.30	3.24	19.9	12.2	12.0	7.3		
	4000	2.0	24.43	31.54	29.03	7.11	4.60	29.1	18.8	16.1	10.4	
		1.5	13.63	15.61	14.38	1.98	0.75	14.5	5.5	4.5	1.7	
		1.6	13.81	15.73	14.29	1.92	0.48	13.9	3.4	4.3	1.1	
800	5000	1.7	13.90	15.83	14.19	1.93	0.29	13.9	2.1	4.4	0.7	
		1.5	21.78	23.59	22.72	1.81	0.94	8.3	4.3	4.1	2.1	
		1.6	23.07	24.41	23.35	1.34	0.28	5.8	1.2	3.0	0.6	
	6000	1.7	23.63	25.00	23.77	1.37	0.14	5.8	0.6	3.1	0.3	
		1.5	32.02	31.14	30.99	-0.89	-1.03	-2.8	-3.2	-2.0	-2.3	
		1.6	34.00	33.12	32.95	-0.88	-1.05	-2.6	-3.1	-2.0	-2.4	
	7000	1.7	36.04	34.68	34.38	-1.36	-1.66	-3.8	-4.6	-3.1	-3.8	
		1.5	37.81	32.44	33.29	-5.37	-4.51	-14.2	-11.9	-12.2	-10.2	
		1.6	41.22	34.66	35.65	-6.56	-5.57	-15.9	-13.5	-14.8	-12.6	
		1.7	44.16	36.84	38.00	-7.32	-6.16	-16.6	-13.9	-16.6	-13.9	

Added Unbalance (mg)	Rotor Speed (RPM)	Bias Current (Amps)	Dynamic Force Amplitude (N)			Error (N)		Error as Percent of Measured Force (%)		Error as Percent of Maximum Measured Force (%)	
			Meas'd	Basic	Char.	Basic	Char.	Basic	Char.	Basic	Char.
8000	1.5	1.5	31.85	28.28	29.46	-3.57	-2.39	-11.2	-7.5	-10.4	-7.0
	1.6	1.6	33.25	29.15	30.46	-4.10	-2.79	-12.3	-8.4	-11.9	-8.1
	1.7	1.7	34.32	29.69	31.18	-4.63	-3.14	-13.5	-9.2	-13.5	-9.2
9000	1.5	1.5	24.88	26.39	26.15	1.51	1.27	6.1	5.1	5.1	4.3
	1.6	1.6	24.37	26.02	25.74	1.64	1.36	6.7	5.6	5.6	4.6
	1.7	1.7	23.98	25.66	25.37	1.68	1.38	7.0	5.8	5.7	4.7
10000	1.5	1.5	29.55	34.38	32.57	4.82	3.01	16.3	10.2	16.3	10.2
	1.6	1.6	28.49	33.66	31.78	5.16	3.28	18.1	11.5	18.1	11.5
	1.7	1.7	27.12	33.17	31.15	6.05	4.03	22.3	14.9	22.3	14.9
			<b>MAXIMUM</b>			<b>9.83</b>	<b>7.86</b>	<b>28.6</b>	<b>19.5</b>	<b>20.1</b>	<b>16.1</b>
			<b>MEAN</b>			<b>2.78</b>	<b>1.63</b>	<b>13.4</b>	<b>6.9</b>	<b>5.8</b>	<b>3.4</b>

**Table C.6: Platform 2 SetUp 3 (perturbed model)**

Added Unbalance (mg)	Rotor Speed (RPM)	Bias Current (Amps)	Dynamic Force Amplitude (N)			Error (N)		Error as Percent of Measured Force (%)		Error as Percent of Maximum Measured Force (%)		
			Meas'd	Basic	Char.	Basic	Char.	Basic	Char.	Basic	Char.	
0	4000	0.50	2.70	6.77	1.68	4.07	-1.01	150.8	-37.6	9.8	-2.4	
		0.65	2.72	9.25	1.33	6.53	-1.39	240.6	-51.0	15.7	-3.3	
		0.80	2.40	12.13	2.19	9.73	-0.21	405.6	-8.8	23.4	-0.5	
	5000	0.50	5.16	9.90	4.52	4.74	-0.65	91.7	-12.5	11.4	-1.6	
		0.65	4.76	11.25	2.49	6.50	-2.27	136.6	-47.7	15.6	-5.5	
		0.80	3.81	13.86	2.73	10.05	-1.09	263.6	-28.5	24.2	-2.6	
	6000	0.50	11.44	18.03	12.96	6.59	1.53	57.6	13.3	15.9	3.7	
		0.65	8.83	18.85	10.45	10.02	1.62	113.5	18.4	24.1	3.9	
		0.80	5.28	17.08	5.04	11.80	-0.25	223.4	-4.7	28.4	-0.6	
	7000	0.50	14.04	15.77	12.62	1.73	-1.42	12.3	-10.1	4.2	-3.4	
		0.65	19.17	20.32	15.25	1.15	-3.92	6.0	-20.5	2.8	-9.4	
		0.80	25.82	24.97	16.01	-0.85	-9.81	-3.3	-38.0	-2.0	-23.6	
	8000	0.50	10.83	13.25	10.82	2.42	-0.01	22.3	-0.1	5.8	0.0	
		0.65	11.89	14.96	11.15	3.07	-0.74	25.8	-6.2	7.4	-1.8	
		0.80	12.91	17.69	10.15	4.79	-2.76	37.1	-21.4	11.5	-6.6	
	9000	0.50	10.40	13.67	11.26	3.27	0.87	31.4	8.3	7.9	2.1	
		0.65	10.40	14.91	10.51	4.51	0.10	43.4	1.0	10.9	0.3	
		0.80	11.48	18.74	10.90	7.26	-0.58	63.3	-5.1	17.5	-1.4	
	10000	0.50	11.86	15.65	13.22	3.79	1.36	32.0	11.5	9.1	3.3	
		0.65	12.08	18.01	13.24	5.93	1.16	49.1	9.6	14.3	2.8	
		0.80	12.63	22.12	14.10	9.50	1.47	75.2	11.6	22.9	3.5	
	100	4000	0.50	1.61	5.00	1.01	3.40	-0.59	211.7	-37.0	8.2	-1.4
			0.65	1.38	7.57	1.52	6.19	0.14	448.3	10.0	14.9	0.3
			0.80	1.28	11.01	2.69	9.73	1.41	762.1	110.4	23.4	3.4
5000		0.50	3.96	6.92	3.23	2.96	-0.74	74.6	-18.6	7.1	-1.8	
		0.65	2.63	8.71	1.42	6.08	-1.22	230.7	-46.1	14.6	-2.9	
		0.80	1.92	11.87	2.08	9.94	0.16	516.7	8.1	23.9	0.4	
6000		0.50	10.30	15.63	10.74	5.32	0.44	51.7	4.3	12.8	1.1	
		0.65	7.49	13.51	6.52	6.02	-0.97	80.3	-13.0	14.5	-2.3	
		0.80	4.86	13.38	2.72	8.52	-2.14	175.3	-44.0	20.5	-5.1	
7000		0.50	16.87	19.20	14.01	2.33	-2.86	13.8	-17.0	5.6	-6.9	
		0.65	23.11	24.66	16.28	1.56	-6.83	6.7	-29.5	3.8	-16.4	
		0.80	33.06	30.50	17.88	-2.55	-15.17	-7.7	-45.9	-6.1	-36.5	
8000		0.50	14.03	17.36	13.36	3.34	-0.67	23.8	-4.7	8.0	-1.6	
		0.65	15.49	19.42	13.51	3.93	-1.98	25.4	-12.8	9.5	-4.8	
		0.80	16.76	20.92	12.36	4.16	-4.40	24.8	-26.3	10.0	-10.6	
9000		0.50	13.44	17.06	13.98	3.62	0.54	26.9	4.0	8.7	1.3	
		0.65	13.86	18.15	13.32	4.29	-0.54	31.0	-3.9	10.3	-1.3	
		0.80	13.67	19.93	12.53	6.26	-1.14	45.8	-8.3	15.1	-2.7	

Added Unbalance (mg)	Rotor Speed (RPM)	Bias Current (Amps)	Dynamic Force Amplitude (N)			Error (N)		Error as Percent of Measured Force (%)		Error as Percent of Maximum Measured Force (%)		
			Meas'd	Basic	Char.	Basic	Char.	Basic	Char.	Basic	Char.	
10000	10000	0.50	13.75	18.00	15.81	4.25	2.05	30.9	14.9	10.2	4.9	
		0.65	13.97	19.23	15.18	5.27	1.22	37.7	8.7	12.7	2.9	
		0.80	14.35	21.30	13.65	6.95	-0.70	48.4	-4.9	16.7	-1.7	
200	4000	0.50	2.04	4.21	1.98	2.16	-0.06	106.0	-3.0	5.2	-0.1	
		0.65	1.31	6.64	2.18	5.33	0.87	407.7	66.5	12.8	2.1	
		0.80	0.83	11.04	2.65	10.22	1.82	1236.7	220.2	24.6	4.4	
	5000	0.50	5.05	6.99	4.95	1.94	-0.10	38.5	-2.0	4.7	-0.2	
		0.65	3.56	7.47	3.05	3.91	-0.50	110.1	-14.1	9.4	-1.2	
		0.80	1.96	10.46	2.79	8.50	0.83	434.2	42.4	20.5	2.0	
	6000	0.50	13.48	18.28	14.08	4.80	0.60	35.6	4.4	11.5	1.4	
		0.65	10.73	14.97	10.79	4.23	0.06	39.5	0.6	10.2	0.1	
		0.80	8.38	11.41	4.88	3.04	-3.50	36.3	-41.8	7.3	-8.4	
	7000	0.50	20.64	22.47	16.78	1.83	-3.86	8.9	-18.7	4.4	-9.3	
		0.65	28.44	28.50	19.14	0.06	-9.31	0.2	-32.7	0.1	-22.4	
		0.80	41.55	35.01	21.08	-6.53	-20.47	-15.7	-49.3	-15.7	-49.3	
	8000	0.50	16.27	19.59	15.16	3.32	-1.11	20.4	-6.8	16.8	-5.6	
		0.65	17.87	21.70	15.26	3.83	-2.60	21.5	-14.6	19.4	-13.2	
		0.80	19.75	22.94	13.83	3.19	-5.92	16.1	-30.0	16.1	-30.0	
	9000	0.50	14.66	18.57	15.32	3.91	0.67	26.7	4.5	25.2	4.3	
		0.65	15.21	19.20	14.34	4.00	-0.87	26.3	-5.7	25.8	-5.6	
		0.80	15.48	20.59	13.06	5.11	-2.42	33.0	-15.6	33.0	-15.6	
	10000	0.50	14.61	18.22	16.40	3.61	1.79	24.7	12.3	24.7	12.3	
		0.65	14.60	19.02	15.26	4.42	0.66	30.3	4.5	30.3	4.5	
		0.80	14.48	19.95	13.15	5.48	-1.33	37.8	-9.2	37.8	-9.2	
	<b>MAXIMUM</b>						<b>11.80</b>	<b>20.47</b>	<b>1236.7</b>	<b>220.2</b>	<b>37.8</b>	<b>49.3</b>
	<b>MEAN</b>						<b>4.99</b>	<b>2.21</b>	<b>121.7</b>	<b>22.8</b>	<b>14.2</b>	<b>6.3</b>

## Vita

Robert Jack Prins received a Bachelor of Science in Mechanical Engineering from Michigan Tech in 1993 and a Master of Science in Mechanical Engineering from the University of Virginia in 1996. He worked in industry at Perceptron Inc (located in Plymouth, MI) and Visteon Inc, Chassis Systems (located in Dearborn, MI) until starting the Ph.D. program at Virginia Tech. He also held a adjunct faculty position at Washtenaw Community College (in Ann Arbor, MI).